Lecture Notes in Applied and Computational Mechanics 95

Aurora Angela Pisano
Konstantinos Vassilios Spiliopoulos
Dieter Weichert *Editors*

Direct Methods

Methodological Progress and Engineering Applications

Springer

Lecture Notes in Applied and Computational Mechanics

Volume 95

This series aims to report new developments in applied and computational mechanics - quickly, informally and at a high level. This includes the fields of fluid, solid and structural mechanics, dynamics and control, and related disciplines. The applied methods can be of analytical, numerical and computational nature. The series scope includes monographs, professional books, selected contributions from specialized conferences or workshops, edited volumes, as well as outstanding advanced textbooks.

Indexed by EI-Compendex, SCOPUS, Zentralblatt Math, Ulrich's, Current Mathematical Publications, Mathematical Reviews and MetaPress.

More information about this series at http://www.springer.com/series/4623

Aurora Angela Pisano ·
Konstantinos Vassilios Spiliopoulos ·
Dieter Weichert
Editors

Direct Methods

Methodological Progress and Engineering Applications

Springer

Editors
Aurora Angela Pisano
PAU
University Mediterranea of Reggio Calabria
Reggio Calabria, Italy

Dieter Weichert
IAM
RWTH Aachen University
Aachen, Germany

Konstantinos Vassilios Spiliopoulos
Institute of Structural Analysis &
Antiseismic Research, National Technical
University of Athens
Athens, Greece

ISSN 1613-7736 ISSN 1860-0816 (electronic)
Lecture Notes in Applied and Computational Mechanics
ISBN 978-3-030-48833-8 ISBN 978-3-030-48834-5 (eBook)
https://doi.org/10.1007/978-3-030-48834-5

Foreword

When Maximilian Tytus Huber published in 1904 his work entitled "Specific work of strain as a measure of material effort" (in Polish), he probably did not realize what effect this article would have on the development of the theory of plasticity. His pioneering work opened the prospect of an extraordinary development of this field of knowledge, both in the context of constitutive modeling of materials, and in the context of direct methods in mechanics. The same approach, based on the concept of shear energy as the driving force of inelastic deformation, has been independently applied by von Mises (1913) and Hencky (1924). For this reason, the most popular yield function ever is called Huber-von Mises-Hencky (HMH). This shows that great discoveries have often a multinational dimension, and when all the components are there, the breakthrough is shared by many enlightened minds, working independently of each other.

The HMH yield function was at the origin of expansion of the constitutive models, starting from the simplest one—the perfect rigid-plastic model. Even if the model was preceded by the Nadai (1923), as well as the Hencky (1924) and Ilyushin (1943) deformation theory, the real breakthrough came with the von Mises (1913) flow theory (inspired by the work of Levy, 1870), that involved the HMH yield function, and—finally—gave birth to the Prandtl (1924) and Reuss (1930) theory of plastic flow for the elastic-perfectly plastic continuum. From this moment on, a bifurcation has been observed, with the constitutive models of materials (including highly dissipative phenomena) developing in one way, and the direct methods in mechanics following their own way, involving the classical theorems of limit loads and the problems of adaptation (shakedown) to cyclic loads. In particular, more and more advanced constitutive models involve such phenomena like the evolution of microstructure, the phase transformations, the evolution of micro-damage or non-standard modes of inelastic behavior, whereas the direct methods address the variables and the limits set to determine the structural safety. Thus, modern, physically based, multiscale constitutive models of materials are usually built by using local approach, and are defined at the level of a point, whereas, the direct methods apply to the structure as a whole.

The first ideas related to the so-called load carrying capacity may be traced back to the eighteenth century, however—historically—the first limit carrying capacity (LCC) of structures was calculated by Kazinczy (1914), Kist (1917), and Ingerslev (1923). A major contribution was brought by Hill (1951, 1952), Prager (1951, 1952), and Drucker (1954). The limit load was defined for a structure made of rigid-plastic hardening material as the yield stress load. It is accompanied by an infinitesimal deformation of the structure. Prager (1952, 1955) used another definition, based on the elastic-perfectly plastic material. The limit load was interpreted as such a load that results in unconstrained plastic flow. Based on these approaches, the so-called extremum theorems of limit analysis were established for the structures made of rigid-plastic material and subjected to quasistatic loads. The theorems refer to the statically admissible stress fields or the kinematically admissible displacement fields, accompanying the mechanism of plastic collapse of a rigid-plastic body, and constituting the lower and the upper bounds of the limit load. The extremum theorems corresponding to the HMH yield surface were proved by Hill (1956, 1957), and extended to large strains in 1958. Another way of establishing the limit loads based on the rigid-perfectly plastic model was the so-called method of characteristics, formulated by Hencky (1923) and Prandtl (1923), and followed by Geiringer (1930), Geiringer and Prager (1933), Sokolovsky (1950, 1958), Shield (1953), Mróz (1967), Kachanov (1969), Dietrich (1970), Szczepiński (1974), Martin (1975), and many others. Going even further, a more advanced concept of the decohesive carrying capacity (DCC) was introduced by Życzkowski (1973), based on the assumption of unbounded dissipation energy.

The limit analysis was extended to variable loads, in particular to cyclic loads, that constitute an important part of the technical reality of structures. In the light of the early achievements in limit analysis, Melan (1930) formulated a theorem, also called the static shakedown theorem, that constitutes a natural generalization of the lower bound theorem for quasistatic loads. A proof of the theorem for three-dimensional continuum was provided by Melan (1938), and later on by Symonds (1951) and Koiter (1955). Extrapolation of the Melan theorem to the structures made of strain hardening material is due to Neal (1950), as well as Symonds and Prager (1950). The Melan theorem has been widely recognized as the most common and efficient tool for the shakedown analysis. Later on, Koiter (1956, 1960) formulated a theorem, often called the kinematic inadaptation theorem, that forms a direct extrapolation of the upper bound theorem for quasistatic loads. The theorem has been generalized to thermal cycles and non-associated flow rules by Maier (1969), as well as to dynamic loads by Corradi and Maier (1973). The theorems have been expressed in terms of the generalized stresses by König (1966, 1974).

Both theorems have become a turning point in the development of direct methods in mechanics. In particular, the shakedown theorem provides a limit against excessive deformation, and this approach is massively used in the design of structures, for instance nuclear power plants. Thermal loads were included into the shakedown analysis already by Prager (1956) and by Rozenblyum (1957, 1958, 1965), as well as by Gokhfeld (1961, 1965, 1970). Shakedown of rigid hardening

structures was addressed by Prager (1974). As both theorems were derived under the assumption of geometrically linear theory, an extension to geometrical nonlinearities was inevitable and is due to Weichert (1986). More recently, an extension of limit and shakedown analysis to general class of yield conditions was proposed by Ponter (2000).

With the development of constitutive models, there were many attempts to extrapolate the theorems to more complex mathematical descriptions. Fast progress of numerical methods, in parallel with much faster processing of data, made it possible to compute the nonlinear behavior of structures in more time-effective way. The finite element method can accommodate mathematically complicated constitutive models in order to solve any sophisticated problem of inelastic behavior of the complex structures. However, the direct methods retain their original, extremely important feature of solving this part of the problem, that is necessary to assess the limit state. They take advantage of the modern computational methods in order to employ the variables required in the design context, to find the bounds for energy dissipation, and to set the appropriate safety factors. This is of primary importance for safe design of structures and efficient communication with the engineers and industry.

In the present volume, novel and important achievements in the domain of direct methods, presented at the 4. Polish Congress of Mechanics and 23. International Conference on Computer Methods in Mechanics (PCM-CMM-2019) in Cracow/Poland, during the session on "Direct Methods: Methodological Progress and Engineering Applications", are contained. The topics stretch from the limit analysis and shakedown problems of different types of structures (including bone-structures) to the limit analysis-based optimization and advanced engineering applications. This book is the best proof that the direct methods in a modern form are actively developing for the benefit of science, technology, and industrial applications.

Cracow, Poland Błażej Skoczeń

Preface

"Direct Methods", embracing Limit- and Shakedown Analysis, allow to answer without cumbersome step-by-step computation one of the oldest and most important questions of design engineering, which is to determine the load carrying capacity of structures and structural elements.

This book is the peer-reviewed collection of papers presented at the Workshop on Direct Methods, held September 10–11, 2019 in Cracow, Poland, giving an insight into the latest developments of this fast progressing field of research. It is in line with similar books on the same subject which have been published as documentation of the previous workshops, held regularly since 2008 at Aachen, Lille, Athens, Reggio Calabria, and Oxford.

Most of the contributions are related to new numerical developments rendering the methods attractive for industrial design in a large panel of engineering applications. Extensions of the general methodology to new horizons of application are presented as well as specific technological problems.

It might be worth noting that the success of the workshops and the growing interest in Direct Methods in the scientific community were motivations to create the association IADiMe (http://www.iadime.unirc.it/) as a platform for exchange of ideas, advocating scientific achievements and not least, promotion of young scientists working in this field. It is open for all interested researchers and engineers.

The editors warmly thank all the scientists who have contributed by their outstanding papers to the quality of this edition.

Special thanks go to the organizers of the 4th Polish Congress of Mechanics & 23rd International Conference on Computer Methods in Mechanics, PCM-CMM-2019, September 8–12, 2019, Cracow, who hosted our meeting in the most comfortable and generous manner.

Reggio Calabria, Italy — Aurora Angela Pisano
Athens, Greece — Konstantinos Vassilios Spiliopoulos
Aachen, Germany — Dieter Weichert

Contents

Evaluation of Human Bones Load Bearing Capacity with the Limit Analysis Theory

Aurora Angela Pisano and Paolo Fuschi

Abstract The present study investigates on the possibility of applying the Limit Analysis structural theory to predict a lower bound to the peak/collapse load of human bones. Such a prediction can be useful to prevent skeletal diseases, osteoporosis and bones fractures; a problem of great interest in biomechanics and of relevant socio-economic impact in modern societies. A constitutive model of Tsai-Wu-type in principal stress space is assumed for the human bone modelled in 3D and viewed, at a macroscopic level, as a structural element made of a composite anisotropic material. Simple numerical tests on in-silico idealized specimens of human femur are performed, analyzed and critically discussed.

1 Premises, Motivations and Goals

Skeletal fractures, osteoporosis and bone-related diseases represent one of the major public health problems that is rising rapidly as the population ages. This has serious consequences on national health budgets. The data reported in the Report EU6, elaborated by the IOF (International Osteoporosis Foundation) at the end of 2018, estimated for the National Health Service of Italy, just to take an example, an expenditure of 9.4 billion euros, related to the cure of bones of population, with an alarming growth forecast, up to about 12 billion euros, by 2030.

The growing interest in research studies aimed at assessing the fracture risk of human bones reflects the increasing incidence of this problem for the modern societies ageing. The lengthening of life expectancy further increases the relevance of this research topic, as a much wider part of the population is vulnerable to the risk of

A. A. Pisano (✉) · P. Fuschi
University Mediterranea of Reggio Calabria, via dell'Universitá,
25 I-89124 Reggio Calabria, Italy
e-mail: aurora.pisano@unirc.it

P. Fuschi
e-mail: paolo.fuschi@unirc.it

A. A. Pisano et al. (eds.), *Direct Methods*, Lecture Notes in Applied and Computational Mechanics 95, https://doi.org/10.1007/978-3-030-48834-5_1

bone fracture. This problem, particularly felt in Italy, due to the ascertained aging of its population, is actually a problem throughout Europe and in all Countries where the economic well-being of the population increases its life expectancy. It has been calculated that in the world a skeletal fracture (mainly generated by osteoporosis) occurs every 3 seconds, and that, in the most serious cases, it can also lead to a partial or total permanent disability. Consequently, the patients can lose their independence, suffer from chronic pain and depression, so generating a significant socio-economic burden, difficult to estimate because it goes far beyond the costs related only to bone care. There is, therefore, an urgent need to recognize skeletal fractures, osteoporosis and in general bone diseases as a priority for public health and to integrate prevention and fracture management into healthy aging strategies.

In this context, the knowledge of *bone strength* is of paramount importance for fracture risk prediction. The awareness of being exposed to a risk of fractures can lead patients to change their level of attention on the problem by following medical and behavioural protocols that lead to lifestyles more appropriate to their condition, without compromising the general quality of their life. Moreover, the knowledge, with a high degree of accuracy and reliability of this data for the patient would lead to prompt intervention in terms of prevention, pharmacological medical care and, alternatively, in terms of surgical interventions or implantation of prostheses. Any of these actions, following anamnesis and deep knowledge of patient-case-history, should be based on the knowledge of the specific-patient bones real conditions in terms of mechanical resistance that should be captured by numerical predictive models in conjunction with non-invasive measurements such as medical imaging describing the actual underlying micro and macro-structure of the bone of the patient.

A great amount of research work has been developed to understand and describe, from a mechanical point of view, the behaviour of human bones in order to develop numerical models able to predict their response under different loading conditions (see e.g. [1–4] and references therein just to have an idea of the impressive number of contributions in this field). The numerical modelling of human bones dates back to the early seventies (see e.g. [5–7] and references therein), however, the developed numerical tools, the proposed constitutive models, are all oriented to the description of the post-elastic behaviour of human bones and are often based on hypotheses on the behaviour of the "bone material" true only for specific cases or for precise bone elements of the human skeleton. The problem, in the authors' opinion, is that, to date, is not available a mechanical constitutive model for human bones, endowed with incremental constitutive laws, capable of accurately managing the post-elastic mechanical behaviour of a "structural element" made by "human bone material". Human bones are not properly engineering materials; the bone tissues are alive. They are able to grow, to adapt themselves to operating loads, to regenerate, but, also, to degrade due to aging or to pathologies well known in the field of medicine and orthopaedic surgery. The engineering description of such kind of material and the knowledge of the behaviour of the bone beyond the elastic phase is very difficult and confined to specific bones and to specific patients.

From the above remarks come the motivations of the present study based fundamentally on a look at what happened in the past in the field of structural engineering.

We refer in particular to the history and evolution of calculation techniques for (large) steel structures. Steel, at the beginning of the twentieth century, constituted a building material of great versatility and easy to use. However, if we consider the numerical methods related to structural steel elements we cannot forget that the first reliable constitutive models for this material are dated 1913 (von Mises) or 1868 (Tresca) or, again, 1924 (Hencky) while the numerical procedures able to describe the post-elastic behavior of steel structures based on such models developed many years later. The theory of plasticity and the methods of step-by-step solution (in the static and dynamic field) have become established and widespread, together with the development of computers, only in the early 1980s. What were then the calculation tools available at the beginning of the twentieth century with reference to steel structures? Just look at the history! Almost everything was based on simple and reliable theories and methods which, renouncing to the step-by-step description of the post-elastic behavior (not available at that time), were limited to the prediction of the ultimate load of the structure (the greater load the structure can bear before collapse) and/or of the examined structural element. The Limit State Design, the Limit Analysis, later followed by Shakedown Analysis and the so-called Direct Methods (see e.g. [8] and references therein for an updated review of the modern techniques in this context), allowed to predict, with a high degree of accuracy, the collapse load of the structure thus providing a useful and fundamental indication for the design, verification and determination of safe operating conditions.

In the context of "structures made up of human bone material" we are today in the same conditions we were for steel constructions in the early twentieth century! In the literature there are constitutive models able to define with sufficient accuracy the field of admissible stresses for bones, also taking into account the microstructure of the different bone tissues, but yet we do not have flow laws that can fully describe the post-elastic behavior of human bones. What to do then? Apply the Limit Analysis. The history suggests. A history known in the field of structural engineering, certainly less known in that of biomechanics or medicine. The pursued goal is then simply to aim at an accurate prediction of the peak/collapse load of the human bone. The idea is therefore that of focusing on the ultimate conditions, i.e. investigating the incipient collapse scenario of the examined bone, directly, to detect the load-bearing capacity of bone and the pertinent collapse mechanism. To this aim the needed information reduce themselves only to bone strengths, to be experimentally detected for a specific patient, a goal more easily reached than the determination of all the material parameters needed for defining the evolutive processes leading to bone crisis. The framework of plasticity theory in conjunction with finite element techniques is referred to and in line with other literature studies.

The peculiarity of the limit analysis approach here promoted is that linear finite element (FE) analyses are involved within an iterative procedure in which the elastic properties of "bone material" are systematically adjusted to simulate the limit state solution. More precisely, the static approach of limit analysis is followed by the Elastic Compensation Method [9, 10] in order to search for a lower bound to the peak/collapse load value. Such numerical procedure has been successfully applied by the authors to structures, or structural elements, made of a variety of materials, each

characterized by a specific yield surface e.g. composites [11–13] complying with a Tsai-Wu criterion or reinforced concrete structures obeying a generalized yield surface in the 3D stress space [14–16]. In the above analyzed cases, effectiveness and versatility of the limit analysis procedure have been broadly demonstrated via direct comparison with experimental findings. It is worth noting that the linear elastic FE analyses involved greatly simplifies the formulation and reduce the number of material parameters required for the model calibration. Actually, the only information needed is a domain of admissibility for the stresses, something already available for bones and not linked to the knowledge of constitutive laws of evolutive type. This represents a competitive aspect of the present approach and makes the proposed procedure of practical connotation for clinical purposes. Critical zones, that needs to be cured or that need reinforcement, are directly highlighted and proper interventions can be planned and carried out in such specific zones that are mostly prone to the fracture risk.

The assumptions on the "bone material" mechanical behaviour are expounded in the following Sect. 2. Limit analysis on human long bones is presented in Sect. 3 together with some numerical simulations. Section 4 is devoted to concluding remarks and future developments.

2 The Human Bone "Material"

Generally speaking, human bone behaves like a composite material whose constituents are minerals, collagen and water. Bone tissue is generally classified, at macroscopic level, into two different types: *spongy* bone tissue, also called *trabecular* or *cancellous* bone and *compact* bone tissue, also known as *cortical* bone. The cortical represents the external part of the bone and is strong, dense and tough, while the inner spongy part is lighter and less dense than cortical one. The trabecular bone tissue is usually found in cuboidal bones, flat bones and at long bones to which we refer in this preliminary study. The properties of the compact and spongy bone tissues are closely related to their conformation, characterized, like most biological tissues, by a very complex and hierarchical structure that can be analyzed at different dimensional scales [17–20].

Without going much into details, mineral elements, collagen, and non-collagenous organic proteins form the sub-nanostructure (below 100 nm), with type-I-collagene fibers permeated with carbonated apatite (hydroxyapatite) nanocrystals. These mineralized collagen fibers at the nanostructure (below 1 μm) are further arranged at a sub-microstructural length scale (1–10 μm) into adjacent lamellae. The lamellar structures are then organized into trabeculae and osteons, also known as Harvesian system, at the microscale (10–500 μm), forming large vascular channels surrounded by circumferential lamellar rings. Finally, at the macroscopic scale, the union of trabeculae give rise to the cancellous (porous) bone tissue and the union of osteons gives rise to the cortical bone tissue. At this scale level, the differences in the density and mechanical characteristics of the bone tissues become evident. The spongy bone

has a honeycomb appearance and a structure characterized by a porosity between 50 and 90%. On the other hand, the compact bone appears to be a solid mass. Compared to the spongy bone, cortical one is characterized by a higher density and therefore a lower porosity, between 5 and 10%.

With few exceptions, the compact and spongy components are present in all bones, with different quantities and distributions depending on the type of bone. Therefore, the mechanical characterization and properties of the bone passes through the characterization of these two macroscopic components as well as of their spatial arrangement and structural organization. For example, the stiffness of a compact bone specimen is a function of the architecture and mechanical properties evaluated at the macroscale, i.e. of the spatial arrangement of the osteons, of the stiffness of the single osteon, of the degree of mineralization of the osteons (spatial arrangement and mechanical properties at microscale), etc. Similarly, the stiffness of a spongy bone sample is a function of its internal organization that is of the spatial arrangement of the trabeculae, of the mechanical properties of the single trabecula and of its internal composition. The mechanical characteristics of the bone "material" (Strengths, Young, shear and Poisson moduli) can be obtained experimentally by making specific measurements with the same logic used for other engineering materials. The relevant literature provides examples of classic tests such as traction, compression, torsion, bending etc., see e.g. [21, 22]. Obviously, the main problem is represented by the specimen that cannot be reproduced in series, as happens for the other engineering materials, and this has focused the attention of the researchers towards other types of investigations, such as those that use ultrasound, computed and micro-computed tomography, magnetic resonance etc.

A close relationship exists nowadays between diagnostic imaging, interpretation of observable parameters at the microscale and in-silico methods oriented to characterize the mechanical properties of human bones and eventually of their behavior at both micro- and macro-scale. These methods allow for the elimination of many of the uncertainties involved with results coming out from mechanical tests and direct fabric measurements, thus enabling to find the relationships between architectural and mechanical parameters, see e.g. [23]. A plethora of research works were focused on the determination of mechanical properties of bones depending on age, gender, as well as patient-specific morphological, chemical and compositional properties provided by computer aided diagnostics and techniques of medical imaging, see e.g. [24, 25].

Another valuable existing research line in this field of bone mechanics is that related to the so-called micro finite element (μFE) simulations performed to determine the apparent mechanical properties of bones. These μFE analyses are aimed at simulate nanoindentation and microindentation tests for calibration purposes, see e.g. [26] and references therein. Indeed, the nanoindentation technique avoids the influences of the inherent defects and inhomogeneities in the microstructure, thus facilitating measurements of the mechanical properties of the individual microstructural components. At present, μFE modeling has gained adequate validation against experimental findings, although in most cases this validation has been limited to in vitro experiments.

Besides the simple pioneering elastic idealizations, several inelastic constitutive models have been proposed in the literature to capture the main physical phenomena associated with post-yielding of bone material, namely stiffness loss, permanent deformation, and hysteretic response. Continuum damage mechanics in conjunction with plasticity has been used [27–30]. Bone fracture mechanics guided many other models, see e.g. [31] and references therein. In the need to adopt a constitutive model, which inevitably can hardly take into account the complexity of the human bone behavior, the attention has been focused on some of the existing models specifically referred to the two macroscopic bone components, precisely for trabecular bone the ones proposed in [32–36] and for cortical bone those promoted in [37–40]. The above quoted papers, whose list is far to be exhaustive, allows one to affirm some peculiarities of bones mechanical behavior. Bones exhibit asymmetric yielding with a higher yield strength in compression than in tension. Due to their composite microstructure, brittle mechanisms occurs within the mineral, ductile mechanisms within the organic matrix, interactions take place between the two phases. The bone material is anisotropic, as the stress-strain relationship changes depending on the direction of the load application (with higher strength in the longitudinal direction than across the bone surface). The bone material is a rate-dependent or viscoelastic, as it responds differently depending on the speed of the applied loads, and this is particularly evident with increasing post-yield deformation, as damage accumulates in the tissue. Moreover, a general remark on the existing constitutive models concerns the circumstance that bone fracture is widely regarded as strain-controlled as most theoretical descriptions of bone mechanical behavior assume that the onset of fracture is triggered by strains. Therefore, strain-based fracture criteria are the more commonly used in predicting the onset of fracture although experimental evidence in this regard is still lacking.

Three more observations have to be made for completeness without claim of exhaustiveness:

(i) almost all criteria are formulated both in stress and strain space but taking into account what is known in the literature as the "fabric tensor concept" considered, by who conceived this operator [41, 42], as the second measure of microstructure in a porous material after porosity. The fabric tensor is a symmetric second rank tensor, which characterizes the geometric arrangement of a porous material microstructure or the local spatial distribution of one phase of a multiphase material relative to the other phases. Many are the related papers oriented to quantify the fabric tensor, see e.g. [22, 33, 43, 44];
(ii) there are criteria constituting a sort of "bridge" between the previous ones, namely the generalized anisotropic quadric yield criterion conceived by Zysset and Co-Workers (see e.g. [45] and references therein). This yield surface has a convex quadric shape with a smooth transition from ellipsoidal (typical of porous composite materials) to cylindrical or conical surfaces (representative of solid matrix materials). The peculiarity of such yield criterion lies in its generality, as it degenerates to several well-known yield surfaces like von Mises, Drucker-Prager, Tsai-Wu, Liu and Hill

criteria as special case under appropriate conditions. Moreover, the different quadric shapes of this model are helpful for fitting yield envelopes at every hierarchical level, from the extra-cellular matrix at the microscale up to the actual bone tissue at the macroscale;
(iii) concepts related to nonlocal and gradient elasticity have been advanced to equip the classical continuum plasticity-damage constitutive laws for bones with higher-order contributions, see e.g. [46, 47]. Following these approaches, the multi-scale nature of bones and the related microstructural phenomena description is achieved via the introduction of internal length material scales into an enriched continuum formulation. The length scale parameters are related to the size of material heterogeneities. These nonlocal or gradient-enhanced formulations for bones, in the context of finite element numerical analysis, improve previous local models of bones in an attempt to minimize the mesh sensitivity in presence of damage and strain softening. It is worth noting that the practical and general applicability of the latter approaches, that are indeed very promising, is however still difficult being related to the identification of a number of material parameters that takes into account, at a macroscopic level, phenomena arising at a nano-scale.

2.1 The Adopted Material Model

For the purposes of this study, oriented to apply Limit Analysis theory valid in the realm of plasticity, a yield criterion with its related yield surface has to be assumed to handle the bone material. It is then essential to define preliminarly "plasticity in bones".

As said bones are characterized by a highly complex and hierarchical structure, [17, 48], in which a mineral phase is embedded in an organic matrix of collagen protein. Elasticity is due to soft collagen which is also able to dissipate energy under mechanical deformations. Plastic deformations in bones, as in metals, imply opening, deforming and rearrangement of bonds. In metals such processes are addressed and explained by dislocations movements, in bones such processes occur at all hierarchical levels, see e.g. [49, 50] and references therein. Plasticity or permanent deformations in bones, as it can be observed through multiscale modeling and techniques able to operate at very small scale of observation, is due to breaking of bonds starting at molecular scale. The breaking under increasing loads of hydrogen bonds within the single collagen molecules is followed by intermolecular sliding and breaking of bonds within collagen fibrils. The latter intermolecular sliding constitutes a mechanism of energy dissipation and plastic deformation. Going to a larger submicrometer scale, the fibrillar sliding is the source of permanent, plastic deformation, in bones. The bone's toughness is due *intrinsically* (at submicrometer scale) to fibrillar sliding responsible of the formation of plastic zones in the vicinity (ahead) of a crack within which dissipation can take place impeding fracture spreading. In particular, plasticity at the crack tip dissipates energy, reduces stresses so blunting the crack tip. The bone's toughness is also due *extrinsically* (at larger osteon structural scales) to

crack bridging/deflection. A mechanism like crack bridging, as known in composite materials context, carries loads that would otherwise drive crack propagation. For completeness it is worth noting that, although many other materials may be mechanically superior, bone is the only one exhibiting the capacity of self-repairing and adapting. Unfortunately, strength, toughness and plasticity of bones degrades with age, [51]. Eventually, although the majority of studies do not use plasticity concepts but rather damage models, bones are fracture resistant, show plastic deformations and plasticity is a major factor reducing bone fragility. Indeed, bones exhibit enough ductility which allows them to absorb impacts reducing the risk of fracture and minimizing skeletal weight.

One of the most accredited criteria in the field of composite materials, namely the quadratic Tsai-Wu failure criterion [52], is here adopted to define a Tsai-Wu-type yield surface. It is expressed in the space of principal stresses in the following form, after [31, 42]:

$$G_{11}\sigma_{11} + G_{22}\sigma_{22} + G_{33}\sigma_{33} + F_{1111}\sigma_{11}^2 + F_{2222}\sigma_{22}^2 + F_{3333}\sigma_{33}^2 + 2F_{1122}\sigma_{11}\sigma_{22} + 2F_{1133}\sigma_{11}\sigma_{33} + 2F_{2233}\sigma_{22}\sigma_{33} = 1 \tag{1}$$

with the coefficients defined as:

$$G_{ii} = \frac{1}{\sigma_i^+} - \frac{1}{\sigma_i^-} \qquad F_{iiii} = \frac{1}{\sigma_i^+\sigma_i^-} \tag{2}$$

$$F_{iijj} = \frac{1}{2}\left(\frac{1}{\sigma_i^+\sigma_i^-} + \frac{1}{\sigma_j^+\sigma_j^-} - \frac{1}{\sigma_{ij}^2}\right) \tag{3}$$

In Eq. (1), $\sigma_{11}, \sigma_{22}, \sigma_{33}$ denote principal stresses; in Eqs. (2) and (3) repeated indices are not summations while $\sigma_i^+, \sigma_i^-, \sigma_{ij}$ are the ultimate strengths (in modulus) in tension, compression and in shear, respectively, along each direction and plane of orthoropy ($i, j = 1, 2, 3$). Referring, as said, to long human bones: direction 1 is the radial or medio-lateral; 2 is the anterior-posterior; 3 is the axial or superior-inferior long bone's axis. No fabric tensor dependence is assumed in the interaction coefficients F_{iijj} as done in the above quoted papers. Such assumption has a twofold reason: (i) it is not essential for verifying, at this stage, the validity of the procedure here promoted; (ii) the fabric tensor should be defined for a specific patient bone which will not be considered hereafter. Moreover the following inequality holds true:

$$F_{iiii}F_{jjjj} - F_{iijj}^2 \geq 0 \tag{4}$$

The latter insures that the Tsai-Wu-type surface will intercept each stress axis, it has an ellipsoidal shape (i.e. it is not open-ended), it contains the stress space origin. The assumed values of strengths are summarized in Table 1 along with the references utilized to fix them and assuming for the apparent density the mean values: $\rho_{cortical} = 1.75\,\mathrm{g/cm^3}$ and $\rho_{trabecular} = 0.4\,\mathrm{g/cm^3}$, see e.g. [53].

In Fig. 1 the Tsai-Wu-type surface is plotted in the space of principal stresses for cortical and trabecular bone and for the assumed strengths values listed in Table 1.

It is worth noting that the axiomatic choice of a yield surface in the shape given by Eq. (1), i.e. starting from the Tsai-Wu failure surface, grounds on the following remarks: (i) The Tsai–Wu interactive failure criterion belongs to the five leading theories selected within the World-Wide-Failure-Exercise conceived to establish the current status of failure prediction theories for composites and as a composite is here modelled the human bone; (ii) The Tsai–Wu-type yield criterion, in the quadratic form adopted, is simple; it allows one to apply the standard rules of transformation, invariance and symmetry; it also contemplates interactions among the stress or strain components analogously to the Von Mises criterion; (iii) The adopted yield criterion is used to locate stress states at which the material has exhausted its strength capabilities, namely stress points lying on the domain boundary. The Tsai-Wu-type yield surface it is easy to handle to this aim; (iv) The further hypothesis of perfect plasticity seems reasonable looking at the stress-strain diagrams on bone tissues, see again [49] and

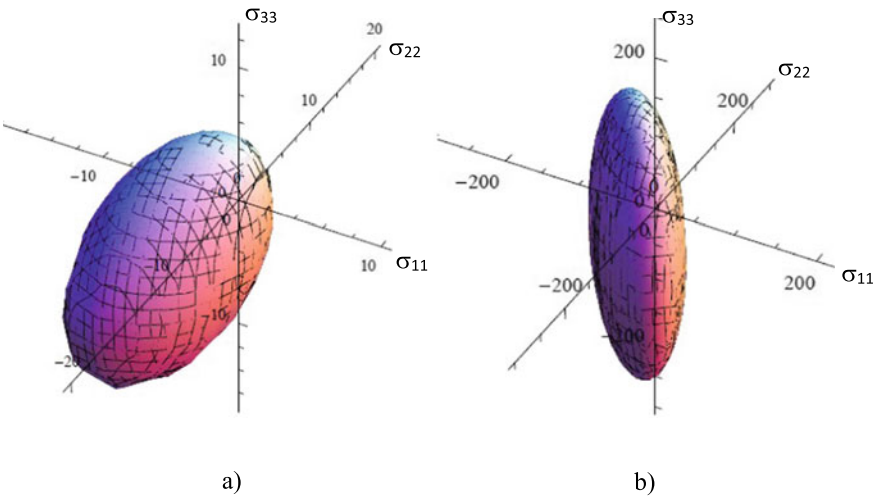

Fig. 1 Tsai-Wu-type surface in principal stress space: **a** Trabecular; **b** Cortical

Table 1 Strengths values for cortical and trabecular bone

Strength (MPa)	Cortical	Trabecular	Reference
$\sigma_1^- = \sigma_2^-$	86.137	6.099	[53–55]
σ_3^-	207.324	7.220	[53–55]
$\sigma_1^+ = \sigma_2^+$	34.455	2.439	[20, 31] ($\sigma_1^+ = \sigma_2^+ = 40\%\sigma_1^-$)
σ_3^+	134.761	4.693	[20, 31] ($\sigma_3^+ = 65\%\sigma_3^-$)
$\sigma_{13} = \sigma_{23}$	51.60*	2.888**	[56]*, [57]** ($\sigma_{13} = \sigma_{23} = 0.4\sigma_3^-$)
σ_{12}	65.30*	2.439**	[56]*, [57]** ($\sigma_{12} = 0.4\sigma_1^-$)

[51] for the experimental findings to this concern. Eventually, the hypothesis that the Tsai-Wu-type yield surface plays also the rule of plastic potential, i.e. that the human bone material obeys to an associated flow rule, or, briefly, is a standard material, is hereafter assumed but could be removed following the so called non standard limit analysis approach, see. e.g. [58].

3 Limit Analysis of Human Bones

The limit analysis numerical method here proposed tackles the human bone mechanical problem at a (macro) structural level. The method is focused on the possibility of predicting a peak load which produces the bone collapse. It might be from many aspects inaccurate but, with all its limits and approximations discussed in the following, it appears simple, rather effective, of general applicability, being also able to catch some important aspects of the overall bone behaviour at collapse. It is worth noting that, as said in Sect. 1, numerical approaches based on finite element analyses have been employed in the context of human bones since the early seventies. The FE analyses proposed in the literature (refer again to [7] and references therein) even if quite effective, just think that led to the design and construction of prostheses, are all based on evolutive approaches linked to an accurate determination of the material parameters and of the flow laws characterizing the post elastic behavior of the human bone material. The latter being for many aspects still controversial and of not general applicability.

The approach here promoted, oriented to the determination of the collapse load in the spirit of the limit analysis theory, it does not need this information. Some basic concepts to this concern are given in the follow. As known, [59], the value of the plastic limit load of a structure, made of a standard material and subjected to body forces and surface tractions, depends on the following factors: (a) structural configuration (geometry, constraints, etc.); (b) plasticity function $f(\boldsymbol{\sigma}) = 0$, here expressed by Eq. (1). The elastic constitutive law is irrelevant for the determination of both the value of the collapse load as well as the collapse mechanism that the plastic collapse load promotes. This irrelevance of elasticity law in the context of plastic collapse analysis is a direct consequence of the concept of limit load itself. In fact, this load is characterized by its ability to induce the existence of: (i) a stress field $\boldsymbol{\sigma}$ statically admissible (SA), i.e. in equilibrium with the external forces, as well plastically admissible (PA), i.e. satisfying the condition $f(\boldsymbol{\sigma}) \leq 0$ everywhere in the structure; (ii) a field of modes of kinematically admissible (KA) incipient plastic strains $\dot{\boldsymbol{\varepsilon}}^p$, i.e. compatible with the incipient displacements $\dot{\boldsymbol{u}}$ ($\dot{\boldsymbol{\varepsilon}}^p = \nabla^s \dot{\boldsymbol{u}}$) with $\dot{\boldsymbol{u}} = 0$ where the constraints are applied, as well plastically compatible (PC), i.e. $\dot{\boldsymbol{\varepsilon}}^p$ obeying the normality rule $\dot{\boldsymbol{\varepsilon}}^p = \dot{\lambda}\partial f/\partial \boldsymbol{\sigma}$ with $\dot{\lambda} > 0$ where $f(\boldsymbol{\sigma}) = 0$ being $\dot{\lambda} = 0$ otherwise. When the above ingredients exist, the structure acquires—under the action of the limit load—the characteristics of a kinematic mechanism capable of performing a motion (theoretically of unlimited amplitude) whose properties in their initial state are defined by the pair of mutually compatible tensors $\dot{\boldsymbol{\varepsilon}}^p$, $\dot{\boldsymbol{u}}$. This incipient motion

is the plastic collapse mechanism. It is proven that for a given structure, subjected to a given proportionally increasing load and for a given plasticity function, the plastic limit of the above load is uniquely determined together with the relative collapse mechanism.

The collapse mechanism is therefore the beginning of a deformation process of exclusively plastic nature that overlaps the state of stress and strain already existing under the action of the limit load, i.e. the SA and PA stresses $\boldsymbol{\sigma}$, as well as the elastic and plastic strains already accumulated at moment of the incipient collapse. These, let's say, pre-stresses and pre-strains do not change after the beginning of the collapse mechanism, as if the structure was rigid in that state, but capable of producing incipient plastic strains $\dot{\boldsymbol{\varepsilon}}^p$. Since the mentioned pre-strains are infinitesimal, it turns out that, by the principle of effects superposition, the mechanism of collapse can be studied ignoring the state of pre-strains and therefore considering the structure as if it were rigid-plastic. The rigid plastic model, often invoked by the plastic collapse design, emphasizes the property of elastic strains, whatever the relative constitutive law, to be ineffective for the determination of the collapse load and of the related collapse mechanism. Moreover the incipient plastic strains are unique in all V (vanishing in those parts of V that do not participate in the collapse mechanism), while the corresponding stresses are unique only in the part of V that participates to the collapse mechanism. Finally the field of incipient displacements $\dot{\boldsymbol{u}}$ can be obtained by integrating the compatibility equations $\dot{\boldsymbol{\varepsilon}}^p = \nabla^s \dot{\boldsymbol{u}}$; the solution is determined to less than a rigid motion, which however must be zero for the presence of constraints.

For loading governed by a single parameter (i.e. the loading is defined by a fixed reference loads distribution amplified by a scalar load multiplier, say P) and following the Limit Analysis Lower-Bound Theorem it can be stated that (borrowing from [59]): the load multiplier, say P_{LB}, that produces loads that are in equilibrium with a stress field that nowhere violates the yield criterion do not exceed the collapse load multiplier, say P_U. The former gives then a Lower Bound (LB) whose maximum defines the collapse load. The computational method here promoted searches for a LB to the bone collapse load and is known as Elastic Compensation Method (ECM), conceived in [9] and applied by the authors in different context (see e.g. [13, 16]). The ECM is aimed to construct a SA and PA stress field, suitable for the evaluation of a P_{LB}. Such goal is pursued by an iterative procedure involving *many sequences* of linear elastic FE analyses, in which highly loaded regions of the structure are systematically weakened by reduction of the local moduli of elasticity. Indeed, by applying the ECM it is not performed any evolutive analysis, it is not solved any optimization problem, it is just simulated the process of *stress redistribution* arising within the structure before attaining its limit strength threshold. Such process is realized referring to an elastic behaviour for operative reasons, indeed, as reminded above, any elastic law can be used the collapse load value does not depend from the elastic behavior of the material.

Precisely, the ECM starts with a first FE analysis of the structure for a given initial design load $P_D^{(1)}\,\bar{p}_i$; where $\bar{p}_i$ are given reference (or basic) loads, $P_D^{(1)}$ is the first design load multiplier (it can be equal to 1 at the beginning). Moreover an initial (arbitrary) distribution of the elastic parameters is assumed (the real ones can be

assumed for simplicity) on the structure subjected to given constraints. The linear elastic solution can then be obtained in terms of stresses measured at each Gauss point (GP) within the elements. In the procedure hereafter employed the principal stresses, averaged within the GPs of the #e-th element, are used to define a, let's say, *element-solution*. Moreover, for reasons that will be clear soon, the process is iterative so, considering that at the beginning is $k = 1$, the computed element-solution locates in the principal stress space, of origin $\mathbb{O}$, a stress point, say $\mathbb{P}_{\#e}^{e(k-1)}$, while $\mathbb{P}_{\#e}^{Y(k-1)}$ denotes the corresponding stress point at yield (i.e. on the Tsai-Wu-type surface), measured on the direction $\overrightarrow{\mathbb{OP}}_{\#e}^{e}/|\overrightarrow{\mathbb{OP}}_{\#e}^{e}|$. Two actions are put in place at this point. Action #1: if the elastic element-solution of the #e-th element is such that $|\overrightarrow{\mathbb{OP}}_{\#e}^{e}|^{(k-1)} > |\overrightarrow{\mathbb{OP}}_{\#e}^{Y}|^{(k-1)}$ i.e. is "outside" the yield surface then the elastic moduli of the #e-th element are *reduced* according to:

$$E_{\#e_{ij}}^{(k)} = E_{\#e_{ij}}^{(k-1)} \left[\frac{|\overrightarrow{O\mathbb{P}}_{\#e}^{Y}|^{(k-1)}}{|\overrightarrow{O\mathbb{P}}_{\#e}^{e}|^{(k-1)}} \right]^2 \quad G_{\#e_{ij}}^{(k)} = G_{\#e_{ij}}^{(k-1)} \left[\frac{|\overrightarrow{O\mathbb{P}}_{\#e}^{Y}|^{(k-1)}}{|\overrightarrow{O\mathbb{P}}_{\#e}^{e}|^{(k-1)}} \right]^2, \tag{5}$$

where, by hypothesis, the Poisson ratios v_{ij} of the #e-th element remain constant. It is worth to remark that the "moduli variation" realized by Eq. (5) on the elements characterized by stresses greater than the yielding ones it is always a reduction which would "bring" the element-solution on the yield surface. Moreover it has been numerically experienced that the convergence rate increases if the square of the updating ratio is used as given by Eq. (5). Action #2: among all the computed element-solutions the *maximum stress values* are detected in the *whole FE mesh*, that is in the cortical elements as well as in the trabecular ones the stress points farthest away from the respective Tsai-Wu-type yield surfaces are located, say $\mathbb{P}_{Max-Cort}^{(k-1)}$ and $\mathbb{P}_{Max-Trab}^{(k-1)}$. If $|\overrightarrow{O\mathbb{P}}_{Max-Cort}|^{(k-1)}$ is greater than $|\overrightarrow{O\mathbb{P}}_{Max-Cort}^{Y}|^{(k-1)}$ or $|\overrightarrow{O\mathbb{P}}_{Max-Trab}|^{(k-1)}$ is greater than $|\overrightarrow{O\mathbb{P}}_{Max-Trab}^{Y}|^{(k-1)}$ a new FE analysis is performed keeping fixed the applied load but with the updated moduli $E_{\#e_{ij}}^{(k)}$, $G_{\#e_{ij}}^{(k)}$ given by Eq. (5). Is this new FE analysis that "realizes" the above mentioned stress redistribution process. The iterations are carried on, for the fixed applied load $P_D^{(1)}\bar{p}_i$, until *all* the stress points just reach or are below their corresponding yield values, say at a last iteration (K), which means that an admissible stress field (i.e. SA and PA) has been built and a LB to the plastic collapse multiplier is given by:

$$P_{LB}^{(1)} = \min \left\{ |\overrightarrow{O\mathbb{P}}_{Max-Cort}^{Y}|^{(K)} \frac{P_D^{(1)}}{|\overrightarrow{O\mathbb{P}}_{Max-Cort}|^{(K)}}; \; |\overrightarrow{O\mathbb{P}}_{Max-Trab}^{Y}|^{(K)} \frac{P_D^{(1)}}{|\overrightarrow{O\mathbb{P}}_{Max-Trab}|^{(K)}} \right\}. \tag{6}$$

This closes a first sequence, say sequence $s = 1$, of elastic FE analyses (performed for $k = 1, 2, ..., K$) carried on for the loads $P_D^{(s)}\bar{p}_i$ (with $s = 1$). Obviously, the computed $P_{LB}^{(1)}$ might be far from the collapse load multiplier and it has to be maximized. This can be simply achieved increasing the applied load and trying a new redistribution of the related higher stresses. Increased values of loads are then considered in subsequent

sequences of analyses, each one with an increased value of $P_D^{(s)}$, till further load increase does not allow the stress points $\mathbb{P}_{Max-Cort}$ and $\mathbb{P}_{Max-Trab}$ to be brought below yield by the iterative redistribution procedure. A P_{LB} load multiplier can eventually be evaluated at *last admissible stress field* attained for a maximum acting load $P_D^{(s)}\bar{p}_i$, say at $s = s_{last}$, and at last successful FE analysis, say at $k = K$, trough Eq. (6). A graphic flow diagram of the ECM is shown at the end of section 4.

Two final general remarks are worth making on the ECM: (i) to the authors' knowledge a theoretical convergence proof for the ECM is not available. Nevertheless the ECM is considered reliable and computationally very efficient and used for industrial applications within the so-called Design by Analysis (DBA) concept. Indeed, the ECM is incorporated into the Japanese codes for Nuclear Implants, JSME—Design & Construction Code, see e.g. the World Nuclear Association Report [60]. For what concern the ECM convergence proof, the papers [61–63] can be also referred to. Eventually, the ECM theoretical validation is definitively an "open point" as asserted by the above quoted valuable Report [60]; (ii) the elastic analysis performed within the ECM can be carried out by *any* commercial FE code. In the following applications the ADINA code [64] has been used while a Fortran main program has been created to drive the FE analysis within the sequences.

As stated before, the adoption of real elastic parameters is not necessary, the limit state solution does not depend on them. It is possible to start the ECM sequences from any distribution of elastic material parameters. Such choice, possibly, would require only a greater number of iterations to complete the stress redistribution process. To avoid this, in the computations it has been preferred to start from real elastic parameters values assuming an orthotropic behavior for the trabecular bone, transversely isotropic for the cortical one and fixing for the marrow (considered isotropic, homogeneous and incompressible) $E = 20$ MPa, $\nu = 0.499$, [31]. Once again no fabric tensor is used, it would not make sense in this case. The elastic constants utilized are summarized in Table 2 and deduced from [65] as a function of the apparent densities $\rho_{cortical} = 1.75\,\mathrm{g/cm^3}$ and $\rho_{trabecular} = 0.4\,\mathrm{g/cm^3}$. It is meant that: direction 1 is the radial or medio-lateral; 2 is the anterior-posterior; 3 the axial or superior-inferior long bone's axis.

3.1 Numerical Tests on Human Bone In-Silico Specimens

For the purposes of this preliminary study four idealized cylindrical specimens of human bone femur have been analyzed. Precisely, the four samples shown in Fig. 2 have been considered imagining they have been extracted from different anatomical femur locations: proximal epiphysis, metaphysis, diaphysis and distal metaphysis, represented by specimens #1, #2, #3 and #4, respectively. The outer cylinder is always the cortical bone, the inner cylinder is assumed made of trabecular bone in specimen #1, half trabecular and half marrow in specimen #2 and #4, marrow in specimen #3. The geometrical dimensions which imply the separation between the cortical external

Table 2 Elastic constants for cortical and trabecular bone[a]

Mat. Parameter	Cortical	Trabecular
E_1 [MPa]	5484.11	137.95
E_2	5484.11	229.29
E_3	9621.24	327.63
G_{12} [MPa]	1924.25	68.37
G_{13}	2790.16	125.02
G_{23}	2790.16	81.31
ν_{12}	0.425	0.293
ν_{13}	0.370	0.162
ν_{23}	0.370	0.149

[a] After [65] and references therein

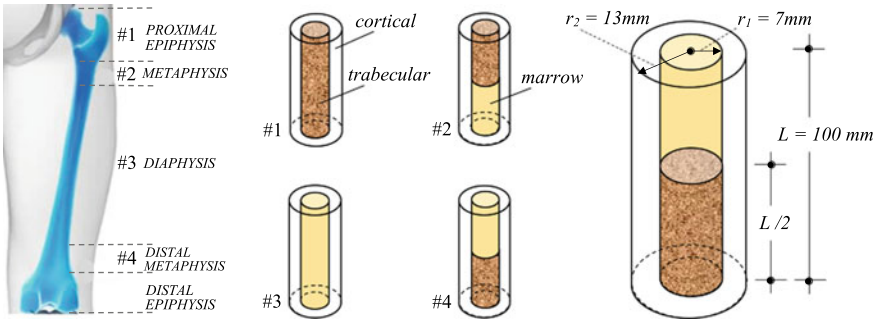

Fig. 2 Anatomical locations and geometry of human femur in-silico specimens ideally extracted from: #1 proximal epiphysis; #2 metaphysis; #3 diaphysis; #4 distal metaphysis

shaft and the internal trabecular and/or marrow matter have been fixed looking at experimental data available in the literature, see e.g. [66].

The sketch of the adopted mechanical model, with the assumed cartesian reference system, boundary and loading conditions is given in Fig. 3a, while the FE mesh utilized for the computations is shown in Fig. 3b. With reference to the human femur, it has been assumed that: axis x is the radial or medio-lateral; y is the anterior-posterior; z the axial or superior-inferior long bone's axis. The cylindrical specimen is clamped at the lower base and subjected to three reference loads (all amplified by the same load multiplier P_D) acting along the directions of cartesians axes and applied at the center of a rigid thin plate on the upper base to mimic the diffuse transmission of the loads acting on the extracted portion of the femur. The intensity of the reference loads, following the suggestions of [67] and for a body weight of $BW = 687N$, are: $F_z = -BW$, $F_y = 0.18BW$, $F_x = 0.43BW$. A mesh of 672 $3D$-Solid Elements, with 27 nodes and 27 Gauss Points per element, has been used for all the numerical simulations.

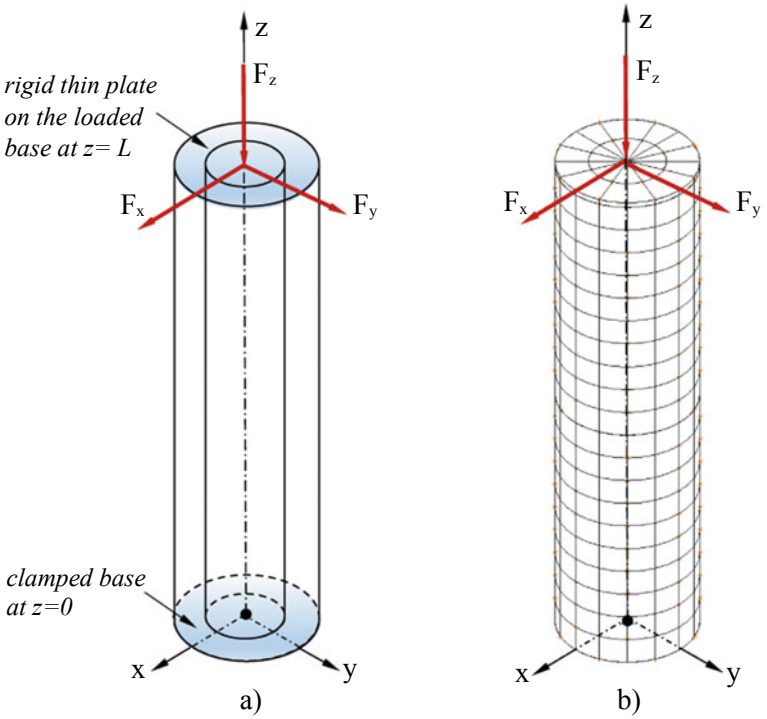

Fig. 3 Human femur in-silico specimen: **a** mechanical model, boundary and loading conditions; **b** FE mesh of 672 3*D*-Solid Elements with 27 nodes and 27 Gauss Points per element

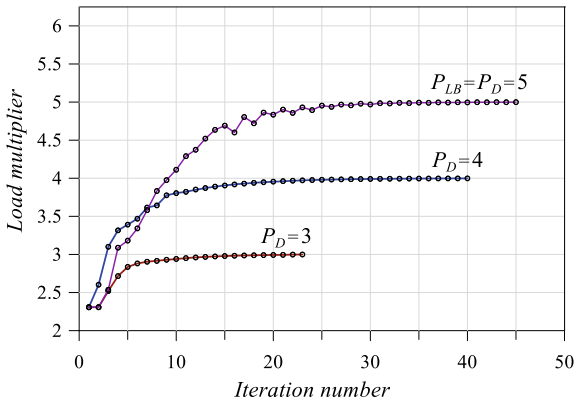

Fig. 4 Load multiplier versus iterations number for three sequences of elastic analyses carried on the human femur in-silico specimens: results for specimens #1 proximal epiphysis and #4 distal metaphysis

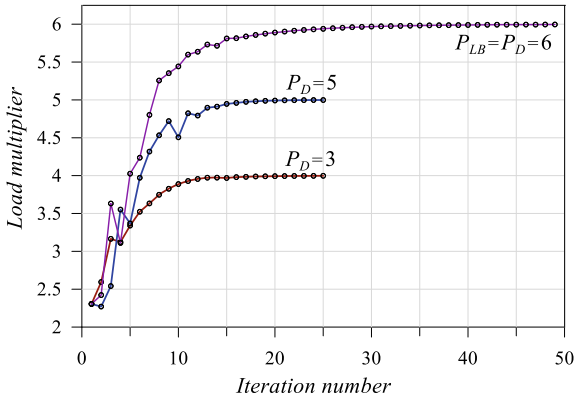

Fig. 5 Load multiplier versus iterations number for three sequences of elastic analyses carried on the human femur in-silico specimens: results for specimens #2 metaphysis and #3 diaphysis

Figures 4 and 5 show the obtained results in terms of load multiplier of the reference loads of Fig. 3a versus iterations number. Precisely, on taking into account the assumed loading and boundary conditions, which imply a stress concentration at the lower clamped part of the specimens, the behavior of specimens #1 and #4, as well as that of specimens #2 and #3, are equal to each other, as it has to be. The clamped zones of the corresponding pairs of specimens exhibit the same material arrangement. Figure 4 is then referred to specimens #1 and #4 while Fig. 5 to specimens #2 and #3.

In each figure three different sequences of elastic analyses (among the ones carried on) are depicted for three increasing values of the load multiplier P_D. The flattening of the curves attained for the value of the applied loads ($P_D F_x$, $P_D F_y$, $P_D F_z$) denotes that a complete redistribution of the stresses has been accomplished, i.e. the acting loads induce the existence of a statically and plastically admissible stress field, P_D being lower than the plastic collapse load multiplier. The maximum redistributable loads, corresponding to the maximum value of P_D, say P_{LB}, is the searched lower bound to the plastic collapse multiplier.

It is worth noting that the P_{LB} is obtained, at maximum, at iteration #40, but one iteration means one elastic FE analysis, so nothing computationally cumbersome. No maximum number of iterations has been fixed, indeed the iterations stop when all the "reduced" stress points (element-solutions where Eq. (5) have been applied) lay on the yield surface, i.e. when the corresponding ratio $|\overrightarrow{\mathbb{OP}}^{Y}_{\#e}|/|\overrightarrow{\mathbb{OP}}^{e}_{\#e}|$ is equal to 1 to within a fixed numerical tolerance. It is also worth to note that the P_{LB} predicted for specimens #1 and #4 ($P_{LB} = 5$) is lower than that ($P_{LB} = 6$) pertaining to specimens #2 and #3. This is a consequence of the presence of trabecular (weaker) bone tissue in the clamped zone of specimens #1 and #4 which activates Eq. (6).

Eventually, considering the resultant of the applied loads, the computed approximations (lower bounds) of the collapse/peak load value, say F_U, are equal to 3790 N and 4548 N for the two pairs of specimens respectively. By inspection of data reported in the relevant literature, see among others [68, 69], the collapse load values here obtained are of the same order of magnitude and definitively within the

range of the experimentally detected ones. Precisely, Yang and Co-Workers [68], for an average BW = 669 ± 175 N, report for all the tested in-vitro specimens (seven pairs of femurs from donors of age between 59 and 90 years) an average ultimate load equal to 3040 ± 720 N and an average fracture force of 4.5 BW. Dall'Ara and Co-Workers [69], with reference to 36 tested in-vitro samples from proximal femur of donors with age 76 ± 12 years, give a failure load (in the loading configuration "both stance", the one more similar to that here analysed) equal to 8.7 ± 2.9 kN. This is, to the authors opinion, a very encouraging result if are taken into account the large approximations in terms of geometry, loads and FE meshes of the examples addressed in this preliminary study. On the other hand, it is also true that there is a great variability of the peak load values detected via experimental tests (see again [69]) either for the impossibility of performing in-vivo experiments and for the difficulty to compare, in-vitro test results on specimens coming from different anatomical locations, species, ages, patients or possessing different geometries and suffering not perfectly equivalent loading conditions.

4 Concluding Remarks and Future Steps

A crucial observation on which this preliminary study is based it is the awareness that almost all the methods or numerical simulation techniques oriented to capture the main features of the mechanical behavior of human bones are often confined to specific cases. The problem, as said, is due to the objective difficulties in the description of the post-elastic behaviour of a structural element consisting of a material as peculiar as human bone which is not inert like most engineering materials but it is alive so it transforms, grows, degrades, adapts, and so on.

The main idea concerning the structural analysis via a numerical finite element based Limit Analysis of the bone is to renounce in following the system mechanical nonlinear response in the post-elastic regime up to collapse and to adopt a so-called direct method. That is a method oriented to predict the ultimate conditions with respect to the load bearing capacity, so investigating and predicting the incipient collapse scenario of bone directly. The reason of such approach relies on the awareness that when dealing with a structure made of a complex material for which the post elastic behavior is not well defined or reliable, as it is the case of the human bone material, the better choice is to focus the attention only on the elastic phase threshold of the structure, i.e. on the limit load value discriminating between elastic and post elastic phase.

The adopted Tsai-Wu-type stress-based criterion as well as the promoted elastic compensation method, seem effective in predicting a lower bound to the plastic collapse load characterizing the load bearing capacity of the addressed case of human femur. Moreover, the presented formulation characterized by a geometry in 3D and a stress treatment in terms of principal stresses seems reliable for handling the complexity of the problem. The run numerical simulations are definitively at an embryonic stage but the obtained results, whose orders of magnitude are those of

literature, make us confident on the validity of the whole approach and they bode well for its ability to constitute a diagnostic tool useful to predict bone fracture risk or, correlated to anamnesis, medical records and clinical patient specific pictures, to help in the diagnosis of the severity of osteoporosis driving the choice of the most appropriate intervention measures to adopt.

It is worth noting that such a tool, once settled, might be easily extended to all the type of human bone tissues as well as to the analysis of a system bone-prosthesis. All the information concerning the nonhuman synthetic materials, characterizing prosthesis and implants, can in facts searched in the relevant literature looking at the traditional metals, or metal-like materials as well as to bio-glasses, biopolymers, nanocomposites, metal matrix nanocomposites, all materials for which the essential information of the promoted approach, i.e. a yield criterion, is already available. Within this wider context the limit analysis design applied to human bones might then become a powerful clinical computer-aided decision-making tool in orthopaedics being able to prevent and predict fractures avoiding surgical complications and reducing the socio-economic impact of the problem.

There are still many points to be addressed, some of them are listed hereafter:

- The numerical analysis of in-silico human bone specimens having a realistic geometry, with a refined definition of cortical thickness, cortical and trabecular distribution, and suffering realistic loading conditions in terms of intensities and directions related, for example, to an external impact produced by a fall or to a muscular contraction without trauma. A related step forward could then be to set up an input data maker, a pre-processor segment of the limit analysis FE code, fully compatible with the data coming out by the molecular imaging and able to perform a mesh generation in an automated way based on pixel density from MRI or CT scanning, see e.g. [23–25].
- The Tsai-Wu-type yield criterion could be fixed/calibrated in terms of strength values different point by point or different among zones/parts of the examined bone so increasing the degree of detail, the correctness of the numerical modeling and the predictive capabilities of the method. To this aim, molecular imaging coupled with the fabric tensor concept, [31, 42, 43], could improve the definition of bone strengths.
- The implementation of the upper bound formulation of limit analysis approach following the authors' previous experiences in different contexts, see e.g. [15, 70]. The so-called linear matching method could indeed be rephrased with reference to human bones. The latter method, beyond an upper bound to the plastic collapse load multiplier, is able to predict the mechanism of collapse/fracture of the bone locating the zones prone to collapse.

The authors are aware that the present study represents, at this stage, a preliminary investigation and that the obtained results, which indeed seem reliable and reasonable from a mechanical point of view, have to be validated by analyzing case-studies, documented patient-specific histories, available in the relevant literature. All this is the object of an ongoing research programme.

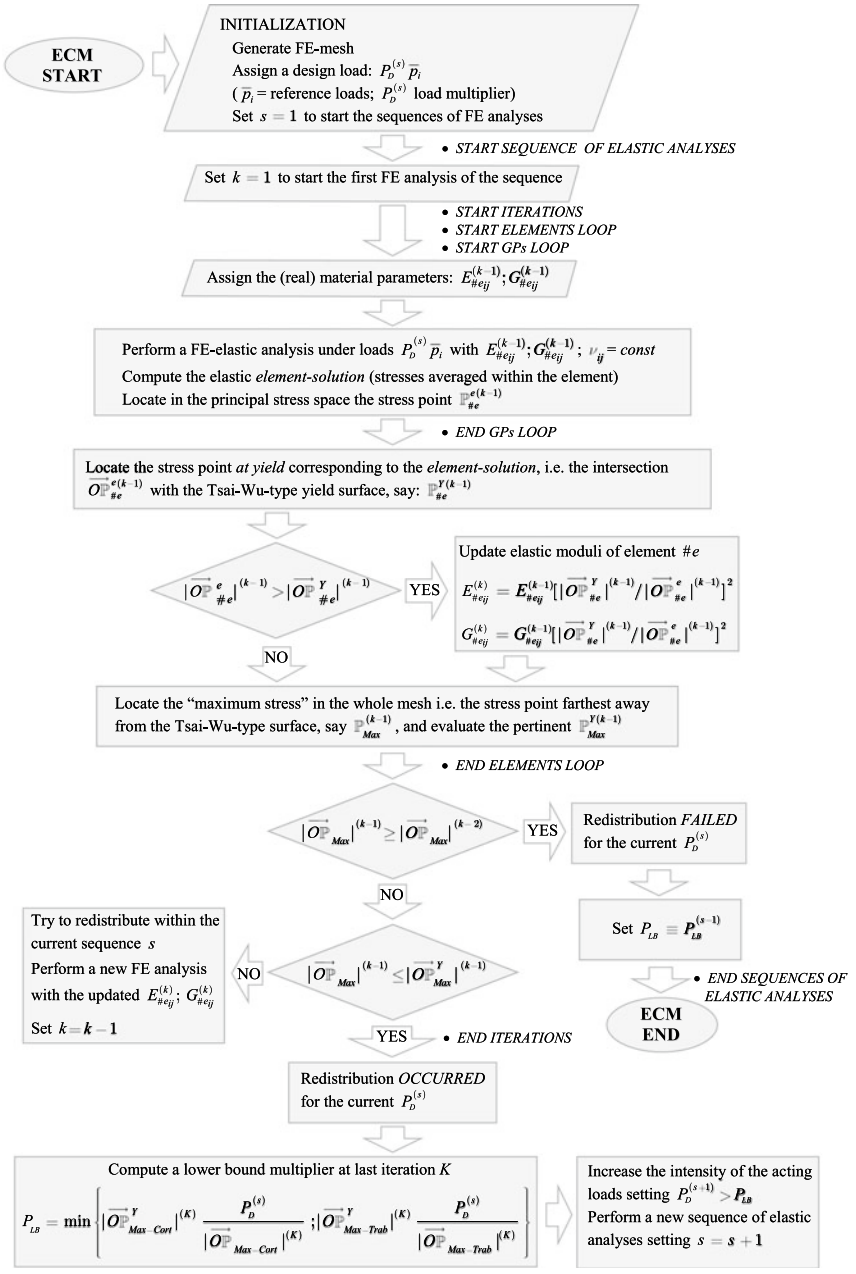

Fig. 6 ECM—graphic flow diagram

References

1. Cowin, S.C.: Bone Mechanics Handbook, 2nd edn. CRC Press, New York, NY (2001)
2. Klika, V.: Theoretical biomechanics. Intechopen (2011). https://doi.org/10.5772/816
3. Martin, B.R., Burr, D.B., Sharkey, N.A., Fyhrie, D.P.: Skeletal Tissue Mechanics. Springer, New York, NY (2015)
4. Murphy, W., Black, J., Hasting, G.: Handbook of Biomaterial Properties, 2nd edn. Springer, New York, NY (2016)
5. Huiskes, R., Chao, E.Y.S.: A survey of finite element analysis in orthopedic biomechanics: the first decade. J. Biomech. **16**(6), 385–409 (1983)
6. Zysset, P.K., Dall'Ara, E., Varga, P., Pahr, D.H.: Finite element analysis for prediction of bone strength. BoneKEy Reports 2, Article number: 386 (2013)
7. Ruffoni, D., van Lenthe, G.H.: Finite element analysis in bone research: a computational method relating structure to mechanical function. In: Comprehensive Biomaterials II, 2nd edn, Elsevier (2017)
8. Fuschi, P., Pisano, A.A, Weichert, D.: Direct Methods for Limit and Shakedown Analysis of Structures: Advanced Computational Algorithms and Material Modelling. Springer International Publishing Switzerland (2014)
9. Mackenzie, D., Boyle, J.T.: A method of estimating limit loads by iterative elastic analysis. I-Simple examples. Int. J. Press. Vessels Pip. **53**(1), 77–95 (1993)
10. Mackenzie, D., Shi, J., Boyle, J.T.: Finite element modelling for limit analysis by the elastic compensation method. Comput. Struct. **51**(4), 403–410 (1994)
11. Pisano, A.A., Fuschi, P.: A numerical approach for limit analysis of orthotropic composite laminates. Int. J. Numer. Methods Eng. **70**, 71–93 (2007)
12. Pisano, A.A., Fuschi, P., De Domenico, D.: A layered limit analysis of pinned-joint composite laminates: numerical versus experimental findings. Compos. Part B: Eng. **43**, 940–952 (2012)
13. Pisano, A.A., Fuschi, P., De Domenico, D.: Peak load prediction of multi-pin joints FRP laminates by limit analysis. Compos. Struct. **96**, 763–772 (2013)
14. Pisano, A.A., Fuschi, P., De Domenico, D.: Peak loads and failure modes of steel-reinforced concrete beams: predictions by limit analysis. Eng. Struct. **56**, 477–488 (2013)
15. De Domenico, D., Pisano, A.A., Fuschi, P.: A FE-based limit analysis approach for concrete elements reinforced with FRP bars. Compos. Struct. **107**, 594–603 (2014)
16. Pisano, A.A., Fuschi, P., De Domenico, D.: Numerical limit analysis of steel-reinforced concrete walls and slabs. Comput. Struct. **160**, 42–55 (2015)
17. Rho, J.Y., Kuhn-Spearing, L., Zioupos, P.: Mechanical properties and the hierarchical structure of bone. Medical Eng. Phys. **20**(2), 92–102 (1998)
18. Weiner, S., Wagner, H.D.: The material bone: structure-mechanical function relations. Ann. Rev. Mater. Sci. **28**(1), 271–298 (1998)
19. Hernandez, C.J.: Cancellous bone. In: Murphy, W., et al. (eds.) Handbook of Biomaterial Properties (Chapter A2). Springer Science + Business Media, New York (2016)
20. Currey, J.: Cortical bone. In: Murphy, W., et al. (eds.) Handbook of Biomaterial Properties (Chapter A1) Springer Science + Business Media New York (2016)
21. Beaupied, H., Lespessailles, E., Benhamou, C.-L.: Evaluation of macrostructural bone biomechanics. Joint Bone Spine **74**(3), 233–239 (2007)
22. Rincón-Kohli, L., Zysset, P.K.: Multi-axial mechanical properties of human trabecular bone. Biomech. Model. Mechanobio. **8**(3), 195–208 (2009)
23. Taghizadeh, E., Reyes, M., Zysset, P., Latypova, A., Terrier, A., Büchler, P.: Biomechanical role of bone anisotropy estimated on clinical CT scans by image registration. Ann. Biomed. Eng. **44**(8), 2505–2517 (2016)
24. Mirzaali, M.J., Schwiedrzik, J.J., Thaiwichai, S., Best, J.P., Michler, J., Zysset, P.K., Wolfram, U.: Mechanical properties of cortical bone and their relationships with age, gender, composition and microindentation properties in the elderly. Bone **93**, 196–211 (2016)

25. Schwiedrzik, J.J., Mirzaali, M.J., Thaiwichai, S., Best, J.P., Michler, J., Zysset, P.K., Wolfram, U.: Response to the commentary on mechanical properties of cortical bone and their relationships with age, gender, composition and microindentation properties in the elderly. Bone **105**, 312–314 (2017)
26. Wolfram, U., Wilke, H.J., Zysset, P.K.: Valid micro finite element models of vertebral trabecular bone can be obtained using tissue properties measured with nanoindentation under wet conditions. J. Biomech. **43**(9), 1731–1737 (2010)
27. Zysset, P.K., Curnier, A.: A 3D damage model for trabecular bone based on fabric tensors. J. Biomech. **29**(12), 1549–1558 (1996)
28. Fondrk, M.T., Bahniuk, E.H., Davy, D.T.: A damage model for nonlinear tensile behavior of cortical bone. J. Biomech. Eng. **121**(5), 533–541 (1999)
29. Keaveny, T.M., Morgan, E.F., Niebur, G.L., Yeh, O.C.: Biomechanics of trabecular bone. Ann. Rev. Biomed. Eng. **3**(1), 307–333 (2001)
30. Garcia, D., Zysset, P.K., Charlebois, M., Curnier, A.: A three-dimensional elastic plastic damage constitutive law for bone tissue. Biomech. Model. Mechanobiol. **8**(2), 149–165 (2009)
31. Doblaré, M., García, J.M., Gómez, M.J.: Modelling bone tissue fracture and healing: a review. Eng. Fract. Mech. **71**, 1809–1840 (2004)
32. Keaveny, T.M., Wachtel, E.F., Zadesky, S.P., Arramon, Y.P.: Application of the Tsai-Wu Quadric Multiaxial Failure Criterion to Bovine Trabecular Bone. J. Biomech. Eng. **121**, 99–107 (1999)
33. Zysset, P.K.: A review of morphology-elasticity relationships in human trabecular bone: theories and experiments. J. Biomech. **36**, 1469–1485 (2003)
34. Bayraktar, H.H., Gupta, A., Kwon, R.Y., Papadopoulos, P., Keaveny, T.M.: The modified superellipsoid yield criterion for human trabecular bone. J. Biomech. Eng. **126**(6), 677–684 (2004)
35. Tellache, M., Pithioux, M., Chabrand, P., Hochard, C.: Femoral neck fracture prediction by anisotropic yield criteria. Revue Europénne de Mécanique Numérique/Europ. J. Comput. Mech. Hermès/Paris: Lavoisier **18**(1), 33–41 (2009)
36. Wolfram, U., Gross, T., Pahr, D.H., Schwiedrzik, J., Wilke, H.J., Zysset, P.K.: Fabric-based Tsai-Wu yield criteria for vertebral trabecular bone in stress and strain space. J. Mech. Behav. Biomed. Mater. **15**, 218–228 (2012)
37. Hayes, W.C., Wright, T.M.: An empirical strength theory for compact bone. Fracture **3**, 1173–1179 (1977)
38. Cezayirlioglu, H., Bahniuk, E., Davy, D.T., Heiple, G.: Anisotropic yield behavior of bone under combined axial force and torque. J. Biomech. **18**(1), 61–69 (1985)
39. Carnelli, D., Gastaldi, D., Sassi, V., Contro, R., Ortiz, C., Vena, P.: A finite element model for direction-dependent mechanical response to nanoindentation of cortical bone allowing for anisotropic post-yield behavior of the tissue. J. Biomech. Eng. **132**, 081008-1–10 (2010)
40. Carnelli, D., Lucchini, R., Ponzoni, M., Contro, R., Vena, P.: Nanoindentation testing and finite element simulations of cortical bone allowing for anisotropic elastic and inelastic mechanical response. J. Biomech. **44**(10), 1852–1858 (2011)
41. Cowin, S.C.: The relationship between the elasticity tensor and the fabric tensor. Mech. Mater. **4**, 137–147 (1985)
42. Cowin, S.C.: Fabric dependence of an anisotropic strength criterion. Mech. Mater. **5**, 251–260 (1986)
43. Matsuura, M., Eckstein, F., Lochmüller, E.M., Zysset, P.K.: The role of fabric in the quasi-static compressive mechanical properties of human trabecular bone from various anatomical locations. Biomech. Model. Mechanobiol. **7**, 27–42 (2008)
44. Tabor, Z.: On the equivalence of two methods of determining fabric tensor. Medical Eng. Phys. **31**, 1313–1322 (2009)
45. Schwiedrzik, J.J., Wolfram, U., Zysset, P.K.: A generalized anisotropic quadric yield criterion and its application to bone tissue at multiple length scales. Biomech. Model. Mechanobio. **12**(6), 1155–1168 (2013)
46. Charlebois, M., Jirásek, M., Zysset, P.K.: A nonlocal constitutive model for trabecular bone softening in compression. Biomech. Model. Mechanobiol. **9**(5), 597–611 (2010)

47. Hosseini, H.S., Horák, M., Zysset, P.K., Jirásek, M.: An over-nonlocal implicit gradient-enhanced damage-plastic model for trabecular bone under large compressive strains. Int. J. Numer. Methods Biomed. Eng. **31**(11), 1–32 (2015)
48. Fratzl, P., Gupta, H.S., Paschalis, E.P., Roschger, P.: Structure and mechanical quality of the collagen-mineral nano-composite in bone. J. Mater. Chem. **14**, 2115–2123 (2004)
49. Gupta, H.S., Fratzl, P., Kerschnitzki, M., Benecke, G., Wagermaier, W., Kirchner, H.O.K.: Evidence for an elementary process in bone plasticity with an activation entalphy of 1 eV. J. R. Soc. **4**, 277–282 (2007)
50. Ritchie, R.O., Buehler, M.J., Hansma, P.: Plasticity and toughness in bone. Phys. Today **62**(6), 41–47 (2009)
51. Zimmermann, E.A., Schaible, E., Bale, H., Barth, H.D., Tang, S.Y., Reichert, P., Busse, B., Alliston, T., Ager, J.W., Ritchie, R.O.: Age-related changes in the plasticity and toughness of human cortical bone at multiple length scales. Proc. Nat. Acad. Sci. **108**(35), 14416–14421 (2011)
52. Tsai, S.W., Wu, E.M.: A general theory of strength for anisotropic materials. J. Compos. Mater. **5**, 58–80 (1971)
53. Wirtz, D.C., Schiffers, N., Pandorf, T., Radermacher, K., Weichert, D., Forst, R.: Critical evaluation of known bone material properties to realize anisotropic FE-simulation of proximal femur. J. Biomech. **33**, 1325–1330 (2000)
54. Lotz, J.C., Gerhart, T.N., Hayes, W.C.: Mechanical properties of trabecular bone from the proximal femur: a quantitative CT study. J. Comput. Assis. Tomogra. **14**, 107–114 (1990)
55. Lotz, J.C., Gerhart, T.N., Hayes, W.C.: Mechanical properties of metaphyseal bone in the proximal femur. J. Biomech. **24**, 317–329 (1991)
56. Turner, C.H., Wang, T., Burr, D.B.: Shear strength and fatigue properties of human cortical bone determined from pure shear tests. Calcif. Tissue Int. **69**, 373–378 (2001)
57. Sanyal, A., Gupta, A., Bayraktar, H.H., Kwon, R.Y., Keaveny, T.M.: Shear strength behavior of human trabecular bone. J. Biomech. **45**, 2513–2519 (2012)
58. Salençon, J.: Applications of the Theory of Plasticity in Soil Mechanics. Wiley, Chichester, England (1977)
59. Lubliner, J.: Plasticity Theory. Macmillan Publishing Company, New York, NY (1990)
60. World Nuclear Association: Non-Linear Analysis Design Rules, Part 1: Code Comparison, Cooperation in Reactor Design Evaluation and Licensing Mechanical Codes and Standards Task Force. Report No.2017/002 (2017)
61. Ponter, A.R.S., Carter, K.F.: Limit state solutions, based upon linear elastic solutions with a spatially varying elastic modulus. Comput. Methods Appl. Mech. Eng. **140**, 237–258 (1997)
62. Mackenzie, D., Boyle, J.T., Hamilton, R.: The elastic compensation method for limit and shakedown analysis: a review. J. Strain Anal. **35**(3), 171–188 (2000)
63. Ponter, A.R.S.: Direct methods derived from linear solution methods with spatial variation of moduli. In: Proceedings 8th World Congress on Computational Mechanics (WCCM8). June 30–July 5, 2008, Venice, Italy (2008)
64. ADINA R&D, Inc.: Theory and Modeling Guide. Adina R&D: Watertown, MA, USA (2002)
65. San, Antonio T., Ciaccia, M., Müller-Karger, C., Casanova, E.: Orientation of orthotropic material properties in a femur FE model: a method based on the principal stresses directions. Medical Eng. Phys. **34**, 914–919 (2012)
66. Huiskes, H.W.J., Janssen, J.D., Slooff, T.J.J.H.: A detailed comparison of experimental and theoretical stress-analysis of a human femur. In: Mechanical Properties of Bone (ASME) American Society of Mechanical Engineers, vol. 45, pp. 211–234 (1983)
67. Lennon, A.B., Prendergast, P.J.: Evaluation of cement stresses in finite element analyses of cemented orthopaedic implants. J. Biomech. Eng. **123**, 623–628 (2001)
68. Yang, K.H., Shen, K.-L., Demetropoulos, C.K., King, A.I., Kolodziej, P., Levine, R.S., Fitzgerald Jr., R.H.: The relationship between loading conditions and fracture patterns of the proximal femur. J. Biomech. Eng. **118**, 575–578 (1996)

69. Dall'Ara, E., Luisier, B., Schmidt, R., Pretterklieber, M., Kainberger, F., Zysset, P., Pahr, D.: DXA predictions of human femoral mechanical properties depend on the load configuration. Medical Eng. Phys. **35**, 1564–1572 (2013)
70. Ponter, A.R.S., Fuschi, P., Engelhardt, M.: Limit analysis for a general class of yield conditions. Europ. J. Mech. A/Sol. **19**, 401–421 (2000)

The Linear Matching Method and Its Software Tool for Creep Fatigue Damage Assessment

Manu Puliyaneth, Graeme Jackson, Haofeng Chen, and Yinghua Liu

Abstract The Linear Matching Method (LMM) is a numerical procedure that has undergone extensive research and development over a number of years to conduct various structural integrity assessments, more recently, the creep-fatigue damage assessment considering full creep-cyclic plasticity interaction using the extended Direct Steady Cycle Analysis. In order to encourage the widespread implementation of the LMM throughout the industry, an Abaqus CAE plug-in has been developed that enables its use by individuals with little or no understanding of the numerical theories involved. This chapter discusses different creep-cyclic plasticity mechanisms and provides a detailed review of the latest developments within the LMM framework for its evaluation. Case studies are included to demonstrate the applicability of LMM in the evaluation of creep-cyclic plasticity response for complicated loads, varying dwell periods and multi-material structures. Further, the flexibility of LMM to couple with Reversed Plasticity Domain Method to design cyclic load levels, and with design codes for creep-fatigue damage evaluation is also presented. All the results from the case studies demonstrate the level of accuracy, efficiency and robustness of the LMM.

1 Introduction

An important consideration when designing engineering components is to determine whether the loading conditions will have a significant impact upon the length of time that a structure can remain in safe operation. This is particularly true in cases where structures are exposed to elevated temperature and cyclic loads since severe complex failure mechanisms, such as creep and fatigue and their interaction if any, must be carefully considered. Over the past few decades, efforts have been made

M. Puliyaneth · G. Jackson · H. Chen (✉)
Department of Mechanical & Aerospace Engineering, University of Strathclyde, Glasgow G1 1XJ, UK
e-mail: haofeng.chen@strath.ac.uk

Y. Liu
Department of Engineering Mechanics, Tsinghua University, Beijing 100084, China

A. A. Pisano et al. (eds.), *Direct Methods*, Lecture Notes in Applied and Computational Mechanics 95, https://doi.org/10.1007/978-3-030-48834-5_2

to combine finite element analysis with continuum damage mechanics to assess the creep-fatigue damage evaluation. But for acceptable results they require numerous material parameters which are not easily available. Another limiting factor is the high computational cost involved. Recently, several direct methods have been developed which uses relatively simpler material models such as Elastic-Perfectly Plastic model (EPP) or Ramberg Osgood (RO) model. They consider a load domain that accounts for all the possible paths between the extremes. LMM is one such direct method that has been developed to include the extended Direct Steady Cycle Analysis (eDSCA) which directly calculates the stabilized response of a structure subjected to a cyclic load at high temperature. The outputs from eDSCA can be coupled with appropriate damage models to conduct creep-fatigue damage analysis.

2 Cyclically Loaded Structures

The minimum load level that a structure is able to withstand under monotonic loading condition is known as the "limit load", loading beyond this will lead to an instantaneous collapse. When subjected to cyclic loading conditions, failure is likely to occur at lower loading levels due to the accumulation of residual stresses and plastic strains throughout the multiple cycles. In the work carried out by Bree [1], in the late 1960s, it was identified that a component subjected to a cyclic thermal load and a constant mechanical load could exhibit one of the four potential cyclic responses, namely purely elastic behaviour, elastic shakedown, reverse plasticity and ratcheting. In order to represent how the cyclic and constant loads interact with one another he proposed an interaction diagram, similar to the one presented in Fig. 1, for a thin cylindrical vessel subject to an internal pressure and a linear temperature gradient across its thickness.

The cyclic thermal load is normalised with respect to the yield stress of the material and is shown on the vertical axis, while the constant mechanical load, which is also

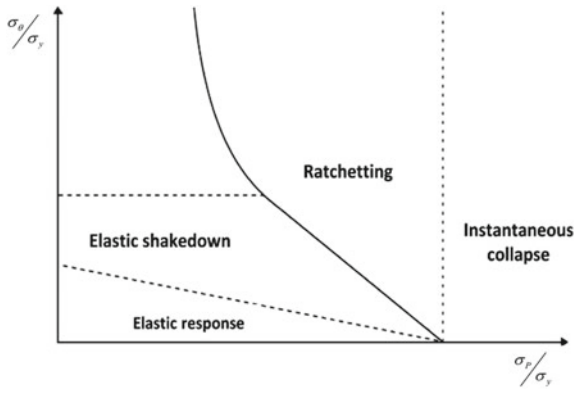

Fig. 1 Classical Bree-like diagram

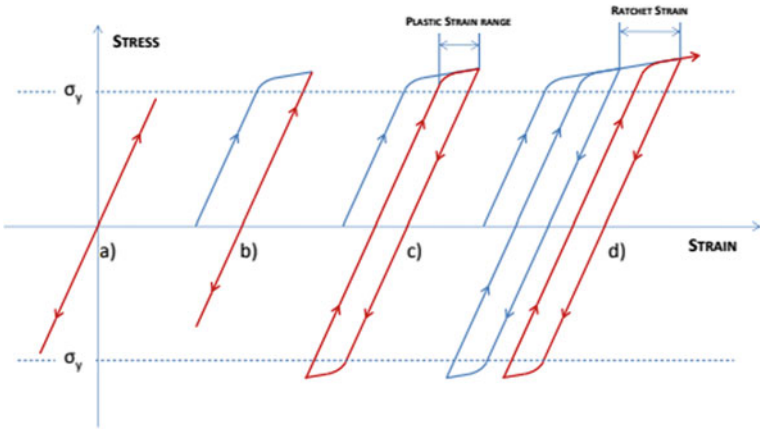

Fig. 2 Steady state structural responses to loads within **a** pure elastic region, **b** elastic shakedown region, **c** reverse plasticity region, **d** ratcheting region [2]

normalised against the yield stress of the structure, is shown on the horizontal axis. It can be observed that for relatively lower loading levels there is no plastic deformation and the structure exhibits purely elastic behaviour. However, for loading cases where this elastic response limit is exceeded, plastic strains begin to develop. As the cyclic thermal load is increased, the response escalates to the elastic shakedown region and then to reverse plasticity region. On increasing the mechanical load, the structure exhibits a ratcheting behaviour. Typical hysteresis loops of structures exhibiting pure elastic, elastic shakedown, reverse plastic and ratcheting mechanisms are presented in Fig. 2.

Elastic shakedown	Plastic strains accumulate during the initial cycles but the response then becomes entirely elastic due to residual stresses, Fig. 2b.
Reverse plasticity	Plastic strains occur during all cycles but there is no net increase and a closed loop is formed throughout the cycle, Fig. 2c.
Ratcheting	Plastic strains accumulate during all cycles and this eventually leads to structural failure via incremental plastic collapse, Fig. 2d.

2.1 Creep—Cyclic Plasticity Interaction

Creep is a time-dependent damage mechanism prevalent in materials when exposed to high temperatures, generally over 30% of its melting point, for a pro-longed period. A typical creep strain curve is retraced in Fig. 3. It consists of three stages; (a) primary; (b) secondary; and (c) tertiary. During the primary phase the creep strain rate decreases. During secondary stage, the creep strain rate remains constant, and

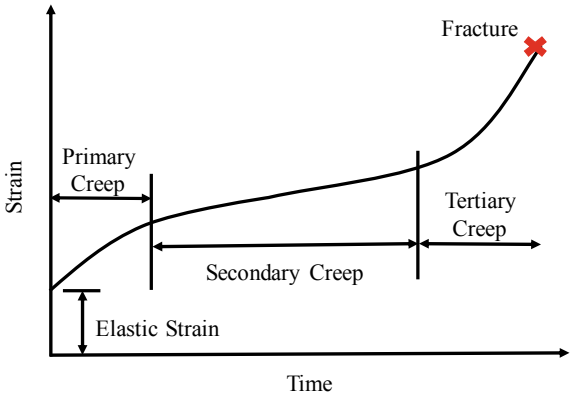

Fig. 3 Schematic of the standard creep curve

generally, the secondary stage is the longest and most prominent phase during the creep dwell. During the tertiary phase, an exponential increase in the creep strain is observed.

Under cyclic loading conditions, the introduction of creep can have severe effects on the cyclic plasticity response of the structure, such that it may introduce creep-fatigue damage mechanism in an otherwise elastic loading condition or the much more dangerous damage mechanism known as creep-ratcheting. Factors such as operating temperature, strain range, frequency of loading and duration of loading are critical and influence the creep-cyclic plasticity interaction. A typical steady state hysteresis loop of a structure under creep-cyclic plasticity mechanism is shown in Fig. 4a.

At steady state, if the reverse plasticity can compensate for the creep strain and the loading strain, if any, a closed hysteresis loop is obtained. On the other hand, if an open loop is obtained, the mechanism is termed as creep-ratcheting. Creep ratcheting may be broadly distinguished as "cyclic enhanced creep" and "creep enhanced plasticity". Where the open hysteresis loop is a result of the large creep strain accumulated, it

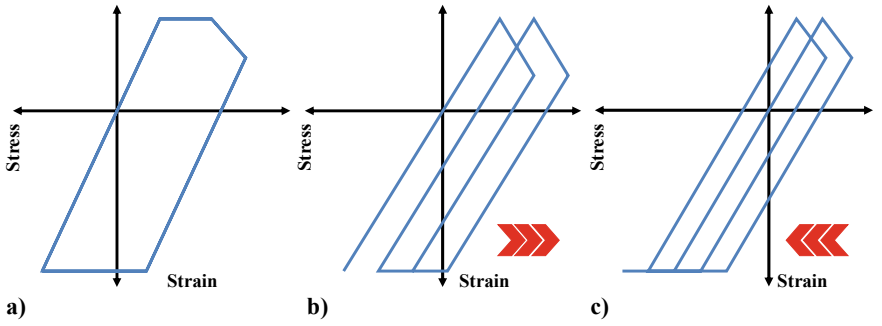

Fig. 4 Steady state hysteresis. **a** Creep-fatigue interaction, **b** cyclically enhanced creep; **c** creep enhanced plasticity

is referred to as cyclic enhanced creep (Fig. 4b). On the other hand, large reverse plastic strain may be dominated in cases with small creep strains but significant stress relaxation during the dwell, and the ratcheting mechanism in such a scenario is referred to as creep enhanced plasticity (Fig. 4c).

3 Creep-Fatigue Damage Assessment

High temperature design codes such as R5 and ASME evaluate the total damage in the following way

$$d_c + d_f \leq \emptyset_{CF} \tag{1}$$

where d_c and d_f are the total creep damage and total fatigue damage; $\emptyset_{CF}$ is the allowable total creep-fatigue damage factor which is depended on the type of material and the standard considered. Essentially, both the creep and fatigue damages are individually calculated and then combined to assess the acceptance based on the code considered. The number of cycles to LCF damage is calculated using the strain-life curve (E-N) curve, for which the total stain range should be known. The fatigue damage per cycle may then be defined as:

$$d_f^{1c} = \frac{1}{N(\Delta\varepsilon_{tot})} \tag{2}$$

where d_f^{1c} is the fatigue damage per cycle and N is the number of cycles to pure fatigue failure corresponding to the total stain range ($\Delta\varepsilon_{tot}$). The two most common creep damage assessment methodologies are the time fraction (TF) rule, in line with ASME recommendation and ductility exhaustion (DE) method, which is recommended by R5. The TF rule to calculate the creep damage can be expressed as:

$$d_{c\_TF}^{1c} = \int_0^{t_h} \frac{dt}{t_f(\sigma, T)} \tag{3}$$

where t_f is the creep rupture time, and it is a function of stress and temperature. dt is the time increment and t_h is the hold time. Creep damage by DE method is calculated using:

$$d_{c\_DE}^{1c} = \int_0^{t_h} \frac{\dot{\bar{\varepsilon}}_c}{\bar{\varepsilon}_c\left(\dot{\bar{\varepsilon}}_c, T\right)} dt \tag{4}$$

where $\dot{\bar{\varepsilon}}_c$ is the instantaneous creep strain rate and $\bar{\varepsilon}_c$ is the material creep ductility. In effect, parameters such as the total strain range, creep strain, start of dwell stress

and the elastic follow up factor at steady state are critical in the assessment of creep-fatigue damage assessment. The eDSCA within the LMM frame work is capable of accurately calculating them.

4 The Linear Matching Method

The LMM is a direct method for structural assessment that has been a part of the R5 research program for many years, having initially been developed from the Elastic Compensation Method (ECM). Over the years LMM has seen extensive theoretical and numerical development and has become one of the most successful direct methods currently available. It is based upon the premise that a non-linear material response can be simulated using a series of linear analyses during which the modulus is modified throughout the structure. Figure 5 demonstrates this concept pictorially.

The first stage of the LMM process is to perform a linear elastic analysis for each of the loads applied to the structure, with the modulus at each point modified such that the stress equals the yield stress (Fig. 5a). These modified values for modulus are then used in the next elastic analysis and this leads to the stress being redistributed throughout the structure (Fig. 5b). Following this the modulus is again modified and the process is repeated multiple times, thereby allowing the stresses to redistribute similarly to an elastic-plastic material (Fig. 5c). The LMM has been developed for

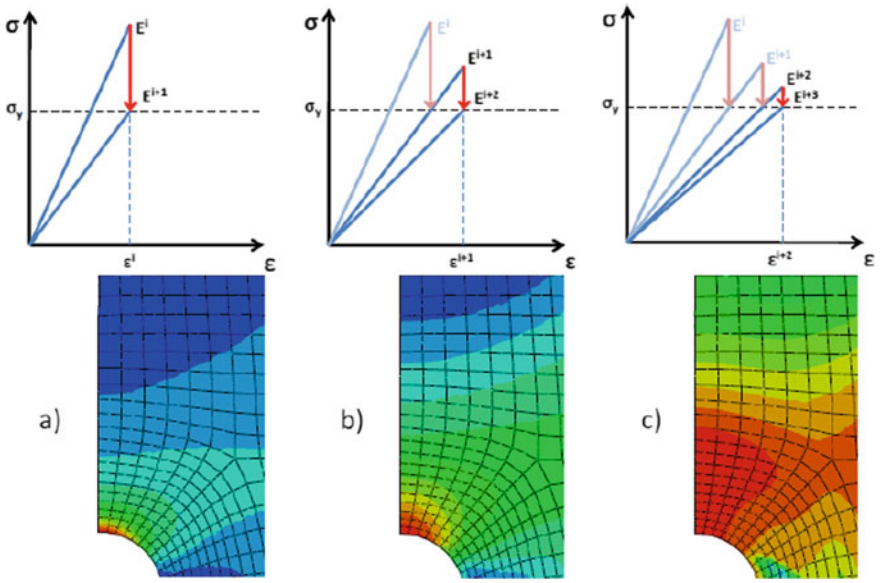

Fig. 5 **a** Initial stress distribution, **b** intermediate stress redistribution, **c** final stress redistribution

limit analysis, shakedown analysis, ratchet analysis, and recently to include steady state cyclic behavior with full creep-cyclic plasticity interaction.

4.1 Numerical Procedures for eDSCA

A flowchart of the eDSCA evaluation procedure is presented in Fig. 6. Detailed discussions on the numerical procedure of the eDSCA has been previously presented in [3]. Revisiting the same would be beyond the scope of this chapter hence a concise discussion highlighting the major aspects of the procedure is presented here.

For a structure subjected to an arbitrary cyclic load, Chen et al. [3, 5] proposed the minimization function $I\left(\dot{\varepsilon}_{ij}^{c}\right) = \sum_{l=1}^{L} I^{l}$ to calculate the steady state cyclic response, where L refers to the total number of load instances, $\dot{\varepsilon}_{ij}^{c}$ indicates the kinematic admissible strain rate and l refers to the load instance considered. Further an incremental form is also suggested for the minimization function as:

$$I^{l}\left(\Delta\varepsilon_{ij}^{l}\right) = \int_{V} \left\{ \sigma_{ij}^{l} \Delta\varepsilon_{ij}^{l} - \left[\widehat{\sigma}_{ij}^{l}(t_l) + \rho_{ij}^{l}(t_l) \right] \Delta\varepsilon_{ij}^{l} \right\} dV \tag{5}$$

where $\Delta\varepsilon_{ij}^{l}$ is the strain increment and $\rho_{ij}^{l}(t_l)$ is the residual stress. Using the minimization function defined above, $\Delta\varepsilon_{ij}^{l}$ is calculated in an iterative manner. The inelastic strain and the residual stress at each increment are computed using the previously accumulated residual stress and the elastic stress. For the load instance t_l during the loading cycle, $\Delta\varepsilon_{ij,k+1}(t_l)$ is calculated by:

$$\Delta\varepsilon_{ij,k+1}(t_l)' = \frac{1}{2\overline{\mu}(t_l)} \left[\widehat{\sigma}_{ij}(t_l) + \rho_{ij,k+1}(t_{l-1}) + \Delta\rho_{ij,k+1}(t_l) \right]' \tag{6}$$

where $\overline{\mu}$ is the iterative shear modulus, $\widehat{\sigma}_{ij}$ is the associated elastic solution, $\rho_{ij,k+1}(t_{l-1})$ is the prior changing residual stress history, $\Delta\rho_{ij,k+1}(t_l)$ is the current changing residual stress associated with that inelastic strain increment and k refers to the number of sub-cycles required to attain convergence. For cyclic load with creep dwell, the accumulated creep strain can be computed by:

$$\Delta\bar{\varepsilon}^{c} = \frac{B(n-1)\Delta t^{m+1}(\bar{\sigma}_s - \bar{\sigma}_c)}{\left(\frac{1}{\bar{\sigma}_c^{n-1}} - \frac{1}{\bar{\sigma}_s^{n-1}}\right)(m+1)} \tag{7}$$

$$\bar{\sigma}_c = \left(\frac{\dot{\bar{\varepsilon}}^{F}}{B\Delta t^{m}} \right)^{\frac{1}{n}} \tag{8}$$

$$\dot{\bar{\varepsilon}}^{F\prime} = \frac{\Delta\bar{\varepsilon}^{c}}{\Delta t} \frac{(m+1)}{(n-1)} \frac{\bar{\sigma}_c^{n}}{(\bar{\sigma}_s - \bar{\sigma}_c)} \left(\frac{1}{\bar{\sigma}_c^{n-1}} - \frac{1}{\bar{\sigma}_s^{n-1}} \right) \tag{9}$$

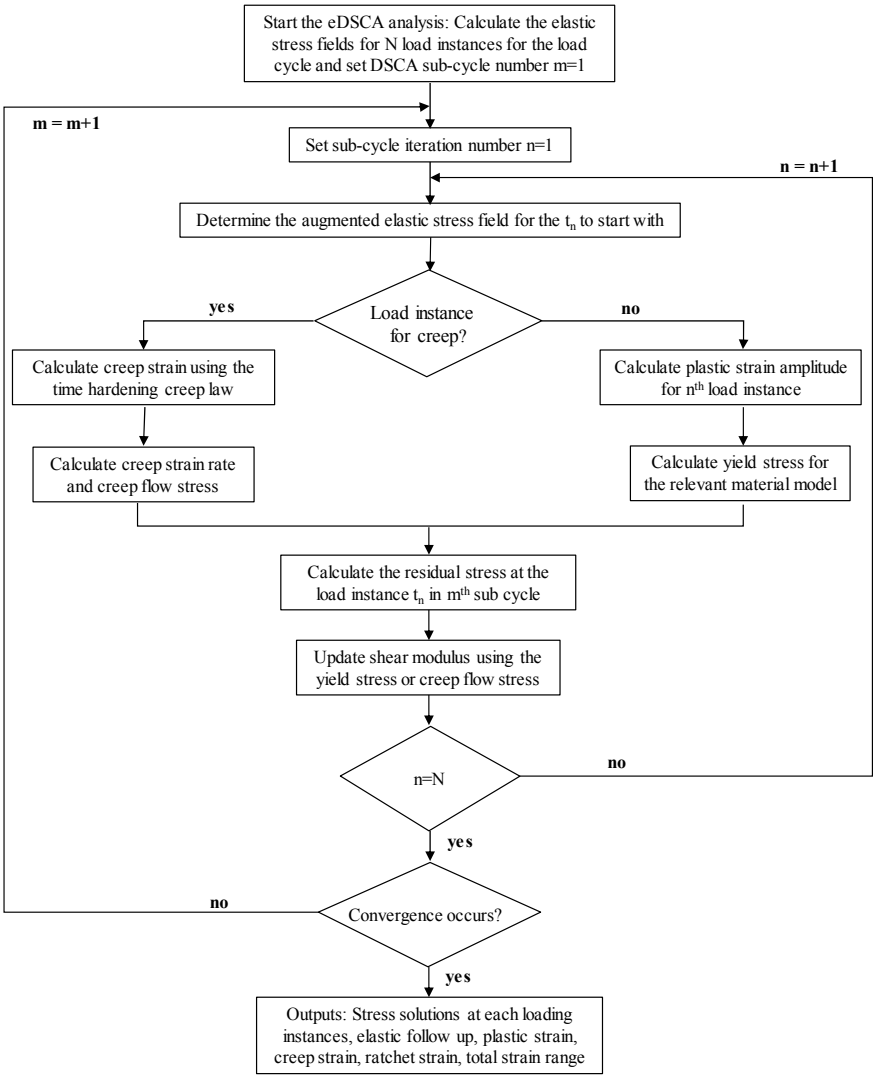

Fig. 6 Flow chart illustrating the eDSCA numerical procedure [4]

where B, m and n indicate the creep parameters, $\bar{\sigma}_c$ refers to the creep flow stress $\bar{\sigma}_c$ is computed using Eq. (8), which is then used as an input in Eq. (9) to calculate the creep strain rate $\dot{\bar{\varepsilon}}^F$. The residual stress and an iterative shear modulus for the increment is then computed as:

$$\bar{\mu}_{k+1}(x, t_l) = \bar{\mu}_k(x, t_l) \frac{\sigma_y^R(x, t_l)_k}{\bar{\sigma}\left(\hat{\sigma}_{ij}(x, t_l) + \rho_{ij}^r(x, t_l)_k\right)} \tag{10}$$

where $\bar{\mu}_k(x, t_l)$ is the iterative shear modulus at the sub-cycle k for lth load instance. $\sigma_y^R(x, t_l)_k$ is either an iterative von-Mises yield stress for the material model considered at load instance t_l or the creep flow stress $\bar{\sigma}_c$. $\rho_{ij}^r(x, t_l)$ is the sum of the constant residual stress field and all previous changing residual stresses at load instance t_l. The procedure briefly detailed in this section helps in determining all the parameters required for the estimation of the saturated hysteresis loop.

4.2 The LMM Software Tool

From its inception, LMM subroutines are coded using FORTRAN language so as to facilitate its use in with Abaqus. This implies that users need to have sufficient programming experience to run the analysis efficiently. But this is not the case especially in an industrial environment. In order to counter this issue, a Graphical User Interface (GUI) and an autonomous Abaqus plug-in have been developed recently. The plug-in provides the user with an interface to select the model, chose the analysis type, define the material properties and define the load in a straight forward manner.

The LMM plug-in, on installation will appear under the "plug-in" menu in Abaqus CAE. A pictorial presentation of the sequence of the different dialog box the user passes through is given in Fig. 7. The first dialog box provides the user the option to select the type of LMM analysis, such as (a) strict shakedown analysis; (b) steady state cycle analysis; (c) steady state cycle and ratchet limit analysis; (d) creep rupture analysis; (e) eDSCA with creep dwell(s) analysis. The next dialog box deals with the material parameter such as the Young's modulus, yield stress, Poisson's ratio, the thermal expansion coefficient and creep constants for each material in the model. This enables the use of LMM in structural analysis of multi-material components such as weldments and Metal Matrix Composites (MMC). In order to achieve a higher level of accuracy, the user has the option of providing temperature dependent properties. The option to choose between EPP or RO material model is also provided. The RO material model option is coded to generate the yield stress from the RO parameters entered by the user.

Once the above steps are complete, the plug-in then presents the load cycle dialog within which a load table is provided to define the load cycle. Defining the load cycle properly is critical in the generation of accurate results. The load at each of the time point along with the corresponding temperature field can specified within the load table. It is to be noted that the user can define any number of time instances. The final dialog box helps in defining the convergence rule, name of the job and the maximum increments. In order to run larger models swiftly, the LMM software is developed to run multiple Computer Processing Units (CPUs).

On completion of the above steps, prior to running the analysis, the plug-in carries a sequence of checks to assure the applicability of LMM analysis on the model. The user is advised of the errors if any, which are to be rectified for the analysis to commence. It should be noted that at each dialog box, the values provided by the

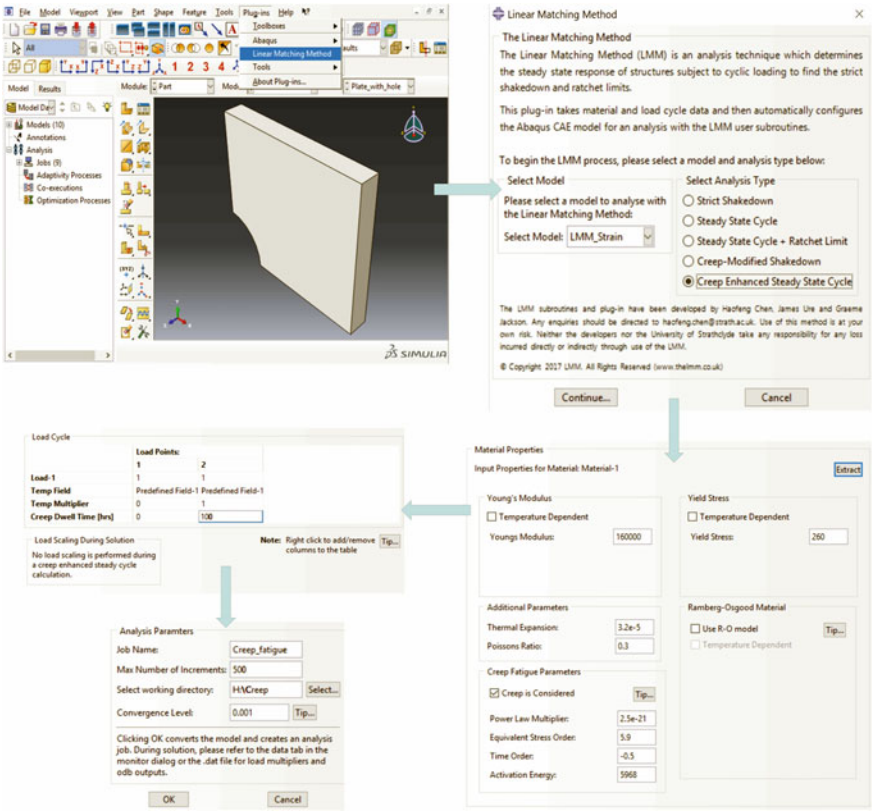

Fig. 7 LMM eDSCA analysis tool procedure

user are also checked for probable errors. In case an error is found, the plug-in produces a dialog box indicating the error and a possible solution for it.

5 LMM Cases Study

5.1 Fatigue Assessment Approach by Direct Steady Cycle Analysis (DSCA)

Recently Zheng et al. [6, 7] combined the Reversed Plasticity Domain Method (RPDM) and the DSCA within the LMM framework to design cyclic load levels for LCF experiments with predefined fatigue life ranges. The example is discussed here as it utilizes various facets within the LMM framework such as shakedown

analysis, ratchet analysis, the use of temperature dependent properties and use of EPP & RO material models.

For LCF experiments of components with a predefined fatigue life range, it is critical to properly define the cyclic load levels, but this is not straight forward and is quite difficult to obtain. The DSCA option within the LMM framework may be used as an aiding tool to obtain the load levels for the experiments. The basic idea is to estimate the total strain range under the considered loading condition using the DSCA and then refine it further until the fatigue life corresponds to the LCF testing requirement. The steps may be elaborated as below:

1. The ratchet and shakedown limits are calculated to obtain the Reversed Plasticity Domain (RPD), and this utilizes the shakedown and ratchet plug-in.
2. The DSCA then calculates the total strain range of the selected load level.
3. The fatigue life is estimated based on the fatigue life curve and total strain range.
4. The above steps are repeated until the fatigue life obtained is in line with the requirements of the LCF testing.

Zheng et al. [6, 7] presented the case study of a pressurized shell made of X2CrNiMo17-12-2 steel used in nuclear power plants. The geometry and the complicated loading condition opted are presented in Fig. 8a. As indicated in Sect. 4.2, LMM has the capacity to work with both temperature dependent and temperature independent properties, though the number of iterations required is higher, as reflected in Fig. 8b.

The shakedown and ratchet limit boundaries (Fig. 9a) are generated using the relevant tools within the LMM plug-in. Load levels below the elastic limit induce HCF damage. Within the RPD, the load levels generally induce LCF damage. The total strain range is computed using the eDSCA for the opted load level (indicated as ⊗ in Fig. 9a) which is within the RPD. A comparison of the elastic strain range, plastic strain range, ratchet strain and total strain range computed using both the RO and EPP models are presented in Fig. 9b. The obtained total strain range, with the help

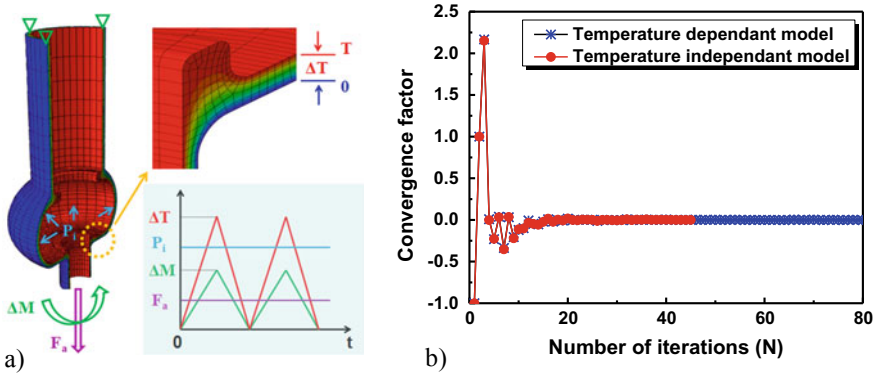

Fig. 8 **a** Geometry and load applied to the pressurized shell; **b** comparison between the number of iterations for temperature dependent and independent material properties [6, 7]

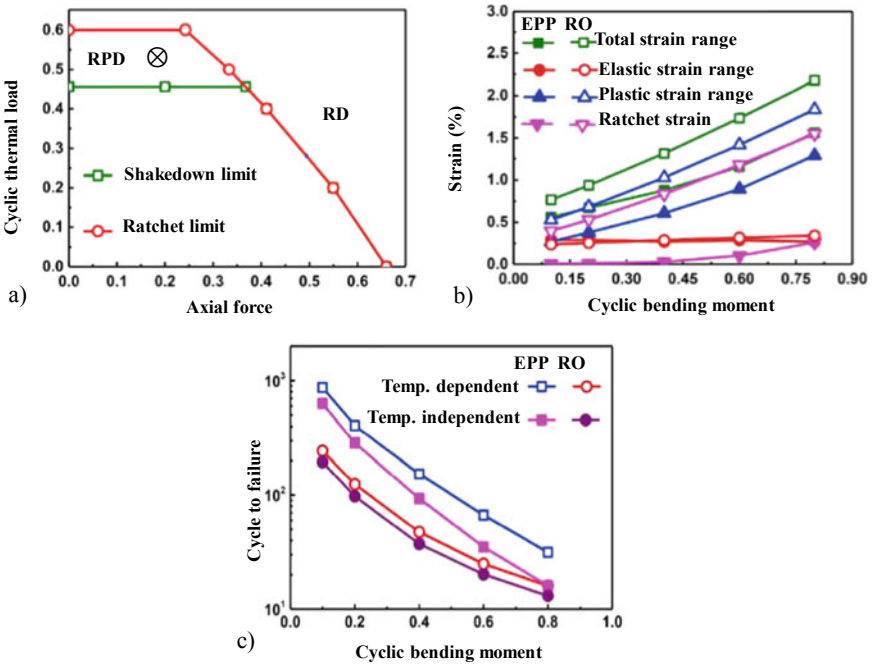

Fig. 9 **a** A typical shakedown-ratchet limit curve. **b** Calculated strains based on the temperature-dependent RO and EPP model; **c** fatigue life assessment based on the calculated strain range [6, 7]

of an E-N diagram is then used to compute the number of cycles (Fig. 9c). For this particular case study, the number of cycles computed by RO model is larger than that computed by EPP model, which is contrary to the normal knowledge which is that the EPP model produces the most conservative results. This unusual result is due to the lower elastic limit for the RO model compared to the EPP model. Nevertheless, this points to the high level of accuracy and the computational excellence LMM exhibits. In case the fatigue life requirements of the LCF testing are not satisfactorily met by the chosen load cycle, other load levels are analysed for their corresponding total strain ranges.

5.2 Creep Fatigue Assessment on Cruciform Weldment

Y. Gorash et al. studied and presented the creep-fatigue damage assessment of a cruciform weldment (Fig. 10a) using LMM in [8–10], a brief overview of which is provided in this section. The loads considered include a cyclic bending moment and a uniform high temperature (Fig. 10b). A reverse pure bending moment is simulated by imposing a cyclic linear distribution of normal pressure at the end of the model.

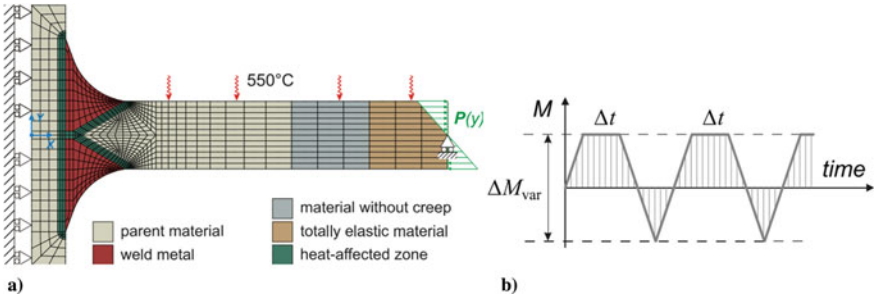

Fig. 10 **a** Finite element model of the weldment; **b** loading condition of the cruciform weldment [8–10]

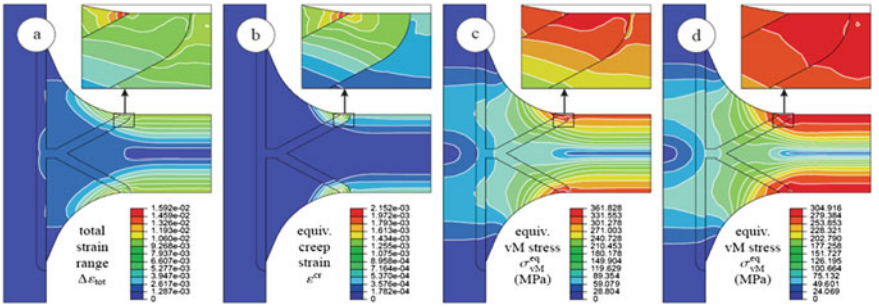

Fig. 11 For dwell time of 5 h. **a** Total Strain Range; **b** creep Strain; **c** start of dwell stress; **d** end of dwell stress [8–10]

The material properties are in line with SS316 N(L) with varying properties for the PM, HAZ and WM.

Analyses were carried out for a pure fatigue case and creep-fatigue interactions scenarios with creep dwells of 1 and 5 h. The variants of bending moments included total strains of 0.25, 0.3, 0.4, 0.6 and 1% of the parent material. The contours for total strain range, creep strain and stress from LMM analysis for a total strain of 1% and dwell time of 5 h are presented in Fig. 11. The most critical zone has been identified as the location at the weld toe near the heat affected zone. Further, Y. Gorash et al. presented a comparison between the available experimental results and the LMM simulation results, which showed a satisfactory comparison for 9 of the 11 results.

5.3 Creep Fatigue Interaction of a MMC

A brief overview of the study done on MMC by Barbera et al. in [4, 11, 12] is discussed here. This case study is particularly interesting as it discusses the effect of a creep dwell on loading conditions which would otherwise resonate an elastic

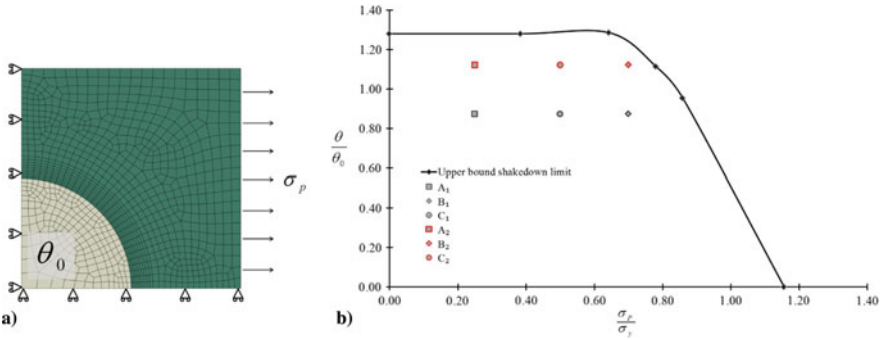

Fig. 12 **a** Finite element model and the loads applied on the MMC; **b** shakedown limit interaction curve [4, 11, 12]

behavior. The loads considered for the MMC consist of a constant mechanical load and a uniform cyclic temperature load (Fig. 12a). The MMC consists of Al_2O_3 fibre and Al 2024 T3 matrix. A shakedown limit interaction curve is obtained using the LMM shakedown analysis initially to identify possible load levels that would exhibit an elastic response in the absence of creep dwell. 6 load points such as A1, A2, B1, B2, C1 and C2 as indicated in Fig. 12b were identified and studied for varying dwell times. For the load levels A1 and A2, where the primary load is relatively lower than B and C, a closed hysteresis loop is obtained for dwell holds of 1 to 100 hours, suggesting the introduction of creep-fatigue interaction. Whereas for all the other load levels considered an increment in the net strain per cycle is present suggesting creep-ratcheting mechanism. The increase in the thermal load further increased the plastic strain increment during loading and the creep strain. As an example, the hysteresis loops for B1 and B2 for dwell times 1 and 100 hours are presented in Fig. 13. It is inferred that the ratcheting mechanism is influenced by the dwell time and the mechanical load. Hence the analysis was repeated considering only cyclic thermal loads. The hysteresis loops so obtained were all closed loop though with increasing the dwell hold, the creep strain and reverse plasticity increased. Using inelastic Abaqus step-by step analysis the LMM results were verified. A comparison of the values and contours of the creep strain increment ε_C^{MMC}, plastic strain increment during loading ε_L^{MMC} and unloading ε_{UL}^{MMC} are present in Table 1 and Fig. 14 respectively.

5.4 Creep Fatigue and Creep Ratcheting of Butt Welded Pipe

The case study discussed here gives an overview of how eDSCA may be used with an appropriate damage model (introduced in Sect. 3) to conduct creep-fatigue damage analysis. Figure 15 presents the general evaluation procedure, which starts with the estimation of the saturated hysteresis loop using eDSCA. Using the total strain

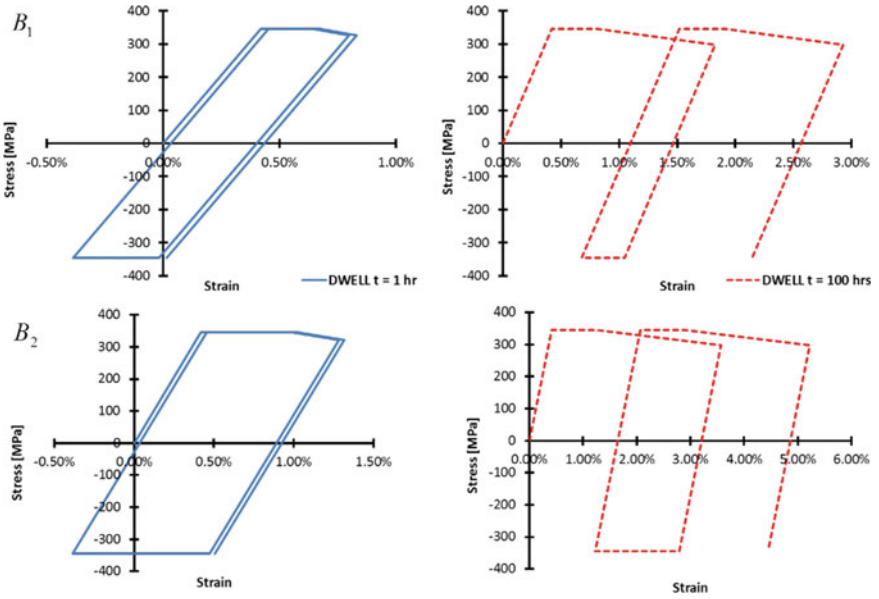

Fig. 13 Response of the steady state stress-strain path at location the critical point for load points B1 and B2 [4, 11, 12]

Table 1 Comparison between LMM and SBS analysis for different cyclic loads

Cyclic load point	ε_L^{MMC}		ε_C^{MMC}		ε_{UL}^{MMC}	
	LMM	Abaqus	LMM	Abaqus	LMM	Abaqus
A_1	0	0	$2.21\ E^{-4}$	$2.53\ E^{-4}$	$1.80\ E^{-4}$	$2.00\ E^{-4}$
B_1	$2.26\ E^{-3}$	$2.01\ E^{-3}$	$1.76\ E^{-3}$	$1.74\ E^{-3}$	$3.70\ E^{-3}$	$3.51\ E^{-3}$
A_2	0	0	$1.20\ E^{-3}$	$1.25\ E^{-3}$	$1.13\ E^{-3}$	$1.20\ E^{-3}$
B_2	$5.726\ E^{-3}$	$5.15\ E^{-3}$	$3.22\ E^{-3}$	$3.14\ E^{-3}$	$8.57\ E^{-3}$	$8.15\ E^{-3}$

obtained, the fatigue damage is calculated and using the creep stresses and strains, the creep damage is calculated. The total damage is then assessed using the considered standard's interaction diagram.

The pipe geometry and loading conditions considered for the case study are presented in Fig. 16. Welding residual stresses are assumed to be minimal due to post weld heat treatment such that their effect on creep behaviour on the welded pipe can be neglected. The most critical region in terms of creep-fatigue crack initiation probability is at the interface between the WM and HAZ where the equivalent creep strain and the total strain are found to be high.

The effect of creep dwell on the cyclic-creep plasticity mechanism of the pipe can be understood from Fig. 17a. Compared to the pure fatigue case, the introduction of a creep dwell increases the reverse plasticity. Increasing the dwell time further

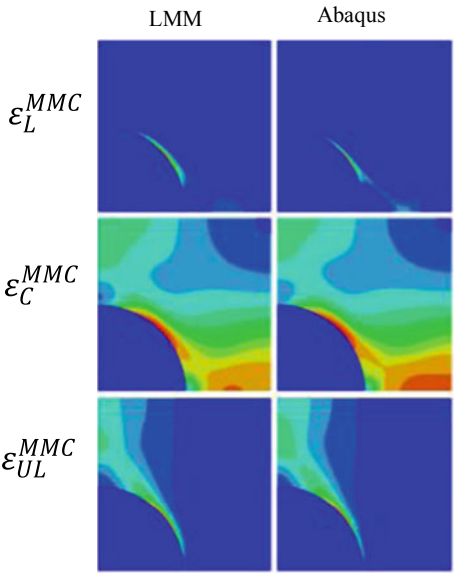

Fig. 14 Comparison between LMM and SBS analysis contours [4, 11, 12]

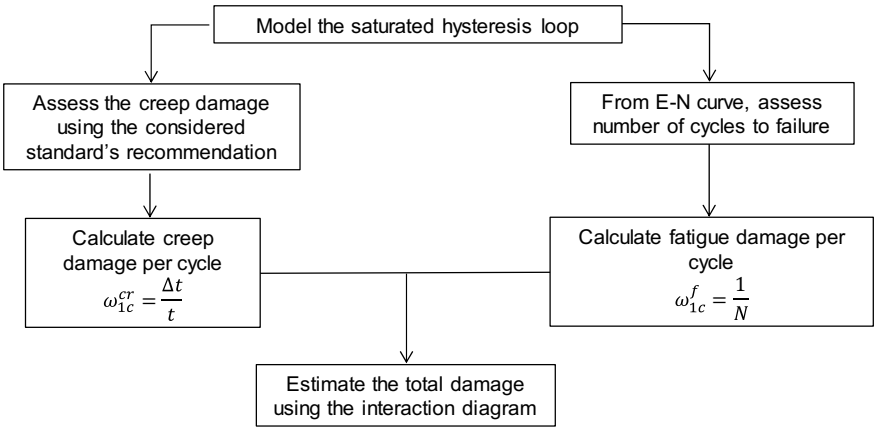

Fig. 15 Flow-chart for the general creep-fatigue evaluation procedure

enhances the creep strain and the subsequent stress relaxation, which further enhances the plastic behaviour during the unloading phase. This results in larger total strain range, indicating a reduction in the fatigue life. It should be noted that this decrease in the fatigue life is in addition to the creep damage accumulated as a result of the creep dwell. The most significant change with respect to the accumulation of creep strain occurs from a dwell time of 10 hours to 100 hours after which it reduces as reflected in Fig. 17b.

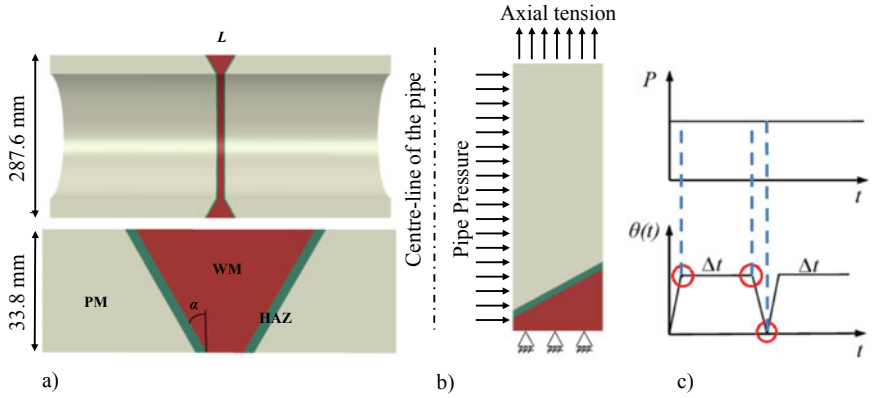

Fig. 16 **a** Butt welded pipe geometry. **b** Boundary condition and load applied; **c** loading condition of the pipe

Figure 17c presents an interaction diagram between the creep strain and the net plastic strain, which is the difference between the plastic strain accumulated during loading and loading. They can be used to understand the drive of the creep-ratcheting phenomena if any. A closed hysteresis loop is obtained when the creep strain is equal to the net plastic strain. The blue line in Fig. 17c represents a closed loop. The area above this line indicates cyclically enhanced creep and the area below indicates creep enhanced plasticity. At lower dwell times, the creep ratcheting mechanism for the welded pipe is driven by creep enhanced plasticity. As the dwell time increases, the creep strain tends to dominate, with a closed loop obtained for dwell time of 100 hours, and slowly shifting towards cyclically enhanced creep mechanism for larger dwell times.

The creep-fatigue life and creep ratcheting life, calculated using the strain ductility approach [13], against dwell time are shown in Fig. 17d. The creep fatigue life decreases with increase in the dwell period, whereas an interesting trend is seen in the case of creep-ratcheting life. For shorter dwell times, creep ratcheting is dominant compared to creep-fatigue damage, which is a result of the creep enhanced plasticity mechanism. As the dwell time increases, a slight increase is observed in the creep-ratcheting life, which is because the creep strain is compensated by the net plastic strain. On further increasing the dwell time, creep ratcheting again dominates, in this case due to cyclically enhanced creep.

6 Conclusions

A complete overview of the high-temperature design and assessment capabilities of the eDSCA within the LMMF is given. The introduction of a software tool

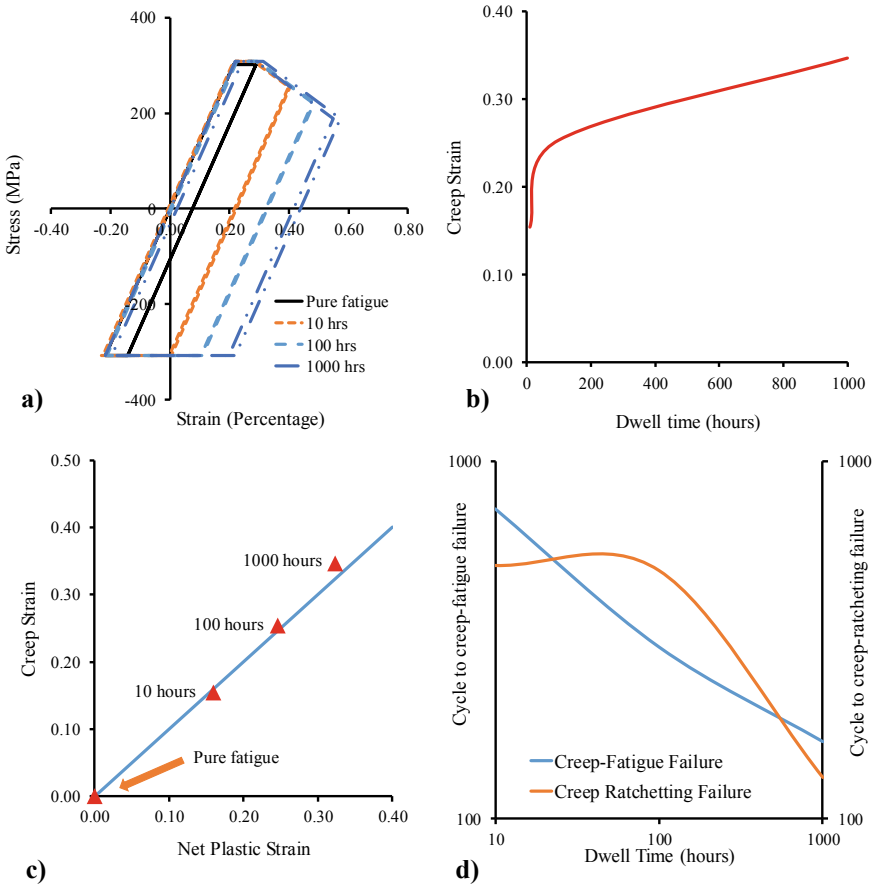

Fig. 17 **a** Stabilized steady state hysteresis loops; **b** creep strain for increasing dwell time; **c** interaction between creep strain and net plastic strain; **d** creep-fatigue life and creep ratcheting life against dwell time

as an Abaqus CAE plug-in with an intuitive GUI makes the LMM easily accessible to a wide range of users, including those who have little theoretical understanding of the LMM and limited programming skills. Four case studies have been presented to showcase the various facets and applications for the LMM. These demonstrate the wide range of complex load interactions that the LMM is capable of assessing. Furthermore, the LMM can also be used in conjunction with other rules based methods in order to assess the component′s life in terms of creep-fatigue and creep-ratcheting failures.

Acknowledgements The authors gratefully acknowledge the supports from the National Natural Science Foundation of China (51828501), University of Strathclyde, Tsinghua University and East China University of Science and Technology during the course of this work.

References

1. Bree, J.: Elastic-plastic behaviour of thin tubes subjected to internal pressure and intermittent high-heat fluxes with application to fast-nuclear-reactor fuel elements. J. Strain Anal. **2**(3), 226–238 (2007)
2. Ure, J.: An advanced lower and upper bound shakedown analysis method to enhance the R5 high temperature assessment procedure. August, 1–170 (2013)
3. Chen, H., Chen, W., Ure, J.: A direct method on the evaluation of cyclic behaviour with creep effect. Lmm, 823 (2013)
4. Barbera, D., Chen, H.F., Liu, Y.H.: On the creep fatigue behavior of metal matrix composites. Procedia Eng. **130**, 1121–1136 (2015)
5. Chen, H., Ponter, A.R.S.: Linear matching method on the evaluation of plastic and creep behaviours for bodies subjected to cyclic thermal and mechanical loading. Int. J. Numer. Methods Eng. **68**(1), 13–32 (2006)
6. Zheng, X.T., Ma, Z.Y., Chen, H.F., Shen, J.: A novel fatigue evaluation approach with direct steady cycle analysis (DSCA) based on the linear matching method (LMM). Key Eng. Mater. **795**, 383–388 (2019)
7. Zheng, X., Chen, H., Ma, Z., Xuan, F.: A novel fatigue assessment approach by direct steady cycle analysis (DSCA) considering the temperature-dependent strain hardening effect. Int. J. Press. Vessel. Pip. **170**, 66–72 (2019)
8. Gorash, Y., Chen, H.: Creep-fatigue life assessment of cruciform weldments using the linear matching method. Int. J. Press. Vessel. Pip. **104**, 1–13 (2013)
9. Gorash, Y., Chen, H.: On creep-fatigue endurance of TIG-dressed weldments using the linear matching method. Eng. Fail. Anal. **34**, 308–323 (2013)
10. Gorash, Y., Chen, H.: A parametric study on creep-fatigue endurance of welded joints. Pamm **13**(1), 73–74 (2013)
11. Barbera, D., Chen, H., Liu, Y.: On creep fatigue interaction of components at elevated temperature. J. Press. Vessel Technol. **138**(4), 041403 (2016)
12. Barbera, D., Chen, H., Liu, Y.: Creep-fatigue behaviour of aluminum alloy-based metal matrix composite. Int. J. Press. Vessel. Pip. **139–140**, 159–172 (2016)
13. Kapoor, A.: A re-evaluation of the life to rupture of ductile metals by cyclic plastic strain. Fatigue Fract. Eng. Mater. Struct. **17**(2), 201–219 (1994)

Limit Analysis of Complex 3D Steel Structures Using Second-Order Cone Programming

Chadi El Boustani, Jeremy Bleyer, and Karam Sab

Abstract The modelling of complex steel structures under static loading using rigid perfectly plastic material is presented within the framework of second-order cone programming (SOCP). The classic upper and lower bound principles of yield analysis, naturally written as optimization problems, are formulated as a pair of dual second-order cone programs which are then solved using a state-of-the art primal-dual interior point method (IPM). The IPM shows good robustness and efficiency along with reduced computational times especially for limit analysis. The whole process is illustrated first with basic steel structures checks of fillet welds or beams under biaxial bending moment, and second with complex 3D steel assemblies. The results show good agreement with the failures modes and resistance values presented in the Eurocode and allows us to obtain a reliable estimate of the ultimate resistance within a reasonable time.

1 Limit Analysis and Yield Design

1.1 Motivation

In various engineering application, one of the main concerns is to find the ultimate supportable load of a structure under a given set of loading parameters and a local material yield criterion.

C. El Boustani (✉) · J. Bleyer · K. Sab
Laboratoire Navier, Ecole des Ponts ParisTech, Univ Gustave Eiffel, CNRS, Marne-la-Vallée, France
e-mail: chadi.el-boustani@enpc.fr

J. Bleyer
e-mail: jeremy.bleyer@enpc.fr

K. Sab
e-mail: karam.sab@enpc.fr

C. El Boustani
Strains, 75012 Paris, France

A. A. Pisano et al. (eds.), *Direct Methods*, Lecture Notes in Applied and Computational Mechanics 95, https://doi.org/10.1007/978-3-030-48834-5_3

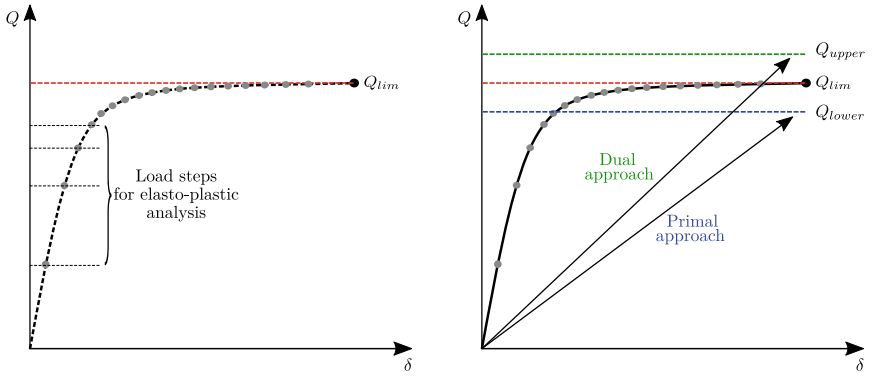

(a) Elastoplastic load-displacement curve (b) Limit load computed using limit analysis

Fig. 1 General idea of limit analysis

Considering an elastoplastic material, determining the ultimate load can be achieved through a series of incremental analyses where the loading parameters are increased until divergence of the solving algorithm as can be seen in Fig. 1a. While this approach is general and applicable in most cases, the process can be incredibly time-consuming and difficult to monitor. Full elastoplastic analyses generally require a certain level of mastery of the mechanical theory involved in modelling non-elastic behaviour and convergence problems are often faced when trying to push the system to its maximum resisting load. This is mainly due to the solving algorithm, commonly the Newton-Raphson method, which requires the computation of a tangent stiffness matrix at each internal iteration: this matrix tends to become singular when plasticity occurs which in consequence causes the algorithm to diverge.

Aiming at computing this limit load in a direct fashion, i.e. without having to run a full elasto-plastic incremental analysis, is the purpose of limit analysis theory (in the case of perfectly plastic materials) [1] or yield design theory [2] in a more general framework. In the following sections, the general approaches of the theory of yield design will be presented. It consists of two main theorems or *approaches*:

1. a primal (static-based) approach which provides a lower bound estimate for the limit load;
2. a dual (kinematic-based) approach which provides an upper bound estimate for the limit load.

This contribution will aim at applying these concepts to the verification of complex 3D steel assemblies which can be encountered in civil engineering.

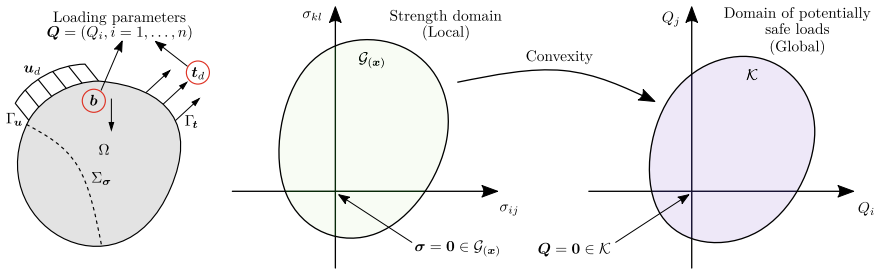

Fig. 2 Reference model and definition of the domain of potentially safe loads

1.2 Static Lower Bound Approach of Yield Design

Let Ω be the total space occupied by the solid and let be Σ_σ an internal surface of potential stress discontinuities (see Fig. 2). The external boundary will be split into three distinct parts such as: $\Gamma = \Gamma_{\mathbf{u}} \cup \Gamma_{\mathbf{t}}$ and $\Gamma_{\mathbf{u}} \cap \Gamma_{\mathbf{t}} = \emptyset$ where:

– displacements $\mathbf{u}$ are imposed to $\mathbf{u}_d$ on $\Gamma_{\mathbf{u}}$;
– surface tractions $\mathbf{t} = \sigma \cdot \mathbf{n}$ are imposed to $\mathbf{t}_d$ on $\Gamma_{\mathbf{t}}$.

Let $\hat{\mathbf{u}}$ be a kinematically admissible (KA) virtual velocity field with the imposed displacements $\mathbf{u}_d$ on $\Gamma_{\mathbf{u}}$ i.e. is piecewise continuous and continuously differentiable and such that $\hat{\mathbf{u}} = \mathbf{u}_d$ on $\Gamma_{\mathbf{u}}$:

$$KA = \left\{ \mathbf{u} \in \mathbb{R}^3 \;\middle|\; \mathbf{u} = \mathbf{u}_d \;\text{ on } \Gamma_{\mathbf{u}} \right\} \tag{1}$$

$\hat{\mathbf{d}} = \nabla^S \hat{\mathbf{u}}$ then denotes the linearized strain rate tensor.

Let σ be a statically admissible (SA) stress field i.e. it satisfies the local equilibrium equations, traction continuity and traction boundary conditions:

$$SA = \left\{ \sigma \in \mathbb{S} \;\middle|\; \begin{array}{ll} \mathrm{Div}(\sigma) + \mathbf{b} = 0 & \text{in } \Omega \\ [\![\sigma.\mathbf{n}]\!] = 0 & \text{through } \Sigma_\sigma \\ \sigma.\mathbf{n} = \mathbf{t}_d & \text{on } \Gamma_{\mathbf{t}} \end{array} \right\} \tag{2}$$

Along with the geometrical and loading data, the third set of data needed for yield design is the constitutive material strength properties. At any point $M(\mathbf{x})$ of Ω, a convex strength domain $\mathcal{G}(\mathbf{x})$ is defined in the 6-dimensional space of the stress tensor $\sigma(\mathbf{x})$. The boundary of the strength domain often noted $f(\sigma_{(\mathbf{x})}) \leq 0$ consists of a level-set function commonly known as the yield function in the context of plasticity or strength criterion in general.

The domain of potentially safe loads $\mathcal{K}$ therefore consists of the set of loads $\mathbf{Q}$ such that there exist a stress field satisfying the equilibrium equations and the material strength conditions [2]:

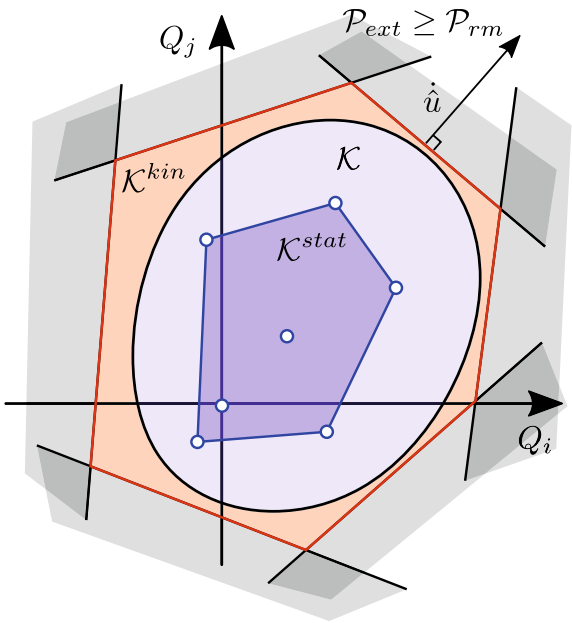

Fig. 3 Schematic representation of the interior and exterior approximation of the domain $\mathscr{K}$

$$\mathbf{Q} \in \mathscr{K} \iff \begin{cases} \exists \sigma_{(\mathbf{x})} \text{ S.A. with } \mathbf{Q} & \text{(Equilibrium condition)} \\ \sigma_{(\mathbf{x})} \in \mathscr{G}_{(\mathbf{x})} \ \forall \mathbf{x} \in \Omega & \text{(Strength condition)} \end{cases} \tag{3}$$

The lower bound approach of yield design consists in approximating $\mathscr{K}$ by determining a stress field verifying the equations given in (3) for a fixed loading direction $\mathbf{Q}_0$. One then looks for the maximum value of a load factor λ such that $\lambda \mathbf{Q}_0 \in \mathscr{K}$. The maximum load factor λ^* and can then be obtained by solving a maximization problem given by:

$$\lambda^* = \max \ \lambda \text{ such that } \exists \sigma_{(\mathbf{x})} \begin{cases} \sigma_{(\mathbf{x})} \text{ S.A. with } \lambda \mathbf{Q}_0 \\ \sigma_{(\mathbf{x})} \in \mathscr{G}_{(\mathbf{x})} \ \forall \mathbf{x} \in \Omega \end{cases} \tag{4}$$

If restricting the above maximization to a subspace of the statically admissible stress fields, e.g. one obtained from a stress-based finite-element discretization, this approach will therefore provide a lower bound $\lambda_{stat} \leq \lambda^*$ to the true limit load factor λ^*. The set of these lower bound approximations for varying loading directions provide an interior approximation $\mathscr{K}_{stat} \subseteq \mathscr{K}$ to the safe load domain $\mathscr{K}$ (see Fig. 3).

1.3 Kinematic Upper Bound Approach of Yield Design

Deriving the dual approach of the theory of yield design starts by writing the the virtual work principle, corresponding to the dualisation of the equilibrium equations given in (2), as follows:

$$\begin{aligned}\mathscr{P}_{int(\hat{\mathbf{u}})} &= \int_{\Omega} \sigma : \hat{\mathbf{d}} d\Omega + \int_{\Sigma} (\sigma.\mathbf{n})[\![\hat{\mathbf{u}}]\!] d\Gamma \\ &= \int_{\Omega} \mathbf{b}\hat{\mathbf{u}} d\Omega + \int_{\Gamma_{\mathbf{u}}} (\sigma.\mathbf{n})\mathbf{u}_d d\Gamma + \int_{\Gamma_{\mathbf{t}}} \mathbf{t}_d \hat{\mathbf{u}} d\Gamma = \mathscr{P}_{ext(\hat{\mathbf{u}})}\end{aligned} \tag{5}$$

Using the properties of convex sets, one can rewrite the convex set $\mathscr{G}$ using support functions:

$$\sigma \in \mathscr{G} \Rightarrow \begin{cases} \sigma : \hat{\mathbf{d}} & \leq \sup\{\sigma : \hat{\mathbf{d}},\ \sigma \in \mathscr{G}\} \quad =: \Pi(\hat{\mathbf{d}}) \\ (\sigma.\mathbf{n})[\![\hat{\mathbf{u}}]\!] & \leq \sup\{(\sigma.\mathbf{n})[\![\hat{\mathbf{u}}]\!],\ \sigma \in \mathscr{G}\} =: \Pi(\mathbf{n}, [\![\hat{\mathbf{u}}]\!]) \end{cases} \tag{6}$$

The work of internal forces $\mathscr{P}_{int(\hat{\mathbf{u}})}$ can then be bounded from above using these support functions as follows:

$$\begin{aligned}\Rightarrow \mathscr{P}_{int(\hat{\mathbf{u}})} &= \int_{\Omega} (\sigma : \hat{\mathbf{d}}) d\Omega + \int_{\Sigma} (\sigma.\mathbf{n})[\![\hat{\mathbf{u}}]\!] d\Sigma \\ &\leq \int_{\Omega} \Pi(\hat{\mathbf{d}}) d\Omega + \int_{\Sigma} \Pi(\mathbf{n}, [\![\hat{\mathbf{u}}]\!]) d\Sigma = \mathscr{P}_{rm(\hat{\mathbf{u}})}\end{aligned} \tag{7}$$

where the last term is corresponds to the maximum resisting work of the structure for a given virtual field $\hat{\mathbf{u}}$.

One can then show that we have:

$$\mathbf{Q} \in \mathscr{K} \Leftrightarrow \forall \hat{\mathbf{u}} \text{ K.A. } \mathscr{P}_{ext(\hat{\mathbf{u}})} \leq \mathscr{P}_{rm(\hat{\mathbf{u}})} \tag{8}$$

Note that for a fixed reference load $\mathbf{Q}_0$, we can therefore characterize the maximum load factor λ associated with $\mathbf{Q}_0$ by:

$$\lambda \leq \lambda^* \Leftrightarrow \forall \hat{\mathbf{u}} \text{ K.A. } \lambda \mathscr{P}_{ext,0(\hat{\mathbf{u}})} \leq \mathscr{P}_{rm(\hat{\mathbf{u}})} \tag{9}$$

i.e.

$$\lambda^* = \min_{\hat{\mathbf{u}} \text{ K.A.}} \frac{\mathscr{P}_{rm(\hat{\mathbf{u}})}}{\mathscr{P}_{ext,0(\hat{\mathbf{u}})}} \tag{10}$$

The equation $\mathscr{P}_{ext(\hat{\mathbf{u}})} \leq \mathscr{P}_{rm(\hat{\mathbf{u}})}$ defines a hyperplane subdividing the space into two half-spaces, one of them containing the strength domain $\mathscr{K}$ and the origin as shown in Fig. 2. Therefore the virtual velocity field approximate the limit load from the exterior.

The upper bound approach of yield design consists in approximating the convex domain $\mathscr{K}$ by minimizing the maximum resisting work for various virtual velocity fields (which can be interpreted as the structure collapse mechanisms). When adding a normalization condition $\mathscr{P}_{ext,0(\hat{\mathbf{u}})} = 1$, the maximum load factor λ^* can be obtained by solving the following minimization problem:

$$\begin{aligned} \lambda_{upper} = \min_{\hat{\mathbf{u}}} \ & \mathscr{P}_{rm(\hat{\mathbf{u}})} \\ \text{s.t. } & \hat{\mathbf{u}} \in \text{K.A.} \\ & \mathscr{P}_{ext,0(\hat{\mathbf{u}})} = 1 \end{aligned} \tag{11}$$

Again, if restricting the above minimization to a subspace of the kinematically admissible fields, e.g. one obtained from a displacement-based finite-element discretization, this approach will therefore provide an upper bound $\lambda_{kin} \geq \lambda^*$ to the true limit load factor λ^*. The set of these upper bound approximations for varying loading directions provide an exterior approximation $\mathscr{K}_{kin} \supseteq \mathscr{K}$ to the safe load domain $\mathscr{K}$ (see Fig. 3).

1.4 The Von-Mises Strength Criterion

In the case of steel structures modelling, the most common strength criterion is the Von-Mises criterion defined as follows:

$$f(\sigma) = \|\text{dev}(\sigma)\| - f_y \leq 0 \tag{12}$$

$$\Pi(\hat{\mathbf{d}}) = \sqrt{\frac{2}{3}} f_y \|\hat{\mathbf{d}}\| \quad \text{if } \text{tr}(\hat{\mathbf{d}}) = 0 \tag{13}$$

$$\Pi(\mathbf{n}, [\![\hat{\mathbf{u}}]\!]) = \sqrt{\frac{1}{3}} f_y \|[\![\hat{\mathbf{u}}]\!]\| \quad \text{if } [\![\hat{\mathbf{u}}]\!].\mathbf{n} = 0 \tag{14}$$

f_y being the tensile yield strength.

2 Upper and Lower Bounds Finite Elements Formulations

Displacement-type elements are used in the finite element discretization of upper bound optimisation program. For the present case, 10-node quadratic tetrahedra will be used [3]. The resulting displacement field will therefore verify kinematic compatibility at every point in Ω and the maximum resisting energy $\mathscr{P}_{rm(\hat{\mathbf{u}})}$ is approximated in Ω and Σ using numerical integration. The minimisation problem (11) can be written in the matrix format as follows:

$$\begin{aligned} \min_{\mathbf{u}} \ & \sum_{i=1}^{N} w_i \Pi_{(\mathbf{d}_i)} + \sum_{j=1}^{M} w'_j \Pi_{(\mathbf{n}, [\![\mathbf{u}_i]\!])} \\ \text{s.t.} \ & \mathbf{Bu} = \mathbf{d} \\ & \mathbf{Au} = \mathbf{u}_d \\ & \mathbf{Cu} = [\![\mathbf{u}]\!] \\ & \mathbf{F}_0^T \mathbf{u} = 1 \end{aligned} \tag{15}$$

where w_i and w'_j are the weights associated to the Gauss integration points, $\mathbf{B} = \nabla^S$ is the classical displacements-to-strains matrix operator, $\mathbf{A}$ and $\mathbf{C}$ are linear constraints matrices used to impose boundary conditions and to express the discontinuity of the displacement field over the potential internal interfaces Σ_σ and $\mathbf{F}_0^T$ is the exterior forces vector or the vector of the loading parameters.

When introducing the Von-Mises criterion in the general kinematic finite-elements problem (15), the trick to efficiently solve this mathematical problem is to cast it into the form of a convex optimisation problem and more specifically a second-order cone program (SOCP) as discussed in Sect. 3. For that, a set of *slack variables* noted γ and ξ are introduced in the objective function (16a) which allows to pass the norms required for Von-Mises criterion as second order cone constraints as seen in Eq. (16c) and (16d). The incompressibility conditions $\mathrm{tr}(\hat{\mathbf{d}}) = 0$ and $[\![\hat{\mathbf{u}}]\!].\mathbf{n} = 0$ are also included using a matrix operator noted $\mathbf{D}$ as seen in Eq. (16b).

$$\min_{\mathbf{u}} \ \sum_{i=1}^{N} w_i \sqrt{\tfrac{2}{3}} f_y \gamma_i + \sum_{j=1}^{M} w'_j \sqrt{\tfrac{1}{3}} f_y \xi_j \tag{16a}$$

$$\text{s.t.} \ \mathbf{Bu} = \mathbf{d}$$

$$\mathbf{Au} = \mathbf{u}_d \qquad \text{on } \Gamma_{\mathbf{u}}$$

$$\mathbf{Cu} = [\![\mathbf{u}]\!]$$

$$\mathbf{F}_0^T \mathbf{u} = 1$$

$$\mathbf{Du} = 0 \qquad \text{(incompressibility condition)} \tag{16b}$$

$$\|\mathbf{d}_i\| \leq \gamma_i \qquad \forall i = 1, \ldots, N \tag{16c}$$

$$\|[\![\mathbf{u}_j]\!]\| \leq \xi_j \qquad \forall j = 1, \ldots, M \tag{16d}$$

Finite element discretization of the lower bound problem (4) can be done using equilibrium tetrahedra. The simplest element can be obtained by considering a linear interpolation of the stress tensor components σ_{ij} over each element [4]. 4-node linear tetrahedra with discontinuous interpolation can be used for which continuity of the stress vector over the element facets should be explicitly written (these faces will be denoted as the set Σ_σ) and included as linear constraints of the corresponding optimization problem. The resulting field will therefore verify equilibrium equations at every point in Ω and verify the strength condition in a certain number of point N_c in Ω. The discretized minimisation problem can then be written as follows:

$$\max_{\lambda,\sigma} \quad \lambda \tag{17a}$$

$$\text{s.t.} \quad \mathbf{H}\boldsymbol{\sigma} = \lambda \mathbf{b} \tag{17b}$$

$$\mathbf{N}\boldsymbol{\sigma} = 0 \qquad \text{on } \Sigma_\sigma \tag{17c}$$

$$\mathbf{N}\boldsymbol{\sigma} = \lambda \mathbf{t}_d \qquad \text{on } \Gamma_\mathbf{t} \tag{17d}$$

$$\boldsymbol{\sigma}_{(\mathbf{x}_c)} \in \mathscr{G}_{(\mathbf{x}_c)} \qquad \forall c = 1, \ldots, N_c \tag{17e}$$

Where $\mathbf{H}$ is the divergence matrix operator and $\mathbf{N}$ is the normal projection matrix operator. The Von-Mises criterion can easily be introduced by replacing Eq. (17e) by the corresponding yield function and by using the deviatoric matrix operator $\mathbf{P}_{dev}$ as follows :

$$\|\mathbf{s}\| = \|\mathbf{P}_{dev}\boldsymbol{\sigma}\| \leq f_y \quad \forall c = 1, \ldots, N_c \tag{18}$$

3 Convex Optimisation and the Interior Point Method

The upper and lower bound limit analysis theorems are naturally written as a set of convex optimisation problems which nowadays can be efficiently solved using state-of-the art optimisation algorithms such as the primal-dual interior point method.

The class of problems related to our case is called second-order cone programs (SOCP) which consists of minimising a linear objective function under specific convex constraints: linear equalities/inequalities and second-order conic constraints:

$$\begin{aligned} \min_{\mathbf{x}} \quad & \mathbf{c}^T\mathbf{x} \\ \text{s.t.} \quad & \mathbf{A}\mathbf{x} = \mathbf{b} \\ & \mathbf{x} \in K \end{aligned} \tag{19}$$

where $\mathbf{A}$ is the linear constraints matrix and K is a Cartesian product of K_i self-dual convex cones such as the Lorentz cone: $K_i = \{\mathbf{x} = (x_0, \bar{\mathbf{x}}) \in \mathbb{R} \times \mathbb{R}^{n-1} | \|\bar{\mathbf{x}}\| \leq x_0\}$.

The interior point method (IPM) has been shown to be well suited for solving these specific types of convex programming problems with guaranteed convergence

in a polynomial time complexity. This method provides a way to solving non-smooth mechanical problems such as the ones encountered in limit analysis whereas classical Newton-Raphson procedures fail to provide an acceptable solution.

The idea of an IPM is to find a solution to the Karush-Kuhn-Tucker (KKT) conditions of problem (19) by following the neighbourhood of a curve called the *central path* given by $(\mathbf{x}(\eta), \boldsymbol{\lambda}(\eta))$ and parametrized by a *barrier parameter* $\eta \geq 0$. This central path is no other than the unique solution to the following perturbation of the KKT system [5]:

Find $(\mathbf{x}(\eta), \boldsymbol{\lambda}(\eta))$ such that:

$$\begin{aligned} \mathbf{c} + \mathbf{A}^T \boldsymbol{\lambda} &= 0 \\ \mathbf{A}\mathbf{x} - \mathbf{b} &= 0 \\ \mathbf{x}_i \circ \mathbf{s}_i &= \eta \mathbf{e}_i \\ \mathbf{x}_i \in K_i \quad \mathbf{s}_i &\in K_i^* \end{aligned} \tag{20}$$

where K_i^* the dual cone of K_i. In the case of Lorentz cones, $K^* = K$ and $\mathbf{x} \circ \mathbf{s} = (x_0, \bar{\mathbf{x}}) \circ (s_0, \bar{\mathbf{s}}) = (x_0 s_0 + \bar{\mathbf{x}}^T \bar{\mathbf{s}}, x_0 \bar{\mathbf{s}} + s_0 \bar{\mathbf{x}})$ and $\mathbf{e} = (1, \mathbf{0})$.

The main property of the central path is that it defines a continuous set of strictly feasible points which are well-centred, i.e. far from the boundary of the feasible region except when reaching the optimum for $\eta \to 0$. This will allow for large descent steps to be taken when minimizing the objective function from points the neighbourhood of the central path.

The only non-linearity found in the equation set (20) is the complementarity condition which depends on the type of the conic constraint. From the perturbed KKT conditions (20), different strategies can be chosen to compute the solutions. More details on the different steps of the IPM method implemented in this work can be found in [5–7].

4 Engineering Applications

In our considered application, steel structures often present surfaces in contact with each other (plate, blots, etc.). Contact conditions should therefore be imposed on these surfaces. In order to keep the framework of convex optimization, we will assume an associated frictional contact law. Contact conditions can therefore be written in terms of the normal and tangential tractions $(\sigma_N, \boldsymbol{\sigma}_T)$ and normal and tangential displacement gap $(g_N, \mathbf{g}_T)$ of the considered surface as follows:

$$\begin{cases} \textbf{if } \|\boldsymbol{\sigma}_T\| = -\mu\sigma_N \textbf{ then } \mathbf{g} = \mathbf{0} & \text{(21a)} \\ \textbf{if } \|\boldsymbol{\sigma}_T\| = -\mu\sigma_N \textbf{ then } \mathbf{g}_T = \lambda \dfrac{\boldsymbol{\sigma}_T}{\boldsymbol{\sigma}_T} \textbf{ with } \lambda = \dfrac{g_N}{\mu} & \text{(21b)} \end{cases}$$

which ensures that the normal components of the gap vector and surface traction are complementary i.e. $\sigma_N \leq 0$, $g_N \geq 0$ in the case of frictionless contact but also couples the normal and tangential gaps using a friction coefficient μ. The previous conditions can be reformulated using a pair of convex second-order cones which can easily be included within the SOCP framework. The details of this formulation can be found in [8].

4.1 Basic Steel Checks According to the Eurocodes

A typical steel design check according to the Eurocodes (EC) [9, 10] relies on a series of basic components checks which are then assembled to derive an estimate of the ultimate resistance of the structure or the joint. In order to show the validity of the yield design SOCP framework, elementary examples such as basic weld checks are presented in the following paragraphs along with a biaxial bending interaction diagram.

4.1.1 Some Fillet Weld Checks

According to EC3-1-8 paragraph 4.5.3 [10], the ultimate resistance of fillet welds can be determined using the *directional method* which makes some allowance for the dependence of the weld strength on the direction of loading by assuming that the normal stress parallel to the axis of the weld throat does not influence the design resistance given by Eq. (4.1) of the EC3-1-8 [10]:

$$\sqrt{\sigma_\perp^2 + 3(\tau_\perp^2 + \tau_\parallel^2)} \leq \frac{f_u}{\beta_w \gamma_{M2}} \quad \text{and} \quad \sigma_\perp \leq \frac{0.9 f_u}{\gamma_{M2}} \tag{22}$$

Using these two inequalities, the ultimate resistance of basic fillet welds can be determined. In the following examples, a fillet weld of throat thickness $a \geq 3\,\text{mm}$, of total length L and of effective length $L_{eff} = L - 2a \geq L_{\min} = \max(30\,\text{mm}, 6a)$ is presented in 3 different configurations:

- a frontal configuration as seen in Fig. 4;
- a lateral configuration as seen in Fig. 5;
- an inclined configuration parametrized with an angle α as seen in Fig. 6.

The assembled pieces are supposed to have the same steel grade where f_u(MPa) is used to denote the ultimate tensile strength. The ultimate resistance $N_{Rd} = \min(N_{Rd,1}; N_{Rd,2})$ can be calculated from the resistance $N_{Rd,i}$ obtained from the two conditions of (22). Results are summarized for the three configurations in Table 1.

Considering $L = 100\,\text{mm}, a = 10\,\text{mm}, \alpha = 45°$ and a steel grade S355N/NL such as $f_u = 490\,\text{MPa}$, $\beta_w = 0.9$ and $\gamma_{M2} = 1.25$, the ultimate strengths of the different configurations are calculated using the EC equations and using the finite-element

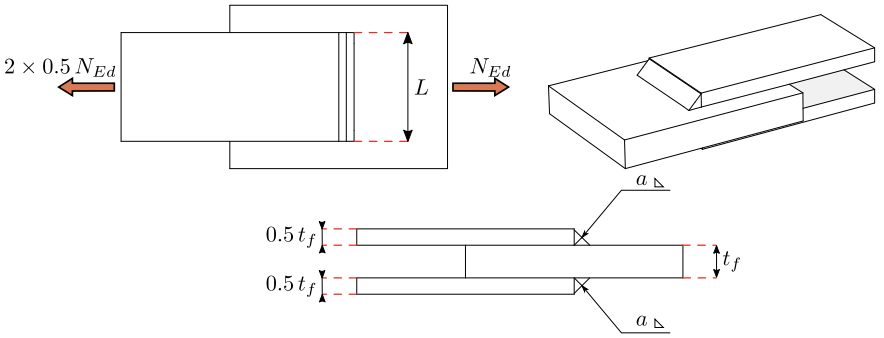

Fig. 4 Frontal fillet weld configuration

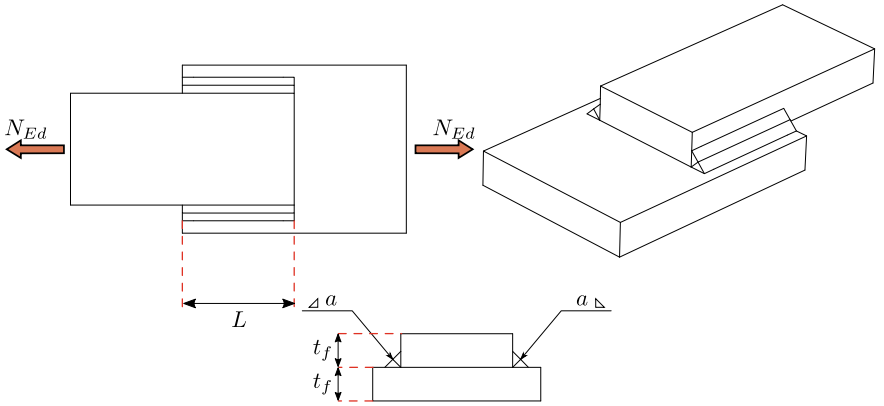

Fig. 5 Lateral fillet weld configuration

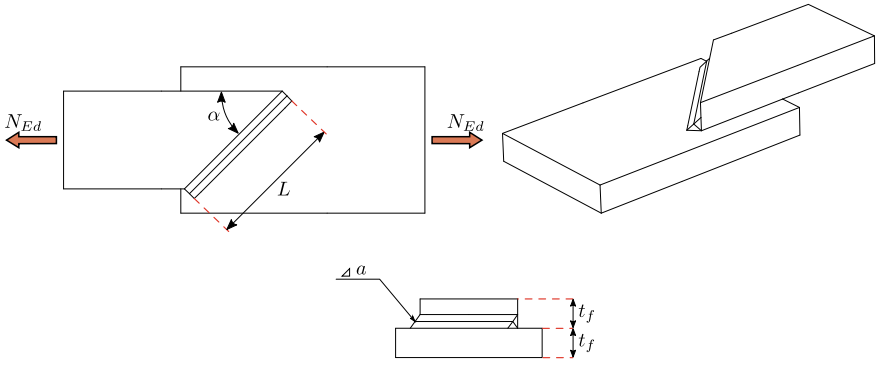

Fig. 6 Inclined fillet weld configuration

Table 1 Ultimate resistance calculated using Eq. (4.1) of EC3-1-8

Configuration	$\sigma_\perp = \tau_\perp$	$\tau_\parallel$	1st criterion $N_{Ed} \leq N_{Rd,1}$	2nd criterion $N_{Ed} \leq N_{Rd,2}$
Frontal configuration	$\frac{N_{Ed}}{2aL_{eff}} \frac{\sqrt{2}}{2}$	0	$\frac{0.9 f_u}{\gamma_{M2}} 2\sqrt{2} aL_{eff}$	$\frac{f_u}{\beta_w \gamma_{M2}} \sqrt{2} aL_{eff}$
Lateral configuration	0	$\frac{N_{Ed}}{2aL_{eff}}$	Verified	$\frac{f_u}{\beta_w \gamma_{M2}} \frac{2aL_{eff}}{\sqrt{3}}$
Inclined configuration	$\frac{N_{Ed}}{aL_{eff}} \sin(\alpha) \frac{\sqrt{2}}{2}$	$\frac{N_{Ed}}{aL_{eff}} \cos(\alpha)$	$\frac{0.9 f_u}{\gamma_{M2}} \frac{\sqrt{2} aL_{eff}}{\sin(\alpha)}$	$\frac{f_u}{\beta_w \gamma_{M2}} \frac{aL_{eff}}{\sqrt{3 - \sin^2 \alpha}}$

Table 2 Ultimate resistance calculated using Eq. (4.1) of EC3-1-8 and the dual SOCP method

Configuration	$N_{Rd,EC}$ (kN)	$N_{Rd,upper}$ (kN)	$N_{Rd,lower}$ (kN)
Frontal configuration	492.7	568.2	531.3
Lateral configuration	402.4	401.3	388.3
Inclined configuration	334.5	385.8	358.1

SOCP limit analysis method using both lower and upper bound approaches. Results are summarized in Table 2. The gap between the upper and lower bound can be reduced when using a finer mesh, although it is already less than 5%. The difference with the EC3-1-8 value is mainly due to the hypothesis taken to apply Eq. (4.1) where the normal stress parallel to the axis of the weld does not influence the design resistance of the weld whereas in finite-element limit analysis computations, a full 3D yield criterion is considered. However, despite these intrinsic differences, the results differ by 7% at most for all cases when comparing the EC prediction with the safe lower bound approximation.

4.1.2 Biaxial Bending of a Beam

The ultimate state check of a steel class 1 or 2 section under biaxial bending action, excluding buckling instability, can be verified using two methods according to the EC3-1-1 [9]:

- A conservative plastic check using Eq. (6.2) [9]:

$$\frac{N_{Ed}}{N_{Rd}} + \frac{M_{y,Ed}}{M_{y,Rd}} + \frac{M_{z,Ed}}{M_{z,Rd}} \leq 1.0 \tag{23}$$

Table 3 HEB300 section characteristics

Section	$A_s = 14900\,\text{mm}^2$
Plastic section modulus along the y axis	$W_{pl,y} = 1{,}869{,}000\ \text{mm}^3$
Plastic section modulus along the z axis	$W_{pl,z} = 870{,}100\ \text{mm}^3$
Equation (6.41) coefficient	$\alpha = 2$
Equation (6.41) coefficient	$\beta = 1$

- A more refined plastic check using Eq. (6.41) [9]:

$$\left[\frac{M_{y,Ed}}{M_{N,y,Rd}}\right]^{\alpha} + \left[\frac{M_{N,z,Ed}}{M_{z,Rd}}\right]^{\beta} \leq 1.0 \tag{24}$$

The equations are most probably obtained via a stress-based formulation, where a plastic or elastic normal stresses distribution is integrated to obtain the interaction diagram. While the first equation is easy to understand as it is just a linear summation of the utilization ratios, the second equation for the non-linear interaction cases are more subtle as they include the coefficients α and β which depends on the section and the normal effort. The different steps to calculate these equations can be found in detail in paragraph 6.2 of the EC3-1-1.

This example is limited to the evaluation of the interaction diagram of HEB300 of steel grade 355N/NL under biaxial bending with no normal force. For this section, the mechanical characteristics are summarised in Table 3.

Using the different equations of the Eurocode, the interaction diagram for this section is determined and is shown in Fig. 7. The normalisation in Eqs. (23) and (24) is done by calculating $M_{y,Rd}$ and $M_{z,Rd}$ using Eq. (6.13) of the EC3-1-1. The interaction diagram is obtained from the numerical results by integration the stress diagram for the lower bound approach as the one seen Fig. 8, and by retrieving the correct Lagrange multipliers corresponding to the reaction moments in the case of the upper bound approach. Eq. (23) is clearly conservative as the full plastic capacity of the section is not mobilised while as Eq. (24) allows a more economical design which coincides well enough with the upper and lower bound approach where a full 3D resistance criterion is used.

4.2 A Quick Summary for More Complex Assemblies

A typical steel-assembly check according to EC3 relies on the components method, where different basic components are determined and different failure mechanisms are verified. In the case of complex steel assemblies, determining the ultimate resistance and the ruin mechanism can be a very hard and a time-consuming process. The proposed upper and lower bound approaches can therefore be used to limit the engi-

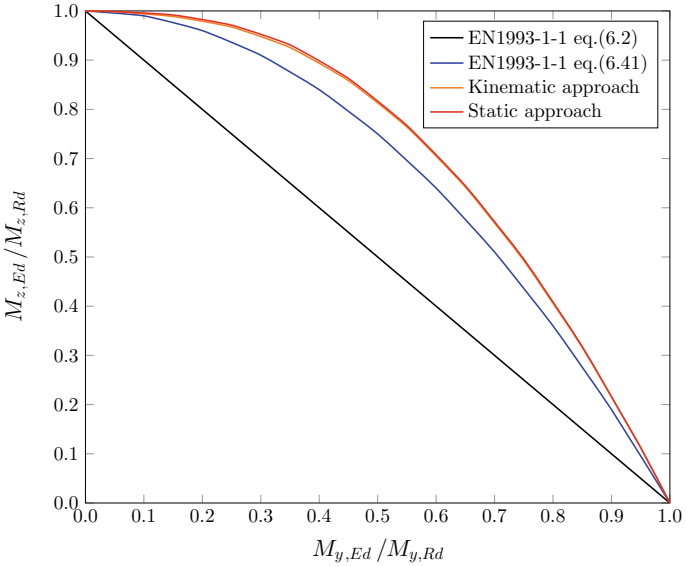

Fig. 7 Interaction diagram under biaxial bending action

neer computational effort and provides a valuable insight to designing more efficient 3D assemblies. It can also be used as design method in cases where the Eurocode recommendations cannot be applied.

In this paragraph, we introduce a quick summary of some of the engineering applications that were made using the software *DS-Steel* developed by *Strains* in collaboration with *Laboratoire Navier*. These assemblies are part of a large set of checks that were made for an structural engineering firm. The geometry details and load cases are omitted in order to simplify the presentation.

Two complex assemblies are briefly presented:

- a 3D bracing assembly as shown in Fig. 9a in which the applied loads are mainly tension or compression efforts in the converging bracing members obtained from a global 3D model of the whole structure;
- a moment transmitting assembly as shown in Fig. 9b in which the applied load is a combination of an uniaxial bending moment, along with a normal and a shear effort.

In these two studies, the friction coefficient was considered equal to 0, therefore only unilateral contact constraints were imposed.

Using the upper bound approach, one can determine the most probable failure mechanism. In the case of the first assembly, failure occurs in one of the bracing members where the web plate fails in bearing due to a critical bearing pressure as shown in Fig. 10a. One can also see in Fig. 10b that the elastic limit, in this case $f_y = 355$ MPa is reached in the same diagonal member. The upper bound provides

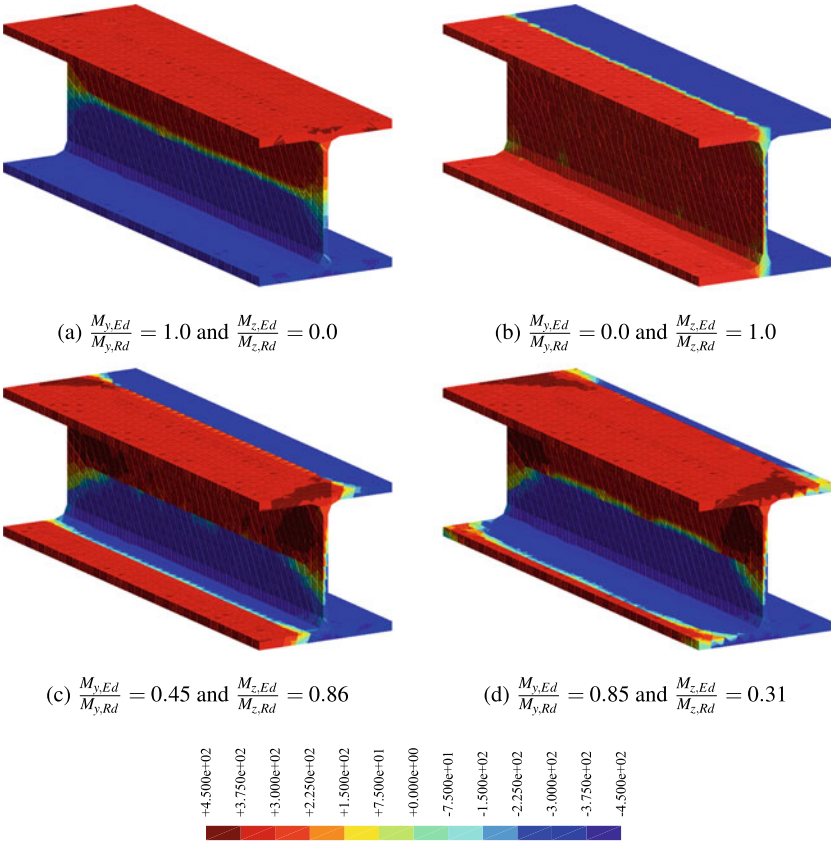

(a) $\frac{M_{y,Ed}}{M_{y,Rd}} = 1.0$ and $\frac{M_{z,Ed}}{M_{z,Rd}} = 0.0$

(b) $\frac{M_{y,Ed}}{M_{y,Rd}} = 0.0$ and $\frac{M_{z,Ed}}{M_{z,Rd}} = 1.0$

(c) $\frac{M_{y,Ed}}{M_{y,Rd}} = 0.45$ and $\frac{M_{z,Ed}}{M_{z,Rd}} = 0.86$

(d) $\frac{M_{y,Ed}}{M_{y,Rd}} = 0.85$ and $\frac{M_{z,Ed}}{M_{z,Rd}} = 0.31$

Fig. 8 Normal stresses isovalues for different loading states

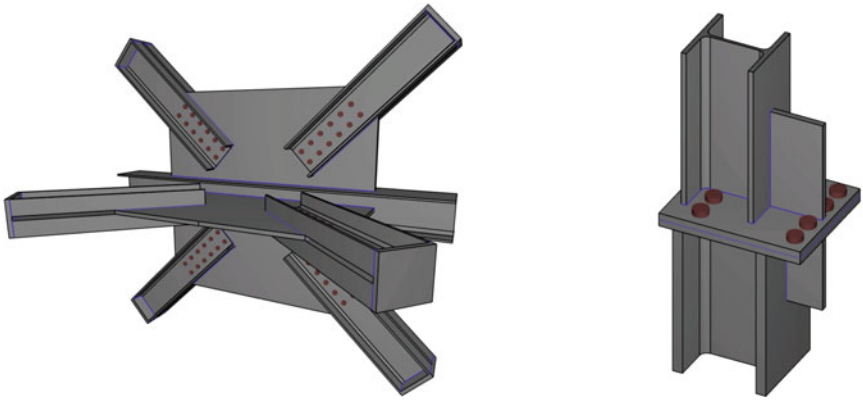

(a) A wind bracing assembly

(b) A continuity assembly

Fig. 9 Complex 3D assemblies

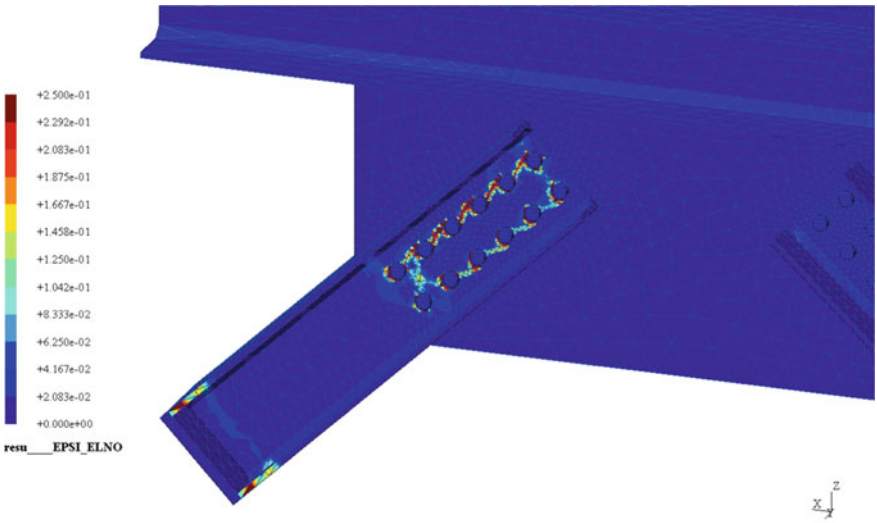

(a) Equivalent Von-Mises plastic strain isovalues in the critical diagonal

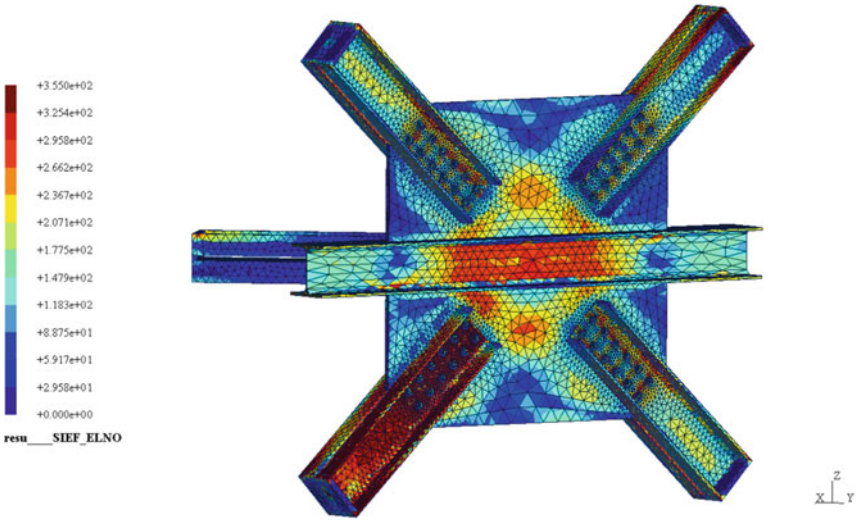

(b) Equivalent Von-Mises plastic stress isovalues

Fig. 10 Equivalent Von-Mises plastic strain and stress isovalues for the wind bracing

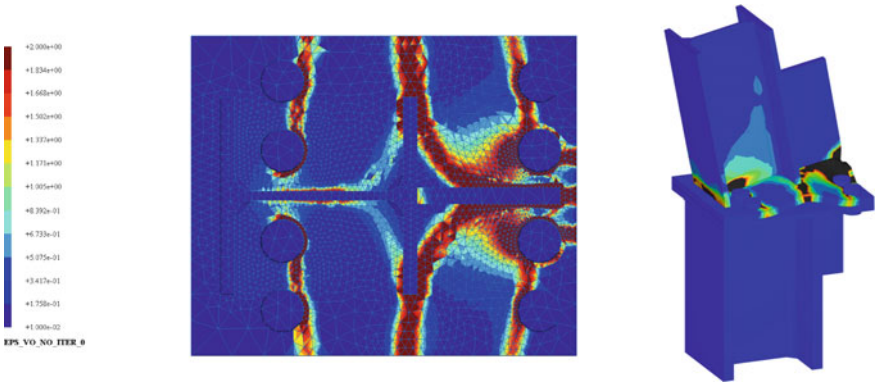

(a) Equivalent Von-Mises plastic strain isovalues (b) Failure mechanism

Fig. 11 Kinematic results for the continuity assembly

a load factor of 2.2 for the corresponding load case while the lower bound approach yields a load factor of 1.9. The gap between the two results can be reduced by reducing the mesh size in the failure area. For the second assembly, failure occurs within the end-plate where clear yield lines can be seen when mapping the plastic strains isovalues as shown in Fig. 11.

The mesh used for each of the two examples consisted of 200,000 quadratic tetrahedrons for the upper bound problem and 800,000 linear tetrahedrons for the lower bound problem, yielding into roughly 5.5 million degrees of freedom for each study. The interior point method shows a very efficient behaviour with a number of iteration remaining stable compared to smaller problems (22–24 iterations) and a CPU time of almost 315 s per iteration an OpenMP parallelisation over 8 cores.

5 Conclusion

This contribution showed that computational techniques for limit analysis/yield design problems have now reached an important level of maturity to tackle complex 3D cases. The performance of these techniques mainly rely on the efficiency of interior point solvers for conic optimization, a framework in which many limit analysis problems can be formulated. In particular for the case of von Mises plasticity and associated frictional model for contact interfaces, the resulting problems fall into the class of Second-Order Cone Programming problems. Besides, lower and upper bound approaches can be respectively computed using equilibrium-based and displacement-based finite elements. Finally, such tools can now be used for industrial applications for instance in the context of the verification of 3D steel assemblies in complex situations which are not described in the corresponding design norms.

References

1. Hill, R.: The Mathematical Theory of Plasticity. Clarendon Press, Oxford (1950)
2. Salençon, J.: Yield Design. Mechanical Engineering and Solid Mechanics Series. ISTE, Wiley, London: Hoboken, NJ (2013). OCLC: ocn847876995
3. Makrodimopoulos, A., Martin, C.M.: Upper bound limit analysis using simplex strain elements and second-order cone programming. Int. J. Numer. Anal. Methods Geomech. **31**(6), 835–865 (2007)
4. Lyamin, A.V., Sloan, S.W.: Lower bound limit analysis using non-linear programming. Int. J. Numer. Methods Eng. **55**(5), 573–611 (2002)
5. Andersen, E.D., Roos, C., Terlaky, T.: On implementing a primal-dual interior-point method for conic quadratic optimization. Math. Program. **95**(2), 249–277 (2003)
6. Alizadeh, F., Goldfarb, D.: Second-order cone programming. Math. Program. **95**(1), 3–51 (2003)
7. Nesterov, Y.E., Todd, M.J.: Primal-dual interior-point methods for self-scaled cones. SIAM J. Optim. **8**(2), 324–364 (1998)
8. El Boustani, C., Bleyer, J., Arquier, M., Ferradi, M.K., Sab, J.: Dual finite-element analysis using second-order cone programming for structures including contact. Eng. Struct. (2019)
9. NF EN 1993-1-1: 2005: Eurocode 3: Design of Steel Structures, Part 1.1: General Rules and Rules for Buildings. AFNOR (2005)
10. NF EN 1993-1-8: 2005: Eurocode 3: Design of Steel Structures, Part 1.8: Design of Joints. AFNOR (2005)

Limit Fire Analysis of 3D Framed Structures Based on Time-Dependent Yield Surfaces

Domenico Magisano, Francesco Liguori, Leonardo Leonetti, and Giovanni Garcea

Abstract The starting point of this work is the definition of an automatic procedure for evaluating the axial force-biaxial bending yield surface of steel and reinforced concrete sections in fire. It provides an accurate time-dependent expression of the yield condition by a section analysis carried out once and for all, accounting for the strength reduction of the materials, which is a function of the fire duration. The equilibrium state of 3D frames with such yield conditions, once discretized using beam finite elements, is then formulated as a nonlinear vectorial equation defining a curve in the hyperspace of the discrete variables and the fire duration. An incremental-iterative strategy is proposed for tracing this curve evaluating a sequence of safe states at increasing fire durations up to the limit fire duration, that is the time of exposure which leads to structural collapse. The procedure represents a global fire analysis able to take account of the stress redistribution over the frame. Numerical examples are given to illustrate the proposal.

1 Introduction

The evaluation of the carrying capacity of a structure has always been a major concern to any design engineer. This regards not only situations of normal service conditions but also exceptional loadings. For 3D frames, an important aspect is to ensure the overall structural integrity during fire events. Usually, frame structures exhibit a rel-

D. Magisano · F. Liguori · L. Leonetti · G. Garcea (✉)
Universitá della Calabria, DIMES, Rende, Italy
e-mail: giovanni.garcea@unical.it

D. Magisano
e-mail: domenico.magisano@unical.it

F. Liguori
e-mail: francesco.liguori@unical.it

L. Leonetti
e-mail: leonardo.leonetti@unical.it

A. A. Pisano et al. (eds.), *Direct Methods*, Lecture Notes in Applied and Computational Mechanics 95, https://doi.org/10.1007/978-3-030-48834-5_4

evant overstrength, that is their ultimate capacity can be significantly higher than the elastic limit, especially in the multi-story multi-span ones. For this reason, the material nonlinear analysis is a necessary tool for designing new buildings as well as for assessing existing structures. A widely employed approach formulates the cross-section yield criterion in terms of generalized stresses, usually axial force and bending moments [1, 2]. A small number of proposals are available to obtain the strength domains of heated sections corresponding to an assigned fire duration or temperature distribution [3–6]. For well-confined reinforced concrete (RC) sections and steel sections, as proposed in many building standards, the strain limit is sufficiently large to allow an approach based on the classical plasticity theory [1, 7, 8]. It consists in evaluating a point cloud of generalized yield stresses by assigning the corresponding collapse mechanisms, that is the position and orientation of the neutral axis at the collapse states. Then, the yield points have to be interpolated in order to handle the yield criteria in structural analysis codes [9, 10]. The Minkowski sum [11] of ellipsoids represents an interesting strategy for the approximation of particular convex shapes known as zonoids, such as the cross-section yield surface, as shown in some recent works [1, 8]. In this work, we use a new approach for constructing the Minkowski sum. It consists in giving a mechanical interpretation to each term of the sum, which corresponds to the contribute of a portion of the cross section to the overall yield surface. As such, after subdividing the cross-section in multiple sub-domains, we approximate the yield surface of each sub-domain as a single ellipsoid. Their Minkowski sum represents the yield surface of the whole cross-section. This strategy is simple, efficient and leads to a good approximation of the yield surface with a low number of ellipsoids [12]. However, the most attractive feature of this particular Minkowski sum is the possibility to account for the strength decrease due to fire exposure. The approach, in fact, allows us to obtain the yield surface at an assigned fire duration, by simply contracting the ambient temperature ellipsoid of each cross-section region accounting for its strength reduction. This makes it possible to define in a closed form the time-dependent yield condition of the cross-section without the need to reconstruct it for different fire durations.

Starting from this cross-section model, we propose an optimization algorithm for assessing the global safety of 3D RC frames in conditions of fire. It consists in a particular strain-driven incremental strategy which evaluates a sequence of safe states for an increasing fire duration. The time-dependent yield surface, together with a finite element beam model allows us to formulate the equilibrium condition of the structure as a nonlinear system of equations defining a curve in the hyperspace of the discrete variables and the fire duration. The evaluation of this curve provides a time history of the fire event taking account of the stress redistribution and, if it exists, the fire duration limit, that is the time of exposure which leads to structural collapse. This analysis can be framed as an optimization strategy which is similar to that used in the static limit analysis [13]. The main difference is that the loads are kept constant and the fire duration, leading to a contraction of the yield surfaces, replaces the load factor as objective function. At each time step of the analysis the nonlinear internal forces are obtained by an elastic predictor-return mapping process based on the closest point projection (CPP) scheme on the yield surfaces at the current fire

duration. The properties of the Minkowski sum can be exploited to define an efficient stress update strategy based on the parametrization of yield surface in terms of its normal vector, representing the cross-section collapse mechanism [12].

2 Mechanics of Cross Sections in Fire

In this section, the mechanical model for RC and steel sections in fire is described. In particular, we define the section yield surface in terms of axial force and bending moments corresponding to an assigned fire duration, taking account of the temperature distribution within the section which reduces the strength of the materials.

2.1 Temperature Distribution

For a generic solid body with thermal boundary conditions, the heat transfer equations can be solved using the finite element method [5]. For the particular simple case of fire exposed rectangular concrete sections, Wickstrom [14] proposed and validated a set of handy formulas to calculate the 2D temperature distribution. Wickstrom's formulas can be applied for any type of concrete or fire scenario. However, they are particularly easy for ISO 834 standard fire and normal weight concrete. The application of Wickstrom's formulas for evaluating the temperature distribution within this section can be summarized as follows:

- The fire temperature (T_f) in Celsius is firstly calculated at a specific fire duration t expressed in hours using an assumed fire temperature-time relationship.
- An equivalent ISO 834 fire duration $t^* = \Gamma t$ is then calculated, that is the corresponding time of exposure to the standard ISO 834 fire to have a temperature of T_f, where Γ is the dimensionless compartment time factor. The ISO 834 standard fire can be described by temperature-fire duration law

$$T_f = 345 \log_{10}(480t^* + 1) \tag{1}$$

- Choosing a reference system with origin at the centroid, the temperature rise at any point (x_2, x_3), with x_2 and x_3 expressed in meters, within the section due to heating can then be estimated as

$$T[x_2, x_3, t] = (n_w(n_x + n_y - 2n_x n_y) + n_x n_y)T_f \tag{2}$$

  where the dimensionless coefficients n_w, n_x, n_y are evaluated by superimposing the effects of the heated sides

$$n_w = 1 - 0.0616(\sqrt{\Gamma}t)^{-0.88} \geq 0$$
$$n_x = \left[0.18 \log \frac{t}{(0.5b + x_2)^2} - 0.81\right]_{\text{left}} + \left[0.18 \log \frac{t}{(0.5b - x_2)^2} - 0.81\right]_{\text{right}} \geq 0$$
$$n_y = \left[0.18 \log \frac{t}{(0.5h + x_3)^2} - 0.81\right]_{\text{bottom}} + \left[0.18 \log \frac{t}{(0.5h - x_3)^2} - 0.81\right]_{\text{top}} \geq 0$$

with b and h in meters being the section width and height respectively.

For steel members, the small thickness of the walls allows us to assume for simplicity a uniform average temperature distribution over the cross-section. The average temperature of the member versus fire duration law depends, apart from the fire temperature T_f given by Eq. (1), on the section factor (a measure of the ratio of the heated perimeter to the area), the presence of protections and the insulation materials. It can be predicted using the Eurocode Method summarized in [15].

2.2 Strength Reduction for Concrete and Steel

The concrete compressive strength experiences significant degradation at elevated temperatures. The reduced compressive strength for concretes f_{cT} can be estimated from its ambient value f_c [16] as

$$f_{cT} = k_c[T] f_c \tag{3}$$

where the dimensionless reduction factor is

$$k_c[T] = 1.76 \cdot 10^{-9} T^3 - 3 \cdot 10^{-6} T^2 + 2.5 \cdot 10^{-4} T + 1$$

with T in Celsius. The concrete tensile strength, as usual, is assumed to be negligible. Lie et al.'s model [17] is used to predict the reduced yield strength of reinforcing bars f_{yT} from its ambient value f_y as $f_{yT} = k_r[T] f_y$, where the dimensionless reduction factor is

$$k_r[T] = \begin{cases} 1 + \dfrac{T}{900} \log\left(\dfrac{T}{1750}\right) & 0 < T \leq 600\,^{\circ}\text{C} \\ \dfrac{340 - 0.34T}{T - 240} & 600\,^{\circ}\text{C} < T \leq 1000\,^{\circ}\text{C} \\ 0 & T > 1000\,^{\circ}\text{C} \end{cases} \tag{4}$$

with T in Celsius. The reduction factors k_c and k_r in Eqs. (3) and (4) are functions of the temperature, which depends on the fire duration and on the point (x_2, x_3) within the section, that is we have $k_c[x_2, x_3, t]$ and $k_r[x_2, x_3, t]$. On the contrary, for steel members, the assumption of uniform temperature distribution leads to a uniform strength reduction $f_{yT} = k_s[T] f_y$ with, according to Eurocode 3,

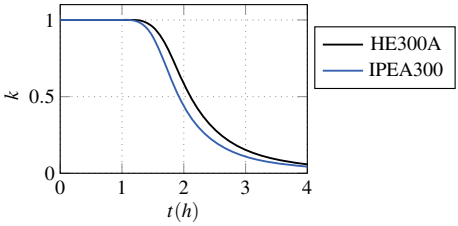

Fig. 1 Strength reduction factor of some steel sections versus fire duration

$$k_s[T] = \left(0.9674\left(1 + e^{\frac{T-482}{39.19}}\right)\right)^{-\frac{1}{3.833}}. \tag{5}$$

Introducing the temperature versus time law, a typical behavior for protected HE300A columns exposed on all four sides and protected IPEA300 beams carrying a concrete floor slab and then exposed on three sides is reported in Fig. 1.

2.3 Section Kinematics and Statics

Let us consider a cylinder occupying a reference configuration $\mathscr{B}$ of length ℓ confined by the lateral boundary denoted by $\partial\mathscr{B}$ and two terminal bases Ω_0 and Ω_ℓ. The cylinder is referred to a Cartesian frame $(\mathscr{O}, x_1 \equiv s, x_2, x_3)$ with unit vectors $\{\mathbf{e}_1, \mathbf{e}_2, \mathbf{e}_3\}$ and $\mathbf{e}_1$ aligned with the cylinder axis. In this system, we denote with $\mathbf{X} = s\mathbf{e}_1 + \mathbf{x}$ the position of a point P, where s is an abscissa which identifies the generic cross-section Ω_s of the beam, while $\mathbf{x} = x_2\mathbf{e}_2 + x_3\mathbf{e}_3$ is the position of P inside Ω_s.

The displacement field $\mathbf{u}[\mathbf{X}]$ of the model is expressed, as usual, as a rigid motion of the section

$$\mathbf{u}[\mathbf{X}] = \mathbf{u}_0[s] + \boldsymbol{\varphi}[s] \times \mathbf{x} \tag{6}$$

where $\mathbf{u}_0[s]$ and $\boldsymbol{\varphi}[s]$ are the mean translation and rotation of the section and the operator $\times$ denotes the cross product. The kinematics assumed in Eq. (6) allows us to evaluate, using a linear Cauchy continuum, the stress-strain work $\mathscr{W}$ in terms of the generalized strains and stresses on the section as

$$\mathscr{W} := \int_\ell (\mathbf{N}[s]^T \boldsymbol{\varepsilon}[s] + \mathbf{M}[s]^T \boldsymbol{\chi}[s]) ds \tag{7}$$

where the generalized strains $\boldsymbol{\varepsilon}[s] = [\epsilon, \gamma_2, \gamma_3]^T$ and $\boldsymbol{\chi}[s] = [\chi_1, \chi_2, \chi_3]^T$ are defined as

$$\boldsymbol{\varepsilon}[s] = \mathbf{u}_{0,s}[s] + \mathbf{e}_1 \times \boldsymbol{\varphi}[s], \quad \boldsymbol{\chi} = \boldsymbol{\varphi}[s]_{,s}, \tag{8}$$

a comma stands for derivative and $\mathbf{N}[s] = [N, V_2, V_3]^T$ and $\mathbf{M}[s] = [M_1, M_2, M_3]^T$ are the resultant force and moment. Finally, the elastic constitutive law [18] is

expressed as

$$\begin{bmatrix} \boldsymbol{\varepsilon} \\ \boldsymbol{\chi} \end{bmatrix} = \mathbf{F} \begin{bmatrix} \mathbf{N} \\ \mathbf{M} \end{bmatrix} \quad , \quad \mathbf{F} = \begin{bmatrix} \mathbf{F}_{NN} & \mathbf{F}_{NM} \\ \mathbf{F}_{NM}^T & \mathbf{F}_{MM} \end{bmatrix}. \tag{9}$$

2.4 The Cross-Section Yield Surface

As usual in practical applications involving slender beams, we assume an elastic behavior of shear and torsion. The material is assumed to be elastic-perfectly plastic with the plastic admissibility condition expressed in terms of normal stress σ_{11} only as $-f_{iT}^- \leq \sigma_{11} \leq f_{iT}^+$ where f_{iT}^+ and f_{iT}^- are the strengths of the ith material for a given temperature T in tension and compression respectively. For concrete $f_{iT}^- = f_{cT}$ and $f_{iT}^- = 0$ while for rebars and structural steel $f_{iT}^- = f_{iT}^+ = f_{yT}$. f_{yT} and f_{cT} depend on the value of the temperature T and then, according to Eqs. (3), (4) from the point coordinates over the section and fire duration t.

In the following the dependence on s is omitted for a clearer exposition. In accordance with [1, 3, 7, 8], we introduce the plastic mechanism of the cross-section as

$$\mathbf{n} = [\dot{\varepsilon}, \dot{\chi}_2, \dot{\chi}_3]^T \tag{10}$$

which defines the position and orientation of the neutral axis for the collapse state from the condition

$$\dot{\varepsilon}_{11} \equiv \dot{\varepsilon} + x_3 \dot{\chi}_2 - x_2 \dot{\chi}_3 = 0. \tag{11}$$

where $\dot{\varepsilon}_{11}$ is the axial strain of the collapse mechanism.

Denoting with Ω the beam section domain, the yield stress vector $\boldsymbol{\tau}_y$ collecting the generalized section resultants associated with $\mathbf{n}$ by the Drucker's condition, at a given fire duration t, is

$$\boldsymbol{\tau}_y[\mathbf{n}, t] = \begin{bmatrix} N_y \\ M_{y2} \\ M_{y3} \end{bmatrix} \quad \text{with} \quad \begin{cases} N_y = \sum_i \left(\int_{\Omega_i^+} f_{iT}^+ d\Omega_i - \int_{\Omega_i^-} f_{iT}^- d\Omega_i \right) \\ M_{y2} = \sum_i \left(\int_{\Omega_i^+} x_3 f_{iT}^+ d\Omega_i - \int_{\Omega_i^-} x_3 f_{iT}^- d\Omega_i \right) \\ M_{y3} = \sum_i \left(\int_{\Omega_i^+} x_2 f_{iT}^- d\Omega_i - \int_{\Omega_i^-} x_2 f_{iT}^+ d\Omega_i \right) \end{cases} \tag{12}$$

where Ω_i^+ and Ω_i^- are the portion of the generic subdomain Ω_i of the section in traction and compression respectively. The integrals can be easily evaluated by the numerical procedure described in [9]. For steel reinforcements the integral can be substituted with a sum of contributions considering the area concentrated in a point.

Equation (12) allows the evaluation, for an assigned fire duration t, of the set of generalized yield stress $\boldsymbol{\tau}_y[\mathbf{n}_k, t]$ associated to the mechanism $\mathbf{n}_k$, simply by assuming uniaxial stress fields reaching their maximum strength capacity in each region, either in tension or in compression. A suitable interpolation or approximation of these points furnishes the cross-section yield surface. Note that vectors $\mathbf{n}_k$ are normal to the yield surface according to the Drucker condition.

3 Construction of the Time-Dependent Yield Surface

In this section a new approach for constructing the yield surface of cross-sections in conditions of fire in terms of the Minkowski sum of ellipsoids [1, 7, 8] is given.

3.1 Construction of Yield Surface at Ambient Temperature

From now on, for a more clear notation, the dependence on the fire duration will be omitted to denote the quantities at ambient temperature. The domain of the cross-section is subdivided into a grid of sub-domains $\Omega_s = \cup_I \Omega_I$ as shown in Fig. 2. Rebars can be collected in groups, one for each edge. Exploiting the properties of the integral in Eq. (12), the true yield stress $\boldsymbol{\tau}_y[\mathbf{n}_k]$ at ambient temperature ($k_c = k_r = k_s = 1$) can be obtained as

$$\boldsymbol{\tau}_y[\mathbf{n}_k] = \sum_I \boldsymbol{\tau}_{yI}[\mathbf{n}_k] \tag{13}$$

Equation (13) can be interpreted as a Minkowski sum.

The yield surface of each sub-domain I, that is the cloud points $\boldsymbol{\tau}_{yI}[\mathbf{n}_k]$ for all the mechanisms $\mathbf{n}_k$, is approximated using a single ellipsoid as

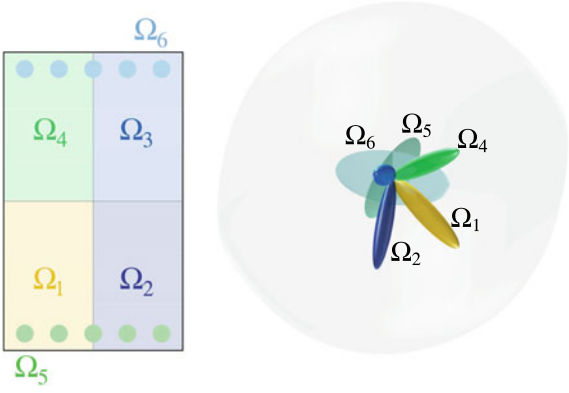

Fig. 2 Geometric construction of the cross-section yield surface as a Minkowski sum of ellipsoids

$$(\boldsymbol{\tau}_I - \mathbf{c}_I)^T \mathbf{C}_I^{-1} (\boldsymbol{\tau}_I - \mathbf{c}_I) - 1 = 0$$

with the stress on the ellipsoid surface which assumes the following expression in terms of a generic normal vector $\mathbf{n}$

$$\boldsymbol{\tau}_I[\mathbf{n}] = \mathbf{c}_I + \frac{\mathbf{C}_I \mathbf{n}}{\sqrt{\mathbf{n}^T \mathbf{C}_I \mathbf{n}}}. \tag{14}$$

The ellipsoidal center $\mathbf{c}_I$ and shape matrix $\mathbf{C}_I$ are obtained, as in [1, 8], by solving, for each sub-domain I, the following least square problem

$$\min_{(\mathbf{c}_I, \mathbf{C}_I)} \sum_k r_k^2 \quad \text{with} \quad r_k = \mathbf{n}_k^T (\boldsymbol{\tau}_{Iy}[\mathbf{n}_k] - \boldsymbol{\tau}_I[\mathbf{n}_k]). \tag{15}$$

Finally, the stress points on the yield surface expressed as a Minkowski sum of ellipsoids can be parametrized in a closed form in terms of the normal vector $\mathbf{n}$ (see [7]), as

$$\boldsymbol{\tau}[\mathbf{n}] = \sum_I \boldsymbol{\tau}_I[\mathbf{n}]. \tag{16}$$

Note that now, in contrast to [1, 7, 8], the least square approximation of the yield surface in Eq. (15) is decoupled for each ellipsoid.

3.2 *Account of the Time-Dependent Strength Reduction*

The reduction factors k_c and k_r in Eqs. (3) and (4) depend on the fire duration and on the point (x_2, x_3) within the section. It is possible to approximate them with a mean value $\bar{k}_I[t]$ within each sub-domain I. This value is chosen as the one which provides an exact axial force, but it furnishes accurate results also for the bending moments when multiple sub-domains are used. For concrete sub-domains, letting $k_I[x_2, x_3, t] = k_c[x_2, x_3, t]$, this means

$$\bar{k}_I[t] = \frac{1}{\Omega_I} \int_{\Omega_I} k_I[x_2, x_3, t] d\Omega_I$$

where the integral can be evaluated analytically as in [19], or numerically using, for instance, the Gauss quadrature. Since $k_I[x, y, t]$ is a quite complicated function we prefer the numerical integration, which makes it possible to avoid the use of complicated formula. A grid of 3×3 Gauss points provides a suitable approximation. For sub-domains collecting steel rebars, the previous equation becomes an average of the reduction factors of the rebars weighted for the corresponding areas. For structural steel, assuming a uniform temperature over the section, we have $\bar{k}_I[t] = k_s, \ \forall I$.

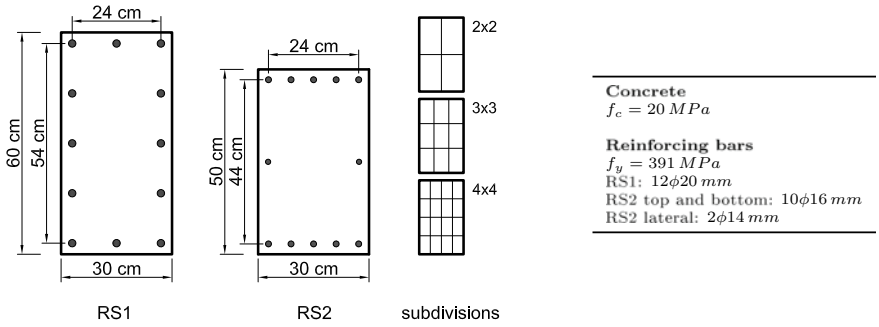

Fig. 3 Rectangular RC sections: geometry, materials and subdivisions for the geometric Minkowski sum

The points belonging to the time-dependent yield surface can then be easily expressed in a closed parametric form, for any t, as

$$\boldsymbol{\tau}[\mathbf{n}, t] = \sum_I \bar{k}_I[t]\boldsymbol{\tau}_I[\mathbf{n}]. \tag{17}$$

This means we do not need to re-compute the yield surface at a given fire duration t, because it is automatically available by simply scaling the ellipsoidal contributions of the yield surface at ambient temperature.

3.3 Some Examples of Yield Surface Evaluation

The proposed strategy for the evaluation of the time-dependent yield surface is now tested for two RC cross-sections, called $RS1$ and $RS2$, with steel reinforcements of diameter ϕ typical of columns and beams respectively and reported in Fig. 3. The accuracy is tested varying the number of sub-domains of the concrete part, while one sub-domain is used for each steel edge. The reference solution is obtained by evaluating the yield points numerically according to Eq. (12) using a very fine discretization of the concrete area and considering the contribution of each rebar separately. The yield surfaces are illustrated in the space of the generalized stresses $\boldsymbol{\tau} = [N, M_2, M_3]^T$.

The $RS1$ section is analyzed considering a fire exposure all along its perimeter. The temperature distributions within the section is predicted by Wickstrom's formulas. Clearly, they are symmetric with respect to the principal axes of the section because of the symmetry in the geometry and thermal boundary conditions. The evolution of yield surface is better illustrated in Fig. 4 for the 4×4 approximation. We can note the symmetry with respect to the $M_2 - M_3$ plane as well as the non-null position of the center along the N axis, due to the zero concrete tensile strength, of the ambient

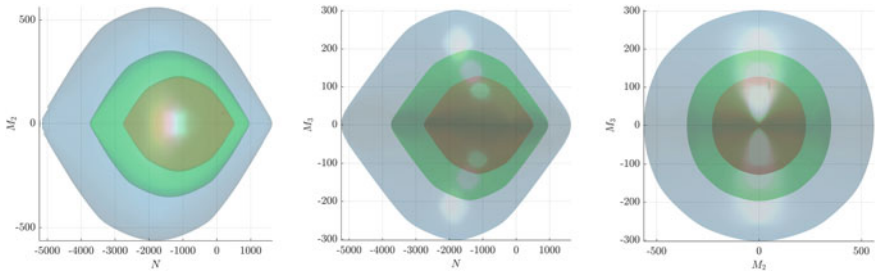

(a) (b) 4x4 subdomains (c)

Fig. 4 $RS1$ section: evolution of the yield surface in terms of $N(kN)$, $M_2(kNm)$, $M_3(kNm)$ for the 4×4 discretization (ambient temperature, 1 and 2 hours of fire exposure)

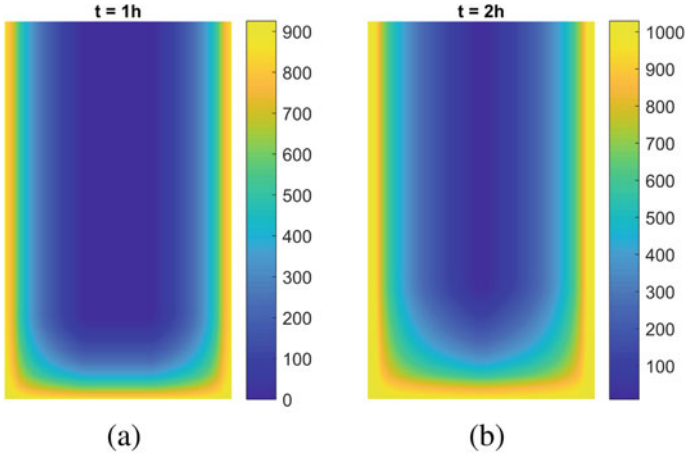

Fig. 5 $RS2$ section: temperature distribution (°C) within the section at 1 and 2 hours of fire exposure

temperature domain. These features are preserved also for the section in fire because of the bi-symmetric temperature distribution.

The $RS2$ section is analyzed considering a fire exposure along three edges: left, bottom and right. Figure 5 shows the temperature distributions within the section predicted by Wickstrom's formulas for 1 and 2 hours of fire. They are not symmetric with respect to the x_3 axis of the section because of the asymmetric thermal boundary conditions. In Fig. 6 we can observe the quality of the proposed Minkowski approximation in fitting the yield points of the reference solution at various fire durations. The 2×2 approximation of the concrete domain provides an excellent fit of the true yield points at ambient temperature, but the solution gets worse increasing the time of exposure to fire. A 4×4 approximation is able to capture the contraction of the yield surfaces more correctly also for increasing fire durations. The evolution of yield surface is better illustrated in Fig. 7 for the 4×4 approximation. We can note

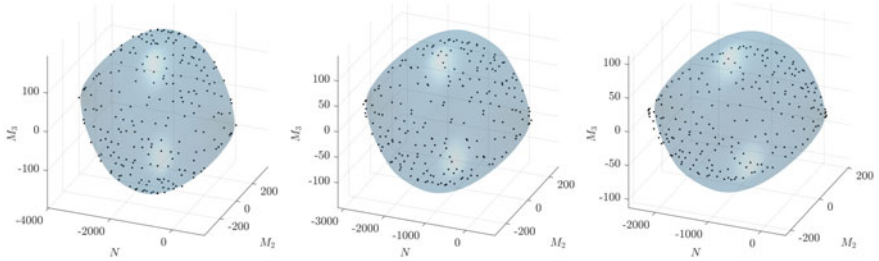

(a) $t = 0$, 2×2 subdomains (b) $t = 1$h, 2×2 subdomains (c) $t = 2$h, 2×2 subdomains

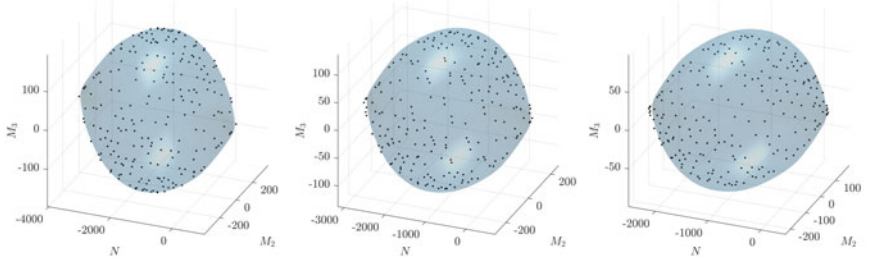

(d) $t = 0$, 4×4 subdomains (e) $t = 1$h, 4×4 subdomains (f) $t = 2$h, 4×4 subdomains

Fig. 6 $RS2$ section: approximation of the true yield points $[N(kN), M_2(kNm), M_3(kNm)]$ for different fire durations

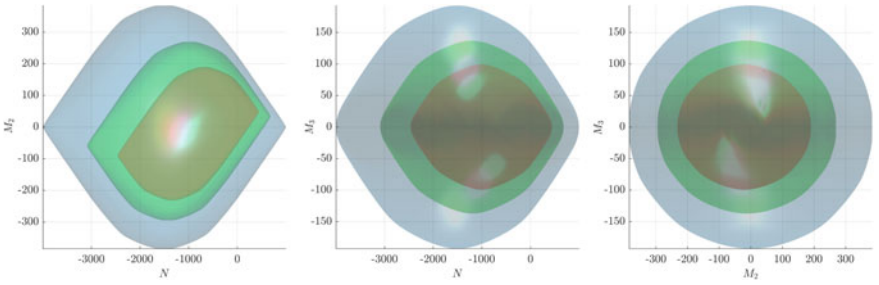

(a) (b) 4x4 subdomains (c)

Fig. 7 $RS2$ section: evolution of the yield surface in terms of $N(kN)$, $M_2(kNm)$, $M_3(kNm)$ for the 4×4 discretization (ambient temperature, 1 and 2 hours of fire exposure)

that, in contrast to the section previously analyzed, the symmetry with respect to the $M_2 - M_3$ plane of the ambient temperature domain is no longer preserved for the section in fire as soon as the heating is non-symmetric.

4 The Finite Element Model for 3D Beams Subjected to Fire

4.1 The 3D Beam Finite Element

The beam finite element adopted (see [8]) uses an interpolation of the generalized stresses $[\mathbf{N}, \mathbf{M}]^T = \mathbf{D}_t[s]\boldsymbol{\beta}$, where the interpolation matrix $\mathbf{D}_t[s]$ is obtained satisfying the equilibrium equations on the element for zero body forces exactly. Body load effects are then included exactly as a "particular solution". The internal work becomes

$$\mathscr{W} \equiv \mathbf{N}^T \left(\mathbf{u}_0[\ell] - \mathbf{u}_0[0]\right) + \mathbf{M}[\ell]^T \boldsymbol{\varphi}[\ell] - \mathbf{M}[0]^T \boldsymbol{\varphi}[0] = \mathbf{d}_e^T \mathbf{Q}_e^T \boldsymbol{\beta} \tag{18}$$

allowing us to directly obtain the discrete form of $\mathscr{W}$ without any FEM interpolation for the kinematic variables. The vectors collecting the kinematics $\mathbf{d}_e$ and static β finite element generalized parameters and the compatibility operator $\mathbf{Q}_e$ are defined as

$$\beta = \begin{bmatrix} N \\ M_2[0] \\ M_3[0] \\ M_2[\ell] \\ M_3[\ell] \\ M_1 \end{bmatrix}, \quad \mathbf{d}_e = \begin{bmatrix} \mathbf{u}_0[0] \\ \boldsymbol{\varphi}[0] \\ \mathbf{u}_0[\ell] \\ \boldsymbol{\varphi}[\ell] \end{bmatrix}, \quad \mathbf{Q}_e = \frac{1}{\ell} \begin{bmatrix} -\ell\, \mathbf{e}_1^T & \mathbf{0} & \ell\, \mathbf{e}_1^T & \mathbf{0} \\ \mathbf{e}_3^T & -\ell\, \mathbf{e}_2^T & -\mathbf{e}_3^T & \mathbf{0} \\ -\mathbf{e}_2^T & -\ell\, \mathbf{e}_3 & \mathbf{e}_2^T & \mathbf{0} \\ -\mathbf{e}_3^T & \mathbf{0} & \mathbf{e}_3^T & \ell\, \mathbf{e}_2^T \\ \mathbf{e}_2^T & \mathbf{0} & -\mathbf{e}_2^T & \ell\, \mathbf{e}_3^T \\ \mathbf{0} & -\ell\, \mathbf{e}_1^T & \mathbf{0} & \ell\, \mathbf{e}_1^T \end{bmatrix}. \tag{19}$$

4.2 The Elastic Problem

The linear elastic problem can be formulated as the stationarity of the Hellinger-Reissner functional Π_{HR} that at the element level can be written as

$$\Pi_{HR} = \mathbf{d}_e^T \mathbf{Q}_e^T \beta - \frac{1}{2} \beta^T \mathbf{F}_e \beta - \mathbf{d}_e^T \mathbf{p}_e$$

where $\mathbf{p}_e$ is the element contribution of the external loads and the elastic compliance matrix of the element $\mathbf{F}_e$ is obtained from the equivalence

$$\int_\ell \left(\begin{bmatrix} \mathbf{N} \\ \mathbf{M} \end{bmatrix}^T \begin{bmatrix} \mathbf{F}_{NN} & \mathbf{F}_{NM} \\ \mathbf{F}_{NM}^T & \mathbf{F}_{MM} \end{bmatrix} \begin{bmatrix} \mathbf{N} \\ \mathbf{M} \end{bmatrix} \right) ds = \boldsymbol{\beta}^T \mathbf{F}_e \boldsymbol{\beta}, \quad \mathbf{F}_e = \int_\ell \mathbf{D}_t[s]^T \mathbf{F} \mathbf{D}_t[s]\, ds. \tag{20}$$

The stationarity of Π_{HR} with respect to the stress variables furnishes the discrete elastic constitutive law

$$\boldsymbol{\beta}[\mathbf{d}_e] = \mathbf{E}_e \mathbf{Q}_e \mathbf{d}_e \quad \text{with} \quad \mathbf{E}_e = \mathbf{F}_e^{-1} \tag{21}$$

which allows us to express the elastic problem in terms of displacement variables only. The stationarity condition with respect to $\mathbf{d}_e$ furnishes the equilibrium equations on the element as

$$\mathbf{s}_e[\mathbf{d}_e] - \mathbf{p}_e = \mathbf{0} \quad \text{with} \quad \mathbf{s}_e[\mathbf{d}_e] = \mathbf{Q}_e^T \boldsymbol{\beta}[\mathbf{d}_e] \tag{22}$$

where $\mathbf{s}_e[\mathbf{d}_e]$ and $\mathbf{p}_e$ are the internal force vector and the external load vector of the element respectively. Equation (22), in the elastic case, becomes

$$\mathbf{K}_e \mathbf{d}_e - \mathbf{p}_e = \mathbf{0} \quad \text{with} \quad \mathbf{K}_e = \mathbf{Q}_e^T \mathbf{E}_e \mathbf{Q}_e.$$

4.3 Stress Update for Time-Dependent Yield Conditions

Denoting with a subscript s the quantities related to the cross-section at abscissa s, the yield function $f_s[t, \boldsymbol{\tau}_s]$ is defined in a 3D space involving axial force N and bending moments $M_2[s]$ and $M_3[s]$ collected in vector $\boldsymbol{\tau}_s = [N, M_2[s], M_3[s]]^T$. The plastic admissibility condition is

$$f_s[t, \boldsymbol{\tau}_s] \leq 0. \tag{23}$$

The update of the stress is obtained, in a strain-driven way, by means of a closest point projection (CPP) which corresponds to a backward Euler scheme for integrating the constitutive law. Starting from a known state $\mathbf{d}_e^0$, $\boldsymbol{\beta}^0$ at time t^0, the stress parameters $\boldsymbol{\beta}$ at time t for an assigned displacement increment $\Delta\mathbf{d}_e = \mathbf{d}_e - \mathbf{d}_e^0$ are obtained by solving, for each element, the optimization problem

$$\begin{aligned} \text{minimize} \quad & \frac{1}{2}(\boldsymbol{\beta} - \boldsymbol{\beta}^*)^T \mathbf{F}_e (\boldsymbol{\beta} - \boldsymbol{\beta}^*) \\ \text{subject to} \quad & f_0[\boldsymbol{\tau}_0, t] \leq 0 \\ & f_\ell[\boldsymbol{\tau}_\ell, t] \leq 0 \end{aligned} \tag{24}$$

where $\boldsymbol{\beta}^* = \boldsymbol{\beta}^0 + \mathbf{E}_e \mathbf{Q}_e \Delta\mathbf{d}_e$ is the elastic predictor. The admissibility condition is checked only on the end nodes of the beam and the generalized normal stress vectors of these sections are extracted directly from $\boldsymbol{\beta}$ as $\boldsymbol{\tau}_s = \mathbf{P}_s \boldsymbol{\beta}$ with $s = 0, \ell$. The extraction operators $\mathbf{P}_0$ and $\mathbf{P}_\ell$ can easily be obtained from Eq. (19). Note that, the stresses at both end sections are coupled with each other by the equilibrated interpolation and, then, the CPP has to be performed at the element level. Moreover Eq. (24) defines the constitutive law with the stresses uniquely defined by their initial values, the time of exposure and the displacement increment. In the following, to simplify the notation, we write $\boldsymbol{\beta} = \boldsymbol{\beta}[\mathbf{d}_e, t]$ omitting the dependence from the known quantity $\boldsymbol{\beta}^0$.

Exploiting Eq. (24), the element equilibrium equations (22) become

$$\mathbf{s}_e[\mathbf{d}_e, t] - \mathbf{p}_e = \mathbf{0} \quad \text{with} \quad \mathbf{s}_e[\mathbf{d}_e, t] = \mathbf{Q}_e^T \boldsymbol{\beta}[\mathbf{d}_e, t]. \tag{25}$$

The problem described in Eq. (24) corresponds to an elastic predictor-return mapping scheme.

5 A Global Fire Analysis for 3D Frames

In this section, an strain driven optimization algorithm is described for the evaluation of limit fire duration.

5.1 The Optimization Algorithm

Once the finite element assemblage has been carried out, the equilibrium condition of a frame subjected to fire can be written as

$$\mathbf{r}[\mathbf{d}, t] = \mathbf{s}[\mathbf{d}, t] - \mathbf{p} = \mathbf{0} \tag{26}$$

where $\mathbf{p}$ and $\mathbf{s}$ are the load vector and the internal force vector of the structure respectively, obtained assembling the finite element contributions in Eq. (25), and $\mathbf{d}$ is the vector collecting the overall kinematic degrees of freedom. This system of nonlinear equations defines a curve in the hyperspace $\mathbf{d}$-t. The curve can exhibit a limit fire duration, that is the time of exposure which leads to structural collapse. For this reason it is not convenient to use a time controlled scheme since Eq. (26) could not have a solution, that is no equilibrium state, for a given fire duration. We propose instead the use of a generalized arc-length method. The equilibrium equations are completed with the additional constraint $g[\mathbf{d}, t] - \xi = 0$, which defines a surface in $\mathbb{R}^{N+1}$. Assigning successive values to the control parameter $\xi = \xi_{(k)}$ the solution of the nonlinear system

$$\mathbf{R}[\mathbf{d}, t] \equiv \begin{bmatrix} \mathbf{r}[\mathbf{d}, t] \\ g[\mathbf{d}, t] - \xi \end{bmatrix} = \mathbf{0} \tag{27}$$

defines a sequence of safe equilibrium points (steps) $\mathbf{z}_{(k)} \equiv \{\mathbf{d}_{(k)},\ t_{(k)}\}$. Starting from a known equilibrium point $\mathbf{z}^0 \equiv \mathbf{z}_{(k)}$, the new one $\mathbf{z}_{(k+1)}$ is evaluated correcting a first *extrapolation* $\mathbf{z}^1 = \{\mathbf{d}^1,\ t^1\}$ by a sequence of estimates $\mathbf{z}^j$ by a Newton–Raphson iteration

$$\begin{cases} \mathbf{J}\delta\mathbf{z} = -\mathbf{R}^j \\ \mathbf{z}^{j+1} = \mathbf{z}^j + \delta\mathbf{z} \end{cases} \tag{28}$$

where $\mathbf{R}^j \equiv \mathbf{R}[\mathbf{z}^j]$ and $\mathbf{J}$ is the Jacobian of the non-linear system (27) at $\mathbf{z}^j$ or its suitable estimate. Also if other choices are possible [20, 21], the simplest and effective choice for $g[\mathbf{d}, t]$ is an adaptive linear constraint corresponding to the orthogonal hyperplane, updated at the beginning of each time step, that is

$$\mathbf{v}_d^T(\mathbf{d} - \mathbf{d}^1) + v_t\,(t - t^1) = \xi - \xi_{(k)} \quad \text{where} \quad \begin{cases} \mathbf{v}_d \equiv \Gamma\,(\mathbf{d}^1 - \mathbf{d}_{(k)}) \\ v_t \equiv \mu\,(t^1 - t_{(k)}) \end{cases} \tag{29}$$

Γ and μ being some suitable metric factors [22, 23] and

$$\mathbf{J} \equiv \left[\frac{\partial \mathbf{R}[\mathbf{z}]}{\partial \mathbf{z}}\right]_{\mathbf{z}^j} = \begin{bmatrix} \mathbf{K}_t & \mathbf{s}_t \\ \mathbf{v}_d^T & v_t \end{bmatrix} \quad \text{with} \quad \mathbf{K}_t = \left.\frac{\partial \mathbf{s}[\mathbf{d}, t]}{\partial \mathbf{d}}\right|_{\mathbf{z}^j}, \quad \mathbf{s}_t = \left.\frac{\partial \mathbf{s}[\mathbf{d}, t]}{\partial t}\right|_{\mathbf{z}^j}. \tag{30}$$

The choice of an adaptive constraint makes the Jacobian matrix in Eq. (30) non singular also when $\mathbf{K}_t$ is singular. The solution of Eq. (28) is conveniently performed in a partitioned way as follows

$$\begin{cases} \delta t = \dfrac{\mathbf{v}_d^T \mathbf{K}_t^{-1} \mathbf{r}^j}{v_t - \mathbf{v}_d^T \mathbf{K}_t^{-1} \mathbf{s}_t} \\ \mathbf{K}_t \delta \mathbf{d} = \delta t \mathbf{s}_t - \mathbf{r}^j \end{cases} \tag{31}$$

in order to exploit the symmetry and the band structure of the tangent stiffness matrix $\mathbf{K}_t$. The tangent operators $\mathbf{K}_t$ and $\mathbf{s}_t$ are obtained assembling the element contributions.

The points $\mathbf{z}_{(n)}$ evaluated by the scheme are, by definition, equilibrated and plastically admissible at time $t_{(n)}$. In other words, they satisfy the hypotheses of the lower bound theorem of the limit analysis and, then, the structure is safe for this fire duration. Furthermore, we have that $\mathbf{z}_{(n)}$ is plastically admissible also for the yield conditions at time $t_k < t_n$ if we assume that the temperature, and then the strength reduction, is a nondecreasing function of the fire duration as stated in Eq. (1). In this situation, it is possible to demonstrate (see [24]) that the sequence of fire duration provided by the proposed incremental-iterative analysis converges, if it exists, to a limit fire duration. In other words, when $\Delta t \equiv t_{(n)} - t_{(n-1)} = 0$, a kinematically admissible mechanism develops and the structure is just at the point of failure because the hypotheses of the upper and lower bound theorems of the limit analysis are satisfied simultaneously.

6 Numerical Tests

The time-dependent yield surfaces and the incremental strategy are employed for assessing the safety of framed structures exposed to fire. A single finite element is used for the columns, while two finite elements are used for the beams. An ISO 834 standard fire is considered. The maximum structural deflection, denoted as u_{max}, is

chosen as control variable and monitored in the numerical tests. The results provided by our fire analysis in terms of limit fire duration are assessed by means of a comparison with a standard elasto-plastic analysis where the yield surfaces are kept constant and the load is amplified by a factor λ. In particular, we show that the limit load provided by the elasto-plastic analysis coincides with the applied one ($\lambda = 1$) when the yield surface of the fire exposed sections is evaluated at the limit fire duration.

6.1 A Simple Steel Frame

This example regards the simple 3D frame reported in Fig. 8. The floor load is uniformly distributed over the four beams. The fire scenario is the one described in Fig. 1.

In Fig. 9 the fire duration-displacement sequence of safe points for the assigned distributed load is reported. The curve is characterized by a significant initial portion with zero displacements. This means that the load is largely inside the initial domain at ambient temperature. 1.75 hours are required to observe the first plastic deformations while the limit fire duration is equal to 2.23. Different cross-section discretizations are employed. The results provided by our fire analysis in terms of limit fire duration are assessed by means of a comparison with a standard elasto-plastic analysis where the yield surfaces are kept constant and the load is amplified by a factor λ. In particular, we show that the limit load provided by the elasto-plastic analysis coincides with the applied one ($\lambda = 1$) when the yield surface of the fire exposed sections is evaluated at the limit fire duration.

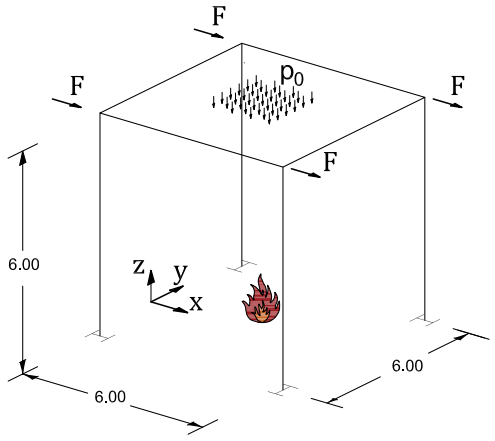

Loads
$p_0 = 15kN/m^2$
$F = 25kN$
Steel
$f_y = 355MPa$
Column section HE300A
Beam section IPEA300

Fig. 8 Simple steel frame: geometry, loads and cross-sections

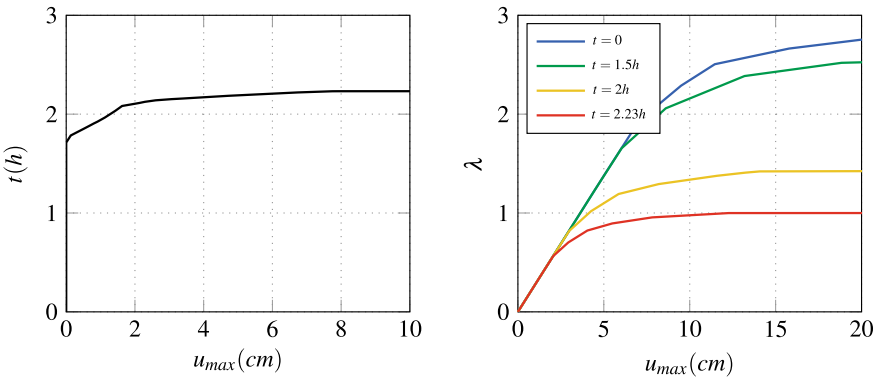

(a) sequence of safe states

(b) elasto-plastic analysis with assigned fire durations

Fig. 9 Simple steel frame: equilibrium paths

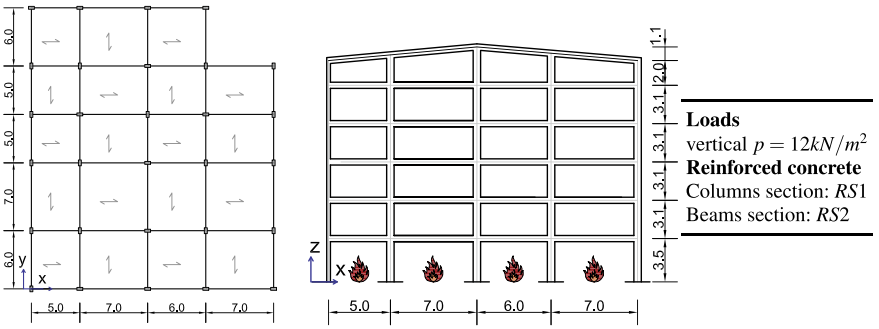

(a) plan view

(b) front view

Fig. 10 Full-scale building: geometry (lengths in meters), loads and cross-sections

6.2 *A Full-Scale Reinforced Concrete Building*

The last test regards the full-scale building reported in Fig. 10. The cross section labeled $RS1$ and $RS2$ in Fig. 3 are used for columns and beams respectively. The vertical story load p of the one way ribbed slab as depicted in Fig. 10 is distributed on the beams. For each floor area, 90% of weight is assigned to the beams orthogonal to the ribs, while the other 10% is applied on the parallel ones. The fire event involves the ground floor only.

In Fig. 11 the fire duration-displacement sequence of safe points for the assigned distributed load is reported. The curve is characterized by an initial portion with zero displacement. This means that the load is sufficiently safe at ambient temperature. 1.3 hours of fire exposure are required for the first plastic deformations, while the limit fire duration is equal to 2.7 hours. We can note that in this case, due the high

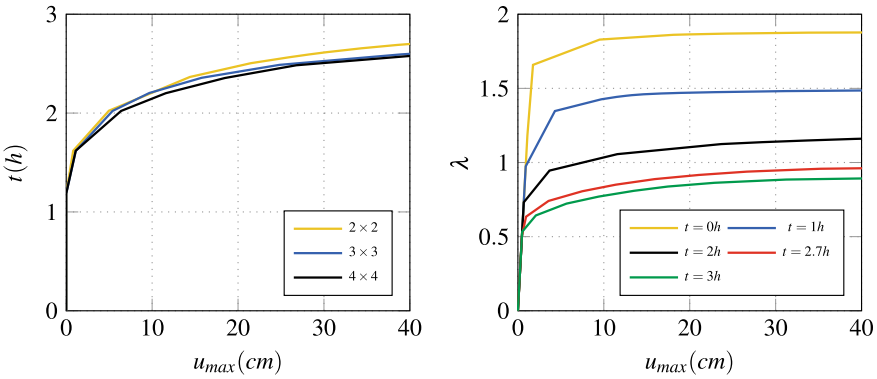

(a) sequence of safe states

(b) elasto-plastic analysis with assigned fire durations

Fig. 11 Full-scale building: equilibrium paths

hyperstaticity of multi-storey multi-span frames, the commonly employed sectional check underestimates the structural safety by about twice the one predicted by our model, which accounts for the redistribution of the stresses and the consequent structural overstrength. Different cross-section discretizations are employed, all of them providing similar results (3×3 practically coincides with the 4×4). Again, the structure is analyzed using the standard elasto-plastic analysis and the corresponding load-displacement paths are reported in Fig. 11 for different fire durations. It is possible to observe how the collapse load factor is equal to one for the yield surface corresponding to the fire duration limit evaluated with the proposed incremental strategy.

7 Conclusions

In this work, we proposed a numerical framework for the global assessment of the fire resistance of 3D frames. First of all, a simple, accurate and efficient numerical procedure for constructing the axial force-biaxial bending yield surface of cross-sections in fire was derived. This is based on a particular Minkowski sum of ellipsoids, where each ellipsoid represents the contribution of a sub-domain of the cross-section to the overall surface. The yield conditions are made time-dependent by assigning a strength reduction factor at each sub-domain. Once the structure is discretized using 3D beam mixed finite elements which check the admissibility condition on the end sections, the equilibrium condition of 3D frames is formulated as a nonlinear system of equations defining a curve in the hyperspace of the discrete variables and the fire duration. An optimization strategy based on a strain-driven formulation was

proposed to evaluate the global fire resistance. It furnishes a sequence of safe states at increasing fire durations up to the limit one. Numerical tests showed that the proposed formulation is well-suited for full-scale buildings.

References

1. Bleyer, J., De Buhan, P.: Yield surface approximation for lower and upper bound yield design of 3D composite frame structures. Comput. Struct. **129**, 86–98 (2013)
2. Skordeli, M.A., Bisbos, C.: Limit and shakedown analysis of 3D steel frames via approximate ellipsoidal yield surfaces. Eng. Struct. **32**(6), 1556–1567 (2010)
3. Pham, D.T., de Buhan, P., Florence, C., Heck, J.-V., Nguyen, H.H.: Interaction diagrams of reinforced concrete sections in fire: a yield design approach. Eng. Struct. **90**, 38–47 (2015). https://doi.org/10.1016/j.engstruct.2015.02.012
4. El-Fitiany, S., Youssef, M.: Fire performance of reinforced concrete frames using sectional analysis. Eng. Struct. **142**, 165–181 (2017)
5. Law, A., Gillie, M.: Interaction diagrams for ambient and heated concrete sections. Eng. Struct. **32**(6), 1641–1649 (2010)
6. Caldas, R.B., Sousa, J.B.M., Fakury, R.H.: Interaction diagrams for reinforced concrete sections subjected to fire. Eng. Struct. **32**(9), 2832–2838 (2010)
7. Sessa, S., Marmo, F., Rosati, L., Leonetti, L., Garcea, G., Casciaro, R.: Evaluation of the capacity surfaces of reinforced concrete sections: eurocode versus a plasticity-based approach. Meccanica **53**(6), 1493–1512 (2018)
8. Leonetti, L., Casciaro, R., Garcea, G.: Effective treatment of complex statical and dynamical load combinations within shakedown analysis of 3D frames. Comput. Struct. **158**, 124–139 (2015)
9. Malena, M., Casciaro, R.: Finite element shakedown analysis of reinforced concrete 3D frames. Comput. Struct. **86**(11), 1176–1188 (2008)
10. Bleyer, J., De Buhan, P.: A greedy algorithm for yield surface approximation. Comptes Rendus Mécanique **341**(8), 605–615 (2013)
11. Fogel, E., Halperin, D.: Exact and efficient construction of minkowski sums of convex polyhedra with applications. CAD Comput. Aided Des. **39**(11), 929–940 (2007)
12. Magisano, D., Liguori, F., Leonetti, L., Garcea, G.: Minkowski plasticity in 3D frames: decoupled construction of the cross-section yield surface and efficient stress update strategy. Int. J. Numer. Methods Eng. **116**(7), 435–464 (2018). https://doi.org/10.1002/nme.5931
13. Garcea, G., Leonetti, L.: A unified mathematical programming formulation of strain driven and interior point algorithms for shakedown and limit analysis. Int. J. Numer. Methods Eng. (2011). https://doi.org/10.1002/nme.3188. n/a-n/a
14. Wickström, U.: A very simple method for estimating temperature in fire exposed concrete structures. Fire Technol. Tech. Rep. SP-RAPP **46**(1986), 186–194 (1986)
15. Buchanan, A.H., Abu, A.K.: Structural Design for Fire Safety, 2nd edn. Wiley, United Kingdom (2017)
16. European Union, EN 1992-Eurocode 2: Design of concrete structures (1992)
17. T. Lie, Structural Fire Protection: ASCE Manuals and Reports on Engineering Practice, vol. 78, 241 pp. (1992). https://doi.org/10.1061/9780872628885
18. Genoese, A., Genoese, A., Bilotta, A., Garcea, G.: A generalized model for heterogeneous and anisotropic beams including section distortions. Thin-Walled Struct. **74**, 85–103 (2014)
19. El-Fitiany, S., Youssef, M.: Interaction diagrams for fire-exposed reinforced concrete sections. Eng. Struct. **70**, 246–259 (2014). https://doi.org/10.1016/j.engstruct.2014.03.029
20. Eriksson, A.: Structural instability analyses based on generalised path-following. Comput. Methods Appl. Mech. Eng. **156**(1), 45–74 (1998)

21. Riks, E.: On formulation of path-following techniques for structural stability analysis. New Adv. Comput. Struct. Mech. **156**(1992), 65–79 (1992)
22. Magisano, D., Leonetti, L., Garcea, G.: How to improve efficiency and robustness of the Newton method in geometrically non-linear structural problem discretized via displacement-based finite elements. Comput. Methods Appl. Mech. Eng. **313**, 986–1005 (2017). https://doi.org/10.1016/j.cma.2016.10.023
23. Magisano, D., Leonetti, L., Garcea, G.: Advantages of the mixed format in geometrically nonlinear analysis of beams and shells using solid finite elements. Int. J. Numer. Methods Eng. **109**(9), 1237–1262 (2017). https://doi.org/10.1002/nme.5322
24. Magisano, D., Liguori, F., Leonetti, L., de Gregorio, D., Zuccaro, G., Garcea, G.: A quasi-static nonlinear analysis for assessing the fire resistance of reinforced concrete 3D frames exploiting time-dependent yield surfaces. Comput. Struct. **212**, 327–342 (2019)

Limit Analysis of Dry Masonry Block Structures with Non-associative Coulomb Friction: A Novel Computational Approach

Nicola A. Nodargi, Claudio Intrigila, and Paolo Bisegna

Abstract The limit analysis of dry-masonry block structures with non-associative Coulomb friction is formulated as a Mixed Complementarity Problem. After highlighting some of its peculiar features, such as the lack of uniqueness of the collapse multiplier, a fixed-point based algorithm is presented for constructing a solution, obtained by iteratively solving straightforward associative limit analysis problems. Supported by the comparison with benchmark problems, the resulting procedure is proven to be able to predict the collapse multiplier of masonry block structures with accuracy, robustness and effectiveness.

1 Introduction

The analysis of the mechanical behavior of historical masonry structures represents a significant research topic in computational mechanics, as related to the preservation and the restoration of architectural heritage and of historical buildings. Many computational strategies have been developed to date, aiming at modeling masonry response at different scales and levels of complexity. Among them, it is worth mentioning micromechanical approaches (e.g., see [13, 30]), multiscale/homogenization approaches (e.g., see [1, 6, 21, 35]) and macromechanical/phenomenological approaches (e.g., see [14, 24, 27, 33, 34]), to be used in conjunction with finite element formulations suitable for the analysis of inelastic structures (e.g., see [7, 8, 23, 25, 26, 28]).

N. A. Nodargi (✉) · C. Intrigila · P. Bisegna
Department of Civil Engineering and Computer Science, University of Rome Tor Vergata, 00133 Rome, Italy
e-mail: nodargi@ing.uniroma2.it

C. Intrigila
e-mail: intrigila@ing.uniroma2.it

P. Bisegna
e-mail: bisegna@ing.uniroma2.it

A. A. Pisano et al. (eds.), *Direct Methods*, Lecture Notes in Applied and Computational Mechanics 95, https://doi.org/10.1007/978-3-030-48834-5_5

Renouncing to a constitutive description of masonry material, the collapse loading of masonry structures can be rigorously determined by limit analysis theory, as first shown by Kooharian and Heyman in their classical works (see [16, 18]). A fundamental contribution in translating limit analysis into a computational strategy was the seminal work by Livesley (see [19]), who proposed to consider a typical masonry structure as a system of rigid blocks, which interact through no-tension frictional interfaces. The attractiveness of such idealization, only requiring the friction angle of block interfaces as material parameter, was also motivated by the simple format of Linear Programming (LP) problem taken by limit analysis theorems. Unfortunately, limit analysis theorems intrinsically presuppose an associative flow law, and, correspondingly to Coulomb friction, the collapse mechanism exhibits interface dilatancy and the collapse multiplier is usually overestimated (as already shown in [10] and [37]).

Abandoning standard limit analysis theorems to assume a non-associative friction flow law, a non-associative limit analysis problem for the analysis of masonry block structures has been progressively formalized in [3, 4, 11, 12, 20]. That is obtained by explicitly considering equilibrium and compatibility equations pertaining to blocks, along with admissibility constraints (including Coulomb friction), flow laws (including non-associative Coulomb friction flow law) and Kuhn-Tucker complementarity conditions pertaining to block interfaces. However, due to the non-convex structure of the complementarity constraint, the resulting coupled static/kinematic Mixed Complementarity Problem (MCP) carries an ill-posedness issue related to lack of uniqueness of the collapse multiplier. Accordingly, by assuming the minimum collapse multiplier as the actual target, a constrained minimization problem is formulated, with constraints given by the MCP conditions. In particular, that can be interpreted as a Mathematical Program with Equilibrium Constraints (MPEC). As nowadays optimization tools for the solution of the MPEC are severely limited in the size of problems they can handle, ad-hoc solution strategies have been explored in [11, 15, 31, 38].

In the present work, a fixed-point based algorithm is discussed for solving the non-associative limit analysis MCP relevant to 2D masonry block structures (see [29]). Basic observation is that a solution can be derived by considering a fixed-point problem, with the fixed-point map involving the solution of a simple associative limit analysis problem. Accordingly, the proposed procedure achieves to construct a non-associative limit analysis solution by iteratively solving straightforward associative limit analysis problems. Numerical results are presented for assessing accuracy, robustness and effectiveness of the proposed computational approach. Possible extensions of the present approach deal with the limit analysis of non periodic block masonry structures (e.g., see [5]) and of 3D block masonry structures, also undergoing large displacements (e.g., see [17, 36]).

The present paper is organized as follows. In Sect. 2 the non-associative limit analysis MCP is formulated. In Sect. 3, a simple two-blocks model problem is presented to highlight some features of the relevant MCP. In Sect. 4 the present fixed-point based solution algorithm is discussed. Numerical simulations are reported in Sect. 5 and conclusions are outlined in Sect. 6.

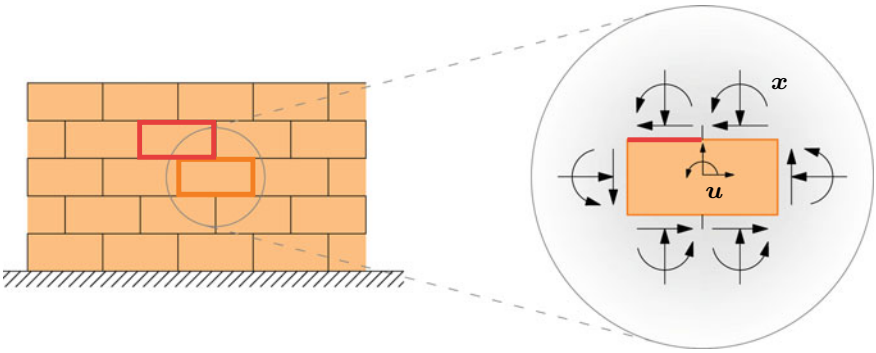

Fig. 1 Blocky model for dry-masonry structures. Block displacements $\boldsymbol{u}$ and block interface forces $\boldsymbol{x}$

2 Limit Analysis Problem for Block Structures

A system of 2D blocks is considered, as shown for example in Fig. 1, to model a typical dry-masonry block structure. It is assumed that the blocks are rigid and that they interact through Coulomb-frictional interfaces. Let b and c respectively denote the number of blocks and of interfaces, and let $\{O; x, y\}$ be a fixed Cartesian reference frame.

In case an associative flow law is considered for the frictional behavior of the interfaces, classical static and kinematic theorems of limit analysis hold. Specifically, assuming that external loads $\boldsymbol{f}_{\mathrm{d}} + \lambda \boldsymbol{f}_{\mathrm{l}}$ are applied at block centroids, with $\boldsymbol{f}_{\mathrm{d}}$ as dead loads, $\boldsymbol{f}_{\mathrm{l}}$ as basic live loads and λ as multiplier of live loads, the static theorem reads:

$$\begin{aligned} \max_{\lambda,\, \boldsymbol{x}} \quad & \lambda \\ \text{s.t.} \quad & \boldsymbol{E}\boldsymbol{x} + \boldsymbol{f}_{\mathrm{d}} + \lambda \boldsymbol{f}_{\mathrm{l}} = \boldsymbol{0} \\ & \boldsymbol{N}_{\mathrm{u}}^{T} \boldsymbol{x} \leq \boldsymbol{0}, \quad \boldsymbol{N}_{\mathrm{f}}^{T} \boldsymbol{x} \leq \boldsymbol{0}, \end{aligned} \tag{1}$$

where $\boldsymbol{x}$ is a $3c \times 1$ vector collecting interface shear forces, normal forces and bending moments, $\boldsymbol{E}$ is a $3b \times 3c$ block equilibrium operator, $\boldsymbol{N}_{\mathrm{u}}^{T}$ is a $3c \times 3c$ interface unilateral constraint operator and $\boldsymbol{N}_{\mathrm{f}}^{T}$ is a $2c \times 3c$ interface friction constraint operator (e.g., see [19]). Conversely, the kinematic theorem yields:

$$\begin{aligned} \min_{\boldsymbol{u},\, z_{\mathrm{u}} \geq \boldsymbol{0},\, z_{\mathrm{f}} \geq \boldsymbol{0}} \quad & -\boldsymbol{f}_{\mathrm{d}}^{T} \boldsymbol{u} \\ \text{s.t.} \quad & \boldsymbol{E}^{T} \boldsymbol{u} + \boldsymbol{N}_{\mathrm{u}} z_{\mathrm{u}} + \boldsymbol{N}_{\mathrm{f}} z_{\mathrm{f}} = \boldsymbol{0} \\ & 1 - \boldsymbol{f}_{\mathrm{l}}^{T} \boldsymbol{u} = 0, \end{aligned} \tag{2}$$

where $\boldsymbol{u}$ is a $3b \times 1$ vector collecting x-displacements, y-displacements and rotations (about block centroid) of blocks, $\boldsymbol{z}_{\mathrm{u}}$ is a $3c \times 1$ vector of interface unilateral

flow multipliers, and $\boldsymbol{z}_\mathrm{f}$ is a $2c \times 1$ vector of interface friction flow multipliers (e.g., see [19]). In a mechanical perspective, the static and kinematic theorems of limit analysis supply dual descriptions of collapse multipliers, respectively obtained by maximizing the load multipliers for which statically admissible equilibrium is feasible or by minimizing the (opposite of) resisting work related to kinematically admissible mechanisms. That duality also holds from an optimization standpoint, i.e. formulations (1) and (2) represent linear programming problems dual to each other, thus guaranteeing the existence of a unique collapse multiplier, which is the common optimal value of the two problems (e.g., see [11]).

Unfortunately, the duality of static and kinematic theorems is a consequence of the friction associative flow law. That is, of the fact that (up to a transposition) the same operator $\boldsymbol{N}_\mathrm{f}$, involving the interface friction angle φ, is used for expressing both the friction flow and the friction constraint. If a non-associative friction flow law is instead postulated to avoid spurious dilatancy, a distinct interface friction flow operator $\boldsymbol{V}_\mathrm{f}$ has to be considered in place of $\boldsymbol{N}_\mathrm{f}$, obtained by replacing the friction angle φ with the dilatancy angle ψ. As a consequence, static and kinematic problems are no longer uncoupled, and the limit analysis problem has to be formulated in the following form (e.g., see [3]):

$$
\begin{aligned}
&\boldsymbol{E}\boldsymbol{x} + \boldsymbol{f}_\mathrm{d} + \lambda \boldsymbol{f}_\mathrm{l} = \boldsymbol{0} \\
&\boldsymbol{E}^T\boldsymbol{u} + \boldsymbol{N}_\mathrm{u}\boldsymbol{z}_\mathrm{u} + \boldsymbol{V}_\mathrm{f}\boldsymbol{z}_\mathrm{f} = \boldsymbol{0} \\
&1 - \boldsymbol{f}_\mathrm{l}^T\boldsymbol{u} = 0 \\
&\boldsymbol{N}_\mathrm{u}^T\boldsymbol{x} \leq \boldsymbol{0}, \quad \boldsymbol{z}_\mathrm{u} \geq \boldsymbol{0}, \quad \boldsymbol{z}_\mathrm{u}^T\boldsymbol{N}_\mathrm{u}^T\boldsymbol{x} = \boldsymbol{0} \\
&\boldsymbol{N}_\mathrm{f}^T\boldsymbol{x} \leq \boldsymbol{0}, \quad \boldsymbol{z}_\mathrm{f} \geq \boldsymbol{0}, \quad \boldsymbol{z}_\mathrm{f}^T\boldsymbol{N}_\mathrm{f}^T\boldsymbol{x} = \boldsymbol{0}.
\end{aligned}
\tag{3}
$$

It is worth noticing that nonlinear (and nonconvex) complementarity constraints $(3)_{6,9}$ are here involved, thus turning the limit analysis into a Mixed Complementary Problem (MCP) (e.g., see [32]). In particular, excluding the simple case of associative friction flow law, it is affected by a ill-posedness issue related to the lack of uniqueness of the collapse multiplier. As several structural collapse states might exist, each attained for a distinct intensity of the live loads, a conservative possibility is to assume the minimum collapse multiplier as the actual target. Accordingly, the following optimization problem is introduced (e.g., see [11]):

$$
\begin{aligned}
&\min_{\lambda,\,\boldsymbol{x},\,\boldsymbol{u},\,\boldsymbol{z}_\mathrm{u},\,\boldsymbol{z}_\mathrm{f}} && \lambda, \\
&\text{s.t.} && \{\lambda,\ \boldsymbol{x},\ \boldsymbol{u},\ \boldsymbol{z}_\mathrm{u},\ \boldsymbol{z}_\mathrm{f}\} \text{ is a solution of (3)},
\end{aligned}
\tag{4}
$$

which is a special case of a Mathematical Program with Equilibrium Constraints (MPEC) (e.g., see [32]).

3 A Two-Blocks Model Problem

In this section a simple model problem is discussed to highlight some features of the non-associative limit analysis problem discussed in Sect. 2. As depicted in Fig. 2, a structure constituted by two blocks is considered, each block being characterized by width b and height h. The two blocks are supported on a base where unilateral and friction constraints, with friction coefficient $\mu = \tan\varphi$, hold. The same constraints are also enforced at the interface between the two blocks. It is assumed that each block is subjected to a dead load coinciding with its weight W, whereas a horizontal force of the same intensity is assumed as basic live load. Accordingly, a parametric analysis of the collapse multiplier λ of the basic live loads is conducted with respect to block slenderness $\eta = h/b$ and friction coefficient μ.

As a reference result, the associative limit analysis problem is initially considered. In such a case, a kinematic approach formulated as in Eq. (2) yields four possible collapse mechanisms, collected in Fig. 3:

- Panel (a) depicts a sliding mechanism with dilatancy, labelled as A1, corresponding to a collapse multiplier $\lambda = \mu$;
- Panel (b) depicts a single rocking mechanism with 'up' dilatancy, labelled as A2-1, corresponding to a collapse multiplier $\lambda = \left[\eta\left(1-\mu^2\right)+\mu\right]^{-1}$;
- Panel (c) depicts a single rocking mechanism with 'down' dilatancy, labelled as A2-2, corresponding to a collapse multiplier $\lambda = \left(1+2\mu^2\right)/\left[\eta\left(1+\mu^2\right)-\mu\right]$;

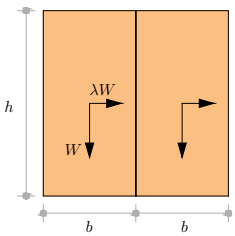

Fig. 2 A two-blocks model problem: geometry and loading conditions

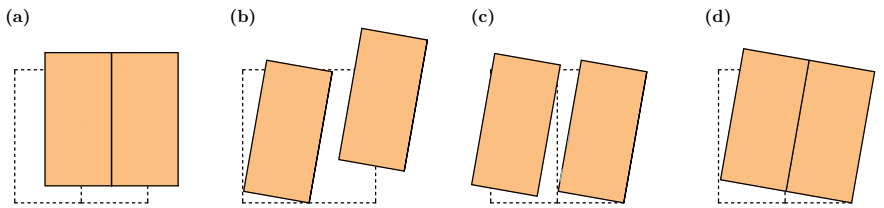

Fig. 3 A two-blocks model problem: collapse mechanisms for associative friction. **a** Sliding with dilatancy, labelled as A1, **b** single rocking with 'up' dilatancy, labelled as A2-1, **c** single rocking with 'down' dilatancy, labelled as A2-2, **d** coupled rocking, labelled as A3

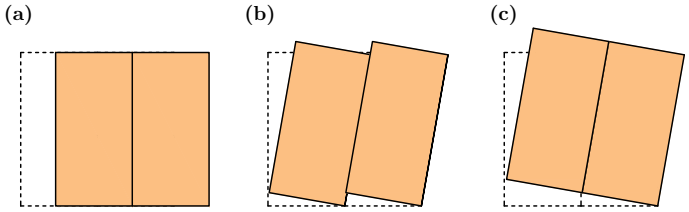

Fig. 4 A two-blocks model problem: collapse mechanisms for non-associative friction. **a** Sliding, labelled as NA1, **b** single rocking, labelled as NA2, **c** coupled rocking, labelled as NA3

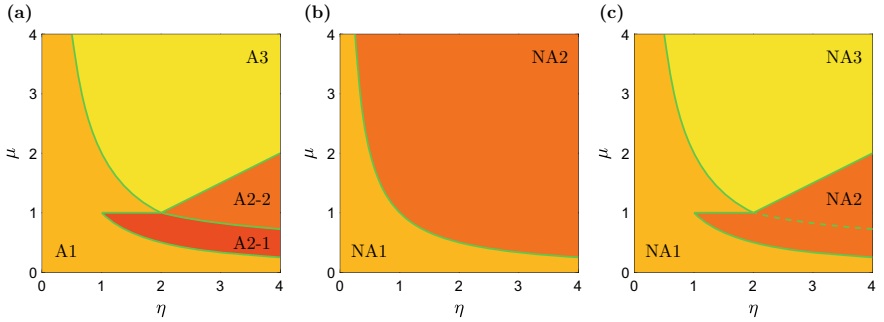

Fig. 5 A two-blocks model problem: partition of parameter space into regions corresponding to different collapse mechanisms, for **a** associative friction, **b** non-associative friction, minimum collapse multiplier, **c** non-associative friction, maximum collapse multiplier

– Panel (d) depicts a coupled rocking mechanism, labelled as A3, corresponding to a collapse multiplier $\lambda = 2/\eta$.

In Fig. 5a the partition of the parameter space into regions corresponding to the different collapse multipliers is shown, whereas in Fig. 6a the collapse multiplier is plotted versus the parameter space.

As for the non-associative limit analysis problem, here addressed under the assumption of vanishing dilatancy $\psi = 0$, the MCP (3) has to be solved. To such an aim, two distinct optimization problems are considered, consisting in the minimization formulation (4) and in the analogous maximization formulation obtained by replacing min with max in equation (4).

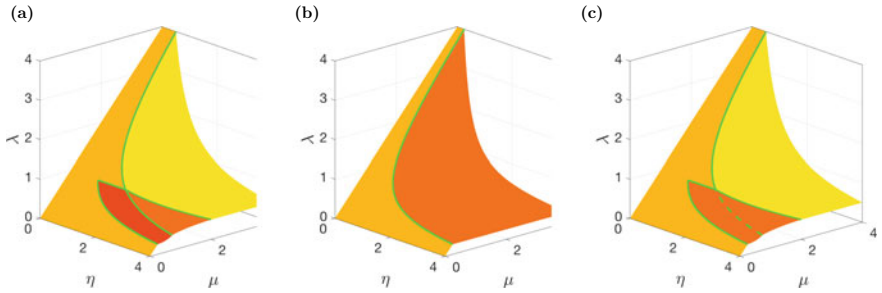

Fig. 6 A two-blocks model problem: collapse multiplier versus parameter space, for **a** associative friction, **b** non-associative friction, minimum collapse multiplier, **c** non-associative friction, maximum collapse multiplier

In detail, the minimum collapse multiplier is attained for:

- a sliding mechanism when $\mu \leq 1/\eta$, with collapse multiplier $\lambda = \mu$. That is labelled as NA1 and depicted in Fig. 4a;
- a single rocking mechanism when $\mu \geq 1/\eta$, with collapse multiplier $\lambda = 1/\eta$. That is labelled as NA2 and depicted in Fig. 4b.

Figures 5b and 6b respectively show the partition of the parameter space corresponding to the two mechanisms and the minimum collapse multiplier as a function of the parameters.

Regarding the maximum collapse multiplier, a more intricate situation emerges. In that case it is convenient to first discuss the plot of the collapse multiplier versus the parameter space, shown in Fig. 6c. Interestingly, the relevant results coincide with those pertaining to the associative limit analysis problem. However, the maximum collapse multiplier is attained by the collapse mechanisms illustrated in Fig. 5c. Specifically, the sliding mechanism with dilatancy A1 switches into the sliding mechanism NA1 and the two single rocking mechanism with 'up' and 'down' dilatancy, respectively A2-1 and A2-2, switch into the single rocking mechanism NA2. Of course, the coupled rocking mechanism A3 coincides with NA3, Fig. 4c, not implying any dilatancy.

For instance, let the point $\eta = 3$ and $\mu = 0.65$ be considered. In that case, the associative collapse multiplier corresponds to the mechanism A2-1 and results to be $\lambda = 0.41973$. That coincides with the maximum non-associative collapse multiplier, though the latter is attained by the mechanism NA2. Under different interface forces, the same mechanism NA2 also provides the minimum non-associative collapse multiplier, $\lambda = 1/3$, with a reduction of 25%. Accordingly, the present model problem exemplifies the following features of the non-associative limit analysis problem: (i) the MCP (3) can suffer from lack of uniqueness of the solution also in terms of collapse multipliers, and (ii) those collapse multipliers might be strictly (and significantly) lower than the associative one.

4 Numerical Solution Algorithm

State-of-the-art optimization tools for the solution of the MPEC (4) are severely limited in the size of problems they can handle, and their applicability to structures of practical interest is precluded (see [11]). On the other hand, also renouncing to global minimization and restricting to the solution of the MCP (3), a numerical solution strategy suitable to the limit analysis of real structures is still missing. As a matter of fact, it is nowadays possible to resort to numerical tools that make the solution of LP problems, also of large size, a straightforward task to accomplish. Accordingly, a novel solution strategy is here conceived to construct a solution of the MCP (3), whose main motive is to exploit the iterated solution of suitable associative limit analysis problems.

Basic idea of the algorithm is to assume the block interface normal forces $\boldsymbol{n}$ as iteration variables. Hence, let the current iterate $\boldsymbol{n}^*$ be given. Without loss of generality, it is assumed that all interfaces have the same friction and dilatancy angles, respectively φ and ψ. Then, an associative limit analysis problem is formulated, comprising the following cohesive-frictional criterion:

$$|\boldsymbol{t}| \leq -\boldsymbol{n} \tan\psi - \boldsymbol{n}^* (\tan\varphi - \tan\psi) , \tag{5}$$

where $\boldsymbol{t}$ collects the block interface shear forces. Accordingly, ψ is assumed as friction angle, whereas a vector of interface cohesions $-\boldsymbol{n}^* (\tan\varphi - \tan\psi)$ is prescribed. Interestingly, the solution of such LP problem fulfills the equilibrium condition $(3)_1$, the compatibility condition $(3)_2$ (in fact an associative flow law with friction angle ψ is assumed), the normalization condition $(3)_3$, and the unilateral constraint and complementarity conditions $(3)_{4–6}$. Contrarily, friction constraint and complementarity conditions $(3)_{7–9}$ are in general not satisfied, as being affected by the cohesive-frictional criterion under consideration. However, as shown in [29], the original Coulomb friction and the cohesive-frictional criterion result to be equivalent if the block interface normal forces $\boldsymbol{n}$ in solution of the LP problem coincide with $\boldsymbol{n}^*$.

The discussion above suggests to introduce the (continuous) function $\mathcal{F}$, mapping a given vector of block interface normal forces $\boldsymbol{n}^*$ into the block interface normal forces $\boldsymbol{n}$ in solution of the modified associative limit analysis problem. Consequently, a solution of the MCP (3) can be constructed by solving the following fixed-point problem:

$$\boldsymbol{n} := \mathcal{F}\left(\boldsymbol{n}^*\right) = \boldsymbol{n}^* . \tag{6}$$

Two concluding remarks are in order. First, problem (6) can be addressed by standard fixed-point iterations, or by a general-purpose derivative-free algorithm (e.g., see [22]). Second, in [15] a heuristic algorithm is proposed to construct a solution of the MPEC (4), by the iterated solution of associative limit analysis problems. As a main difference with respect to the present algorithm, in that case convergence is assumed when the collapse multiplier does not change in two successive iterations.

Contrarily, no check is therein required on the difference of block interface normal force, which might produce a not-negligible error in the friction admissibility condition (see [29]).

5 Numerical Simulations

In this section, numerical simulations are reported for assessing the performances of the present fixed-point algorithm. For comparison, other computational strategies available in the literature are also considered, specifically: the PATH solver proposed in [9], implementing a stabilized Newton method for the solution of general MCPs; the iterative relaxed nonlinear programming (NLP) algorithm proposed in [11], addressing the MPEC (4) by relaxation of the complementary constraints with a progressively reduced relaxation parameter; and the sequentially LP-based (SLP) algorithm proposed in [15], solving a succession of associative limit analysis sub-problems and controlling the difference of collapse multipliers in successive iterations.

Four benchmark problems are analyzed, modeling a round arch structure (Fig. 7a), an arch on buttresses structure (see [2]) (Fig. 8a), and two wall structures (see [3]) (Figs. 9a and 10a). Each structure is composed of equal-sized blocks (blocks having aspect ratio of $1:2$) and is supposed to be supported on a base, where unilateral and friction constraints are enforced. Blocks are subjected to vertical dead loads $\boldsymbol{f}_{\mathrm{d}}$ and

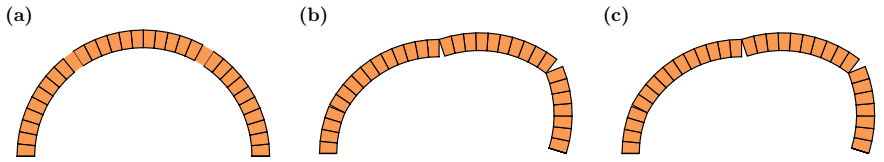

Fig. 7 Numerical simulations: round arch problem. **a** Geometry, **b** collapse mechanism with associative Coulomb friction and **c** collapse mechanism with non-associative Coulomb friction

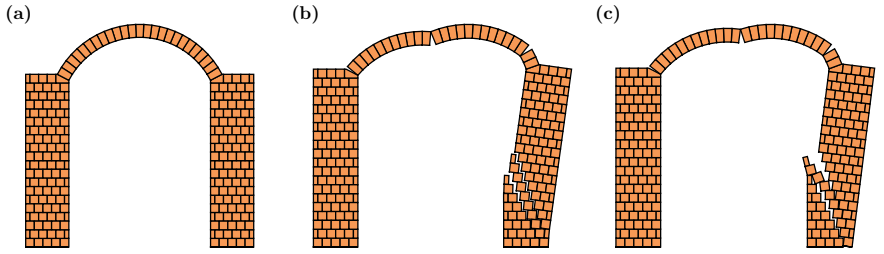

Fig. 8 Numerical simulations: arch on buttresses problem (see [2]). **a** Geometry, **b** collapse mechanism with associative Coulomb friction and **c** collapse mechanism with non-associative Coulomb friction

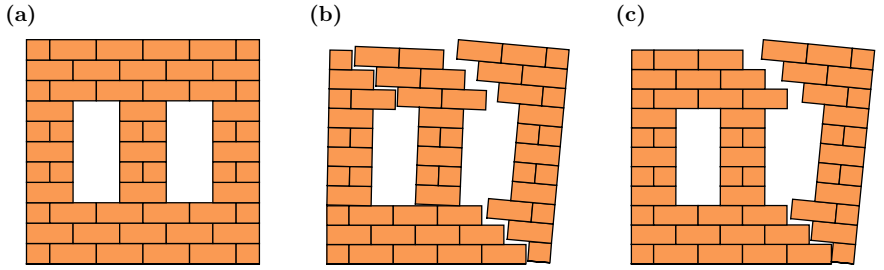

Fig. 9 Numerical simulations: 2×1 wall problem (see [3]). **a** Geometry, **b** collapse mechanism with associative Coulomb friction and **c** collapse mechanism with non-associative Coulomb friction

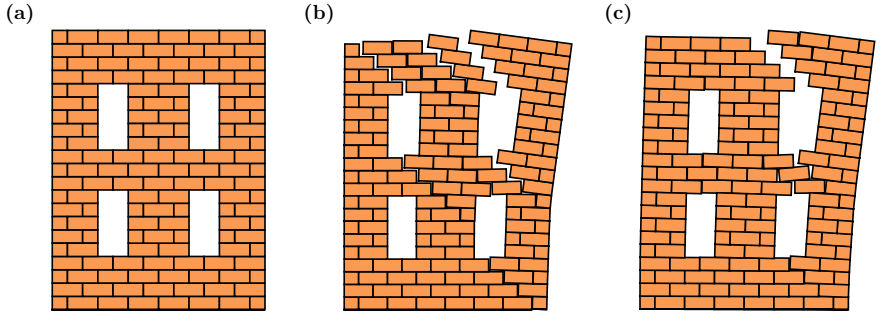

Fig. 10 Numerical simulations: 2×2 wall problem (see [3]). **a** Geometry, **b** collapse mechanism with associative Coulomb friction and **c** collapse mechanism with non-associative Coulomb friction

horizontal basic live loads $\boldsymbol{f}_1$, which are both proportional to the block volumes to mimic a pseudo-static earthquake loading. The material parameters are: the friction angle $\varphi = \arctan(0.65)$ and the dilatancy angle $\psi = 0$.

Panel (b) of Figs. 7–10 depicts the collapse mechanisms of the structures assuming associative friction flow law, whereas Panel (c) of the same figures depicts the collapse mechanisms predicted by the present fixed-point algorithm assuming non-associative friction flow law. The corresponding collapse multipliers are reported in Table 1, where also the results computed with the above competing algorithms are displayed.

Except for the round arch problem, whose collapse mechanism only involves unilateral failures, a reduced collapse multiplier corresponds to the non-associative friction flow law with respect to the associative one. Concerning the different estimation of non-associative collapse multipliers supplied by the algorithms under investigation, it can be noticed that the PATH solver converges to one of the (possibly many) solutions of the MCP (3), without any further specification. Conversely, the NLP algorithm explicitly seeks for a (local) minimum of the MPEC (4), thus justifying a demanding computational cost which precludes its use for large-size block structures (see [29]). On the other hand, the SLP and the present algorithms intend to construct a solution of the MCP (3) by iteratively addressing a static theorem formulation of modified associative limit analysis problems. Hence, those are methods

Table 1 Numerical simulations: collapse multiplier obtained by the present fixed-point algorithm. Corresponding values relevant to a in-house implementation of PATH algorithm (see [9]), NLP algorithm (see [11]) and SLP algorithm (see [15]) are reported (with × denoting lack of convergence)

Problem	Collapse multiplier				
	Associative	Non-associative			
		PATH	NLP	SLP	Present
Round arch	0.16034	0.16034	0.16034	0.16034	0.16034
Arch on buttresses	0.09085	0.08466	×	0.08195	0.08690
2 × 1 wall	0.33194	0.26374	0.26374	0.26374	0.26374
2 × 2 wall	0.34782	0.29725	0.29577	0.29649	0.29611

Table 2 Numerical simulations: relative errors in compatibility and friction admissibility conditions. For comparison, the corresponding values relevant to a in-house implementation of SLP algorithm (see [15]) are reported

Problem	Relative error in friction admissibility	
	SLP	Present
Round arch	0	0
Arch on buttresses	8.43×10^{-2}	1.84×10^{-4}
2 × 1 wall	4.56×10^{-2}	2.62×10^{-9}
2 × 2 wall	7.04×10^{-2}	1.97×10^{-4}

characterized by a reduced computational cost, which in turn cannot aim to a minimality property of the collapse multiplier. In order to highlight the main difference between the SLP and the present algorithms, the relevant solution quality has to be considered. Table 2 shows the relative error in the friction admissibility condition, defined as $\|(\boldsymbol{N}_{\mathrm{f}}^T\boldsymbol{x})_+\|/\|\boldsymbol{N}_{\mathrm{f}}^T\boldsymbol{x}\|$ (here $\|\cdot\|$ denotes the Euclidean norm and $(\cdot)_+$ the positive part operator), which results in the order of 10% for the SLP algorithm and much smaller for the present one. As that error is proportional to the difference of normal forces in successive iterations (see [29]), the improved solution quality of the proposed algorithm relies in explicitly assuming a convergence criterion on block interface normal forces, instead of collapse multipliers as in the SLP algorithm.

6 Conclusions

The limit analysis of dry-masonry block structures with non-associative Coulomb friction has been considered. Its formulation has been obtained as a Mixed Complementarity Problem, comprising equilibrium and compatibility equations pertaining to blocks, along with admissibility constraints (including Coulomb friction), flow laws (including non-associative Coulomb friction flow law) and Kuhn-Tucker

complementarity conditions relevant to block interfaces. A simple two-blocks model problem has been presented to remark well-known peculiar features of non-associative limit analysis problem, such as the lack of uniqueness of the collapse multiplier and the fact that non-associative collapse multipliers are smaller than the associative one. A fixed-point based algorithm has been proposed for constructing a solution of the non-associative limit analysis problem, obtained by iteratively solving straightforward associative limit analysis formulations. Numerical simulations have been presented to investigate the performances of the resulting procedure. Compared to computational costly available methods, which explicitly seek for the minimum collapse multiplier, the proposed algorithm gives reasonable estimation of the collapse multiplier. Conversely, compared to similar procedures, which aim at deriving a solution iteratively attacking associative limit analysis problems, the present approach guarantees accuracy of the solution, also with respect to the friction admissibility condition.

References

1. Addessi, D., Sacco, E.: A multi-scale enriched model for the analysis of masonry panels. Int. J. Solids Struct. **49**(6), 865–880 (2012). https://doi.org/10.1016/j.ijsolstr.2011.12.004
2. Alexakis, H., Makris, N.: Hinging mechanisms of masonry single-nave barrel vaults subjected to lateral and gravity loads. J. Struct. Eng. **143**(6), 04017,026 (2017). https://doi.org/10.1061/(ASCE)ST.1943-541X.0001762
3. Baggio, C., Trovalusci, P.: Limit analysis for no-tension and frictional three-dimensional discrete systems. Mech. Based Des. Struct. **26**(3), 287–304 (1998). https://doi.org/10.1080/08905459708945496
4. Baggio, C., Trovalusci, P.: Collapse behaviour of three-dimensional brick-block systems using non-linear programming. Struct. Eng. Mech. **10**(2), 181–195 (2000). https://doi.org/10.12989/sem.2000.10.2.181
5. Baraldi, D., Cecchi, A.: Discrete model for the collapse behavior of unreinforced random masonry walls. In: Di Tommaso, A., Gentilini, C., Castellazzi, G. (eds.) Mechanics of Masonry Structures Strengthened with Composite Materials II (MuRiCo5), Key Eng. Mater., vol. 747, pp. 3–10. Trans Tech Publications, Ltd., (2017). https://doi.org/10.4028/www.scientific.net/KEM.747.3
6. Braides, A., Nodargi, N.A.: Homogenization of cohesive fracture in masonry structures. Math. Mech. Solids. **25**(2), 181–200(2020). https://doi.org/10.1177/1081286519870222
7. Brasile, S., Casciaro, R., Formica, G.: Finite element formulation for nonlinear analysis of masonry walls. Comput. Struct. **88**(3–4), 135–143 (2010). https://doi.org/10.1016/j.compstruc.2009.08.006
8. Cervera, M., Chiumenti, M., Codina, R.: Mixed stabilized finite element methods in nonlinear solid mechanics Part II: Strain localization. Comput. Meth. Appl. Mech. Eng. **199**(37–40), 2571–2589 (2010). https://doi.org/10.1016/j.cma.2010.04.005
9. Dirkse, S.P., Ferris, M.C.: The path solver: a nommonotone stabilization scheme for mixed complementarity problems. Optim. Method Softw. **5**(2), 123–156 (1995). https://doi.org/10.1080/10556789508805606
10. Drucker, D.C.: Coulomb friction, plasticity, and limit loads. J. Appl. Mech. Trans. ASME **21**, 71–74 (1954)
11. Ferris, M.C., Tin-Loi, F.: Limit analysis of frictional block assemblies as a mathematical program with complementarity constraints. Int. J. Mech. Sci. **43**(1), 209–224 (2001). https://doi.org/10.1016/S0020-7403(99)00111-3

12. Fishwick, R.J.: Limit analysis of rigid block structures. Ph.D. thesis, Department of Civil Engineering, University of Portsmouth (1996)
13. Gambarotta, L., Lagomarsino, S.: Damage models for the seismic response of brick masonry shear walls. Part I: the mortar joint model and its applications. Earthquake Eng. Struct. Dyn. **26**(4), 423–439 (1997). https://doi.org/10.1002/(SICI)1096-9845(199704)26
14. Gatta, C., Addessi, D., Vestroni, F.: Static and dynamic nonlinear response of masonry walls. Int. J. Solids Struct. **155**, 291–303 (2018). https://doi.org/10.1016/j.ijsolstr.2018.07.028
15. Gilbert, M., Casapulla, C., Ahmed, H.M.: Limit analysis of masonry block structures with non-associative frictional joints using linear programming. Comput. Struct. **84**(13–14), 873–887 (2006). https://doi.org/10.1016/j.compstruc.2006.02.005
16. Heyman, J.: The stone skeleton. Int. J. Solids Struct. **2**(2), 249–279 (1966). https://doi.org/10.1016/0020-7683(66)90018-7
17. Intrigila, C., Nodargi, N.A., Bisegna, P.: Square cross vaults on spreading supports. In: Aguilar, R., Torrealva, D., Moreira, S., Pando, M., Ramos, L.F. (eds.) Structural Analysis of Historical Constructions, RILEM Bookseries, vol 18, pp. 1045–1053. Springer (2019). https://doi.org/10.1007/978-3-319-99441-3_113
18. Kooharian, A.: Limit analysis of voussoir (segmental) and concrete archs. Proc. Am. Concrete Inst. **89**, 317–328 (1952)
19. Livesley, R.K.: Limit analysis of structures formed from rigid blocks. Int. J. Numer. Methods Eng. **12**(12), 1853–1871 (1978). https://doi.org/10.1002/nme.1620121207
20. Lo Bianco, M., Mazzarella, C.: Sulla sicurezza sismica delle strutture in muratura a blocchi. In: Proceedings of Stato dell'arte in Italia sulla meccanica delle murature, pp. 577–596 (1985)
21. Milani, G.: Simple homogenization model for the non-linear analysis of in-plane loaded masonry walls. Comput. Struct. **89**(17–18), 1586–1601 (2011). https://doi.org/10.1016/j.compstruc.2011.05.004
22. Morini, B., Porcelli, M., Toint, P.L.: Approximate norm descent methods for constrained nonlinear systems. Math. Comput. **87**, 1327–1351 (2018). https://doi.org/10.1090/mcom/3251
23. Nodargi, N.A.: An overview of mixed finite elements for the analysis of inelastic bidimensional structures. Arch. Comput. Method Eng. **26**(4), 1117–1151 (2019). https://doi.org/10.1007/s11831-018-9293-0
24. Nodargi, N.A., Bisegna, P.: State update algorithm for isotropic elastoplasticity by incremental energy minimization. Int. J. Numer. Methods Eng. **105**(3), 163–196 (2015). https://doi.org/10.1002/nme.4966
25. Nodargi, N.A., Bisegna, P.: A novel high-performance mixed membrane finite element for the analysis of inelastic structures. Comput. Struct. **182**, 337–353 (2017). https://doi.org/10.1016/j.compstruc.2016.10.002
26. Nodargi, N.A., Bisegna, P.: A mixed finite element for the nonlinear analysis of in-plane loaded masonry walls. Int. J. Numer. Methods Eng. **120**(11), 1227–1248 (2019). https://doi.org/10.1002/nme.6179
27. Nodargi, N.A., Artioli, E., Caselli, F., Bisegna, P.: State update algorithm for associative elastic-plastic pressure-insensitive materials by incremental energy minimization. Fract. Struct. Integrity **29**, 111–127 (2014). https://doi.org/10.3221/IGF-ESIS.29.11
28. Nodargi, N.A., Caselli, F., Artioli, E., Bisegna, P.: A mixed tetrahedral element with nodal rotations for large-displacement analysis of inelastic structures. Int. J. Numer. Methods Eng. **108**(7), 722–749 (2016). https://doi.org/10.1002/nme.5232
29. Nodargi, N.A., Intrigila, C., Bisegna, P.: A variational-based fixed-point algorithm for the limit analysis of dry-masonry block structures with non-associative coulomb friction. Int. J. Mech. Sci. **161–162**(105), 078 (2019). https://doi.org/10.1016/j.ijmecsci.2019.105078
30. Oliveira, D.V., Lourenço, P.B.: Implementation and validation of a constitutive model for the cyclic behaviour of interface elements. Comput. Struct. **82**(17–19), 1451–1461 (2004). https://doi.org/10.1016/j.compstruc.2004.03.041
31. Orduña, A., Lourenço, P.B.: Three-dimensional limit analysis of rigid blocks assemblages. Part I: Torsion failure on frictional interfaces and limit analysis formulation. Int. J. Solids Struct. **42**(18–19), 5140–5160 (2005). https://doi.org/10.1016/j.ijsolstr.2005.02.010

32. Papadimitriou, C.H., Steiglitz, K.: Combinatorial Optimization: Algorithms and Complexity. Mathematical Optimization. Prentice Hall, Mineola, New York (1998)
33. Pelà, L., Cervera, M., Roca, P.: Continuum damage model for orthotropic materials: application to masonry. Comput. Meth. Appl. Mech. Eng. **200**(9–12), 917–930 (2011). https://doi.org/10.1016/j.cma.2010.11.010
34. Pelà, L., Cervera, M., Roca, P.: An orthotropic damage model for the analysis of masonry structures. Constr. Build Mater. **41**, 957–967 (2013). https://doi.org/10.1016/j.conbuildmat.2012.07.014
35. Petracca, M., Pelà, L., Rossi, R., Oller, S., Camata, G., Spacone, E.: Regularization of first order computational homogenization for multiscale analysis of masonry structures. Comput. Mech. **57**(2), 257–276 (2016). https://doi.org/10.1007/s00466-015-1230-6
36. Portioli, F., Cascini, L.: Large displacement analysis of dry-jointed masonry structures subjected to settlements using rigid block modelling. Eng. Struct. **148**, 485–496 (2017). https://doi.org/10.1016/j.engstruct.2017.06.073
37. Radenkovic, D.: Théorèmes limites pour un materiau de Coulomb à dilatiation non standardisée. C R Acad. Sci. Paris **252**, 4103–4104 (1961)
38. Trentadue, F., Quaranta, G.: Limit analysis of frictional block assemblies by means of fictitious associative-type contact interface laws. Int. J. Mech. Sci. **70**, 140–145 (2013). https://doi.org/10.1016/j.ijmecsci.2013.02.012

Homogenization of Ductile Porous Materials by Limit and Shakedown Analysis

Zhang Jin, Abdelbacet Oueslati, Wanqing Shen, and Géry de Saxcé

Abstract This paper is a survey of recent trends in the poroplasticity combined with Direct methods. Using the hollow sphere model as Reference Elementary Volume (REV) with a matrix obeying von Mises microscopic plastic yield criterion, a stress variational model (SVM), dual of Gurson's one, has been proposed to find by the Limit Analysis a macroscopic criterion depending on the porosity. Remarkably, it depends on the third invariant J_3 but only through its sign. Applying the normality law to the macroscopic criterion, the evolution of porosity with respect to the stress triaxiality exhibit clear discrepancies with Gurson's one which is known to overestimate the variation of the porosity. Some extensions has been proposed to obtain a continuous dependence with respect to J_3 through Lode's angle, to improve the strength value for the pure deviatoric loading. Thanks to the bipotential formulation, a macroscopic yield criterion was also proposed for a non associated Drucker-Prager matrix. Using the Shakedown Analysis, the method has been extended to the repeated variable loadings to obtain a fatigue criterion for the porous materials. It depends on the porosity but also strongly on Poisson's coefficient. The general case involving shear effects with any cyclic load fluctuations ranging from the pulsating load to the alternating one is considered. The macroscopic criteria depend on the first and second macroscopic stress invariants and the sign of the third one.

Z. Jin
Key Laboratory of Ministry of Education for Geomechanics and Embankment Engineering, Hohai University, Nanjing, China
e-mail: chelseazhangjin@gmail.com

A. Oueslati
Univ. Lille, CNRS, Centrale Lille, UMR 9013 – LaMcube – Laboratoire de mécanique multiphysique multiéchelle, 59000 Lille, France
e-mail: abdelbacet.oueslati@univ-lille.fr

W. Shen · G. de Saxcé (✉)
LaMcube, Lille, France
e-mail: gery.de-saxce@univ-lille.fr

W. Shen
e-mail: wanqing.shen@polytech-lille.fr

A. A. Pisano et al. (eds.), *Direct Methods*, Lecture Notes in Applied and Computational Mechanics 95, https://doi.org/10.1007/978-3-030-48834-5_6

1 Introduction

The direct methods may be applied to the structural mechanics but also to the homogenization of porous materials:

- **Limit analysis**: when the loading is proportional to find yield criteria depending on the porosity,
- **Shakedown analysis**: when the loading is repeated variable to find fatigue criteria for the porous materials [8, 13].

The methodology developped is based on the following key points:

- we modelize the Reference Elementary Volume (REV),
- we choose **trial fields** to capture the main physical effects,
- we apply the **variational formulations** to obtain approximations,
- we deduce the analytical form of the **strength criterion** of the homogenized material.

Although the obtained expression is approximative, it may be useful for experimeters as source of inspiration. They can introduce additional parameters of which the values are determined to fit better the experimental testing data [22, 23].

1.1 A Fragrance of Poroplasticity

Before getting to the heart of the matter, it is worth to recall the basic tools of homogenization in poroplasticity. At Fig. 1, we consider a hollow sphere, of which the Reference Elementary Volume V is enclosed by a surface ∂V, made up of a spherical cavity V_f embedded in a homothetic cell V_M of a given rigid-plastic material for Limit analysis or an elasto-plastic material for Shakedown analysis. S_f denotes the void-matrix interface. The inner and outer radii are respectively denoted a and b, giving the void volume fraction $f = V_f/V = (a/b)^3 < 1$. This simple modelling, called hollow sphere model, turned out to be sufficiently accurate, the analytical results being validated by numerical simulations with fine meshes.

The porosity and the constitutive law of the matrix being given in terms of microscopic fields of stress $\boldsymbol{\sigma}$ and plastic strain rate $\boldsymbol{d}$, our main issue is to deduce the corresponding ones of the REV in terms of macroscopic fields $\boldsymbol{\Sigma}$, $\boldsymbol{D}$ obtained as averages:

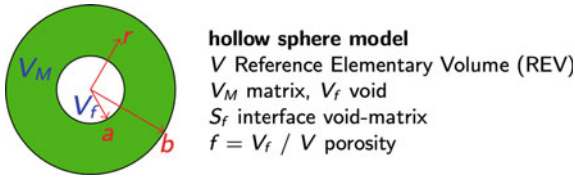

Fig. 1 Hollow sphere model

$$\boldsymbol{D} = \frac{1}{V}\int_V \boldsymbol{d}\, dV, \qquad \boldsymbol{\Sigma} = \frac{1}{V}\int_V \boldsymbol{\sigma}\, dV = \frac{1}{V}\int_{\partial V} (\boldsymbol{\sigma}\cdot\boldsymbol{n})\otimes\boldsymbol{x}\, dS \tag{1}$$

For $\boldsymbol{\Sigma}$, the last expression where $\boldsymbol{n}$ is the unit outward normal to ∂V and $\boldsymbol{x}$ is the position vector, obtained for statically admissible fields, is useful to calculate more simply the average by integration on a surface instead of a volume.

Considering the mean stress $\sigma_m = \frac{1}{3}\,Tr(\boldsymbol{\sigma})$, the deviatoric stress $\boldsymbol{\sigma}_d$, von Mises comparison stress $\sigma_e = \sqrt{\frac{2}{3}\boldsymbol{\sigma}_d : \boldsymbol{\sigma}_d}$, the macroscopic counterparts and the third invariant are:

$$\Sigma_m = \frac{1}{3}\,Tr(\boldsymbol{\Sigma}),\ \ \Sigma_e = \sqrt{\frac{2}{3}\boldsymbol{\Sigma}_d : \boldsymbol{\Sigma}_d},\ \ J_3 = \det(\boldsymbol{\Sigma}_d)$$

For the boundary conditions, we claim that S_f is stress free and the velocity $\bar{\boldsymbol{v}}(\boldsymbol{x}) = \boldsymbol{D}\,\boldsymbol{x}$ is imposed on ∂V. According to Hill's lemma, we have for any statically admissible stress field:

$$\frac{1}{V}\int_{\partial V} (\boldsymbol{\sigma}\cdot\boldsymbol{n})\cdot\bar{\boldsymbol{v}}\, dS = \boldsymbol{D} : \boldsymbol{\Sigma}$$

1.2 Motivations

The microscopic plastic yielding criterion for the matrix:

$$F(\boldsymbol{\sigma}) \le 0$$

being given and using the hollow sphere model, our goal is to deduce the macroscopic strength criterion (plastic yielding or fatigue):

$$\mathscr{F}(\boldsymbol{\Sigma}, f) \le 0$$

representing the plastic behaviour of the homogenized material and depending on the void volume fraction f. The choice of the hollow sphere as REV is motivated by the fact that its geometry is simpler as the one of the classical parallelepiped because of the central symmetry. Even so, the functional space where are living the stress field being of infinite dimension, it would be illusory to find the exact solution. Hence we use a variational method that gives the best solution, according to the assumptions made to obtain simplifications making workable the calculus. However, some calculations are very cumbersome then skipped. In this paper, emphasis is put on ideas and assumptions rather than on technicalities.

2 Limit Analysis

2.1 Stress Variational Model (SVM) for von Mises Porous Medium

Starting from von Mises model for the matrix

$$F(\boldsymbol{\sigma}) = \sigma_e(\boldsymbol{\sigma}) - \sigma_0 \leq 0$$

and using Markov's velocity principle, Gurson proposed in a pionnering work the following macroscopic yield criterion:

$$\left(\frac{\Sigma_e}{\sigma_0}\right)^2 + 2f\ \cosh\left(\frac{3\,\Sigma_m}{2\,\sigma_0}\right) - (1+f^2) = 0\,.$$

Recently, we developped the dual approach based on Hill's stress principle particularized to homogenization:

$$\min_{\boldsymbol{\sigma}\in\mathscr{S}_a}\left(\frac{1}{V}\int_{V_M}\varphi^*(\boldsymbol{\sigma})\,dV - \boldsymbol{D}:\boldsymbol{\Sigma}\right) = \min_{\boldsymbol{\sigma}\in\mathscr{S}_a \quad and \quad F(\boldsymbol{\sigma})\leq 0\ in\ V_M}(-\boldsymbol{D}:\boldsymbol{\Sigma})$$

where φ^* is the stress pseudopotential of plasticity (indicatory function of the elastic domain) and the minimum value is taken on the set of statically admissible fields:

$$\mathscr{S}_a = \left\{\boldsymbol{\sigma} \quad | \quad div\,\boldsymbol{\sigma} = \mathbf{0} \quad in\ V_M, \quad \boldsymbol{\sigma}\cdot\boldsymbol{n} = \mathbf{0} \quad on\ S_f\right\}$$

The functional and the equilibrium equations are linear. The main difficulty lies in the yield criterion which is non linear and difficult to satisfy a priori. Our strategy is to relax it, enforcing only the yield criterion "in the mean":

$$\mathscr{F}(\boldsymbol{\Sigma}) = \frac{1}{V}\int_{V_M} F(\boldsymbol{\sigma})\,dV \leq 0 \tag{2}$$

that leads to a saddle point problem:

$$\max_{\dot{\Lambda}\geq 0}\min_{\boldsymbol{\sigma}\in\mathscr{S}_a}\left(\mathscr{L}(\boldsymbol{\sigma},\dot{\Lambda}) = \dot{\Lambda}\frac{1}{V}\int_{V_M} F(\boldsymbol{\sigma})\,dV - \mathbf{D}:\boldsymbol{\Sigma}\right)$$

providing only a quasi-lower bound. The Lagrange multiplier $\dot{\Lambda}$ is interpreted as the plastic multiplier of the macroscopic yielding law.

The next step consist in choosing a trial field to capture the main physical effects:

$$\boldsymbol{\sigma} = \boldsymbol{\sigma}^{(1)} + \boldsymbol{\sigma}^{(2)}$$

where:

- The first part is the exact trial stress field for the pure hydrostatic loading (easy to calculate thanks to the central symmetry), expressed here in spherical coordinates:

$$\boldsymbol{\sigma}^{(1)} = -A_0 \left(\ln\left(\frac{a}{r}\right) \cdot \mathbf{1} - \frac{1}{2}(\mathbf{e}_\theta \otimes \mathbf{e}_\theta + \mathbf{e}_\phi \otimes \mathbf{e}_\phi) \right) \tag{3}$$

- completed by an additional part to capture the shear effects, expressed here in cylindrical coordinates:

$$\boldsymbol{\sigma}^{(2)} = A_1 \, (\mathbf{e}_\rho \otimes \mathbf{e}_\rho + \mathbf{e}_\phi \otimes \mathbf{e}_\phi) + A_2 \, \mathbf{e}_z \otimes \mathbf{e}_z \tag{4}$$

The latter part, uniform on the REV, is a too poor approximation to satisfy the equilibrium condition $\boldsymbol{\sigma n} = 0$ on the void boundary S_f, then we relaxe it, satisfying it also in the sense of a average weighted by the position:

$$Tr(\frac{1}{V} \int_{S_f} (\boldsymbol{\sigma n}) \otimes \boldsymbol{x} dS) = 0$$

Introducing the effective stresses:

$$\tilde{\Sigma}_e = \frac{\Sigma_e}{1-f} = 3 \mid A_1 \mid, \quad \tilde{\Sigma}_m = -\frac{3\Sigma_m}{2 \ln f} = \frac{A_0}{2}, \quad \tilde{J}_3 = \frac{J_3}{(1-f)^3} = -2A_1^3$$

that appear naturally in the calculation, we obtained a new macroscopic criterion [4]:

$$\mathscr{F}(\boldsymbol{\Sigma}, f) = \sqrt{\tilde{\Sigma}_e^2 + \tilde{\Sigma}_m^2} \; \mathscr{J} \left(27 \frac{\tilde{J}_3}{\tilde{\Sigma}_e^3} \frac{\tilde{\Sigma}_e \tilde{\Sigma}_m}{\tilde{\Sigma}_e^2 + \tilde{\Sigma}_m^2} \right) - \sigma_0 \; \leq 0$$

where the function $\mathscr{J}$ is smooth over $[-1, 1]$ with extreme values $\mathscr{J}_{max} = \mathscr{J}(0) = 1$, $\mathscr{J}_{min} = \mathscr{J}(1) = 0.976$ over $[0, 1]$ and $\mathscr{J}_{min} = \mathscr{J}(-1) = 0.962$ over $[-1, 0]$.

In [2], Cazacu and coworkers success to obtain a kinematically based criterion without Gurson approximation. This allowed them to point out and to address the role of the third invariant J_3 of the stress deviator. The present criterion can be viewed as a statical counterpart of this result. In our approach, J_3 appears naturally because it is derived from a stress-based Limit Analysis. Due to the approximations introduced for the analytical derivation, the new criterion SVM could be seen just as a quasi-lower bound. However, it still preserves the exact solution of the hollow sphere subjected

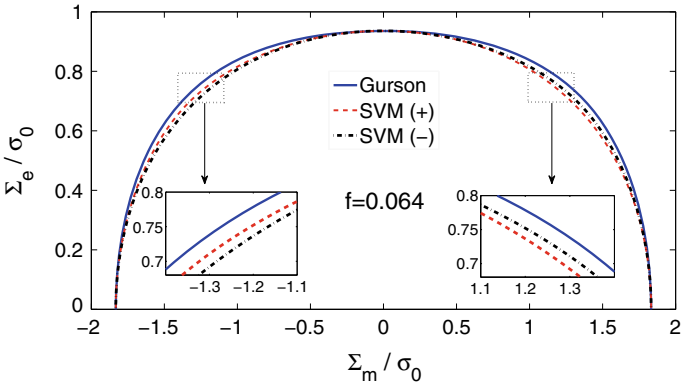

Fig. 2 Comparison between the obtained yield surfaces and Gurson's model [11], porosité: 0.064

to a hydrostatic loading, $\Sigma_m/\sigma_0 = -2/3ln(f)$, and leads to the same expression of the limit pure shear load as that given by Gurson criterion, $\Sigma_e/\sigma_0 = 1 - f$.

Due to the dependance of the SVM criterion on J_3 through its sign, there are two yield surfaces with the notations of SVM(+) and SVM(−) corresponding to $J_3 > 0$ and $J_3 < 0$, respectively, plotted on Fig. 2 for the porosity value $f = 0.064$ and compared to Gurson model. It is noted that the SVM criterion presents some slight differences with Gurson one, the surfaces predicted by SVM being strictly "below" Gurson's one, simultaneously coincident with them for hydrostatic loading (exact result) and pure deviatoric one (as mentioned before).

Due to the role played by the sign of third invariant in the SVM criterion, it is interesting to derive the macroscopic flow rule giving the plastic deformation (through its volumetric and deviatoric parts) by means of the normality rule:

$$D_e = \dot{\Lambda}\frac{\partial \mathscr{F}}{\partial \Sigma_e}, \qquad D_m = \frac{1}{3}\dot{\Lambda}\frac{\partial \mathscr{F}}{\partial \Sigma_m}$$

Figure 3 illustrates the evolution of porosity given as function of stress triaxiality $T = \Sigma_m/\Sigma_e$. It is noted that despite the few influence of the sign of third invariant on the macroscopic criterion, a noticeable effect is noted for the porosity variation. The results are also compared with that predicted by the Gurson model. Clear differences are observed, particularly for high stress triaxialities for which the Gurson model is known to overestimate the variation of the porosity. It is worth to observe that such difference is obtained only using the exact analytical expression of the function $\mathscr{J}$ occuring in the SVM criterion. Then, although its value is closed to 1, it would not be a good idea to simplify the criterion by replacing it by the unity.

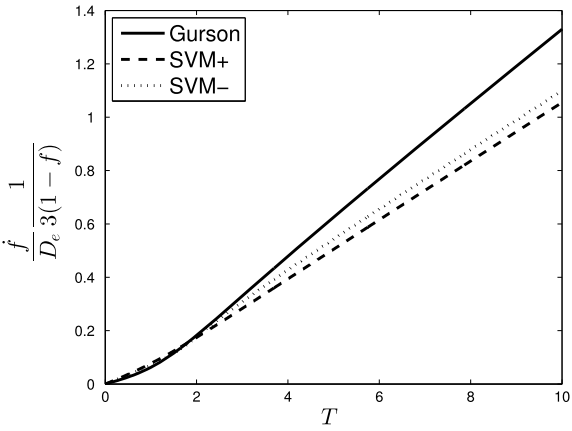

Fig. 3 Evolution of porosity as function of the stress triaxiality for initial porosity $f = 0.064$. Comparison between SVM predictions and the ones of Gurson's model

2.2 *Various Extensions*

It should be underlined that the SVM criterion depends on the third invariant J_3 through its sign. This restriction can be removed by considering the general case of non-axisymmetric loadings. Then we replace the homogeneous deviatoric part (4) for capturing the shear effect by:

$$\boldsymbol{\sigma}^{(2)} = B_1(\boldsymbol{e}_x \otimes \boldsymbol{e}_x - \boldsymbol{e}_z \otimes \boldsymbol{e}_z) + B_2(\boldsymbol{e}_y \otimes \boldsymbol{e}_y - \boldsymbol{e}_z \otimes \boldsymbol{e}_z),$$

The new criterion proposed in [5]:

$$\mathscr{F}(\boldsymbol{\Sigma}, f) = \sqrt{\tilde{\Sigma}_e^2 + \tilde{\Sigma}_m^2}\left(1 - \frac{\tilde{\Sigma}_m^2\tilde{\Sigma}_e^2}{10\,(\tilde{\Sigma}_m^2\tilde{\Sigma}_e^2)^2} - \frac{\tilde{\Sigma}_m^3\tilde{\Sigma}_e^3}{10\,(\tilde{\Sigma}_m^2\tilde{\Sigma}_e^2)^3}\cos(3\theta_L)\right) - \sigma_0 \leq 0$$

depends continuously on J_3 through the Lode angle θ_L and not only on the two signs corresponding to the values 0° and 60°. Five yield loci are studied on Fig. 4 with different values of Lode angle: $\theta_L = 0$, 15°, 30°, 45° and 60°, while the first and the last ones are corresponding to the macroscopic model obtained from the axisymmetric trial stress field. It can be observed that the yield surfaces obtained from other values of the Lode angle are absolutely between the above two ones.

Another extension is based on the following remarks. The first part $\boldsymbol{\sigma}^{(1)}$ given by (3) verifies obviously the stress condition $\boldsymbol{\sigma} \cdot \boldsymbol{n} = \boldsymbol{0}$ on the pore boundary S_f, while the second one $\boldsymbol{\sigma}^{(2)}$ given by (4) is too poor to do it exactly and it was relaxed in [4]. We overcome this pitfall by enhancing the previous trial field with a new additional term $\boldsymbol{\sigma}^{(3)}$ in order to fulfill the stress condition exactly. We claim that the new trial stress field $\boldsymbol{\sigma} = \boldsymbol{\sigma}^{(1)} + \boldsymbol{\sigma}^{(2)} + \boldsymbol{\sigma}^{(3)}$ satisfies the two conditions:

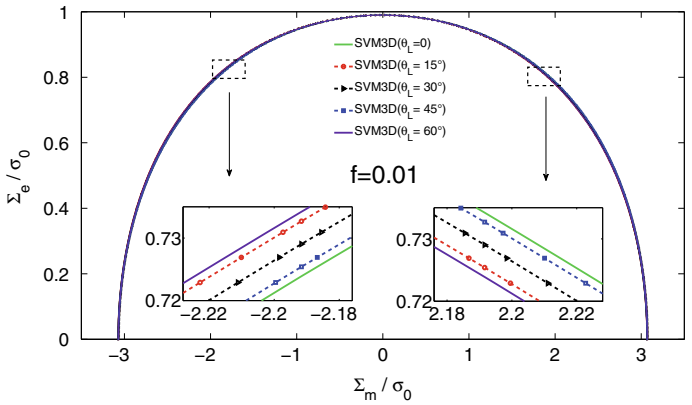

Fig. 4 Obtained yield surfaces for 5 values of Lode angle: $\theta_L = 0, 15°, 30°, 45°$ and $60°$. Porosity: $f = 0.01$

- it is statically admissible,
- the deviatoric parts $\boldsymbol{s}^{(1)}$, $\boldsymbol{s}^{(3)}$ of $\boldsymbol{\sigma}^{(1)}$, $\boldsymbol{\sigma}^{(3)}$ are orthogonal:

$$\boldsymbol{s}^{(1)} : \boldsymbol{s}^{(3)} = 0$$

This last condition is required in order to eliminate coupling between the first and third parts of $\boldsymbol{\sigma}$ in the equivalent stress and to do not have too difficulty in calculating the integral in (2). We skip cumbersome calculations. Finally, the additional term reads:

$$\boldsymbol{\sigma}^{(3)} = A_2 \left(S(r)\left(1 + 3\cos(2\theta)\right)\mathbf{1} + K(r)\sin(2\theta)(e_r \otimes e_\theta + e_\theta \otimes e_r)\right)$$

where:

$$S(r) = \frac{\sqrt{15}}{30}\frac{a^{3/2}}{r^{3/2}}\left(-9\sin\left(\frac{\sqrt{15}}{2}\ln(\frac{a}{r})\right) + \sqrt{15}\cos\left(\frac{\sqrt{15}}{2}\ln(\frac{a}{r})\right)\right)$$

$$K(r) = \frac{\sqrt{15}}{10}\frac{a^{3/2}}{r^{3/2}}\left(-15\cos\left(\frac{\sqrt{15}}{2}\ln(\frac{a}{r})\right) - 7\sqrt{15}\sin\left(\frac{\sqrt{15}}{2}\ln(\frac{a}{r})\right)\right)$$

Finally, the macroscopic criterion reads [20]:

$$\mathscr{F}(\boldsymbol{\Sigma}, f) = \sqrt{\frac{P_0(f)}{(1 - f + P_1)^2}\Sigma_e^2 + \frac{9}{4\ln(f)^2}\Sigma_m^2}\,\xi(\zeta) - \sigma_0 \leq 0$$

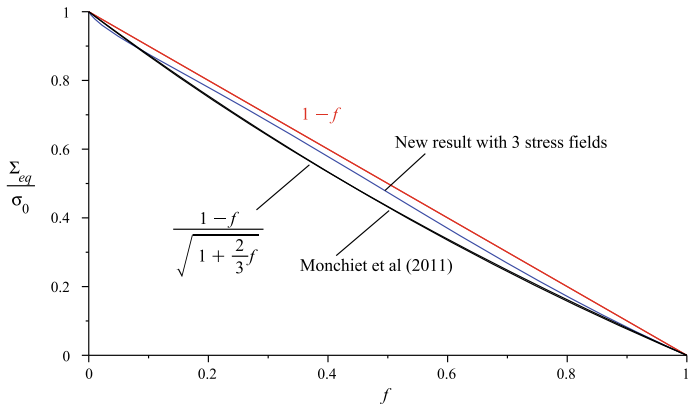

Fig. 5 Comparison of the values of the equivalent stress proposed by new criteria and the ones proposed by Gurson $(1-f)$, Ponte-castañeda [18], Monchiet et al. [17] $((1-f)/\sqrt{1+2f/3})$, as function of the porosity f

where

$$\zeta = sign(J_3)\frac{\dfrac{3\Sigma_m \Sigma_e \cdot \sqrt{P_0(f)}}{(1-f+P_1)\ln(f)}}{\dfrac{P_0(f)}{(1-f+P_1)^2}\Sigma_e^2 + \dfrac{9}{4\ln(f)^2}\Sigma_m^2}$$

and the parameter P_0 which is depending on spherical coordinates is approximated by:

$$P_0(r,\theta) \simeq P_0(f) = \frac{1+\frac{11}{25}f - \frac{64}{75}f\ln(f) - \frac{2}{25}\sqrt{f}N + \frac{2}{375}fM}{1-f}$$
$$M = 105\cos\left(\frac{\sqrt{15}}{3}\ln(f)\right) + 17\sqrt{15}\sin\left(\frac{\sqrt{15}}{3}\ln(f)\right)$$
$$N = 25\cos\left(\frac{\sqrt{15}}{6}\ln(f)\right) + \sqrt{15}\sin\left(\frac{\sqrt{15}}{6}\ln(f)\right)$$

The function $\xi\,(\zeta)$ is given by:

$$\xi(\zeta) = \begin{cases} \dfrac{\sqrt{6}(2\sqrt{P_0}-\zeta)}{24\sqrt{\zeta}\,P_0^{1/2}}\ln\left(\dfrac{\sqrt{2\zeta(\zeta+P_0^{1/2})}+\sqrt{3}\zeta}{\sqrt{2\zeta(\zeta+P_0^{1/2})}-\sqrt{3}\zeta}\right) + \frac{1}{2}\dfrac{\sqrt{P_0^{1/2}+\zeta}}{P_0^{1/4}}, & \zeta \geq 0 \\ \dfrac{(2\sqrt{P_0}-\zeta)\arcsin\left(\frac{\sqrt{-3\zeta}}{\sqrt{2\sqrt{P_0}-\zeta}}\right)}{2P_0^{1/4}\sqrt{-6\zeta}} + \frac{1}{2}\dfrac{\sqrt{P_0^{1/2}+\zeta}}{P_0^{1/4}}, & \zeta \leq 0 \end{cases}$$

This fully statically admissible model is expected to give a much more satisfactory value of the strength for the pure deviatoric case. In Fig. 5, the new result with three field is ploted and compared to previous models.

Finally, we extended the SVM model for a matrix with a non associated Drucker-Prager model where the microscopic criterion is depending also on the first invariant. The non associativity of the rule is represented thanks to the bipotential theory. Unlike

the classical presentation of the non associated constitutive laws by means of the yield function and the plastic potential, the bipotential formulation naturally opens into a variational formulation, paving the way to an extension of the SVM method to non associated laws. Combining with the Limit Analysis, we obtained in [6] a closed form analytical criterion generalizing the criterion obtained by Guo and coworkers for the associated case in [10].

3 Shakedown Analysis

3.1 State of the Art

Experimental observations on fatigue of porous materials. Although the bibliography on the ductile failure of porous materials under monotonic loads is abundant and renewed, there is a few papers dealing with the modeling of ductility under cyclic loadings and most of them concern micromechanics-based numerical approaches. Available experiments regarding structures made up with ductile metals [12, 19] have revealed that fracture strains under cyclic loads are significantly lower than the ones reached under monotonic load conditions.

Numerical simulations. Basing upon incremental finite element simulations of the elastic plastic response of a hollow cylinder subjected to repeated loads, Gilles al [9] have suggested that this strength reduction under cyclic conditions is due to a gradual increase void growth during each cycle, an occurrence called 'ratcheting of porosity'. Later, this observation has been confirmed by Devaux et al. [7] through numerical computations similar to those of Gilles et al., but with a better control of the triaxiality. Also, the authors have demonstrated that classical Gurson's model is unable to predict this phenomenon. Besson et al. [1] have included isotropic and linear kinematic hardening in a Gurson-like model, but, their model has been found insufficient to predict correctly the ratcheting effect. A more satisfactory reproduction of numerical results, particularly the void ratcheting, has been derived by Lacroix et al. [14] by the use of an improved variant of the so-called LPD model due to Leblond et al. [15] with a more refined description of strain hardening.

Intriguingly, all theoretical studies cited above utilize Gurson-like approach within the framework of limit analysis for the study of voided ductile media subjected to cyclic loads. It is our belief that the natural and correct context for such studies should be the shakedown analysis, as used in [3, 16, 25] for the fatigue of composite materials.

3.2 Statical Approach

For a given **repeated variable loading** $\boldsymbol{\Sigma}(t)$ in the domain $\mathscr{S}$ (Fig. 6), the REV **shakes down** if the plastic strain is stabilized (Fig. 7) anywhere in the REV and the total plastic dissipation is bounded. After a transient phase, the REV response becomes linear elastic back (Fig. 8). The adaptation ensures that the material behavior is safe.

This results from the development of **residual stresses**:

$$\boldsymbol{\rho}(\boldsymbol{x}, t) = \boldsymbol{\sigma}(\boldsymbol{x}, t) - \boldsymbol{\sigma}^E(\boldsymbol{x}, t)$$

where $\boldsymbol{\sigma}(\boldsymbol{x}, t)$ is the stress response in the elastoplastic REV and $\boldsymbol{\sigma}^E(\boldsymbol{x}, t)$ is the stress response in the fictitious purely elastic REV. $\boldsymbol{\rho}$ belongs to the set of **residual stress fields**:

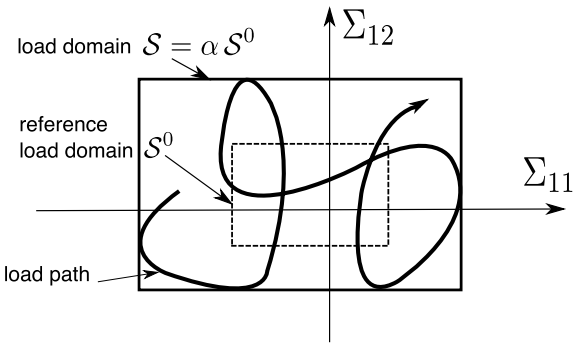

Fig. 6 Load domain

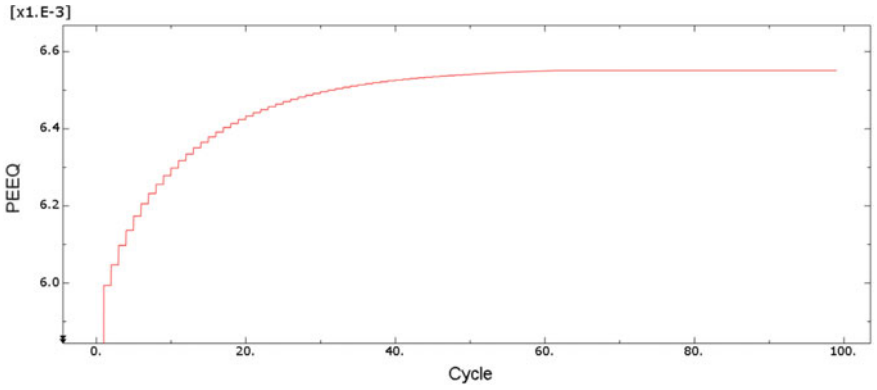

Fig. 7 Accumulated equivalent plastic strain (PEEQ) under pulsating load on the internal boundary at the equator $\theta = \pi/2$ when shakedown occurs for the stress triaxiality $T = 1.8333$

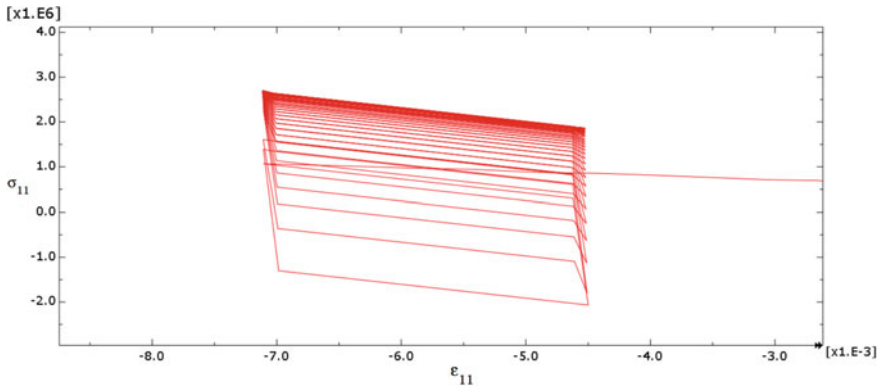

Fig. 8 σ_{11} versus ε_{11} under pulsating load when shakedown occurs for $T = 1.8333$

$$\mathscr{N} = \left\{ \boldsymbol{\rho} \quad | \quad div\, \boldsymbol{\rho} = \mathbf{0} \quad in\, V_M, \quad \boldsymbol{\rho} \cdot \boldsymbol{n} = \mathbf{0} \quad on\, S_f, \quad \boldsymbol{\rho} = \mathbf{0} \quad on\, S_f \right\} \tag{5}$$

where the condition of vanishing $\boldsymbol{\rho}$ on S_f is imposed for convenience, as explained below. Although it is artificial, the experience showed that it does not deteriorate the accuracy of the solutions.

For the loading domain $\mathscr{S} = \alpha\, \mathscr{S}^0$, the key-idea is to define **strictly admissible residual stress fields** (in Melan's sense) $\bar{\boldsymbol{\rho}}(\boldsymbol{x})$, such that:

- $\bar{\boldsymbol{\rho}}$ is **time independent**,
- $\bar{\boldsymbol{\rho}}$ is a **residual stress field**: $\bar{\boldsymbol{\rho}} \in \mathscr{N}$,
- $\bar{\boldsymbol{\rho}}$ is **strictly plastically admissible** in the sense that:

$$F(\boldsymbol{\sigma}^E(\boldsymbol{x}, t) + \bar{\boldsymbol{\rho}}(\boldsymbol{x})) < 0 \quad dans \quad \Omega \quad for \quad all \quad t$$

Then **Melan's theorem** claims that:

> If a strictly plastically admissible residual stress field $\bar{\boldsymbol{\rho}}$ can be found, the REV shakes down.

Otherwise, if the **load factor** α controlling the domain size reaches a threshold α^{SD} called **shakedown limit**, the REV collapses by formation of a **mechanism** (as in limit analysis) or by **plastic fatigue**. Then it is a powerful tool to predict the collapse of materials by **fatigue**. It is worth mentioning that, in the numerical simulations outlined below, ratchet mechanisms have never been observed. Then they are not considered in the theoretical developments.

3.3 Macroscopic Fatigue Criterion

In the same spirit as for Limit Analysis solution, the trial stress field for Shakedown Analysis: $\boldsymbol{\sigma} = \boldsymbol{\sigma}^{(1)} + \boldsymbol{\sigma}^{(2)}$ is the sum of two fields:

- the stress response under hydrostatic loadings: $\boldsymbol{\sigma}^{(1)} = \boldsymbol{\sigma}^{E(1)} + \bar{\boldsymbol{\rho}}^{(1)}$ decomposed into:
  - the elastic stress field (exact for pure hydrostatic loading)

$$\boldsymbol{\sigma}^{E(1)} = \frac{\Sigma_m}{1-f}\left(\mathbf{1} + \frac{1}{2}\left(\frac{a}{r}\right)^3 (\mathbf{e}_\theta \otimes \mathbf{e}_\theta + \mathbf{e}_\phi \otimes \mathbf{e}_\phi - 2\,\boldsymbol{e}_r \otimes \boldsymbol{e}_r)\right)$$

  - and the residual stress field

$$\bar{\boldsymbol{\rho}}^{(1)} = -A_0\left(\ln\left(\frac{a}{r}\right)\mathbf{1} - \frac{1}{2}\left(\boldsymbol{e}_\theta \otimes \boldsymbol{e}_\theta + \boldsymbol{e}_\phi \otimes \boldsymbol{e}_\phi\right)\right)$$

$$-\frac{\Sigma_{m+}}{1-f}\left(\mathbf{1} + \frac{1}{2}\left(\frac{a}{r}\right)^3 (\boldsymbol{e}_\theta \otimes \boldsymbol{e}_\theta + \boldsymbol{e}_\phi \otimes \boldsymbol{e}_\phi - 2\,\boldsymbol{e}_r \otimes \boldsymbol{e}_r)\right)$$

    inspired from the exact solution for the pure hydrostatic loading (in this case, the stress parameter A_0 is equal to $2\,\sigma_0$).

- an additional deviatoric part to capture the shear effects $\boldsymbol{\sigma}^{(2)} = \boldsymbol{\sigma}^{E(2)} + \bar{\boldsymbol{\rho}}^{(2)}$, of which the rather complicated analytical expression depending on Poisson's coefficient ν can be found in [27]. It is decomposed into:
  - the elastic stress field of a hollow sphere subjected to a deviatoric load $\boldsymbol{\sigma}^{E(2)}$ inspired form Boussinescq-Papkovich-Neuber solution [21] for the hollow sphere under pure deviatoric load
  - and the corresponding admissible residual stress field $\bar{\boldsymbol{\rho}}^{(2)}$:

Although it is not strictly imposed by the equilibrium conditions but to decrease the amount of calculations, it is shrewd to build an admissible residual stress field such that the stress vector on the REV boundary ∂V vanishes, as stated in (5). Indeed, according to (1), the average residual stress:

$$\boldsymbol{\Sigma}_r = \frac{1}{|\,\Omega\,|}\int_{\partial\Omega} (\bar{\boldsymbol{\rho}} \cdot \mathbf{n}) \otimes \boldsymbol{x}\; dS$$

vanishes and the average stress is equal to the corresponding value in the fictitious elastic body:

$$\boldsymbol{\Sigma} = \boldsymbol{\Sigma}_r + \boldsymbol{\Sigma}^E = \boldsymbol{\Sigma}^E$$

The microscopic plastic yielding criterion for the matrix:

$$F(\boldsymbol{\sigma}) \leq 0$$

being given, our goal is to deduce the macroscopic fatigue criterion:

$$\mathscr{F}(\boldsymbol{\Sigma}, f, \nu) \leq 0$$

depending on the void volume fraction f but also on Poisson's coefficient ν.

3.4 Macroscopic Fatigue Criterion for von Mises Porous Materials

The critical points where fatigue first occurs are situated on the interface void-matrix ($r = a$). For an alternating load ($\Sigma_{e+} = \Sigma_{e-}$, $sign(J_{3+}) = -sign(J_{3-})$), we find the condition:

$$\left(\frac{3}{4}\frac{\Delta\Sigma_m}{1-f}\right)^2 + \frac{3}{2}\frac{\Delta\Sigma_m}{1-f}\frac{-sign(J_{3+})\,\Sigma_{e+}}{1-f}P_1(a,\theta) + P_3(a,\theta)\left(\frac{\Sigma_{e+}}{1-f}\right)^2 \leq \sigma_0^2$$

given in the spherical coordinates (r, θ, ϕ) and where the expressions of the functions P_n are rather complicated, for instance:

$$P_1(r,\theta) = \frac{(-5\nu(\frac{a}{r})^5 + 10\nu(\frac{a}{r})^3 + 18(\frac{a}{r})^5 - 20(\frac{a}{r})^3 + 7)}{7-5\nu}\frac{(3\cos^2(\theta)-1)}{2}$$

For a pulsating load ($\Sigma_{e-} = 0$), we find the condition:

$$\left(\frac{3}{4}\frac{\Delta\Sigma_m}{1-f}\right)^2 + \frac{3}{2}\frac{\Delta\Sigma_m}{1-f}\frac{-sign(J_{3+})\Sigma_{e+}}{1-f}\frac{P_1(a,\theta)}{2} + P_5(a,\theta)\left(\frac{P_3(a,\theta)}{P_4(a,\theta)}\right)^2\left(\frac{\Sigma_{e+}}{1-f}\right)^2 \leq \sigma_0^2$$

Both conditions depend naturally on the sign of the third invariant J_3 of the deviator. The analysis of these conditions for the alternating load leads to the following results:

- When $J_{3+} > 0$, the REV shakes down if the condition is fulfilled at the equator $\theta = \pi/2$ where the left part of the previous condition takes its maximum value
- When $J_{3+} < 0$, the REV shakes down if the condition is fulfilled at the poles $\theta = 0$ and $\theta = \pi$

When $J_{3+} > 0$, the fatigue criterion is:

$$\left(\frac{3}{2}\frac{\Sigma_m}{1-f}\right)^2 - 3\,C_1\frac{\Sigma_m}{1-f}\frac{sign(J_3)\,\Sigma_e}{1-f} + C_2\left(\frac{sign(J_3)\,\Sigma_e}{1-f}\right)^2 \leq \sigma_0^2$$

where $C_1 = \frac{5\nu+5}{2(5\nu-7)}$ $\quad C_2 = \frac{25(7\nu^2-13\nu+7)}{(5\nu-7)^2}$. When $J_{3+} < 0$, one can find a similar criterion [27].

If we introduce the macroscopic stress ratio $R = \Sigma_-/\Sigma_+$, where Σ_- and Σ_+ are the minimum and maximum load during the cyclic loading process, respectively, the alternating load and pulsating load can be considered as two particular loading cases for which $R = -1$ and $R = 0$, respectively. Besides, $R = 1$ represents the monotonic loading condition where the collapse occurs by development of a mechanism. The previous fatigue criteria for $R = -1$ and $R = 0$ were extended to the general loading case with arbitrary values of R in [28] and to porous materials with pressure sensitive matrix obeying Drucker-Prager model in [29].

3.5 Numerical Results: Cell Model and Implementations

An initially axisymmetric spherical model of radius b, containing an initially concentric spherical void of radius a, is considered for the simulation. As shown on Fig. 9, taking into account the central symmetry, only a quarter discretized by 60,601 nodes and 20,000 symmetric elements is taken into consideration.

To fulfill the imposed conditions of homogeneous boundary strain rate $\bar{\boldsymbol{v}} = \boldsymbol{D} \cdot \boldsymbol{x}$ and loading with different macroscopic stress triaxiality $T = \Sigma_m/\Sigma_e$, we use a user subroutine MPC (Multi-Points Constraints) of the finite element software Abaqus. This procedure is implemented by applying a constant macroscopic stress ratio $\phi = \Sigma_\rho/\Sigma_z$, where $T = (1 + 2\phi)/(3(1 - \phi))$ as in Cheng et al. [4]. We consider the following data: $\sigma_0 = 480\,\text{MPa}$, $E = 210000\,\text{MPa}$ and $\nu = 0.3$.

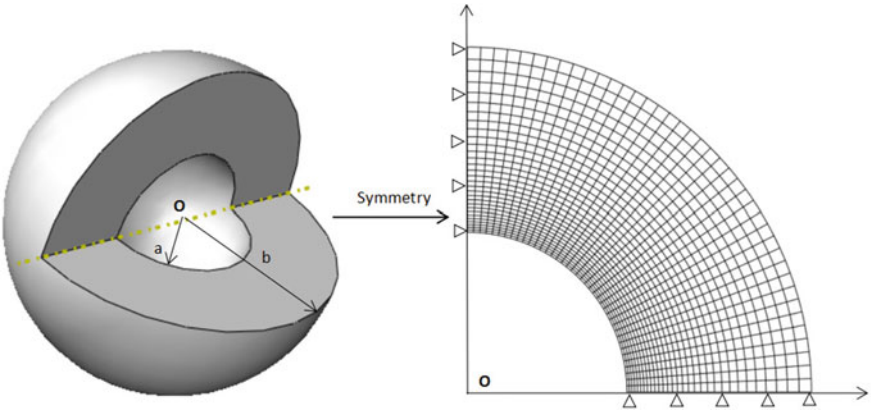

Fig. 9 Hollow sphere model and initial mesh

3.6 Direct Numerical Simulations to Assess the Fatigue Limit

We can start simply by determining the fatigue limit, firstly calculating the elastic solution for the two elementary loads $\boldsymbol{\Sigma}_{\pm}^{0}$ defining the reference load domain $\mathscr{S}^{0}$.

For each Gauss point $\boldsymbol{x}_g$, let $\boldsymbol{\sigma}_{\pm}^{E0}(\boldsymbol{x}_g)$ be the corresponding elastic stress response and α_g the solution of the local problem:

$$\max_{\bar{\boldsymbol{\rho}},\alpha},\ \left\{\alpha \quad | \qquad F(\alpha\,\boldsymbol{\sigma}_{\pm}^{E0}(\boldsymbol{x}_g)+\bar{\boldsymbol{\rho}})\le 0\right\}$$

For the alternating loading case, $\boldsymbol{\sigma}_{+}^{E0}(\boldsymbol{x}_g)=-\boldsymbol{\sigma}_{-}^{E0}(\boldsymbol{x}_g)$, and $\boldsymbol{\sigma}_{-}^{E0}(\boldsymbol{x}_g)=0$ for the pulsating one. So the simulation has been reduced to the solution of a big number of problems of optimization of small dimension.

The fatigue limit α is obtained as the minimum value of α_g for all Gauss points $\boldsymbol{x}_g$. Also we can obtain the corresponding residual stress and the location of the first point of the model where the fatigue first occurs.

3.7 Step by Step Computations to Analyse the Transient Phase Before Shakedown

We apply $\Sigma_{e+}=\Sigma_{e-}$ for the alternating loading case and $\Sigma_{e-}=0$ for the pulsating loading case respectively for various values of macroscopic stress triaxiality T. We choose a value of loading factor α and we perform cycles within $\mathscr{S}=\alpha\,\mathscr{S}^{0}$ for the pure hydrostatic loading and then coupling with the deviatoric loading. If the macro-element shakes down, we increase the load factor and we repeat the procedure until the fatigue or mechanism occurs.

For a certain triaxiality T, in order to determine numerically the shakedown load, we fix a maximum displacement on the external boundary of the hollow sphere, which gives $\Delta\Sigma_m=2\Sigma_{m+}$ for alternating loading case and $\Delta\Sigma_m=\Sigma_{m+}$ for pulsating loading case respectively and 100 cycles of loading.

For the pulsating loading case, if the maximum load $\Delta\Sigma_{m+}$ is less than the shakedown limit, the strain-stress curve tends to a linear response and the value of PEEQ (Accumulated Equivalent Plastic Strain) does not increase any more (Fig. 7) after a certain number of cycles, hence the body shakes down. In practice, the computation is stopped when the variation of PEEQ reaches a given tolerance and, as expected, the width of the cycle for strain tends to zero after certain cycles on the internal boundary at $\theta=\pi/2$ for $J_{3+}>0$ and $\theta=0$ for $J_{3+}<0$ as shown on Fig. 8.

On the contrary, for alternating loading case, when the maximum load Σ_{m+} exceeds the fatigue limit, plastic shakedown (accommodation) occurs immediately at the first cycle. The equivalent plastic strain continues to accumulate and the dissipation remains increasing in each cycle.

It is worth to note the results by step-by-step method match the computation by the direct method.

3.8 Comparison Between Analytical Results and Numericals Simulations

Direct numerical computations to determine the fatigue limit and step-by-step simulations to analyse the transient phase before shakedown or collapse are both performed to validate the new analytical criterion for stress ratio $R = -1, -1/5, 0$ and $1/5$ with the porosity $f = 0.01$ (Fig. 10). Poisson's coefficient is equal to $\nu = 0.3$. In practice, $\Delta\Sigma_m$ and $\Delta\Sigma_e$ are expressed by Σ_{m+} and Σ_{e+}. Note that the detailed descriptions and implementation of the numerical computations and the analytical results for $R = 0$ (pulsating) and $R = -1$ (alternating) were already provided in [27].

The safety domain is defined by the new shakedown criterion and the yield surface proposed by Shen et al. [20], corresponding to the collapse by development of a mechanism at the first cycle. With the increase of the stress ratio R, the surface of collapse by mechanism becomes larger and, until the extreme case $R = 1$, in which

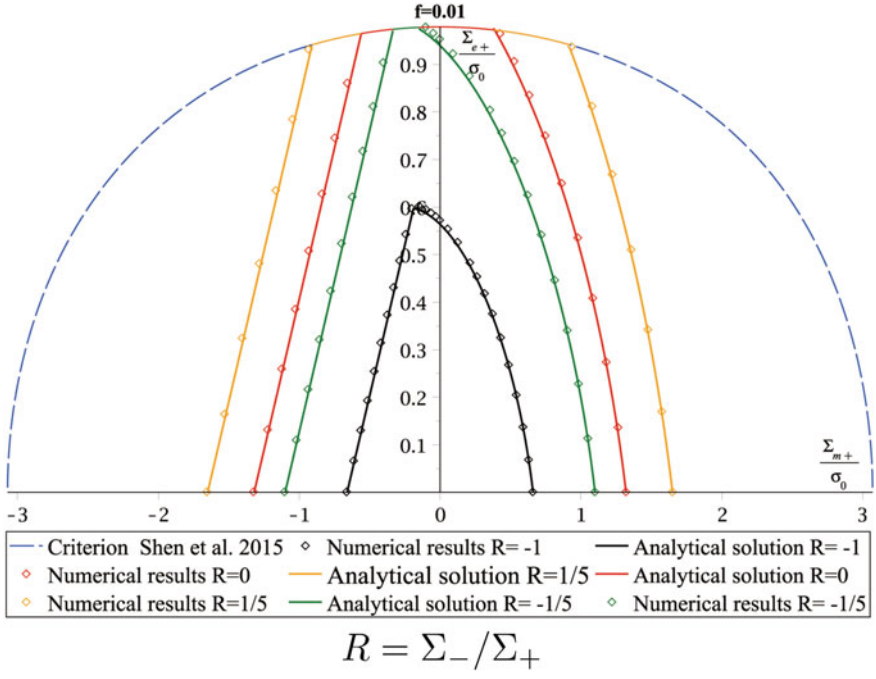

Fig. 10 Interaction curve for porosity $f = 0.01$

the cyclic load turns into monotonic one. Hence the shakedown criterion is identical to the plastic limit derived from the limit analysis.

It is readily seen that the new criterion is strictly inside the numerical results, then delivers a quasi-lower bound, because of the statical approach based on Melan's theorem. The first point where the fatigue occurs is located on the internal boundary $r = a$ at the equator $\theta = \pi/2$ for $J_{3+} > 0$ and at the poles $\theta = 0$ or π for $J_{3+} < 0$, according to the analytical solution.

4 Conclusions and Perspectives

In this paper, we presented an unified approach to build macroscopic strength criteria of ductile porous materials:

- For a von Mises matrix, a stress variational model (SVM), dual of Gurson's one, has been proposed to find by the Limit Analysis a macroscopic plastic yield criterion depending on the porosity. It naturally depends on the third invariant J_3 but only through its sign.
- For the evolution of porosity with respect to the stress triaxiality predicted by SVM, clear discrepancies appear between our model and Gurson's one which is known to overestimate the variation of the porosity.
- Some extensions have been proposed to obtain a continuous dependence with respect to J_3 through Lode's angle, to improve the strength value for the pure deviatoric loading and to propose, thanks to the bipotential formulation, a yield criterion for a non associated Drucker-Prager matrix.
- Using the Shakedown Analysis, the method has been extended to the repeated variable loadings to obtain a fatigue criterion for the porous materials. It depends on the porosity but also strongly on Poisson's coefficient.

Among future investigations of which some of ones are in progress, the following points can be highlighted:

- All the methods developed, whether for the macroscopic plastic yielding criteria or the fatigue criteria of the porous materials, could be adapted to the study of composite materials.
- Another interesting extension will concern the shakedown of ductile porous materials involving the kinematical hardening.
- In Dang Van's theory of fatigue spirit [24, 26], we hope apply the shakedown analysis to the monocrystals and polycrystals to propose new fatigue criteria exhibiting the dependence with respect to the porosity and Poisson's coefficient.

References

1. Besson, J., Guillemer-Neel, C.: An extension of the Green and Gurson models to kinematic hardening. Mech. Mater. **35**, 1–18 (2003)
2. Cazacu, O., Revil-Baudard, B., Lebensohn, R., Garajeu, M.: On the combined effect of pressure and third invariant on yielding of porous solids with von Mises matrix. J. Appl. Mech. (2013). https://doi.org/10.1115/1.4024074
3. Chen, G., Ozden, U.A., Bezold, A., Broeckmann, C., Weichert, D.: On the statistical determination of yield strength, ultimate strength, and endurance limit of a particle reinforced metal matrix composite (PRMMC). In: Weichert, D., Fuschi, P., Pisano, A.A. (eds.) Direct Methods for Limit and Shakedown Analysis of Structures: Advanced Computational Algorithms and Material Modelling. Springer, pp. 105–122 (2015)
4. Cheng, L., de Saxcé, G., Kondo, D.: A stress-based variational model for ductile porous materials. Int. J. Plast. **55**, 133–151 (2014)
5. Cheng, L., Monchiet, V., Morin, L., de Saxcé, G., Kondo, D.: An analytical Lode angle dependent damage model for ductile porous materials. Eng. Fract. Mech. **149**, 119–133 (2015)
6. Cheng, L., Jia, Y., Oueslati, A., de Saxcé, G., Kondo, D.: A bipotential-based limit analysis and homogenization of ductile porous materials with non-associated Drucker-Prager matrix. J. Mech. Phys. Solids **77**, 1–26 (2015)
7. Devaux, J., Gologanu, M., Leblond, J.B., Perrin, G.. On continued void growth in ductile metals subjected to cyclic loadings. In: Willis, J. (ed.) Proceedings of the IUTAM Symposium on Nonlinear Analysis of Fracture. Kluwer, Cambridge, GB, pp. 299–310 (1997)
8. Drucker, D.C., Prager, W.: Soil mechanics and plastic analysis or limit design. Quart. Appl. Math. **10**, 157–165 (1952)
9. Gilles, Ph., Jullien, B., Mottet, G.: Analysis of cyclic effects on ductile tearing strength by a local approach of fracture. In: Advances in Fracture/Damage Models for the Analysis of E of Engineering Problems, vol. 137. ASME Publication AMD, pp. 269–284 (1992)
10. Guo, T.F., Faleskog, J., Shih, C.F.: Continuum modeling of a porous solid with pressure-sensitive dilatant matrix'. J. Mech. Phys. Solids **56**, 2188–2212 (2008)
11. Gurson, A.L.: Continuum theory of ductile rupture by void nucleation and growth – part I: Yield criteria and flow rules for porous ductile media. J. Eng. Mater. Technol. **99**, 2–15 (1977)
12. Kobayashi, H., Kusumoto, T., Nakazawa, H.: Cyclic J-R-curve and upper limit characteristic of fatigue crack growth in 2-1/2 Cr-Mo steel. In: 11th International Conference on Structural Mechanics in Reactor Technology (SMIRT 11), Tokyo, Japan, paper G27/1 (1991)
13. König, J.A.: Shakedown of Elastic-plastic Structures. Elsevier, Amsterdam (1987)
14. Lacroix, R., Leblond, J.B., Perrin, G.: Numerical study and theoretical modelling of void growth in porous ductile materials subjected to cyclic loadings. Eur. J. Mech. A Solids **55**, 100–109 (2016)
15. Leblond, J.B., Perrin, G., Devaux, J.: An improved Gurson-type model for hardenable ductile metals. Eur. J. Mech. A Solids **14**, 499–527 (1995)
16. Magoariec, H., Bourgeois, S., Débordes, O.: Elastic-plastic shakedown of 3D periodic heterogeneous media: a direct numerical approach. Int. J. Plast. **20**, 1655–1675 (2004)
17. Monchiet, V., Charkaluk, E., Kondo, D.: A micromechanics-based modification of the Gurson criterion by using Eshelby-like velocity fields'. Eur. J. Mech. A Solids **30**, 940–949 (2011)
18. Ponte Castañeda, P.: The effective mechanical properties of nonlinear isotropic composites. J. Mech. Phys. Solids **39**, 45–71 (1991)
19. Schmidt, R.A., Wilkowski, G.M., Mayfield, M.E.. The International Piping Re- search Group (IPIRG) program. An overview. In: 11th International Conference on Structural Mechanics in Reactor Technology (SMIRT 11), Tokyo, Japan, paper G23/1 (1991)
20. Shen, W.Q., Oueslati, A., de Saxcé, G.: Macroscopic criterion for ductile porous materials based on a statically admissible microscopic stress field. Int. J. Plast. **70**, 60–76 (2015)
21. Soutas-Little, R.W.: Elasticity. Courier Corporation (1999)
22. Tvergaard, V.: Influence of voids on shear band instabilities under plane strain conditions. Int. J. Fract. **17**, 389–407 (1981)

23. Tvergaard, V.: On localization in ductile materials containing spherical voids. Int. J. Fract. **18**, 237–252 (1982)
24. Van Dang, K.: Sur la résistance à la fatigue des métaux. Sci. Tech. Armement. **47**, (1973)
25. Weichert, D., Hachemi, A., Schwabe, F.: Application of shakedown analysis to the plastic desigm of composites. Arch. Appl. Mech. **69**, 623–633 (1999)
26. Weichert, D., Maier, G. (eds.): Inelastic Behaviour of Structures Under Variable Repeated Loads, CISM International Centre for Mechanical Sciences, Courses and Lectures, vol. 432. Springer, Wien, New York (2002)
27. Zhang, J., Shen, W.Q., Oueslati, A., de Saxcé, G.: Shakedown of porous materials. Int. J. Plast. **95**, 123–141 (2017)
28. Zhang, J., Shen, W.Q., Oueslati, A., de Saxcé, G.: A macroscopic criterion of shakedown limit for ductile porous materials subjected to general cyclic loadings. Mech. Mater. **115**, 76–87 (2018)
29. Zhang, J., Oueslati, A., Shen, W.Q., de Saxcé, G.: Shakedown of porous material with Drucker-Prager dilatant matrix under general cyclic loadings. Compos. Struct. **220**, 566–579 (2019)

Recent Updates of the Residual Stress Decomposition Method for Shakedown Analysis

Ioannis A. Kapogiannis and Konstantinos V. Spiliopoulos

Abstract Almost every structure or mechanical component is exposed to repeated loading conditions. As a result, materials exceed the elastic regime and plastic strains develop. The outcome of these loadings may be estimated either using a time-consuming step by step analysis or adopting modern Direct Methods which are capable to predict final cyclic states, like the elastic shakedown (safe state), the alternating plasticity, or the ratcheting (unsafe states). Towards this direction, the Residual Stress Decomposition Method (RSDM) was developed. The RSDM estimates the asymptotic cyclic state of a structure exposed to a given cyclic loading. The RSDM-S is based on the same theoretical background as RSDM and was developed in order to estimate the shakedown domain of a structure. Both methods have been tested for cyclic thermal and mechanical loads. In the present work, the RSDM-S is updated towards faster convergence by avoiding some unnecessary calculations and extended to account also for cyclic imposed displacements. Computational implementation was performed in an open source research oriented finite element analysis program. Three-dimensional brick elements are used to deal model complex geometries. The material adopted is elastic perfectly plastic von Mises type of law. Examples of application are given, proving the versatility of the approach.

1 Introduction

Most structures and mechanical components are subjected to variable repeated loads and applied displacements. Typical variable loadings, like traffic loads, are applied to bridges, pavements, railway structures. Other structures, like buildings, bridges, pipelines, during their lifetime, undergo different earthquake actions, which may be

I. A. Kapogiannis · K. V. Spiliopoulos (✉)
Department of Civil Engineering, Institute of Structural Analysis & Antiseismic Research, National Technical University of Athens, Zografou Campus, 157-80 Zografos, Athens, Greece
e-mail: kvspilio@central.ntua.gr

I. A. Kapogiannis
e-mail: john.kapogiannis@gmail.com

A. A. Pisano et al. (eds.), *Direct Methods*, Lecture Notes in Applied and Computational Mechanics 95, https://doi.org/10.1007/978-3-030-48834-5_7

considered as variable imposed displacements to their base. Mechanical engineering parts may also be subjected to variable mechanical and/or thermal loads. All these structures are usually designed to operate in the elastic regime, even if this leads to cost-ineffective solutions. However, the high level of variable loading or excessive applied displacements may force structural or mechanical members to develop plastic strains that eventually will end up to an asymptotic limit state such as ratcheting, low cycle fatigue or shakedown [1]. It may happen that, up to a specific limit of imposed displacement or load, inside the plastic regime, the plastic strains are stabilized and the structure responds elastically again. This safe state is known as shakedown, which has an effect to extend the life cycle of a structure.

When the exact load history is known one may estimate whether a structure will shakedown, using time-consuming step-by-step procedures. Thus, there is a need for faster procedures. Direct methods offer this possibility, as they attempt to find the stabilized state without tracing the whole load path. Also, when the exact loading history is not known, but only its variation intervals, they offer the only way to determine the shakedown limits. Most of these approaches are connected to the extremum theorems of structural plasticity and use optimization algorithms. Recent applications include railway structures [2] and pavements [3]. Direct methods, not related to mathematical programming, have also been proposed like the Simplified Theory of Plastic Zones (STPZ) method [4] or the Linear Matching Method (LMM) which has been recently extended to include limited kinematic hardening [5].

Another direct method, that does not use optimization algorithms, called Residual Stress Decomposition Method for Shakedown (RSDM-S) has been developed for the evaluation of shakedown domains [6, 7]. Its roots are in RSDM [8, 9], a direct method that may estimate the asymptotic cyclic state of a structure under a given cyclic loading. The basic idea behind both approaches is the decomposition of the expected in this state cyclic residual stresses in Fourier series, whose coefficients are estimated in an iterative way. The two procedures may be easily attached to any existing finite element program.

In the present work RSDM-S is slightly reformulated to avoid unnecessary calculations. Also, the initial parameters of the method are revisited towards the minimum number of iterations needed for a smooth and robust convergence. In the previous versions of the RSDM-S the loading was considered to be mechanical and/or thermal. However, boundary displacements varying within prescribed limits, are also possible [10]. The RSDM-S is herein extended to account for cyclic imposed displacements. Additionally, the portability of the method is demonstrated, while it is embedded in an open source finite element research-oriented computer code FEAP [11]. Brick elements have been used so that difficult geometries may be handled in either two or three dimensions. Examples of application are also presented.

2 Theoretical Considerations

The RSDM-S was developed in previous years [6, 7] and refers to structures made of elastic-perfectly plastic von Mises type of material, subjected to cyclic thermo-mechanical loadings varying inside a prescribed field. These loads may have a cyclic variation between a specified maximum and a minimum value.

2.1 The Case of Imposed Displacements

In Fig. 1 one may see a structure of volume V and surface S, which is partially rigidly supported (S_u) and partially subjected to cyclically imposed displacements (S_{pr}). The rest of its surface is free. There are no surface tractions or body forces applied on the structure.

Let us suppose that the displacements are applied periodically with period T, i.e. $\bar{\mathbf{u}}(t) = \bar{\mathbf{u}}(t + T)$. One and two-dimensional displacement domains are considered herein.

Without loss of generality, we assume that the minimum values of the two prescribed displacements are zero with the starred quantities representing their maximum values. The corresponding cyclic program of the imposed displacements, is $(0 \rightarrow \bar{u}_1^* \rightarrow (\bar{u}_1^*, \bar{u}_2^*) \rightarrow \bar{u}_2^* \rightarrow 0)$ (Fig. 2). These variations are shown [6] in either the time domain (a), or the applied displacement domain, which, in the sequel, will be called loading domain (b).

It has been proved in [1] that, for stable materials, if a structure shakes down under a cyclic loading program containing the vertices of the loading domain then it will shake down for any loading path contained in this domain. This domain may be isotropically varied if multiplied with a load factor γ. Thus, the idea behind RSDM-S is to find the largest loading domain for which shakedown occurs.

In response to the cyclic loading program, the stresses in the structure at a cycle point $\tau = t/T$ are decomposed into an elastic part $\boldsymbol{\sigma}_{pr}^{el}$, in response to the applied external cyclic displacement, assuming a completely elastic behavior, and a residual stress part $\boldsymbol{\rho}$. In the search for the shakedown factor γ, the elastic stresses are themselves multiplied by this factor. Thus, the total stress vector can now be written:

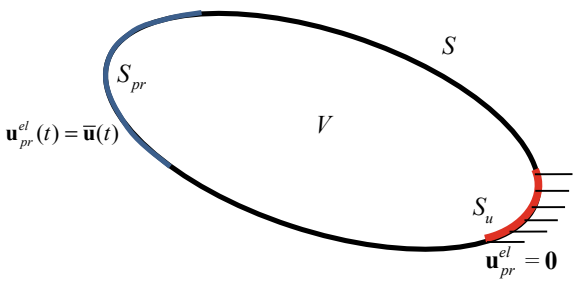

Fig. 1 Body subjected to time dependent imposed displacement

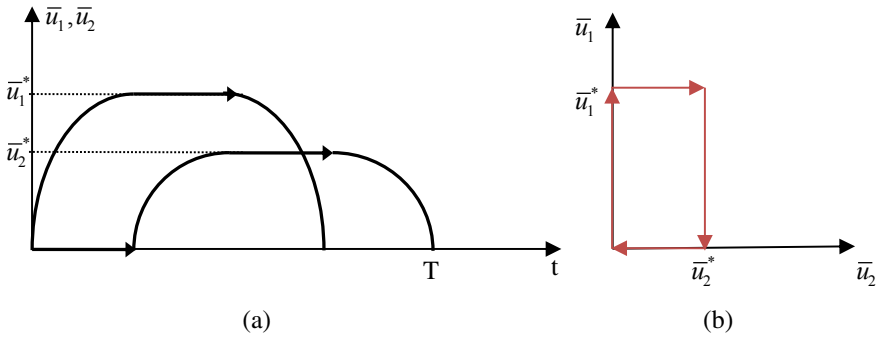

Fig. 2 Independent cyclic imposed displacement variation over one time period **a** time domain, **b** loading (applied displacement) domain

$$\boldsymbol{\sigma} = \gamma \boldsymbol{\sigma}_{pr}^{el} + \boldsymbol{\rho} \tag{1}$$

The elastic problem is solved first. Using the principle of virtual displacements (PVD), one may write:

$$\int_V \left(\delta \boldsymbol{\varepsilon}_{pr}^{el}\right)^T \boldsymbol{\sigma}_{pr}^{el}\, dV = \int_{S_{pr}} \left(\delta \mathbf{u}_{pr}^{el}\right)^T \mathbf{f}_{pr}\, dS = 0 \tag{2}$$

Since due to the fact that $\mathbf{u}_{pr}^{el} = \bar{\mathbf{u}}$, $\delta \mathbf{u}_{pr}^{el} = \mathbf{0}$ on S_{pr}.

We partition the nodes of the finite element (FE) mesh into those over the volume, the free boundary, the rigid boundary and the nodes on the prescribed displacement boundary. Denoting their corresponding displacements by $\mathbf{r}_{pr}^{el}$ and $\bar{\mathrm{r}}^{el}$ one may connect them to the strains through two different FE compatibility matrices $\mathbf{B}$ and $\mathbf{B}'$:

$$\boldsymbol{\varepsilon}_{pr}^{el} = \mathbf{B}\mathbf{r}_{pr}^{el} + \mathbf{B}'\bar{\mathbf{r}}^{el} \tag{3}$$

Because of (3) the virtual strain increment is:

$$\delta \boldsymbol{\varepsilon}_{pr}^{el} = \mathbf{B}\left(\delta \mathbf{r}_{pr}^{el}\right) \tag{4}$$

The stresses are related to the elastic strains through the material matrix $\mathbf{D}$

$$\boldsymbol{\sigma}_{pr}^{el} = \mathbf{D}\boldsymbol{\varepsilon}_{pr}^{el} \tag{5}$$

Substituting Eqs. (3)–(5) to (2) and doing the algebraic manipulation one may get:

$$\mathbf{K}\mathbf{r}_{pr}^{el} = -\left(\int_V \mathbf{B}^T\mathbf{D}\mathbf{B}'\,dV\right)\bar{\mathbf{r}}^{el} \tag{6}$$

where $\mathbf{K} = \int_V \mathbf{B}^T\mathbf{D}\mathbf{B}\,dV$ is the stiffness matrix of the structure.

With the displacements $\bar{\mathbf{r}}^{el}$ known, the Eq. (6) may be solved to obtain $\mathbf{r}_{pr}^{el}$ and therefore $\boldsymbol{\varepsilon}_{pr}^{el}$ and $\boldsymbol{\sigma}_{pr}^{el}$ may be obtained.

The total strain rate may be decomposed into three terms:

$$\dot{\boldsymbol{\varepsilon}} = \dot{\boldsymbol{\varepsilon}}_{pr}^{el} + \dot{\boldsymbol{\varepsilon}}_{\mathbf{r}}^{el} + \dot{\boldsymbol{\varepsilon}}^{pl} \tag{7}$$

Note that the terms $\dot{\boldsymbol{\varepsilon}}$ and $\dot{\boldsymbol{\varepsilon}}^{el}$ in (7) are kinematically admissible. Thus, the sum:

$$\dot{\boldsymbol{\varepsilon}}_r = \dot{\boldsymbol{\varepsilon}}_{\mathbf{r}}^{el} + \dot{\boldsymbol{\varepsilon}}^{pl} \tag{8}$$

is also kinematically admissible. This may be expressed as $\dot{\boldsymbol{\varepsilon}}_r = \mathbf{B}\dot{\mathrm{r}}_r$, where r_r are the FE displacements of the sought solution of the boundary value problem to account for the residual stresses.

The elastic term $\dot{\boldsymbol{\varepsilon}}_{\mathbf{r}}^{el}$ is related to the residual stress via the material matrix $\mathbf{D}$. Thus, one may write:

$$\dot{\boldsymbol{\varepsilon}}_r = \mathbf{D}^{-1}\dot{\boldsymbol{\rho}} + \dot{\boldsymbol{\varepsilon}}^{pl} \rightarrow \dot{\boldsymbol{\rho}} = \mathbf{D}\dot{\boldsymbol{\varepsilon}}_r - \mathbf{D}\dot{\boldsymbol{\varepsilon}}^{pl} \tag{9}$$

Equilibrium of the residual stresses with zero loads may be manifested through the PVD:

$$\begin{aligned}\int (\delta\dot{\boldsymbol{\varepsilon}}_r)^{\mathrm{T}}\dot{\boldsymbol{\rho}}dV = 0 \rightarrow \left(\int (\mathbf{B}^T\mathbf{D}\mathbf{B})dV\right)\dot{\mathbf{r}}_r &= \int \mathbf{B}^T\mathbf{D}\dot{\boldsymbol{\varepsilon}}^{pl}dV \\ \rightarrow \mathbf{K}\dot{\mathbf{r}}_r &= \int \mathbf{B}^T\mathbf{D}\dot{\boldsymbol{\varepsilon}}^{pl}dV\end{aligned} \tag{10}$$

The above formulation avoids the additional evaluation of the derivatives of the elastic stresses in contrast to the original RSDM-S [6–8] and thus shortens the amount of calculations.

The rhs of (10) is determined in a simple radial return type of algorithm as was proposed in [6]. Solving (10) one may evaluate through (9) the residual stress rate $\dot{\boldsymbol{\rho}}$ at a cycle point τ.

The expected cyclic nature of the residual stresses at the asymptotic cycle allows one to evaluate the residual stresses themselves. This may be done by their decomposition into Fourier series [6]:

$$\boldsymbol{\rho}(\tau) = \frac{1}{2}\mathbf{a}_0 + \sum_{k=1}^{\infty}\{\cos(2k\pi\tau)\cdot\mathbf{a}_k + \sin(2k\pi\tau)\cdot\mathbf{b}_k\} \tag{11}$$

The Fourier coefficients are evaluated by numerical time integration of the computed $\dot{\boldsymbol{\rho}}$ vectors at each cycle point τ [6].

Equations (9)–(11) together with Eq. (1) are continuously updated [6–8] through an iterative sequence of lowering the load factor, which starts from a high initial value. Iterations stop when the only remaining term in (11) is the constant term $\mathbf{a}_0$ which is the condition that the structure has shaken down [12, 13]. Thus, the shakedown factor γ_{sh} may be evaluated and the shakedown domain may be established.

Note: The RSDM-S was published in 2014. A method, called SCM, that does not employ Fourier series, was published in 2019 [14]. However, it is virtually the same with RSDM-S, as features and methodology are the same. The residual stresses' derivatives are evaluated in the same way and integration is also carried out over time points inside a period. SCM uses just the vertices of the loading domain, as time points, and thus it is wrongly stated [14] that, because of the Fourier series, the RSDM-S is slow, as it must utilize many time points inside the cycle to represent the applied loading. Unfortunately, it is not realized that the number of the time points used, is a direct consequence of a proper description of the cyclic loading program, either in the time domain or in the loading domain ([6], Fig. 2) and has nothing to do with the Fourier series. For example, if the loading domain (see Fig. 2b) is employed, RSDM-S, uses also only the vertices, as time points. At the same time only three coefficients of the Fourier series have proved sufficient, with the convergence being continuously descending and smooth [6], something which does not appear with SCM.

Moreover the criterion of convergence of the SCM is a direct result of the convergence criterion of the RSDM-S.

2.2 Numerical Modifications on the RSDM-S

Except for the theoretical modification discussed above, some numerical interventions to the original RSDM-S are presented herein. Although necessary to be introduced for the applied displacement loading case, they are also applicable to the cases of thermomechanical loading domains.

In the previous work [6], the "ω" factor has been introduced in order to prevent overshooting of the shakedown load. However, in case of imposed displacement, the use of "ω" could lead to a continuous halving of itself, being finally ineffective. To account for such cases, the following calibration procedure is proposed. In order to follow the path towards the shakedown factor γ_{sh}, in each convergence step, the sum of norms $\varphi(\gamma) = \sum_{k=1}^{\infty} \|\mathbf{a}_k\| + \sum_{k=1}^{\infty} \|\mathbf{b}_k\|$ is used to contract the loading domain [6–8]. The contraction factor should always be positive. However, this is not always the case, as the magnitude of φ depends on the initial elastic stresses used to start the iterations. It has been observed that a good ratio of the maximum initial elastic stress over the yield stress should be lower than 10^{-4}. So, a recalculation of the initial elastic stress vector is proposed, by multiplying it with this initial stress multiplication factor of the value of 10^{-4}. If this ratio is greater than 10^{-4}, for example 10^{-3}, the method

may not converge, because the shakedown factor could be overshot. On the other hand, if the ratio was lower, namely 10^{-5}, the convergence was slowing down. The proposed remedy appears to be general as it works for all the considered examples, either past or present.

The updates and modifications of the RSDM-S were programmed inside the source code of FEAP. FEAP is a research oriented finite element analysis software developed in Berkeley [10]. Thus RSDM-S is fully functional in FEAP for the case of structures, modelled by brick elements and subjected to cyclic thermomechanical loadings with or without imposed displacements.

3 Application Examples

Several examples of application have been tested using the updated RSDM-S. The first example considers cyclic mechanical loading and the next two, of increasing complexity, are examples with applied cyclic displacements.

3.1 The Simple Frame

The first example is the simple frame of Fig. 3a, considered also in [6, 15, 16]. Two distributed loads (P_1 and P_2) act independently, varying from the value "0" to the maximum values P_1^* and P_2^*, as shown in Fig. 3b. The ratio P_1^* over P_2^* is equal to 3. The mechanical properties were E = 20,000 kN/cm^2, $\nu = 0.3$, $\sigma_y = 10$ kN/cm^2.

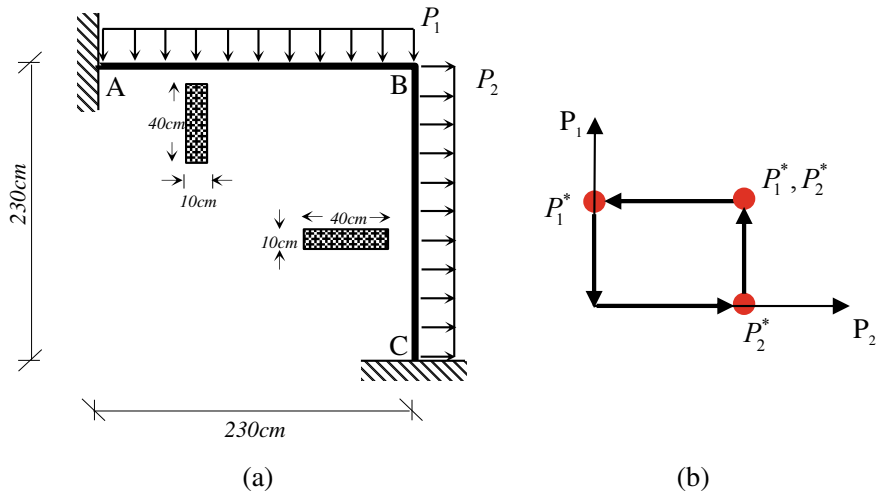

Fig. 3 **a** Geometry and loads, **b** loading cycle

The updated RSDM-S was run considering five time points of the loading cycle (that coincide with the vertices of the loading domain) and three Fourier coefficients. 350 brick elements were used for the discretization (Fig. 4). The saving in the computing time, as compared with the original RSDM-S is about 30%.

Three different cases were considered, accounting for different initial setups of the method:

– Case A: Three Fourier coefficients were used and the initial stress multiplication factor was 10^{-6}. Although starting from a very high initial loading factor, a smooth convergence (Fig. 5) towards the shakedown factor was observed which was found

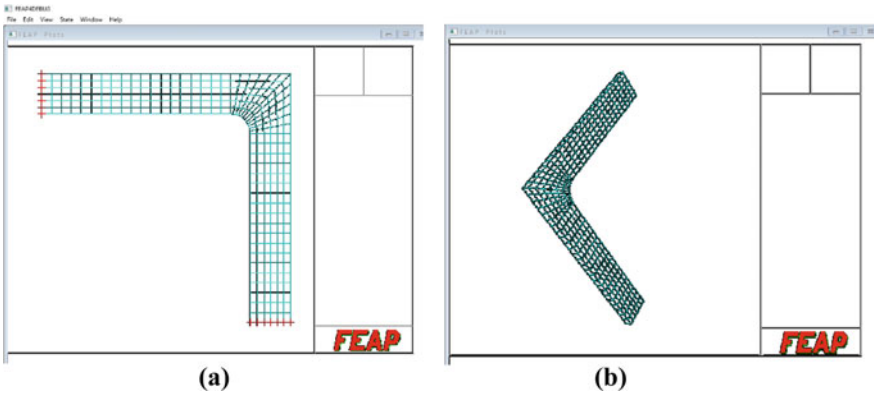

Fig. 4 2D view and 3D view of the frame using 350 brick elements

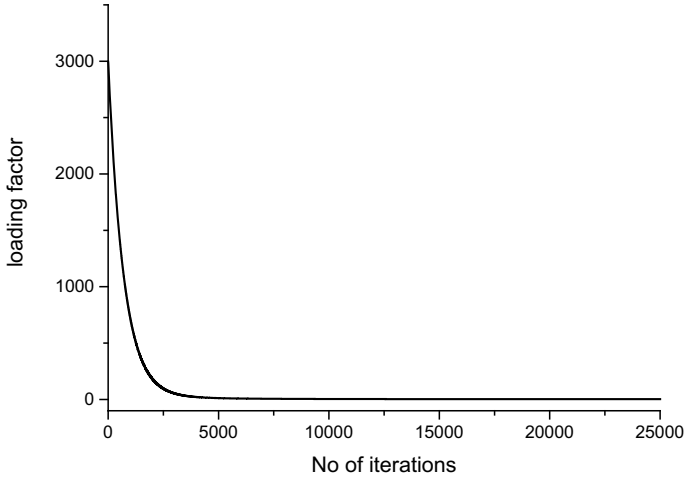

Fig. 5 Convergence of the loading factor when the initial elastic stresses multiplication factor is equal to 10^{-6}

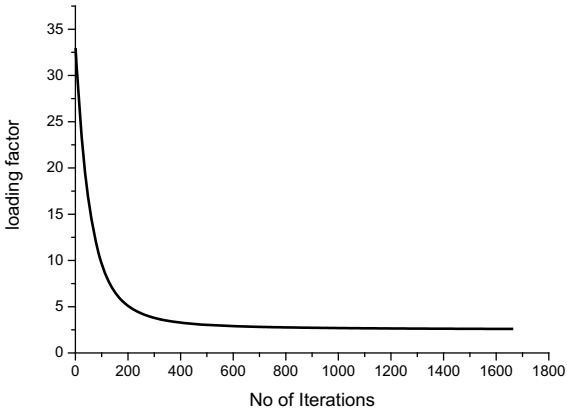

Fig. 6 Convergence of the loading factor considering 3 Fourier coefficients when the initial elastic stress multiplication factor is equal to 10^{-2}

2.8; however, the rate was slow since it required almost 20,000 iterations. The reason is the small initial stress multiplication factor. As a result, the rate of decrease of φ is quite small.

– Case B: Three Fourier Coefficients were used and the initial stress multiplication factor was 10^{-2}. The shakedown factor is equal to 2.59 and the convergence is smooth as presented in Fig. 6. It coincides with [6], whereas other results reported in the literature, are 2.473 [15] and 2.487 [16], using different meshes of plane triangular elements.
  The method needed 1637 iterations to calculate the shakedown factor. Note that, in case A, even if the starting loading factor was 32, as the one used in the present case, still almost 15,000 iteration would be necessary to converge.
– Case C: Eighty Fourier Coefficients were used and the initial stress multiplication factor was 10^{-2}. The shakedown factor is equal to 2.58 and the convergence is smooth as presented in Fig. 7.

The method needed 1875 iterations to calculate the shakedown factor.

If someone compares the cases B and C, it is obvious that the use of three Fourier coefficients is enough to achieve a fast and accurate estimation of the shakedown factor. The comparison of the two cases is presented in Fig. 8.

3.2 The Slab with the Hole

The benchmark problem of the square plate having a circular hole in its center, is the next example considered. The plate is subjected to imposed displacements along its edges. Due to symmetry, only one quarter of the plate is discretized (Fig. 9). Let D be the diameter of the circle, L the length of the slab and d the thickness, then $D/L = 0.2$, $d/L = 0.05$. In the present work, L is equal to 10 m. The boundary conditions along the X-axis and the Y-axis are considered rolled. Results for one

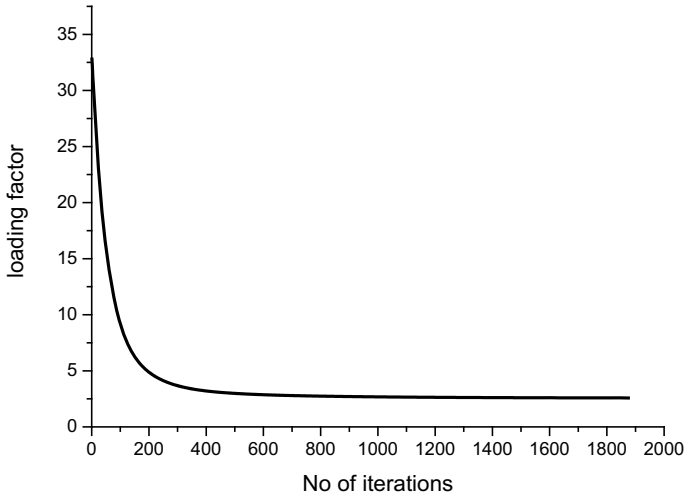

Fig. 7 Convergence of the loading factor considering 80 Fourier coefficients

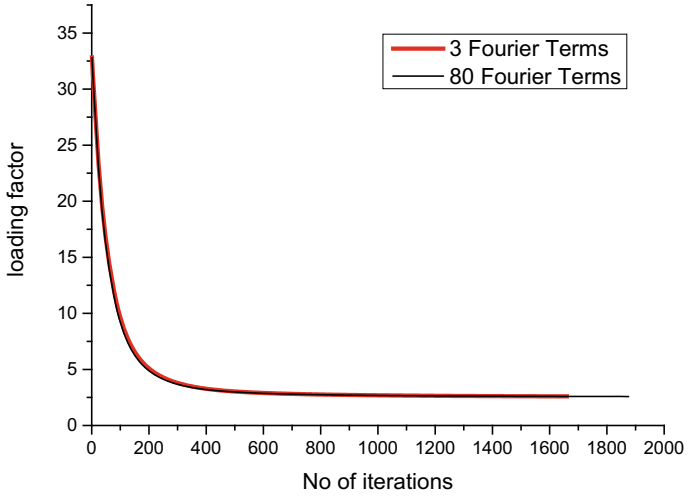

Fig. 8 Comparison of case B and case C

and two cyclic displacements $\bar{u}_1$ and $\bar{u}_2$ varying proportionally from *0* to $\bar{u}_1^*$ and $\bar{u}_2^*$ (Fig. 10) will be investigated. The material properties are E = 180 GPa, v = 0.3 and $\sigma_y = 200$ MPa. The model consists of 220 brick elements. The shakedown limit was estimated, using the RSDM-S for the following cases:

– Case A: Only the displacement $\bar{u}_1$ is applied.
– Case B: Both displacements $\bar{u}_1$ and $\bar{u}_2$ are applied

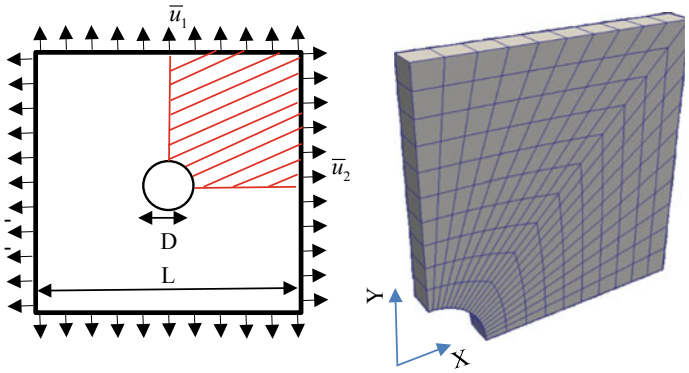

Fig. 9 Geometry, loading and discretization of the slab

Fig. 10 Proportionally imposed displacements

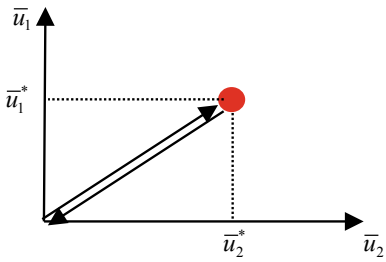

It is pointed out that the results of case A were validated performing step-by-step analyses using the Abaqus software.

In case A the shakedown displacement is equal to 0.15 mm and the convergence appears smooth (Fig. 11). It is pointed out that, the shakedown factor starts from a high value, namely 6000, and quite fast converges to the shakedown limit.

In order to check the validity of the results, step-by-step analyses were performed. The first simulation considered cyclic imposed displacements with magnitude varying from 0 to 0.14 mm. The analysis ran over 100 cycles and the structure finally shaked down and the plastic strain stabilized. Contour plotting of the equivalent plastic strain at the last step is shown in Fig. 12.

The Fig. 13 depicts the evolution of the plastic strain at the critical point A of Fig. 12.

In the second simulation with Abaqus, the magnitude of the imposed displacement varied from 0 to 0.20 mm. The plastic strains developed inside the grey-zone (Fig. 14) were continuously increasing, revealing a ratchet mechanism. Figure 15 depicts the equivalent plastic strain at the critical point A.

In the case B, the displacements $\bar{u}_1$ and $\bar{u}_2$ act, proportionally, along the free sides of the slab. Having performed shakedown analyses with the RSDM-S, for different ratios of $\bar{u}_1^*/\bar{u}_2^*$, the results are depicted in Fig. 16.

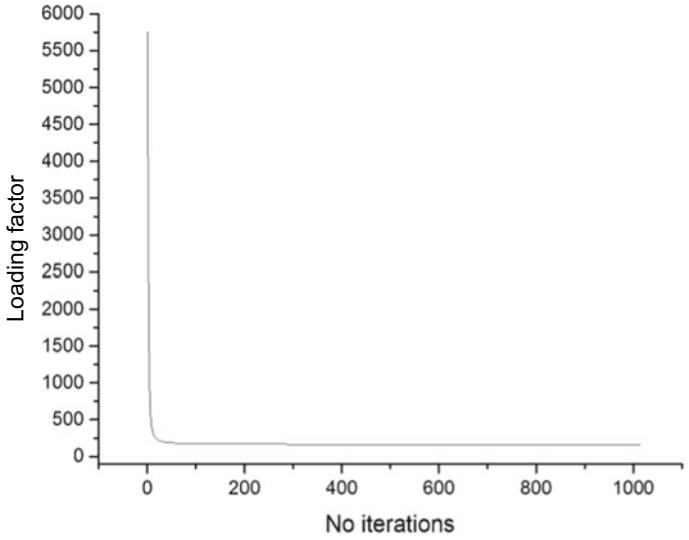

Fig. 11 Convergence of the loading factor

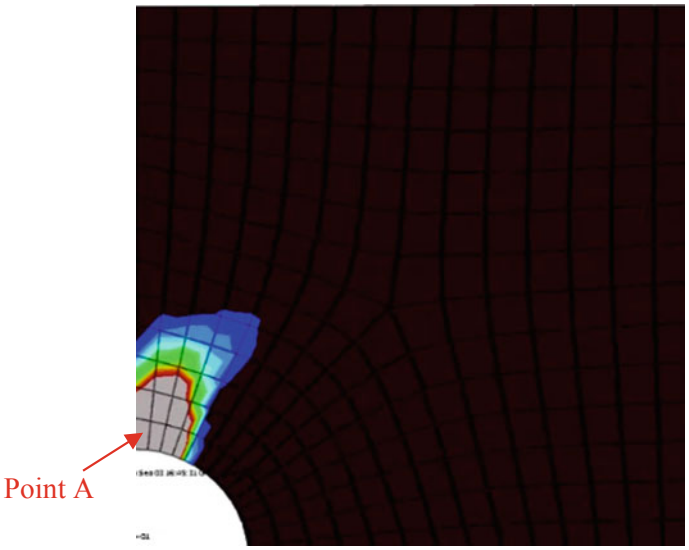

Fig. 12 Contour plot of equivalent plastic strain at the end of the step by step analysis when the magnitude of the imposed displacement is equal to 0.14 mm

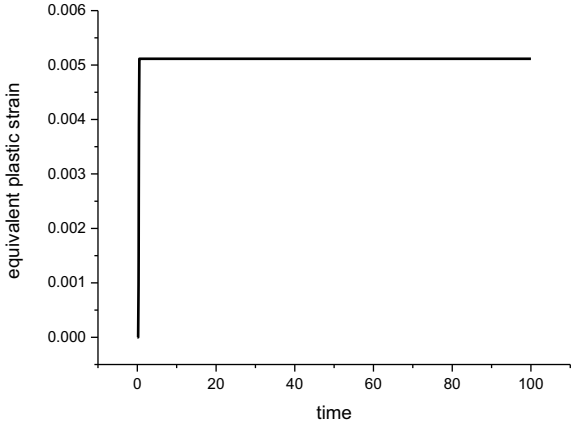

Fig. 13 Equivalent plastic strain of point A in case of 0.14 mm

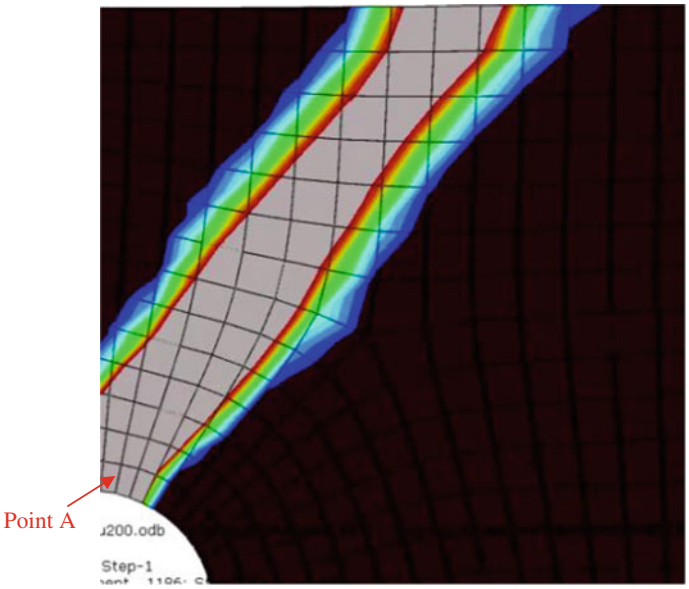

Fig. 14 Contour plot of equivalent plastic strain in the end of step by step analysis when the magnitude of the displacement is equal 0.2 mm

It is pointed out that, in the case of the two imposed displacements, the Abaqus step-by-step analyses could not converge. Thus, the results could not be validated.

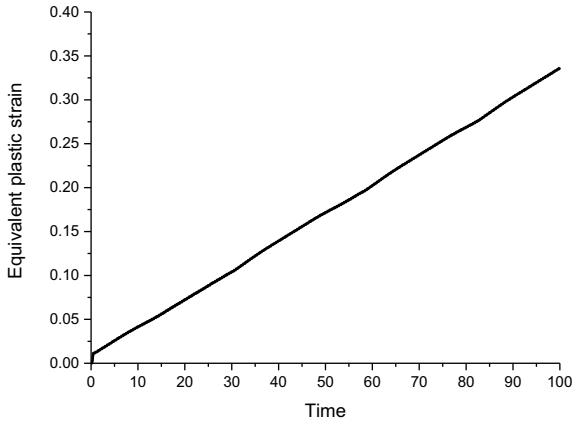

Fig. 15 Equivalent plastic strain of point A in case of the maximum cyclic displacement of 0.2 mm

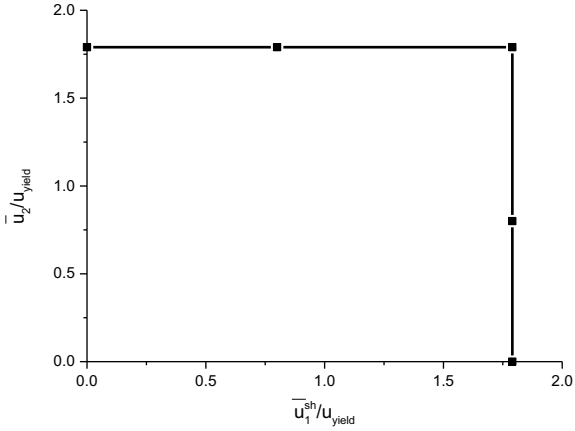

Fig. 16 Shakedown domain in case of two imposed displacements. The yield displacement corresponds to the yielding due to both actions

3.3 The Tee-Junction

This example discusses the shakedown domain for a common tee junction in the case of cyclic imposed displacement. Tee-junctions are widely used for the connection of different piping elements. Being parts of pipelines, these components usually undergo severe repeated earthquake loading.

The junction of Fig. 17 consists of a main pipe, with 8-inch outer diameter, connected to a secondary pipe with a smaller 6-inch diameter. The secondary pipe is also called "branch". In the present example, the main pipe is considered fixed at the ends and the imposed displacements are applied to the free end of the branch.

The model consists of 9936 brick elements. The following load cases were examined

- Case A: The displacement is applied along the X-axis

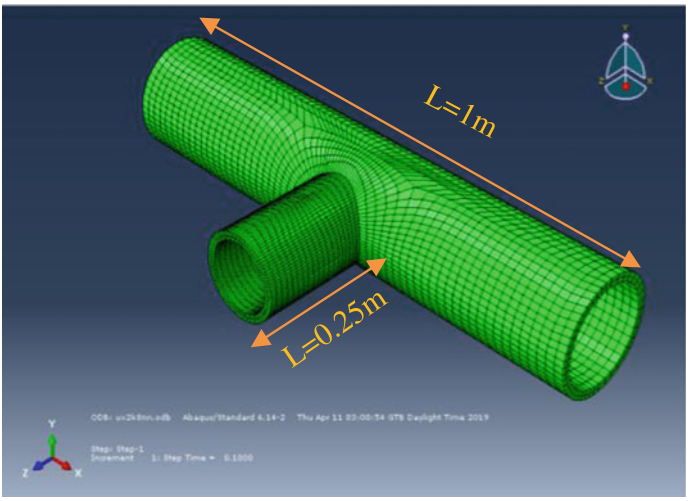

Fig. 17 Mesh of the tee junction

- Case B: The displacement is applied along the Y-axis

In case A the yield displacement is equal to 1.43 mm and the shakedown displacement was estimated, by the RSDM-S, as 2.6 mm. The convergence of the applied displacement towards shakedown is smooth and is presented in the Fig. 18.

The result was validated with step-by-step inelastic analyses, using the Abaqus software. Two different analyses were performed, one below and one above the

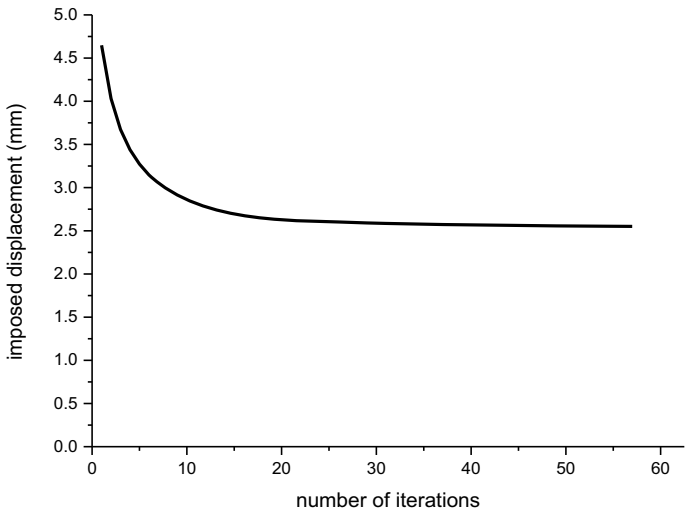

Fig. 18 Convergence of the displacement towards its shakedown value

estimated shakedown value. Thus, the first case run was of a maximum cyclic applied displacement of 2.4 mm, and the second, of 3.2 mm. It turned out that, in the 2.4 mm case the structure shakes down. Figure 19 depicts the spread of the equivalent plastic strain at the last time-step of the analysis. Also, the equivalent plastic strain evolution, in the most stressed point A, is presented in Fig. 20. After the first cycles, the plastic strain does not increase, thus the structure responds elastically.

In the second analysis, the magnitude of the maximum applied displacement was set equal to 3.2 mm. As a result, ratcheting appeared. The Fig. 21 shows the evolution of the equivalent plastic strain for this case, at the same point A.

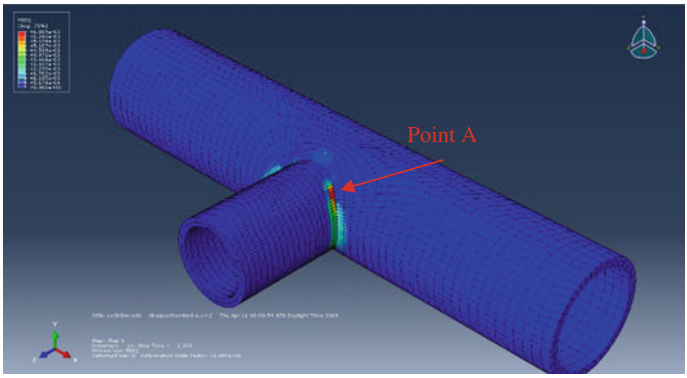

Fig. 19 Contour of the plastic strain in the shakedown state

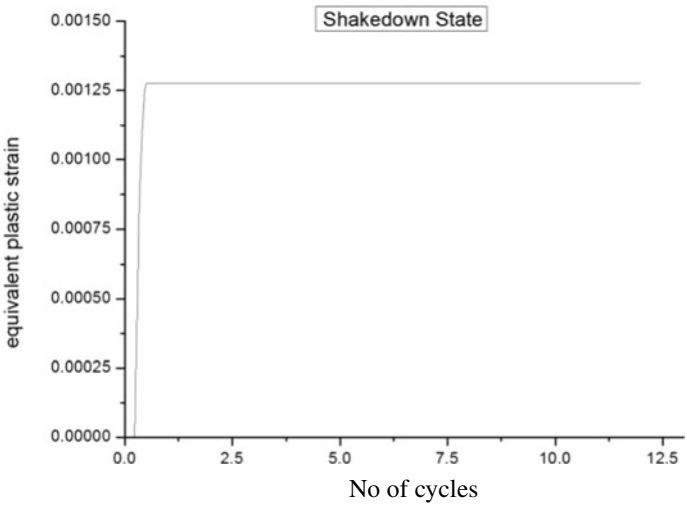

Fig. 20 Equivalent plastic strain evolution for the critical Gauss point for maximum cyclic imposed displacement equal to 2.4 mm

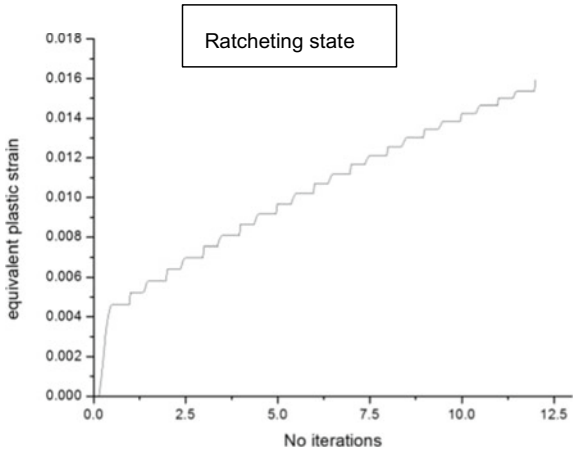

Fig. 21 Equivalent plastic strain evolution for the critical Gauss point for cyclic imposed displacement equal to 3.2 mm

Similar results came up for the case B, where the displacement is applied along the Y-axis. The yield displacement is equal to 1.89 mm and the shakedown displacement evaluated by RSDM-S is equal to 3.2 mm. The convergence of the applied displacement towards shakedown is smooth, as presented in Fig. 22.

Once again for the validation of the results, the problem was imported to Abaqus and was solved twice, using step-by-step analyses. The maximum value of the cyclic displacement was considered equal to 3 mm and 5 mm respectively.

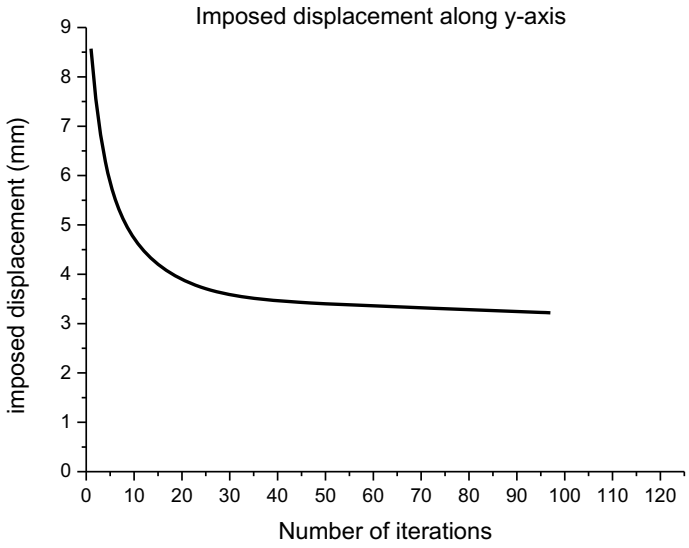

Fig. 22 Convergence of the loading factor in case B

Figure 23 depicts the distribution of the equivalent plastic strain at the last step of the analysis for the 3 mm.

As expected, the structure shakes down, and one may see that the corresponding equivalent plastic strain, for the point A, after a few cycles, does stabilize (Fig. 24).

In the case of greater maximum imposed displacement (5 mm) the structure is shown to have exceeded the shakedown limit and the point A lies on a ratcheting area (Fig. 25).

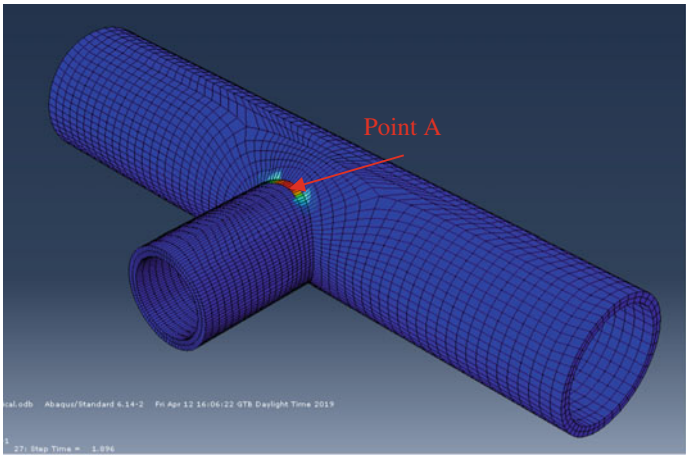

Fig. 23 Distribution of equivalent plastic strain

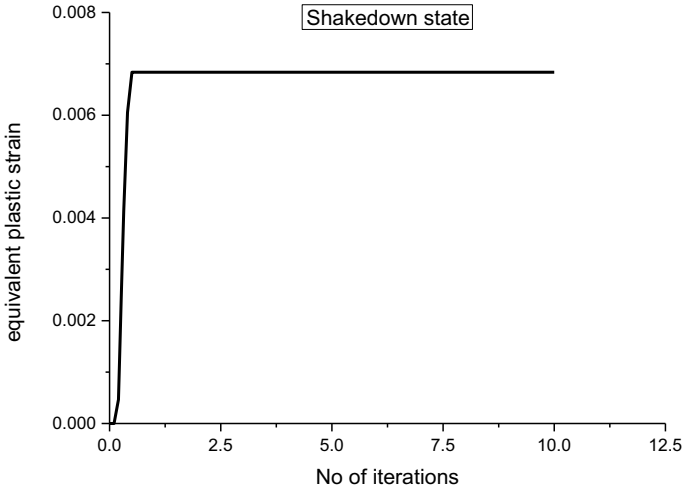

Fig. 24 Equivalent plastic strain evolution for the critical Gauss point for cyclic imposed displacement equal to 3.0 mm (Case B)

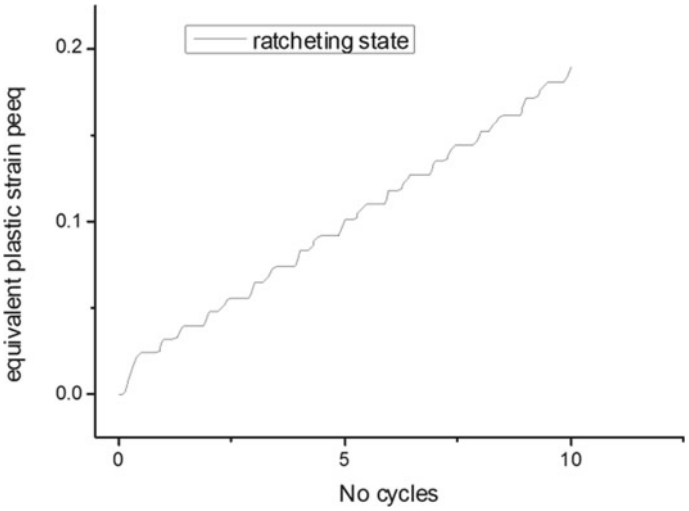

Fig. 25 Plastic strain evolution for the critical Gauss point for cyclic imposed displacement equal to 5.0 mm (Case B)

4 Concluding Remarks

The present work presents an evolution of the Residual Stress Decomposition Method for Shakedown of elastoplastic structures (RSDM-S) towards better efficiency and robustness. It has also been modified to account for cyclically imposed displacements. A convergence factor, which in the previous versions has been used to overcome overshooting, appears not to be working properly for the case of applied displacements. A different factor that was called initial stress multiplication factor was used instead. This factor multiplies the elastic stresses, which for the case of applied displacements could be quite high. It appears to be efficient in all the cases of loading either mechanical or applied displacements. The updated method was used successfully to evaluate the shakedown load and domains of a holed slab and a tee junction, which were subjected to cyclic displacements. As in the previous version of the RSDM-S the use of no more than three Fourier terms together with the least amount of time points to describe the cyclic loading program proved to be enough for an approach that is numerically stable and with a smooth and fast convergence.

Acknowledgements The authors wish to acknowledge the financial support by the State Scholarships Foundation (IKY), through program "Research Projects for Excellence IKY/SIEMENS".

References

1. König, J.: Shakedown of Elastic-Plastic Structures. Elsevier (1987)
2. Zhuang, Y., Wang, K. Y., Li, H. X., Wang, M., Chen, L.: Application of three-dimensional shakedown solutions in railway structure under multiple Hertz loads. Soil Dyn. Earthq. Eng. 328–338 (2019)
3. Qian, J., Dai, Y., Huang, M.: Dynamic shakedown analysis of two-layered pavement under rolling-sliding contact. Soil Dyn. Earthq. Eng. (2020)
4. Hübel, H.: Simplified theory of plastic zones for cyclic loading and multilinear hardening. Int. J. Press. Vessels Pip. **129–130**, 19–31 (2015)
5. Ma, Z., Chen, H., Liu, Y., Xuan, F.Z.: A direct approach to the evaluation of structural shakedown limit considering limited kinematic hardening and non-isothermal effect. Eur. J. Mech. A/Solids (2020)
6. Spiliopoulos, K.V., Panagiotou, K.D.: A residual stress decomposition based method for the shakedown analysis of structures. Comput. Methods Appl. Mech. Eng. **276**, 410–430 (2014)
7. Spiliopoulos, K.V., Panagiotou, K.D.: An enhanced numerical procedure for the shakedown analysis in multidimensional loading domains. Comput. Struct. **193**, 155–171 (2017)
8. Spiliopoulos, K.V., Panagiotou, K.D.: A direct method to predict cyclic steady states of elastoplastic structures. Comput. Methods Appl. Mech. Eng. **223–224**, 186–198 (2012)
9. Spiliopoulos, K.V., Panagiotou, K.D.: The residual stress decomposition method (RSDM): a novel direct method to predict cyclic elastoplastic states. In: Spiliopoulos, K., Weichert, D. (eds.) Direct Methods for Limit States in Structures and Materials, 139–155, Springer Science + Business Media, Dordrecht (2014)
10. König, J.A., Kleiber, M.: On a new method of shakedown analysis. Bulletin del' Academie Polonaise des Sciences, Serie des sciences techniques **26**, 165–171 (1978)
11. Taylor, R.L.: FEAP—Finite Element Analysis Program. University of California, Berkeley (2014). http://www.ce.berkeley/feap
12. Melan, E.: Zur Plastizität des räumlichen Kontinuums. Ing. Arch. **9**, 116–126 (1938)
13. Gokhfeld, D.A., Cherniavsky, O.F.: Limit Analysis of Structures at Thermal Cycling. Sijthoff & Noordhoff (1980)
14. Peng, H., Liu, Y., Chen, H.: A numerical formulation and algorithm for limit and shakedown analysis of large-scale elastoplastic structures. Comput. Mech. **63**, 1–22 (2019)
15. Garcea, G., Armentano, G., Petrolo, S., Casciaro, R.: Finite element shakedown analysis of two-dimensional structures. Int. J. Numer. Methods Eng. **63**, 1174–1202 (2005)
16. Tran, T.N., Liu, G.R., Nguyen, X.H., Nguyen, T.T.: An edge-based smoothed finite element method for primal-dual shakedown analysis of structures. Int. J. Numer. Methods Eng. **82**, 917–938 (2010)

Stress Compensation Method for Shakedown Analysis and Its Engineering Applications

Heng Peng, Yinghua Liu, and Haofeng Chen

Abstract This paper introduces a recently proposed direct method, the so-called stress compensation method (SCM), for shakedown analysis of engineering structures under variable repeated mechanical and thermal loads. Instead of establishing the mathematical programming formulation, the SCM performs a two-level iterative procedure based on a series of linear finite element (FE) solutions. By adding an extra stress (named the compensation stress) to the yield regions which may occur at every load vertex of the given loading domain to adjust the total stress to the yield surface and re-solving the equilibrium equations, the residual stress field for static shakedown analysis is constructed. An effective and robust iteration control scheme is presented to check the change of the compensation stress in the inner loop and to update the shakedown load multiplier in the outer loop. The numerical scheme of this method is successfully implemented into the Abaqus platform, which makes it become a general utility tool for shakedown analysis of complex structures. Numerous examples related to pressure vessel and power plant engineering are presented to illustrate the performance of the method for shakedown analysis of large-scale engineering structures under multi-dimensional loading domain.

Keywords Direct method · Shakedown · Stress compensation method · Cyclic loading

H. Peng · Y. Liu (✉)
Department of Engineering Mechanics, AML, Tsinghua University, Beijing 100084, China
e-mail: yhliu@mail.tsinghua.edu.cn

H. Peng
e-mail: pengheng17@mails.tsinghua.edu.cn

H. Chen
Department of Mechanical and Aerospace Engineering, University of Strathclyde, Glasgow G1 1XJ, UK
e-mail: haofeng.chen@strath.ac.uk

A. A. Pisano et al. (eds.), *Direct Methods*, Lecture Notes in Applied and Computational Mechanics 95, https://doi.org/10.1007/978-3-030-48834-5_8

1 Introduction

In the fields of petrochemical industry, nuclear energy, civil engineering and power plant engineering, many structural components made of ductile metals operate under cyclic loadings. Locally, these components may exhibit material plastic yielding during operation. In this case, it is rather conservative to adopt the traditional elastic analysis design. On the contrary, the limit and shakedown analysis makes use of the plasticity of materials, and therefore reflects the nature of bearing capacity and the actual safety margin of structures. Design methods considering the limit and shakedown analysis are now becoming increasingly popular in practical engineering applications [1].

The shakedown analysis aims to determine the load-bearing capacity of structural components under the action of cyclic loadings, so that these components will not fail due to the instantaneous collapse, incremental collapse or alternating plasticity. As is known that, there are two methods of evaluating the shakedown limit [2]: step-by-step (SBS) incremental procedures and direct method.

In the SBS method, a sequence of cyclic steady calculations at different loading levels are performed, and meanwhile, the loads are adjusted to approach to the shakedown limit using the trial-and-error procedures [2]. However, these time stepping calculation processes are often cumbersome and time-consuming, because every load cycle may include many increments and it usually takes a number of load cycles to compute the response of structure to be stable. Furthermore, the shakedown limit calculated may be inaccurate because of the ambiguous stopping conditions and the accumulative errors in numerical calculations.

In the direct method, the shakedown limit is calculated directly using the shakedown theory, with no needing to perform these cumbersome time stepping calculations. In addition, only the bounding envelope rather than the detailed history of applied loads is required. Most of the direct methods transform the shakedown analysis into a special mathematical programming problem, which contains many equal and unequal restriction conditions. Many optimization methods, such as the second order cone programming [3], the sequential quadratic programming, the complex method [4], the interior point method (IPM) [5, 6], and the nonlinear Newton-type iteration algorithms [7–9], are widely applied for solving the shakedown problems. However, the mesh discretization of finite element (FE) analysis produces a great deal of degrees of freedom, which will generate a large-scale mathematical programming problem, especially when a practical engineering structure is considered. Except for the mathematical programming methods, some other numerical direct methods have been developed which avoid the difficulties of direct optimization, including the elastic compensation method [10, 11], the linear matching method [12–14], the residual stress decomposition method [15, 16], and the stress compensation method (SCM) [17, 18]. Up to now, it is still a challenge and important topic to develop efficient and reliable computational methods so that the limit and shakedown theories can display well their applications in engineering practice and solve broader practical problems.

As one of direct methods recently proposed, the SCM presents good computational advantages in solving the shakedown problem of elastic-perfectly plastic (EPP) material under multiple thermomechanical loadings, especially for large-scale complex engineering structures. In this paper, the authors introduce the SCM from the fundamental theory, the numerical procedure, and its applications to practical engineering structures in the fields of pressure vessel and power plant engineering.

2 SCM for Shakedown Analysis

2.1 Melan's Static Shakedown Theorem

For a body of volume V, the stress $\boldsymbol{\sigma}(\mathbf{x}, t)$ of a point $\mathbf{x}$ at the instant t can be decomposed into a fictitious elastic stress $\boldsymbol{\sigma}^E(\mathbf{x}, t)$ and a residual stress $\boldsymbol{\rho}(\mathbf{x}, t)$, i.e.

$$\boldsymbol{\sigma}(\mathbf{x}, t) = \boldsymbol{\sigma}^E(\mathbf{x}, t) + \boldsymbol{\rho}(\mathbf{x}, t) \tag{1}$$

where $\boldsymbol{\sigma}^E(\mathbf{x}, t)$ is the stress solution of an elastic body with the same geometry and load conditions as the body.

If a structure is subjected to multiple loads $\mathbf{P}_i(\mathbf{x}, t)$, $i = 1, 2, \ldots, N$, where each load $\mathbf{P}_i(\mathbf{x}, t)$ is decided by a time-dependent loading parameter $\mu_i(t)$ and a base load $\mathbf{P}_i^0(\mathbf{x})$. The loading history $\mathbf{P}(\mathbf{x}, t)$ can be expressed as

$$\mathbf{P}(\mathbf{x}, t) = \sum_{i=1}^{N} \mathbf{P}_i(\mathbf{x}, t) = \sum_{i=1}^{N} \mu_i(t)\mathbf{P}_i^0(\mathbf{x}) \tag{2}$$

Referring to Eq. (2), the fictitious elastic stress $\boldsymbol{\sigma}^E(\mathbf{x}, t)$ is expressed as

$$\boldsymbol{\sigma}^E(\mathbf{x}, t) = \sum_{i=1}^{N} \boldsymbol{\sigma}_i(\mathbf{x}, t) = \sum_{i=1}^{N} \mu_i(t)\boldsymbol{\sigma}_i^0(\mathbf{x}) \tag{3}$$

where $\boldsymbol{\sigma}_i^0(\mathbf{x})$ is the elastic stress for the base load $\mathbf{P}_i^0(\mathbf{x})$.

The static shakedown theorem is stated as follows: a body will shake down, if there exists a time-independent residual stress field $\boldsymbol{\rho}(\mathbf{x})$, such that its superposition with the fictitious elastic stress field $\lambda \cdot \boldsymbol{\sigma}^E(\mathbf{x}, t)$, resulting in a stress state $\boldsymbol{\sigma}(\mathbf{x}, t)$, does not violate the yield condition at every material point [19].

$$\boldsymbol{\sigma}(\mathbf{x}, t) = \lambda \cdot \boldsymbol{\sigma}^E(\mathbf{x}, t) + \boldsymbol{\rho}(\mathbf{x}) \tag{4}$$

$$\begin{aligned} f = F(\boldsymbol{\sigma}(\mathbf{x}, t)) - \sigma_y(\theta) \le 0 \qquad & \forall \mathbf{x} \in V, \forall t \\ \nabla \cdot \boldsymbol{\rho}(\mathbf{x}) = 0 \qquad & \text{in } V \\ \boldsymbol{\rho}(\mathbf{x}) \cdot \mathbf{n} = 0 \qquad & \text{on } S_t \end{aligned} \tag{5}$$

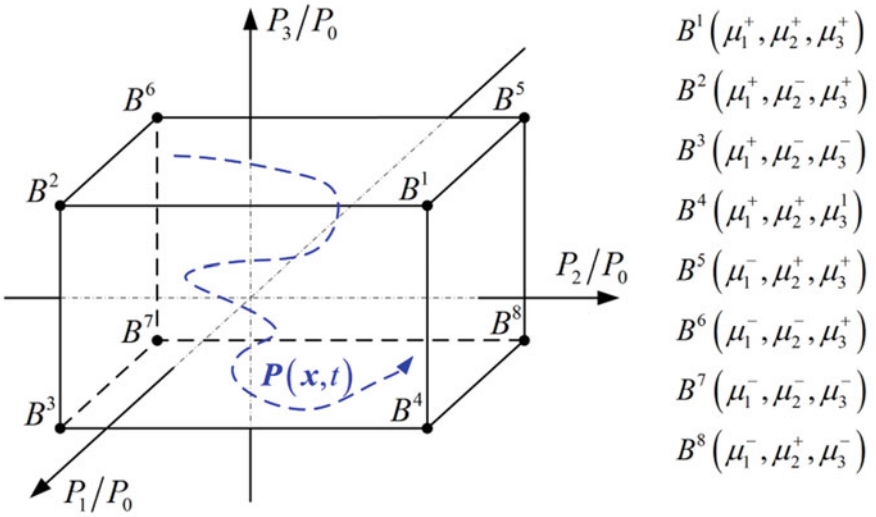

Fig. 1 A polyhedron of eight vertices in 3D loading space [21]

where λ is the load multiplier; f is the yield function; $\sigma_y(\theta)$ is the temperature-dependent yield stress corresponding to temperature θ; $\nabla\cdot$ is the divergence operator; and $\mathbf{n}$ is the unit outward normal to the surface S_t . It is worth noting that the yield function f is required to be convex in $\sigma - \theta$ space [20]. After each update of the load multiplier, the yield stress is also calculated and updated.

It is noted that in most situations the loading parameters $\mu_i(t)$ are not known but only their bounds. If the bounds of each loading parameter are as follows:

$$\mu_i^- \le \mu_i(t) \le \mu_i^+ \tag{6}$$

the bounding envelope of applied loads is determined, which is a polyhedron of $NV = 2^N$ vertices. Figure 1 displays a polyhedron of eight vertices (B^1, B^2, B^3, B^4, B^5, B^6, B^7 and B^8) in three-dimensional (3D) loading space when three loads varying independently within their own limits are considered [21].

The theorem proposed by König indicates that, if a body shakes down over a specific load path traversing all vertices of a polyhedron, then it shakes down over any load path contained within the bounding envelope [2]. Therefore, the shakedown conditions are only tested on these load vertices.

2.2 Description of the SCM

The total strain rate $\dot{\boldsymbol{\varepsilon}}(t)$ contains the elastic strain rate $\dot{\boldsymbol{\varepsilon}}^E(t)$, thermal strain rate $\dot{\boldsymbol{\varepsilon}}_\theta(t)$, plastic strain rate $\dot{\boldsymbol{\varepsilon}}^p(t)$, and residual elastic strain rate $\dot{\boldsymbol{\varepsilon}}_r^e(t)$, i.e.

$$\dot{\boldsymbol{\varepsilon}}(t) = \lambda\left[\dot{\boldsymbol{\varepsilon}}^{E}(t) + \dot{\boldsymbol{\varepsilon}}_{\theta}(t)\right] + \dot{\boldsymbol{\varepsilon}}^{p}(t) + \dot{\boldsymbol{\varepsilon}}_{r}^{e}(t) \tag{7}$$

Making use of the principle of virtual work, the FE global equilibrium equation is established as

$$\left(\int_{V} \mathbf{B}^{T} \cdot \mathbf{D} \cdot \mathbf{B} dV\right) \cdot \dot{\mathbf{u}}(t) = \lambda \int_{V} \mathbf{B}^{T} \cdot \mathbf{D} \cdot \left[\dot{\boldsymbol{\varepsilon}}^{E}(t) + \dot{\boldsymbol{\varepsilon}}_{\theta}(t)\right] dV + \int_{V} \mathbf{B}^{T} \cdot \mathbf{D} \cdot \dot{\boldsymbol{\varepsilon}}^{p}(t) dV \tag{8}$$

Here $\mathbf{D} \cdot \dot{\boldsymbol{\varepsilon}}^{p}(t)$ is replaced by the compensation stress $\boldsymbol{\sigma}^{C}(t)$, which is calculated by

$$\boldsymbol{\sigma}^{C}(t) = \xi(t) \cdot \boldsymbol{\sigma}(t), \xi(t) = \begin{cases} \frac{\bar{\sigma}(t) - \sigma_{y}(\theta)}{\bar{\sigma}(t)} & \left(\bar{\sigma}(t) > \sigma_{y}(\theta)\right) \\ 0 & \left(\bar{\sigma}(t) \le \sigma_{y}(\theta)\right) \end{cases} \tag{9}$$

where $\bar{\sigma}(t)$ is the equivalent stress. Then Eq. (8) is written as

$$\mathbf{K} \cdot \dot{\mathbf{u}}(t) = \lambda \int_{V} \mathbf{B}^{T} \cdot \dot{\boldsymbol{\sigma}}^{E}(t) dV + \lambda \int_{V} \mathbf{B}^{T} \cdot \mathbf{D} \cdot \dot{\boldsymbol{\varepsilon}}_{\theta}(t) dV + \int_{V} \mathbf{B}^{T} \cdot \boldsymbol{\sigma}^{C}(t) dV$$
$$\text{where } \mathbf{K} = \int_{V} \mathbf{B}^{T} \cdot \mathbf{D} \cdot \mathbf{B} dV \tag{10}$$

The residual stress field for static shakedown is obtained by

$$\dot{\boldsymbol{\rho}}(t) = \mathbf{D} \cdot \mathbf{B} \cdot \dot{\mathbf{u}}(t) - \lambda \dot{\boldsymbol{\sigma}}^{E}(t) - \lambda \mathbf{D} \cdot \dot{\boldsymbol{\varepsilon}}_{\theta}(t) - \boldsymbol{\sigma}^{C}(t) \tag{11}$$

$$\boldsymbol{\rho}(t + \Delta t) = \boldsymbol{\rho}(t) + \int_{t}^{t+\Delta t} \dot{\boldsymbol{\rho}}(t) dt \tag{12}$$

The SCM for shakedown analysis consists of two iteration loops. The numerical implementation is as follows:

(1) Calculate the fictitious stress field for each base load, initialize the residual stress field $\boldsymbol{\rho} = 0$, and set an initial load multiplier λ^{ini} . Enter the outer loop where the number of iterations is marked as k.
(2) Enter the inner loop where the number of iterations is marked as m. For each load vertex i, calculate the total stress at every Gauss point.

$$\boldsymbol{\sigma}(t_i) = \lambda^{(k)} \boldsymbol{\sigma}^{E}(t_i) + \boldsymbol{\rho}(t_i) \tag{13}$$

(3) Calculate the compensation stress $\boldsymbol{\sigma}^{C}(t_i)$ and the dimensionless parameter ξ using Eq. (9).
(4) After traversing all the load vertices, the residual stress $\boldsymbol{\rho}_{0}^{(m+1)}$ is updated by Eqs. (14)–(16).

$$\mathbf{K}\cdot\Delta\mathbf{u}=\sum_{i=1}^{NV}\left\{\lambda^{(k)}\int_V\mathbf{B}^T\cdot\left[\Delta\boldsymbol{\sigma}^E(t_i)+\mathbf{D}\cdot\Delta\boldsymbol{\varepsilon}_\theta(t_i)\right]dV+\int_V\mathbf{B}^T\cdot\boldsymbol{\sigma}^C(t_i)dV\right\} \tag{14}$$

$$\Delta\boldsymbol{\rho}=\mathbf{D}\cdot\mathbf{B}\cdot\Delta\mathbf{u}-\lambda^{(k)}\sum_{i=1}^{NV}\Delta\boldsymbol{\sigma}^E(t_i)-\lambda^{(k)}\mathbf{D}\cdot\sum_{i=1}^{NV}\Delta\boldsymbol{\varepsilon}_\theta(t_i)-\sum_{i=1}^{NV}\boldsymbol{\sigma}^C(t_i) \tag{15}$$

$$\boldsymbol{\rho}_0^{(m+1)}=\boldsymbol{\rho}_0^{(m)}+\Delta\boldsymbol{\rho}_0^{(m+1)},\qquad\text{where}\quad\Delta\boldsymbol{\rho}_0^{(m+1)}=\frac{1}{NV}\Delta\boldsymbol{\rho}^{(m+1)} \tag{16}$$

(5) Check the convergence of the dimensionless parameter ξ for all Gauss points using

$$\left|\xi^{(m+1)}(t_i)-\xi^{(m)}(t_i)\right|\le tol1 \tag{17}$$

where $tol1$ is tolerance limit parameter. If ξ is convergent the execution step continues, which means the completion of an inner loop, otherwise the procedure returns to Step (2).

(6) Calculate the maximum value of the dimensionless parameter $\xi^{(m+1)}(t_i)$, i.e.

$$\xi_{\max}^{(k+1)}=\max\left(\xi^{(m+1)}(t_i)\right) \tag{18}$$

(7) Examine the convergence rate

$$\frac{\xi_{\max}^{(k+1)}}{\xi_{\max}^{(k)}}\le tol2,\text{ and }\omega>0.1 \tag{19}$$

where ω is a control parameter. If Condition (19) is satisfied, the load multiplier $\lambda^{(k)}$ is modified by

$$\lambda^{(k+1)}=\frac{\lambda^{(k)}\left(1-\frac{\omega}{2}\cdot\xi_{\max}^{(k+1)}\right)}{\left(1-\omega\cdot\xi_{\max}^{(k+1)}\right)} \tag{20}$$

and ω is halved $\omega=\omega/2$. Otherwise, the load multiplier $\lambda^{(k+1)}$ is updated by

$$\lambda^{(k+1)}=\lambda^{(k)}\left(1-\omega\cdot\xi_{\max}^{(k+1)}\right) \tag{21}$$

(8) Check whether $\xi_{\max}^{(k+1)}$ vanishes within a desired tolerance $tol3$.

$$\xi_{\max}^{(k+1)}\le tol3 \tag{22}$$

(9) Repeat Steps 2–8 till Condition (22) holds. The shakedown limit multiplier λ_{sh} is determined as

$$\lambda_{sh} = \lambda^{(k+1)} \tag{23}$$

The flowchart of the SCM for shakedown analysis is shown in Fig. 2. The iteration control scheme presented allows the numerical procedure to generate a series of decreasing load multipliers, and if the tolerance parameters are appropriately adopted the load multipliers will approach smoothly to the shakedown limit multiplier. The value of $tol1$ in Eq. (17) used to stop the inner loop can influence the accuracy and efficiency of the method. Given that the accuracy of shakedown limit multiplier depends on the final solution of the residual stress and has little relationship to the intermediate solutions, the dynamically changed values of $tol1$ are used here to balance the accuracy and efficiency of the method. The update of load multiplier via Eq. (21) cannot strictly prevent the load multipliers from overshooting below the target value of shakedown limit multiplier. To address this problem, the numerical strategy via (19)–(21) is followed. Although the overshooting might happen in extreme cases, the value is small enough to be negligible. When Condition (19) is satisfied, the load multiplier is adjusted to a value above the shakedown limit multiplier and the process goes on. Thus, the presented method generates a series of decreasing load multiplier approaching to the actual shakedown limit multiplier from above. Because Melan's static shakedown theorem is adopted and when the procedure ends all conditions of this theorem are satisfied, the shakedown limit multiplier calculated is a lower bound solution within the predefined tolerance $tol3$.

3 Numerical Examples and Engineering Applications

The SCM has the significant advantage that it can be incorporated into commercial FE software so that users can establish FE models conveniently. The numerical procedure is implemented into Abaqus platform via user subroutines in this work. The SCM is applied to solve numerous numerical examples. In all examples presented, the materials are assumed homogeneous, isotropic and elastic-perfectly plastic and obey von Mises yield criterion. It is noted that the limit analysis is a special case of shakedown analysis of only one load vertex. All calculations are performed on the computer with 16 GB RAM and Intel Core i7 at 3.39 GHz.

3.1 Square Plate with a Central Circular Hole

The first example is a square plate with a central circular hole under a combination of biaxial mechanical loads and thermal load [18]. Figure 3 displays the structural geometry of $d/L = 0.05$, $D/L = 0.2$ and the quarter FE model. The mesh discretization consists of 432 elements (Abaqus CPS8) with 3×3 Gauss points. The material properties of the structure are listed in Table 1.

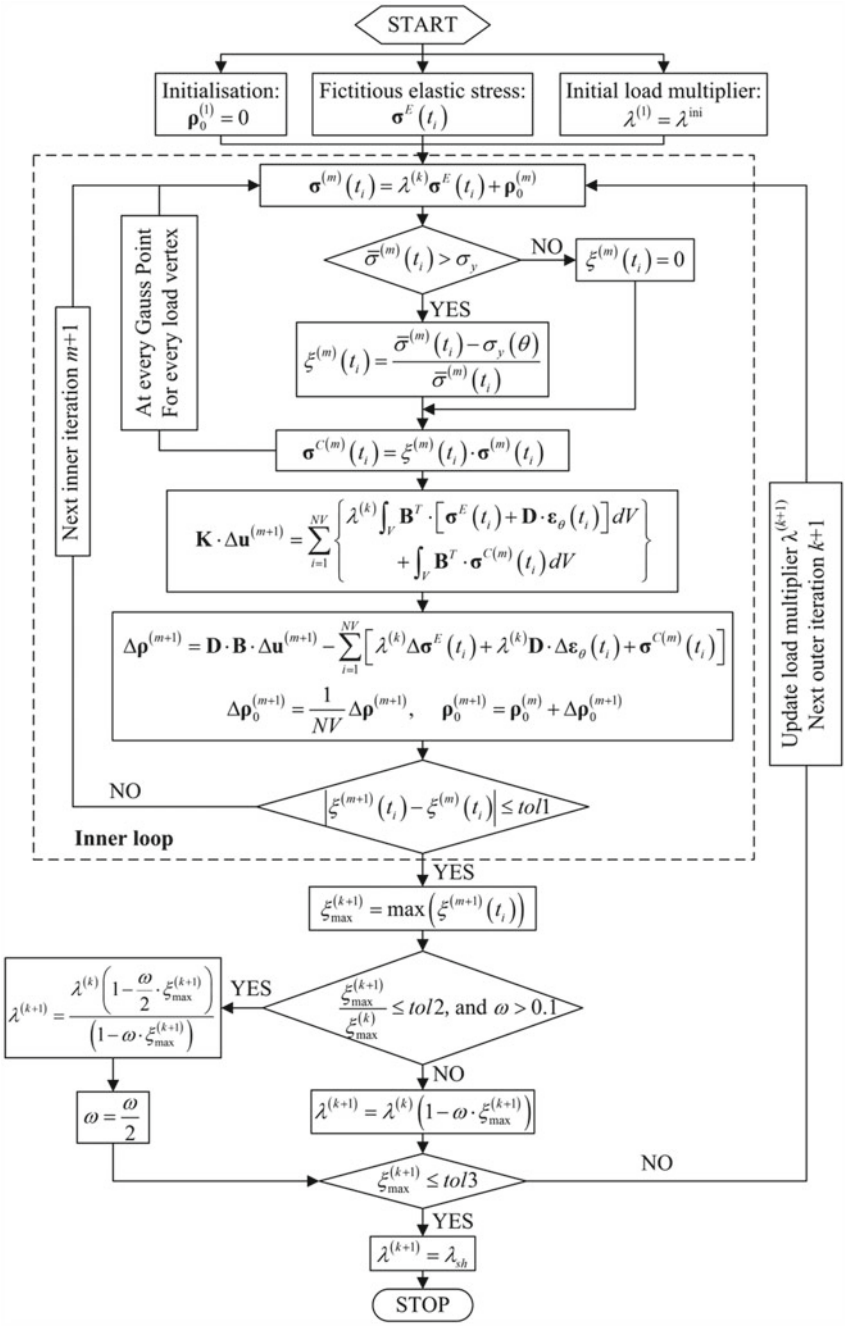

Fig. 2 Flowchart of the SCM for shakedown analysis [21]

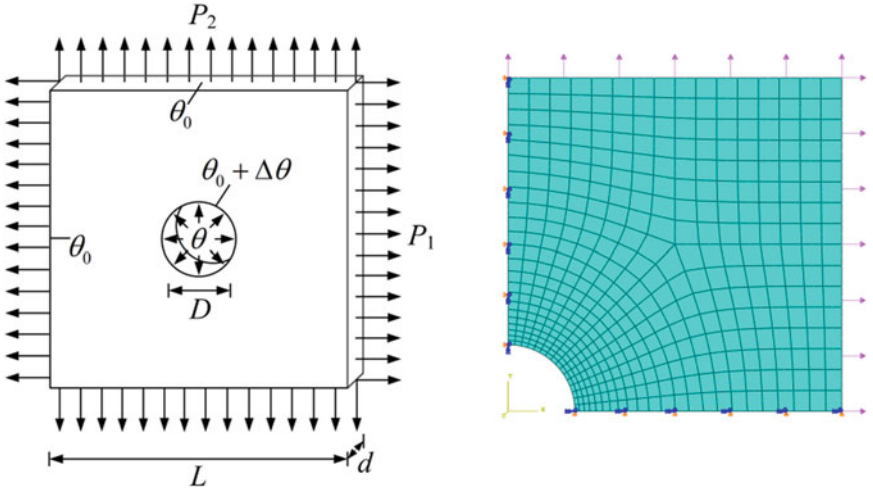

Fig. 3 Geometry of the holed plate and its quarter FE model

Table 1 Material properties of the square plate with a central circular hole

Young's modules E (GPa)	Poisson's ratio v	Yield stress σ_y (MPa)	Coefficient of thermal expansion α ($^\circ C^{-1}$)
208	0.3	360	5×10^{-5}

The holed plate is subjected to three loads, including two uniform normal tractions, P_1 and P_2, and a temperature difference, $\Delta\theta(t)$,

$$\theta = \theta_0 + \Delta\theta \frac{\ln(5D/2r)}{\ln(5)} \tag{24}$$

The base loads are selected as $P_1^* = P_2^* = 360\,\text{MPa}$, $\theta_0 = 0$, and $\Delta\theta^* = 90.2$ °C. The maximum von Mises stress of the holed plate under the base thermal load is σ_θ. Three loading cases are considered here.

(1) Case I

The three loads vary independently in their own ranges.

$$\begin{aligned} 0 \le P_1 &\le \mu_1 P_1^* \\ 0 \le P_2 &\le \mu_2 P_2^* \\ 0 \le \Delta\theta &\le \mu_3 \Delta\theta^* \end{aligned} \tag{25}$$

(2) Case II

The normal traction, P_2, and the thermal load, $\Delta\theta$, vary independently, but the normal traction, P_1, keeps constant.

$$\begin{aligned} P_1 &= \mu_1 P_1^* \\ 0 \le P_2 &\le \mu_2 P_2^* \\ 0 \le \Delta\theta &\le \mu_3 \Delta\theta^* \end{aligned} \tag{26}$$

(3) Case III

The normal tractions, P_1 and P_2, keep constant, but the thermal load, $\Delta\theta$, varies.

$$\begin{aligned} P_1 &= \mu_1 P_1^* \\ P_2 &= \mu_2 P_2^* \\ 0 \le \Delta\theta &\le \mu_3 \Delta\theta^* \end{aligned} \tag{27}$$

The SCM is applied to calculate the shakedown domains of the plate for the three loading cases. Figure 4a, b and c show the 3D shakedown domains of the plate for cases I, II and III, respectively. In Fig. 4a, 111 computed points plot the shakedown surface, consisting of the planes A-B-C and B-C-D. It is noted that all the shakedown limit points are dominated by alternating plasticity. In Fig. 4b, the shakedown surface consists of the plane B-C-D-E and surface A-B-E. It is noted that the points in the plane B-C-D-E are dominated by alternating plasticity whilst the points in the surface A-B-E are dominated by ratcheting. In Fig. 4c, the shakedown surface consists of the surfaces A-B-E-D, B-C-F-E and the plane D-E-F-G. It is noted that the points in the plane D-E-F-G are dominated by alternating plasticity whilst the points in the surfaces A-B-E-D and B-C-F-E are dominated by ratcheting.

To verify the correctness of the calculated results, the SBS incremental elastic-plastic calculations are performed for several specified load points that are depicted as the red, black and blue markers with letters M, N and P in Fig. 4b and c. It should be noted that, in both Fig. 4b and c, the load points M, N, P are located in shakedown region, alternating plasticity region and ratcheting region, respectively. As results, for the load points M, N and P (Fig. 4b), the effective plastic strain histories of a Gauss point over the first 15 load cycles are displayed in Fig. 5. And for the load points M, N and P (Fig. 4c), the effective plastic strain histories of a Gauss point over the first 30 load cycles are displayed in Fig. 6. It can be seen clearly from Fig. 5 and Fig. 6 that the effective plastic strain histories for load points M, N and P exhibit the shakedown, alternating plasticity and ratcheting behavior, respectively. These SBS incremental elastic-plastic analyses reveal the different failure mechanisms expected and verify the correctness the results calculated by the SCM.

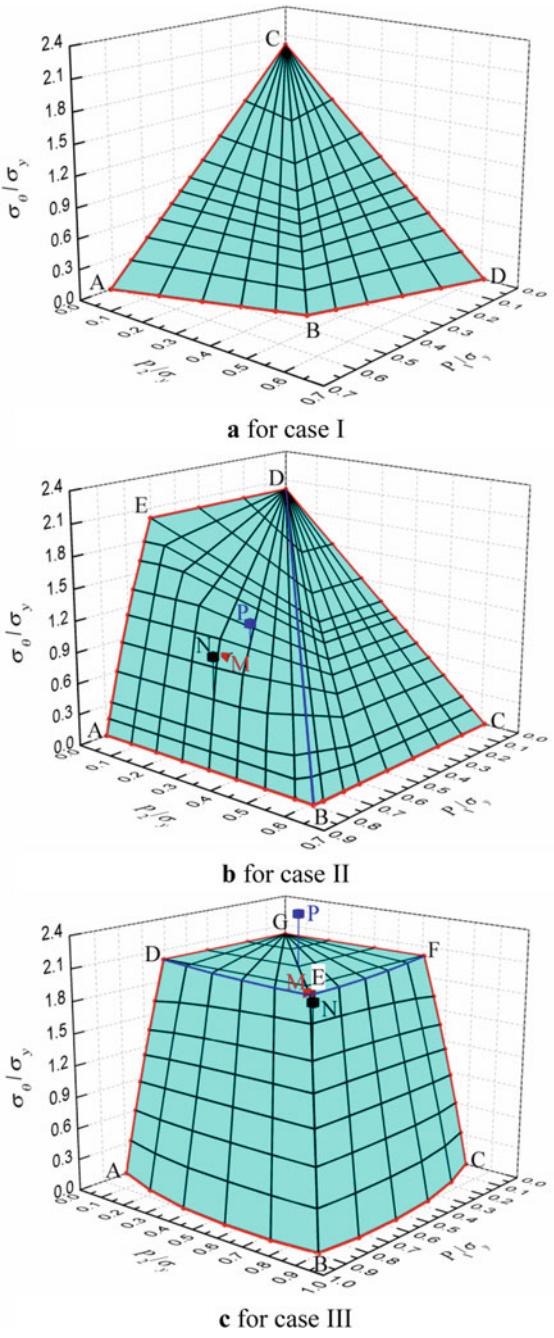

a for case I

b for case II

c for case III

Fig. 4 Shakedown domains of the holed plate in 3D loading space

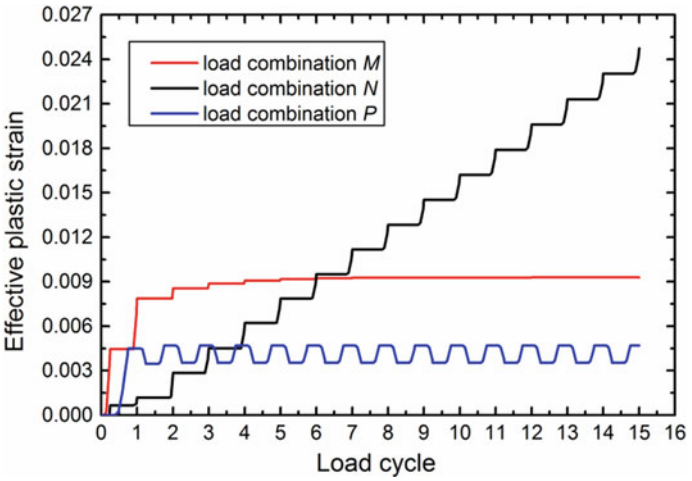

Fig. 5 Effective plastic strains over the first 15 load cycles at a Gauss point of the holed plate from load combinations *M*, *N* and *P* for case II

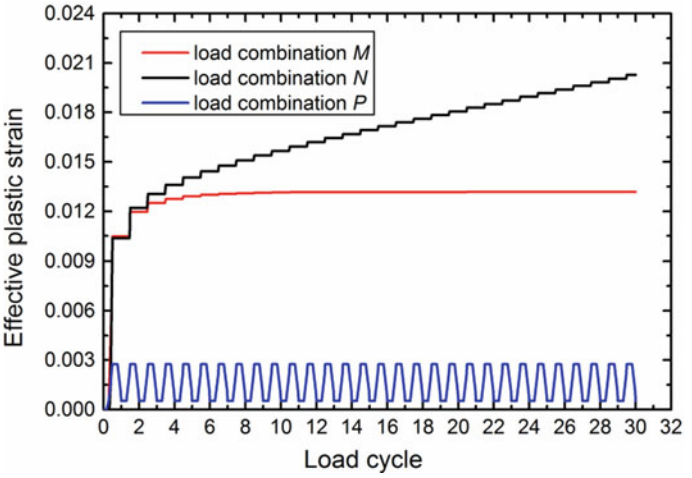

Fig. 6 Effective plastic strains over the first 30 load cycles at a Gauss point of the holed plate from load combinations *M*, *N* and *P* for case III

3.2 Header Component

The second example is a header component from power plant engineering. As shown in Fig. 7, the header component includes a main pipe and two vertical branch pipes with same geometric dimensions. The mesh discretization consists of 27,540 elements (Abaqus C3D20R) and 139,251 nodes, as shown in Fig. 8. The material

properties are listed in Table 2. In the cooling and reheating process, the header component bears complicated load conditions because of the mutual effects with the rest parts of piping system.

Two clusters of loads are applied to the header component, whose base loads are listed in Table 3. For the first load cluster, the internal pressure, P_i, is applied to inner surfaces, and additional tensions caused by the internal pressure are applied to the ends of main and branch pipes. For the second load cluster, the bending moments,

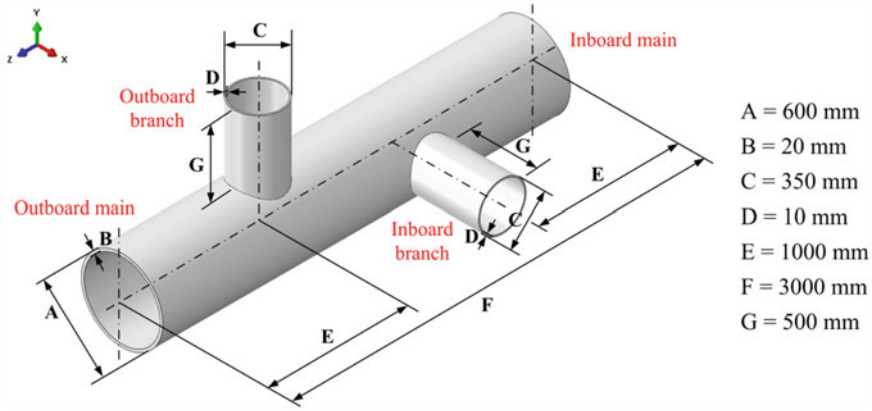

Fig. 7 Geometry of the header component

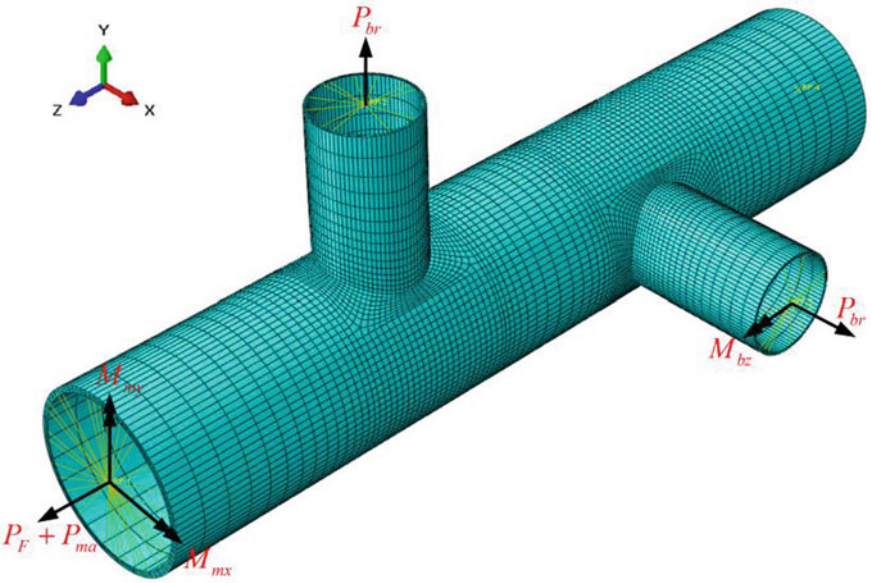

Fig. 8 FE model of the header component

Table 2 Material properties of the header component

Young's modules E (GPa)	Poisson's ratio v	Yield stress σ_y (MPa)
200	0.3	165

M_{mx} and M_{my}, are applied to the outboard main pipe end, and the bending moment M_{bz} is applied to the inboard branch pipe end. It is noted that three bending moments vary simultaneously. Hence, the amplitudes of two clusters of loads are determined by two dimensionless factors, P_0, and M_0. The loading cases of interest are displayed in Fig. 9.

The SCM is applied to calculate the shakedown limits of the header component for the four loading cases. As results, four corresponding shakedown boundaries are presented in Fig. 10. For the loading cases a and b, the shakedown boundaries are all dominated by alternating plasticity whilst for the loading cases c and d, the shakedown boundaries (curve 1 and curve 4 in Fig. 10) are dominated by alternating plasticity and the shakedown boundaries (curve 2 and curve 3 in Fig. 10) are dominated by ratcheting. It is noted that the loading case b is proportional loading. Thus, the

Table 3 Base loads applied to the header component

Load	P_0			M_0		
	Internal pressure P_i (MPa)	Main tension P_{ma} (MPa)	Branch tension P_{br} (MPa)	M_{mx} (kN m)	M_{my} (kN m)	M_{bz} (kN m)
Value	3.64	−24.60	−29.15	240	−160	−9.6

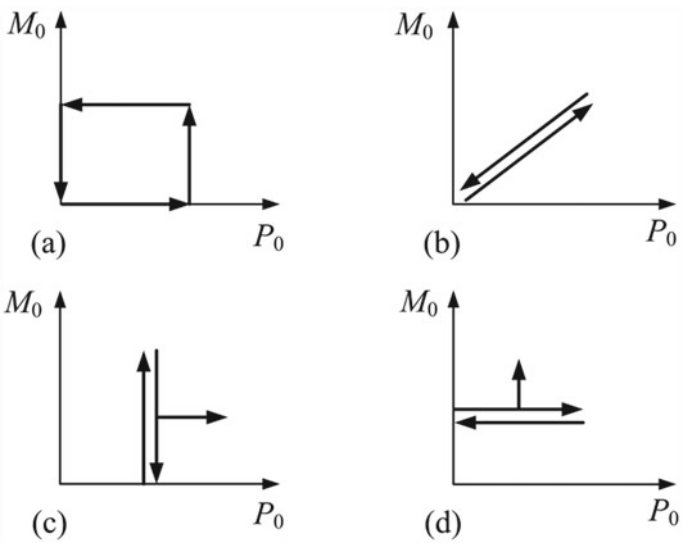

Fig. 9 Four loading cases of interest

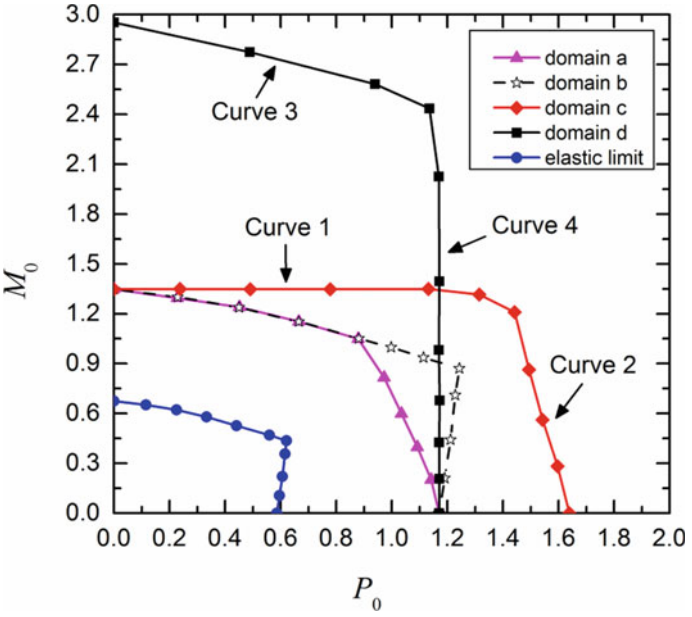

Fig. 10 Shakedown domains of the header component: P_0 versus M_0

shakedown limit will be the lower one between the plastic limit load and the twice of elastic limit load. As a comparison, the elastic boundary is also plotted in Fig. 10. The shakedown boundary curve for the loading case b coincides well with the curve decided by the twice of elastic limit load.

To the authors' knowledge from literature reported, it is the first to show the solution of the shakedown problem with comparable degrees of freedom of FE model [17]. The SCM iterative procedure for shakedown analysis presents good convergence. The CPU time required to complete a calculation does not exceed 40 min using this personal computer. The equivalent residual stress field constructed for static shakedown for the header component is shown in Fig. 11.

3.3 Pipe with an Oblique Nozzle

The third example is a pipe with an oblique nozzle considering the temperature-dependent yield stress. Figure 12 displays the geometry of the structure. This component is subjected to high temperature and internal pressure. When equipment starts up or shuts down, the component bears large temperature variation, and the material properties vary with temperature. Figure 13 displays the FE model that consists of 3,170 elements and 16,928 nodes.

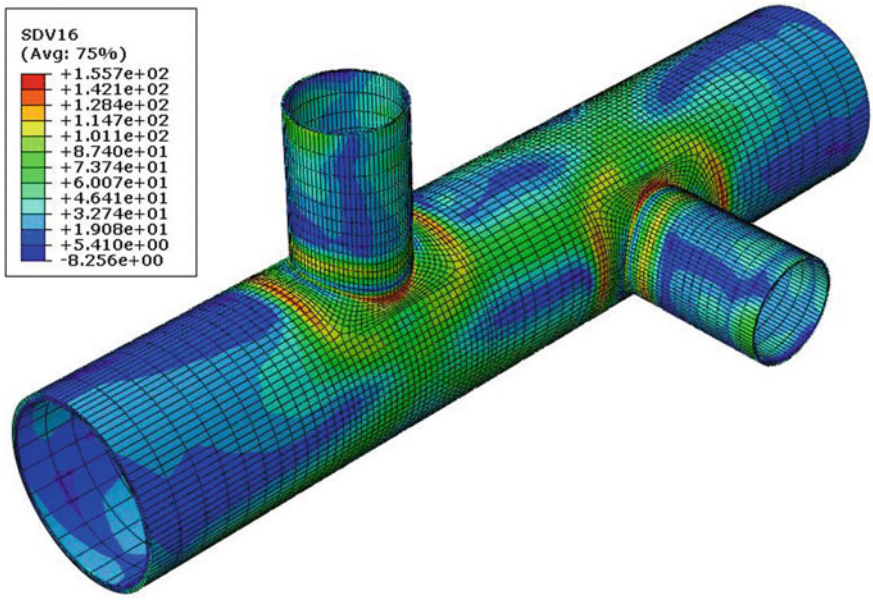

Fig. 11 The equivalent residual stress field constructed for static shakedown for the header component

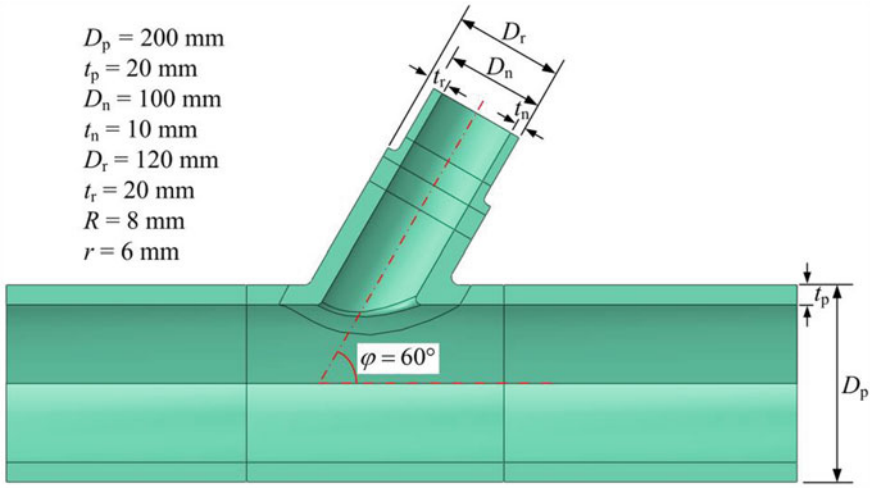

Fig. 12 Geometry of the pipe with oblique nozzle

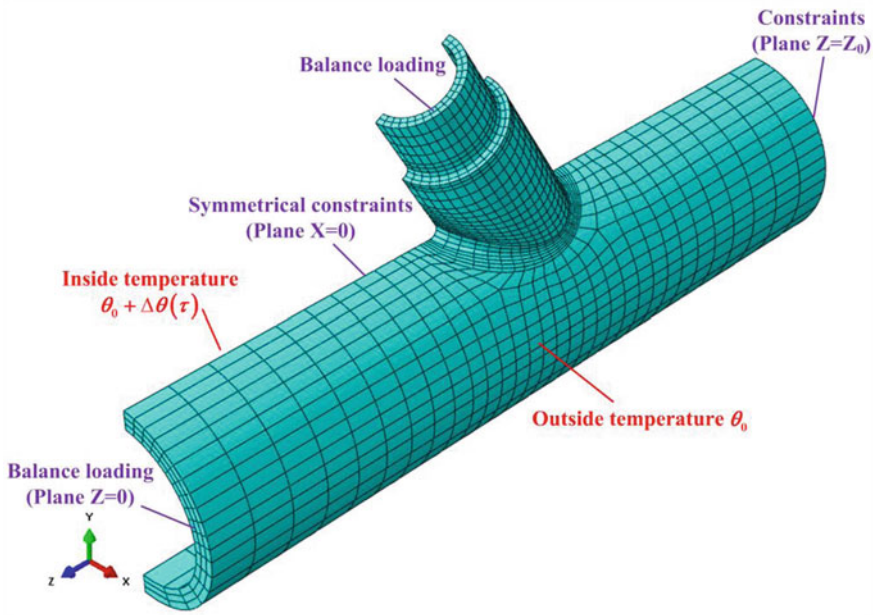

Fig. 13 FE model of the pipe with oblique nozzle

Outside air keeps constant temperature θ_0 and the temperature of inside fluid follows the curve in Fig. 14, which is expressed as $\theta(t) = \theta_0 + \Delta\theta(t)$. The initial temperature of structure and the environment temperature are both $\theta_0 = 20$ °C. The base pressure is $P_0 = 16.5$ MPa. Some material parameters are listed in Table 4. The temperature-dependent yield stress is as follow:

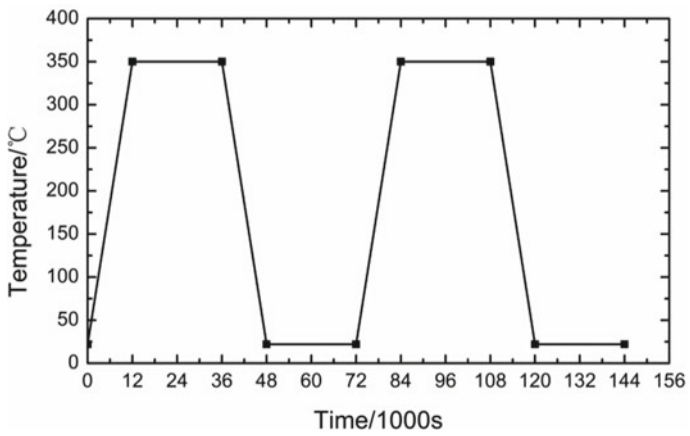

Fig. 14 Temperature history of the inside fluid

Table 4 Material parameters of the pipe with oblique nozzle

Parameters	Value
Thermal expansion coefficient α	2.0×10^{-5}
Thermal conductivity k (W/(m °C))	20
Specific heat capacity c (J/(kg·°C))	440
Transfer coefficient pipe-air h_1 (W/(m^2·°C))	300
Transfer coefficient pipe-fluid h_2 (W/(m^2·°C))	800
Density ρ (kg/m^3)	7800
Yield stress σ_y (MPa)	240
Young's modulus E (MPa)	2.1×10^5
Poisson's ratio v	0.3

$$\sigma_y(\theta) = \sigma_{y_0} + 3\ \text{MPa} - 0.15\ \text{MPa}/^{\circ}\text{C} \times \theta \tag{28}$$

First, the temperature history is calculated via a transient heat transfer analysis. Then, the thermal elastic stress history is calculated based on the obtained temperature via the structural stress analysis. Nodes 5,451 and 6,308 are selected to show the temperature histories of inside and outside surfaces of the structure, as displayed in Fig. 15. It is obvious from Fig. 15 that the structure bears the maximum temperature gradient at $t = 12{,}000$ s, which leads to the maximum thermal elastic stress. Figure 16a and b, display the von Mises stress fields of the pipe under single thermal load and single base pressure, respectively. Figure 17 displays two typical loading cases considered. For loading case I, temperature and internal pressure vary independently. For loading case II, temperature is cyclic but internal pressure keeps constant. The SCM is applied to calculate the shakedown limits of this pipe considering the temperature-dependent yield stress.

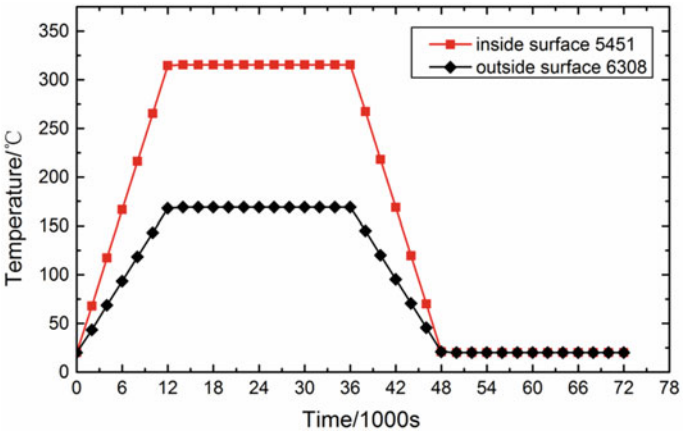

Fig. 15 Temperature histories of node 5451 and node 6308

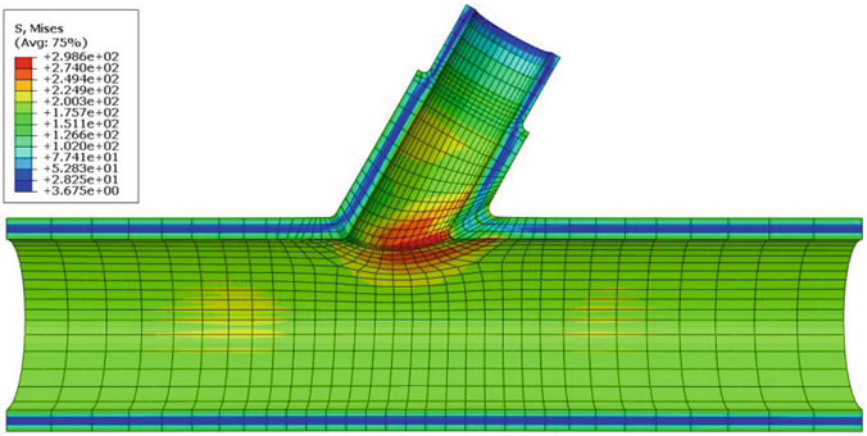

a Thermal stress field at t=12000 s

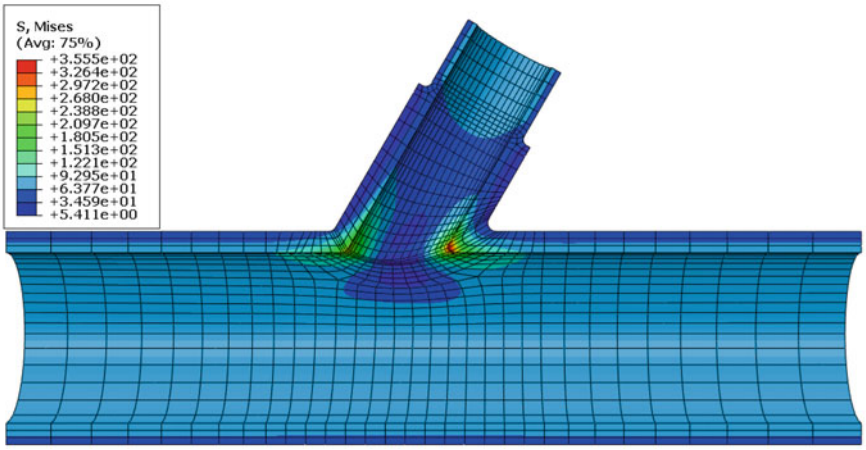

b Mechanical stress field

Fig. 16 Von Mises stress fields of the pipe with oblique nozzle

The shakedown domains of the pipe considering the temperature-dependent and temperature-independent yield stresses for two loading cases are shown in Fig. 18. For loading case I, shakedown boundaries AD and A′D are dominated by alternating plasticity. For loading case II, shakedown boundaries AB and A′B′ are dominated by alternating plasticity but shakedown boundaries BC and B′C are dominated by ratcheting. For both loading cases, shakedown boundaries are narrowed when considering the reduction of yield stress by temperature. It is noted that in regions AB and A′B′, the thermal loading is dominant and the yield stress is largely reduced by high temperature, thus the shakedown limit is significantly decreased.

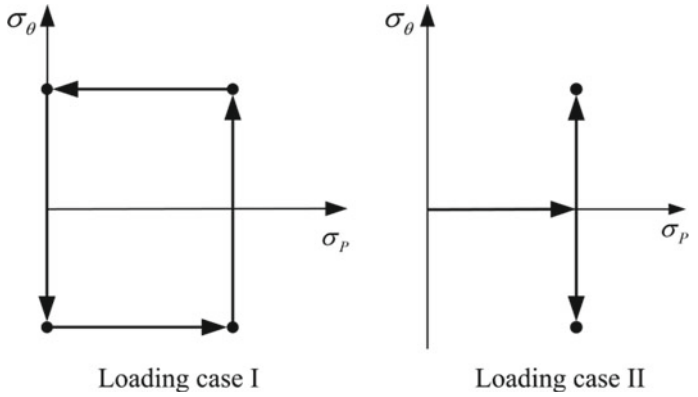

Fig. 17 Two typical loading cases

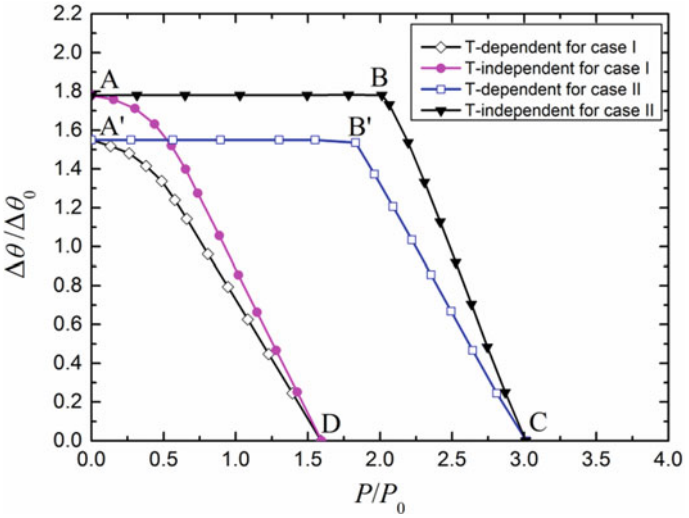

Fig. 18 Shakedown domains of the pipe with oblique nozzle considering temperature-dependent and temperature-independent yield stresses under two loading cases

Figure 19 displays a typical iteration process of load multipliers for shakedown analysis of the pipe with oblique nozzle considering the temperature-dependent yield stress. The horizontal segment indicates the execution of inner loop whilst the leap indicates an update of the load multipliers in the outer loop. The CPU time required for each iteration is about one quarter of that for a complete elastic FE analysis.

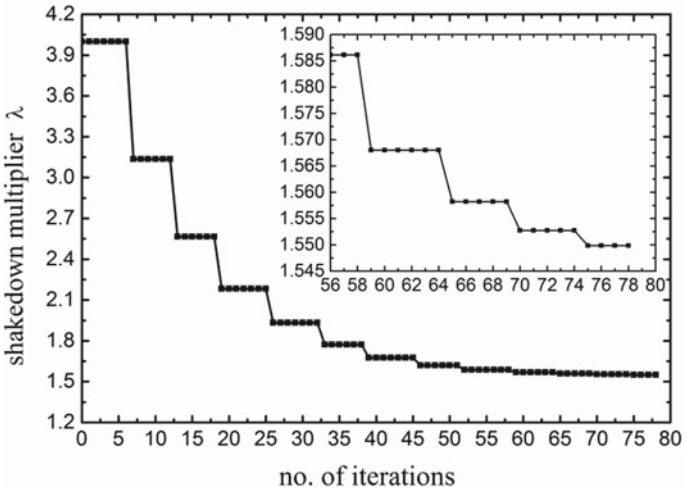

Fig. 19 Typical iteration process of load multipliers for shakedown analysis of the pipe with oblique nozzle considering the temperature-dependent yield stress

3.4 Torispherical Head with a Piping Nozzle

The forth example is a torispherical head with a piping nozzle, whose geometric parameters are shown in Fig. 20 [21–24]. The applied loads include uniform pressure P, axial force F, in-plane bending moment M_{in}, out-of-plane bending moment M_{out}, twisting moment T, and thermal loading defined by a temperature difference $\Delta\theta$. The basic material properties are listed in Table 5.

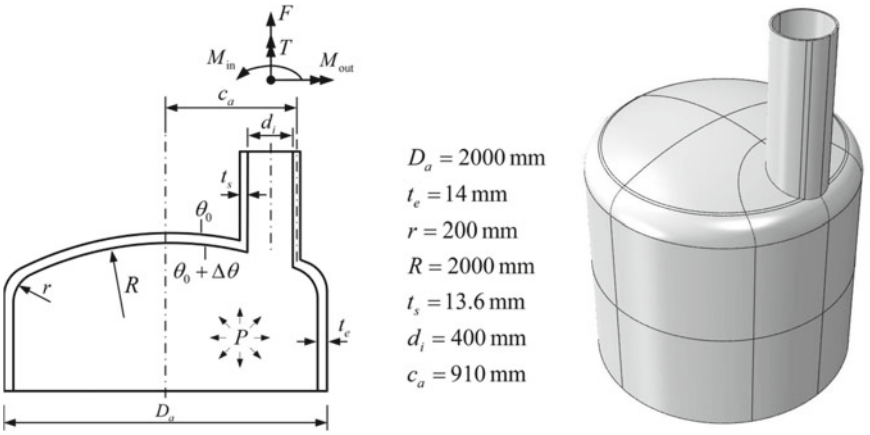

Fig. 20 Geometry of the torispherical head with a piping nozzle

Table 5 Material properties of the torispherical head with a piping nozzle

Yield stress, σ_{y0} (MPa)	340
Young's modulus, E (MPa)	2.0×10^5
Poisson's ratio, v	0.3
Coefficient of thermal expansion, α (/°C)	1.6×10^{-5}
Specific heat capacity, c (J/(kg·°C))	500
Thermal conductivity, k (W/(m·°C))	15
Density, ρ (kg/m^3)	7900

Figure 21 displays the FE model of the torispherical head with a piping nozzle that includes 10,809 elements (Abaqus C3D20R) and 54,804 nodes. To eliminate boundary effects, the lengths of nozzle and of cylindrical shell are about $3d_i$ and D_a, respectively. The cylindrical shell end is restrained in vertical direction but is free in radial direction. It is noted that an additional equivalent axial tension induced by internal pressure is applied to the nozzle end. All nozzle loads are applied to a master node which is coupled to the nozzle end using the Beam-type MPC constraint technique.

The SCM is applied to calculate the plastic limit and shakedown limit loads of the torispherical head with a piping nozzle under various loading conditions, whose results are listed in Table 6. For comparison and verification, the results calculated by the elastic-plastic incremental method within Abaqus are also listed in Table 6. It is noted that the plastic limit load is determined by 15-times elastic slope criterion

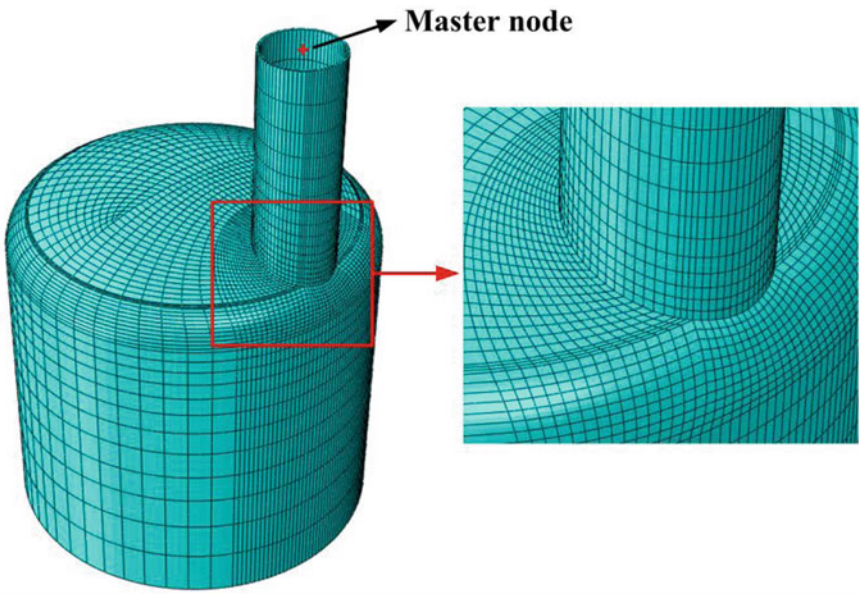

Fig. 21 FE model of the torispherical head with a piping nozzle

Table 6 Shakedown limit and plastic limit loads calculated with two methods

Loading case	SCM		Abaqus	
	Shakedown limit load	Plastic limit load	Double elastic limit load	Plastic limit load
Pressure, P (MPa)	3.004	3.511	3.004	3.523
Axial force, F (kN)	833.8	1451.8	833.9	1463.2
Twisting moment, T (kN m)	364.5	546.4	364.5	551.9
Out-of-plane moment, M_{out} (kN m)	127.9	237.8	127.9	239.2
In-plane moment, M_{in} (kN m)	107.6	248.7	107.7	252.1
Thermal loading, $\Delta\theta$ (°C)	236.0	–	236.0	–

[23] is adopted and the shakedown limit load is determined as the lower one between the plastic limit load and the twice of elastic limit load.

It is evident from Table 6 that the shakedown limit loads calculated with the SCM are very close to the twice of elastic limit loads calculated with Abaqus and are lower than the plastic limit loads. This indicates that these shakedown limit loads are all dominated by alternating plasticity. Furthermore, the good agreement, a maximum relative error of 1.36%, of the plastic limit loads calculated with the SCM and Abaqus shows that the SCM is reliable. It is noted that the thermal loading, causing secondary stress, will not lead to the plastic collapse of structures.

For further comparison, Table 7 gives the comparison of the present solutions [21] with results from literature [22, 23] for different single loads. The present results are approximately in agreement with these reported in [22, 23]. The small difference in value is due to different methods used and different types and sizes of FE meshes selected.

The 3D shakedown domains of the torispherical head with a piping nozzle are investigated. The loading conditions of interest include three independently varying loads, as listed in Table 8. The corresponding loading domain is similar to that displayed in Fig. 1.

As results, four 3D shakedown domains obtained by the SCM are displayed in Figs. 22, 23, 24 and 25. It is noted that the dimensionless loads, normalised by the yield stress σ_{y_0}, are adopted, and more than 100 calculated points are used to depict each of the shakedown boundary surface. In these figures, the red lines represent the

Table 7 Comparison of the present solutions with results from literature

Type	Loading case	Present [21]	Hsieh [23]	Simon [22]
Elastic limit load	Pressure (MPa)	1.502	1.370	1.524
	Axial force (kN)	416.9	450.0	483.1
	In-plane moment (kN m)	53.9	64.7	55.4
	Out-of-plane moment (kN m)	64.0	66.5	–
	Twisting moment (kN m)	182.3	193.8	–
Shakedown limit load	Pressure (MPa)	3.004	–	3.047
	Axial force (kN)	833.8	–	965.9
	In-plane moment (kN m)	107.6	–	110.7
	Out-of-plane moment (kN m)	127.9	–	–
	Twisting moment (kN m)	364.5	–	–
Plastic limit load	Pressure (MPa)	3.511	3.54	–
	Axial force (kN)	1451.8	1630.0	–
	In-plane moment (kN m)	248.7	282.6	–
	Out-of-plane moment (kN m)	237.8	265.8	–
	Twisting moment (kN m)	546.4	625.0	–

Table 8 3D loading domains of interest

Loading condition	Loading domain
P, F, and M_{in}	$0 \le P \le \mu_1^+ P_0,\ 0 \le F \le \mu_2^+ F_0$ and $0 \le M_{\text{in}} \le \mu_3^+ M_{\text{in0}}$
P, F, and M_{out}	$0 \le P \le \mu_1^+ P_0,\ 0 \le F \le \mu_2^+ F_0$ and $0 \le M_{\text{out}} \le \mu_3^+ M_{\text{out0}}$
P, F, and T	$0 \le P \le \mu_1^+ P_0,\ 0 \le F \le \mu_2^+ F_0$ and $0 \le T \le \mu_3^+ T_0$
P, F, and $\Delta\theta$	$0 \le P \le \mu_1^+ P_0,\ 0 \le F \le \mu_2^+ F_0$ and $0 \le \Delta\theta \le \mu_3^+ \Delta\theta_0$

shakedown boundary curves of the structure under specific two-dimensional loading domains.

In above examples, the material properties are independent to temperature (see Table 5). Here a temperature-dependent yield stress $\sigma_y(\theta)$ is considered, which is a linear function of θ, i.e.

$$\sigma_y(\theta) = \sigma_{y_0} - 0.3 \times (\theta - 20\ ^\circ\text{C}) \tag{29}$$

Taking a loading condition as an example, i.e.

$$0 \le P \le \mu_1^+ P_0,\ 0 \le F \le \mu_2^+ F_0 \text{ and } 0 \le \Delta\theta \le \mu_3^+ \Delta\theta_0 \tag{30}$$

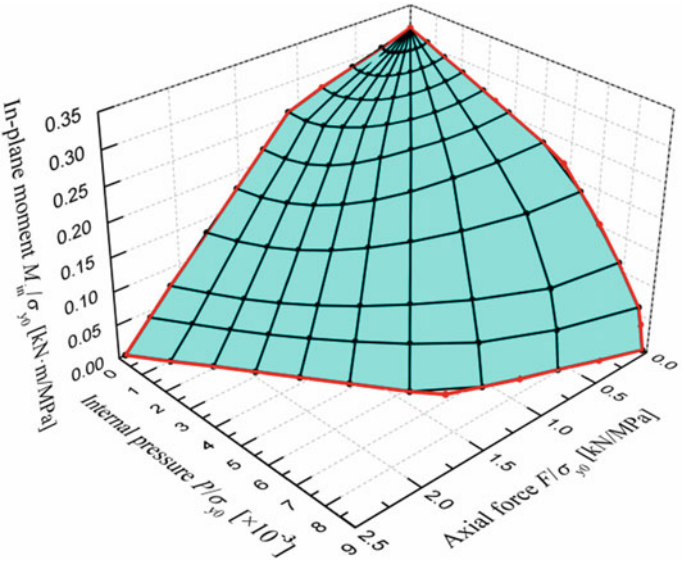

Fig. 22 3D shakedown domain: in-plane bending moment, internal pressure, and axial force

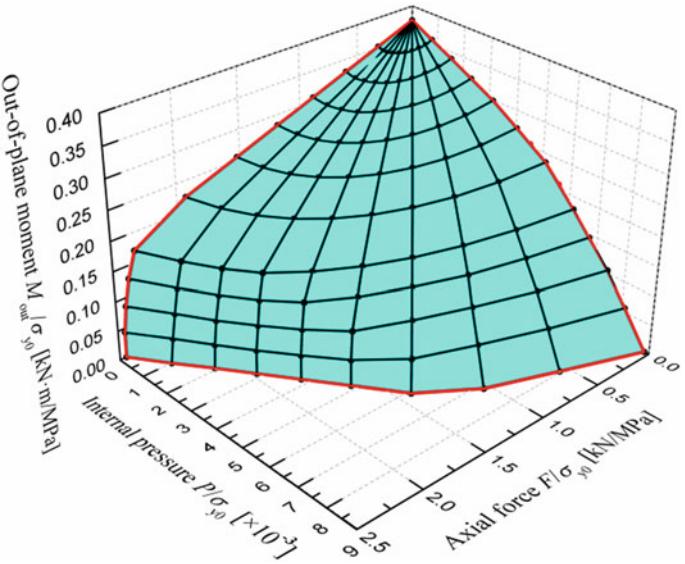

Fig. 23 3D shakedown domain: out-of-plane bending moment, internal pressure, and axial force

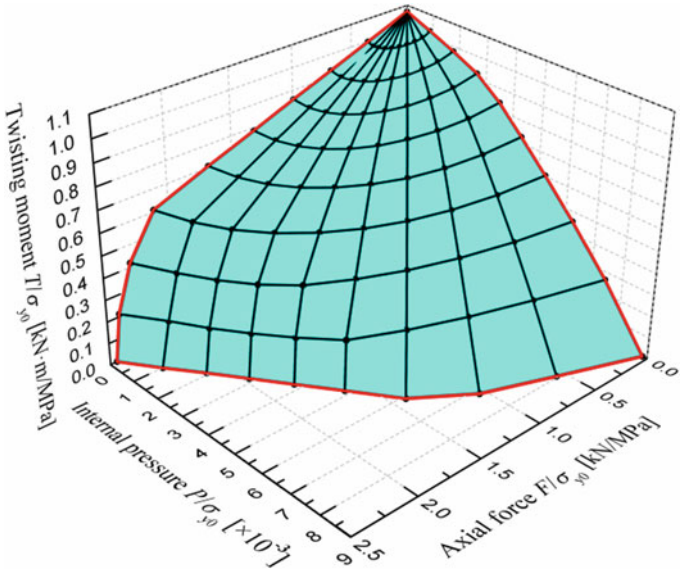

Fig. 24 3D shakedown domain: twisting moment, internal pressure, and axial force

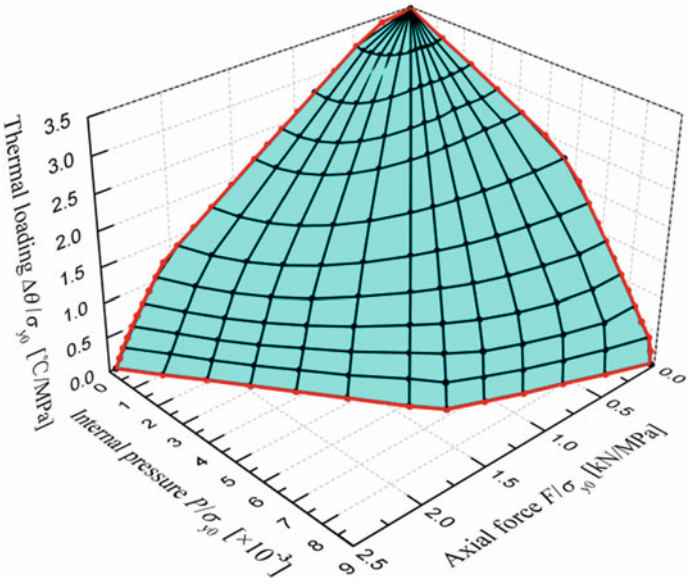

Fig. 25 3D shakedown domain: thermal loading, internal pressure, and axial force

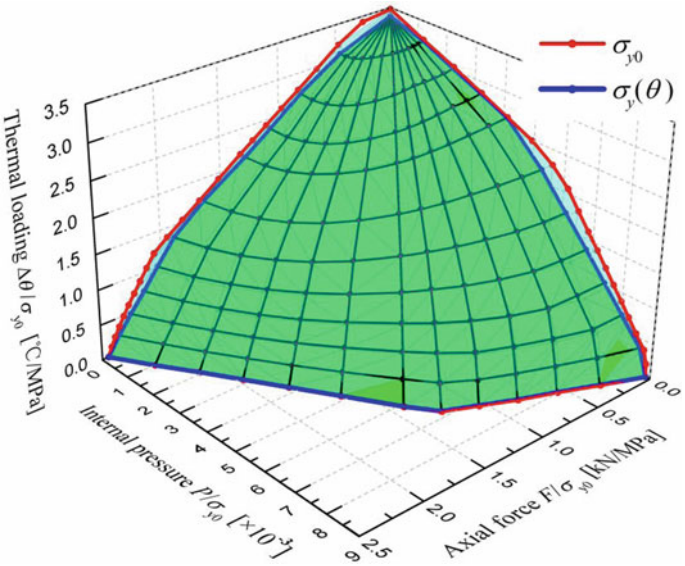

Fig. 26 3D shakedown domains with the temperature-dependent and temperature-independent yield stresses: thermal loading, internal pressure, and axial force

the resulting 3D shakedown domain considering the temperature-dependent yield stress $\sigma_y(\theta)$ is displayed as the green surface in Fig. 26. For comparison, the 3D shakedown domain with a constant yield stress σ_{y0} is displayed in Fig. 26 (the cyan surface) additionally.

Although the same geometric parameters and similar loading conditions with the paper by Simon et al. [22] are used, the completely different shakedown analysis method is employed to demonstrate the performance of the presented SCM in solving large-scale shakedown problem. More complicated loading cases including out-of-plane moment is considered in this paper so that the full geometric model is established while only one-half of the geometric model is adopted in [22]. In addition, this paper investigates the influence of temperature-dependent yield stress on shakedown boundary. In general, when using the mathematical programming method, such as the IPM, to solve shakedown problem, the computing time depends on the number of loads [22, 25]. However, the computing time has little relationship to the loading scenario using the SCM presented in this paper. For a FE model consisting of 10,809 quadratic elements and 54,804 nodes in this numerical example, the CPU time required by the SCM varies from 0.2 h to 0.4 h, while for a FE model consisting of 6,376 linear elements and 9,645 nodes, the computing time by the IPM is less than 10 h [22]. It is evident that the SCM is capable of solving the shakedown problem for large-scale practical engineering structures in reasonable time.

4 Concluding Remarks

In this paper, a recently proposed direct method, SCM, has been introduced to solve the shakedown problem for large-scale practical engineering structures considering the complex loading conditions. In first, the theoretical and numerical aspects of the SCM have been presented. The SCM includes the two-level iterative procedure based on a series of linear FE solutions, instead of using a mathematical programming technique. The inner loop constructs the residual stress field for static shakedown while the outer loop updates load multipliers using an effective and robust iteration control scheme. Then the numerical procedure of the SCM has been implemented into the Abaqus platform, making it become a general utility tool for shakedown analysis of complex structures. Next four numerical examples, including square plate with a central circular hole, header component, pipe with an oblique nozzle, torispherical head with a piping nozzle, have been presented to illustrate the performance of the method. The 3D loading domain and the effect of temperature on yield stress have also been considered. The calculated results have been validated with the SBS elastic-plastic incremental method and results from literature. It has been proven that the SCM is a powerful tool for performing shakedown analysis of large-scale structures under complex multi-loading systems with huge computational advantage, and has application prospects in the structural design and integrity assessment of practical engineering structures. Although the present paper only introduces the application of the method to the elastic-perfectly plastic material, the shakedown analysis with consideration of material hardening has been accomplished and these works will be reported in forthcoming paper.

Acknowledgements The authors gratefully acknowledge the support of the National Science Foundation for Distinguished Young Scholars of China (Grant No. 11325211) and the National Natural Science Foundation of China (Grant No. 11672147).

References

1. Weichert, D., Ponter, A.: A historical view on shakedown theory. In: Stein, E. (ed.) The History of Theoretical, Material and Computational Mechanics-Mathematics Meets Mechanics and Engineering, pp. 169–193. Springer (2014). https://doi.org/10.1007/978-3-642-39905-3_11
2. König, J.A.: Shakedown of Elastic-Plastic Structures. Elsevier, Warszawa, Poland (1987)
3. Makrodimopoulos, A., Martin, C.M.: Lower bound limit analysis of cohesive-frictional materials using second-order cone programming. Int. J. Numer. Meth. Eng. **66**(4), 604–634 (2006). https://doi.org/10.1002/nme.1567
4. Zhang, X.F., Liu, Y.H., Zhao, Y.N., Cen, Z.Z.: Lower bound limit analysis by the symmetric Galerkin boundary element method and the Complex method. Comput. Method Appl. Mech. **191**(17–18), 1967–1982 (2002). https://doi.org/10.1016/s0045-7825(01)00363-2
5. Garcea, G., Leonetti, L.: A unified mathematical programming formulation of strain driven and interior point algorithms for shakedown and limit analysis. Int. J. Numer. Meth. Eng. **88**(11), 1085–1111 (2011). https://doi.org/10.1002/nme.3188
6. Simon, J.W., Weichert, D.: Numerical lower bound shakedown analysis of engineering structures. Comput. Method Appl. Mech. **200**(41–44), 2828–2839 (2011). https://doi.org/10.1016/j.cma.2011.05.006
7. Zhang, Y.: An iteration algorithm for kinematic shakedown analysis. Comput. Method Appl. Mech. **127**(1–4), 217–226 (1995). https://doi.org/10.1016/0045-7825(95)00121-6
8. Liu, Y.H., Cen, Z.Z., Xu, B.Y.: A numerical-method for plastic limit analysis of 3-D structures. Int. J. Solids Struct. **32**(12), 1645–1658 (1995)
9. Zouain, N., Borges, L., Silveira, J.L.: An algorithm for shakedown analysis with nonlinear yield functions. Comput. Method Appl. Mech. **191**(23–24), 2463–2481 (2002). https://doi.org/10.1016/S0045-7825(01)00374-7
10. Mackenzie, D., Shi, J., Boyle, J.T.: Finite-element modeling for limit analysis by the elastic compensation method. Comput. Struct. **51**(4), 403–410 (1994)
11. Ponter, A.R.S., Carter, K.F.: Shakedown state simulation techniques based on linear elastic solutions. Comput. Method Appl. Mech. **140**(3–4), 259–279 (1997). https://doi.org/10.1016/S0045-7825(96)01105-X
12. Chen, H.F., Ponter, A.R.S.: Shakedown and limit analyses for 3-D structures using the linear matching method. Int. J. Press. Vessels Pip. **78**(6), 443–451 (2001). https://doi.org/10.1016/S0308-0161(01)00052-7
13. Chen, H.F., Ponter, A.R.S.: A method for the evaluation of a ratchet limit and the amplitude of plastic strain for bodies subjected to cyclic loading. Eur. J. Mech. A-Solid **20**(4), 555–571 (2001). https://doi.org/10.1016/S0997-7538(01)01162-7
14. Lytwyn, M., Chen, H.F., Ponter, A.R.S.: A generalised method for ratchet analysis of structures undergoing arbitrary thermo-mechanical load histories. Int. J. Numer. Meth. Eng. **104**(2), 104–124 (2015). https://doi.org/10.1002/nme.4924
15. Spiliopoulos, K.V., Panagiotou, K.D.: A residual stress decomposition based method for the shakedown analysis of structures. Comput. Method Appl. Mech. **276**, 410–430 (2014). https://doi.org/10.1016/j.cma.2014.03.019
16. Spiliopoulos, K.V., Panagiotou, K.D.: An enhanced numerical procedure for the shakedown analysis in multidimensional loading domains. Comput. Struct. **193**(Suppl. C), 155–171 (2017). https://doi.org/10.1016/j.compstruc.2017.08.008
17. Peng, H., Liu, Y., Chen, H.: A numerical formulation and algorithm for limit and shakedown analysis of large-scale elastoplastic structures. Comput. Mech. **63**(1), 1–22 (2019). https://doi.org/10.1007/s00466-018-1581-x
18. Peng, H., Liu, Y., Chen, H., Shen, J.: Shakedown analysis of engineering structures under multiple variable mechanical and thermal loads using the stress compensation method. Int. J. Mech. Sci. **140**, 361–375 (2018). https://doi.org/10.1016/j.ijmecsci.2018.03.020
19. Gokhfeld, D.A., Charniavsky, O.F.: Limit Analysis of Structures at Thermal Cycling, vol. 4. Sijthoff & Noordhoff edn. Alphen aan den Rijn, The Netherlands (1980)

20. Borino, G.: Consistent shakedown theorems for materials with temperature dependent yield functions. Int. J. Solids Struct. **37**(22), 3121–3147 (2000). https://doi.org/10.1016/S0020-7683(99)00114-6
21. Peng, H., Shen, J., Liu, Y., Chen, H.: Shakedown analysis of a torispherical head with a piping nozzle under combined loads by the stress compensation method. Int. J. Press. Vessels Pip. **172**, 107–118 (2019). https://doi.org/10.1016/j.ijpvp.2019.03.028
22. Simon, J.W., Chen, G., Weichert, D.: Shakedown analysis of nozzles in the knuckle region of torispherical heads under multiple thermo-mechanical loadings. Int. J. Press. Vessels Pip. **116**, 47–55 (2014). https://doi.org/10.1016/j.ijpvp.2014.01.004
23. Hsieh, M.F., Moffat, D.G., Mistry, J.: Nozzles in the knuckle region of a torispherical head: limit load interaction under combined pressure and piping loads. Int. J. Press. Vessels Pip. **77**(13), 807–815 (2000). https://doi.org/10.1016/S0308-0161(00)00073-9
24. Saal, H., Bauer, H., Häderle, M.-U.: Flexibility factors for nozzles in the knuckle region of dished pressure vessel heads. Int. J. Press. Vessels Pip. **70**(3), 151–160 (1997). https://doi.org/10.1016/S0308-0161(96)00020-8
25. Simon, J.W., Weichert, D.: Shakedown analysis with multidimensional loading spaces. Comput. Mech. **49**(4), 477–485 (2012). https://doi.org/10.1007/s00466-011-0656-8

On Cyclic Steady States and Elastic Shakedown in Diffusion-Induced Plasticity

Michaël Peigney

Abstract This chapter is devoted to media in which plasticity and diffusion are coupled, such as electrode materials in lithium ion batteries. We present some recent results on the large time behavior of such media when they are submitted to cyclic chemo-mechanical loadings. Under suitable technical assumptions, we notably show that there is convergence towards a cyclic steady state in which the stress, the plastic strain rate, the chemical potential and the concentration of guest atoms are all periodic in time (with the same period as the applied loading). A special case of interest is that of elastic shakedown, which corresponds to the situation where the medium behaves elastically in the large time limit. We present general theorems that allow one to construct both lower and upper bounds of the set of loadings for which elastic shakedown occurs, in the spirit of Melan and Koiter theorems in classical plasticity. An illustrative example—for which all the relevant calculations can be done in closed-form—is presented.

1 Introduction

This chapter is devoted to cyclically loaded media in which plasticity and diffusion are coupled. An example of such media is electrode materials in lithium-ion batteries: in those batteries, the flow of electrons is the result of lithium ions diffusing in electrode particles (and in an electrolyte). The absorption of lithium in electrode particles produces some swelling, which in certain situations can be large enough to trigger plastic flow. In the media considered—of which electrode materials are an example—plastic flow and diffusion act as two concurrent dissipative processes. This results in a complex evolution problem in which the interplay between plastic flow and diffusion may lead to some unusual behavior. For instance, under a *monotone* loading, a particle may flow plastically for some time and later unloads elastically [1].

M. Peigney (✉)
Lab Navier, University Gustave Eiffel, ENPC, CNRS, 77447 Marne la Vallée, France
e-mail: michael.peigney@polytechnique.org

A. A. Pisano et al. (eds.), *Direct Methods*, Lecture Notes in Applied and Computational Mechanics 95, https://doi.org/10.1007/978-3-030-48834-5_9

The main objective in this chapter is to study the large-time behavior of solutions to the evolution problem in the case of cyclic chemo-mechanical loadings. In classical plasticity (without diffusion), some general results are available [2–4] and fostered the development of direct methods aiming at determining the large-time response without resorting to step-by-step incremental analysis [5–8]. A central question, which we address in this chapter, is to investigate whether similar general results can be established for media coupling plasticity with diffusion. The outline of this chapter is as follows: In Sect. 2 are derived the governing equations of the evolution problem. As an illustration, some finite element simulations on a model problem related to lithium-ion batteries are presented. In Sect. 3 are presented the main results on cyclic steady states in diffusion-induced plasticity. Under suitable technical assumptions, we notably show that any solution to the evolution problem converges towards a cyclic steady state in which the stress, the plastic strain rate, the chemical potential and the concentration of guest atoms are all periodic in time (with the same period as the applied loading). Section 4 focuses on elastic shakedown, defined as the special case where the plastic dissipation is bounded on the time interval $[0, +\infty)$ (or, in more intuitive terms, that the medium behaves elastically in the large time limit). In classical plasticity, Melan and Koiter theorems deliver bounds on the set of loadings for which elastic shakedown occurs. Those theorems (Melan theorem especially) have been extended to several types of nonlinear behaviors, see e.g. [9–14] for recent examples. Building on the results of Sect. 3 we show that both a Melan-type theorem and a Koiter-type theorem can be obtained for media coupling plasticity with diffusion. An illustrative example—for which all the relevant calculations can be done in closed-form—is presented.

2 Diffusion-Induced Plasticity in a Cyclically Loaded Continuum

2.1 Conservation Equations

Consider a deformable continuum occupying a domain Ω, in which guest atoms diffuse. The continuum is submitted to a body force $\mathbf{f}$. Tractions $\mathbf{T}$ are prescribed on a part Γ_T of the boundary and displacements $\mathbf{U}$ are prescribed on $\Gamma_u = \partial\Omega - \Gamma_T$. A normal flux J of guest atoms is prescribed on a part Γ_J of the boundary. On $\Gamma_\mu = \partial\Omega - \Gamma_J$, the chemical potential μ is prescribed to take a given value M. The functions $\mathbf{f}$, $\mathbf{U}$, $\mathbf{T}$, M, J define the chemo-mechanical loading history. Those functions are assumed to be periodic in time, with the same period T. Functions that are periodic in time with a period T as referred to as *T-periodic* in the following.

For the problem at hand, the two main conservation equations are the diffusion equation (expressing the mass conservation of guest atoms)

$$\dot{c} + \mathrm{div}\mathbf{j} = 0 \text{ in } \Omega, \tag{1}$$

and the equilibrium equation (assuming quasi-static evolutions)

$$\mathrm{div}\boldsymbol{\sigma} + \mathbf{f} = 0 \text{ in } \Omega. \tag{2}$$

In (1) and (2), c is the concentration of guest atoms, $\mathbf{j}$ is the flux and $\boldsymbol{\sigma}$ is the stress. Equations (1) and (2) are complemented by the boundary conditions

$$\mu = M \text{ on } \Gamma_\mu, \quad \mathbf{j}\cdot\mathbf{n} = J \text{ on } \Gamma_J, \quad \boldsymbol{\sigma}\cdot\mathbf{n} = \mathbf{T} \text{ on } \Gamma_T, \quad \mathbf{u} = \mathbf{U} \text{ on } \Gamma_u. \tag{3}$$

2.2 Constitutive Equations

The constitutive material is assumed to be elastic-plastic. Following the thermodynamic framework of [15] in small perturbations, the local state of the material is described by the total linearized strain $\boldsymbol{\varepsilon}$, the (deviatoric) plastic strain $\boldsymbol{\varepsilon}^p$ and the concentration c of guest atoms. The free energy w of the material is taken as a quadratic function of the form

$$w(\boldsymbol{\varepsilon}, \boldsymbol{\varepsilon}^p, c) = \frac{1}{2}(\boldsymbol{\varepsilon} - \boldsymbol{\varepsilon}^p) : \mathbb{L} : (\boldsymbol{\varepsilon} - \boldsymbol{\varepsilon}^p) + \frac{1}{2}kc^2 + c\mathbf{A} : (\boldsymbol{\varepsilon} - \boldsymbol{\varepsilon}^p) + c\mu_0 \tag{4}$$

where the fourth-order symmetric tensor $\mathbb{L}$, the symmetric second-order tensors $\mathbf{A}$, the scalars k and μ_0 are material parameters satisfying

$$\mathbb{L} \succ 0, \quad k > 0, \quad k - \mathbf{A} : \mathbb{L}^{-1} : \mathbf{A} > 0 \tag{5}$$

where the notation $\succ$ indicates that a tensor is positive definite. The requirements (5) ensure that w is convex and guarantee the uniqueness of the evolution starting from a given initial state, as will be later discussed. From (4) we obtain the constitutive relations

$$\boldsymbol{\sigma} = \frac{\partial w}{\partial \boldsymbol{\varepsilon}} = \mathbb{L} : (\boldsymbol{\varepsilon} - \boldsymbol{\varepsilon}^p) + c\mathbf{A}, \quad \mu = \frac{\partial w}{\partial c} = \mu_0 + kc + \mathbf{A} : (\boldsymbol{\varepsilon} - \boldsymbol{\varepsilon}^p). \tag{6}$$

It can be observed that the tensor $\mathbf{A}$ in (6) induces a two-way coupling between mechanics and diffusion. In particular, the concentration c has a linear influence on the stress, in a way similar to thermal stress. Similarly, the chemical potential μ depends linearly on the elastic strain.

The constitutive equations (6) are complemented by a law of diffusion and a plasticity flow rule complying with the second law of thermodynamics. In more detail, the flux $\mathbf{j}$ of guest atoms is assumed to obey the relation

$$\mathbf{j} = -\psi'(\nabla\mu). \tag{7}$$

where ψ is a positive, differentiable and strictly convex function such that $\psi(0) = 0$. The special case of Fick's law (linear diffusion) corresponds to the situation $\psi = \frac{1}{2}\mathbf{j}\cdot\mathbf{D}\cdot\mathbf{j}$ for some symmetric second order tensor $\mathbf{D} \succ 0$.

2.3 Illustrative Example

In order to illustrate the type of behavior that arises in the media considered, we present some finite-element simulations performed on a plane strain problem related to lithium-ion batteries. We consider a free-standing cylinder electrode particle with radius R. Cyclic lithiation-delithiation is achieved by applying a $T-$periodic flux

$$J(t) = -\frac{R\omega}{4} H \sin \omega t \tag{8}$$

on the boundary. In (8), ω and $H > 0$ are given. The loading parameter H in (8) is directly related to the maximum number of inserted lithium ions which is indeed equal to $-2\pi RL\int_0^{T/2} J(t)dt = \pi R^2 LH$ where L is the length of the cylinder in the $\mathbf{e}_z$ direction.

The free energy w is taken as an isotropic version of (4), i.e.

$$w(\boldsymbol{\varepsilon}, \boldsymbol{\varepsilon}^p, c) = \frac{1}{2}K(\mathrm{tr}\boldsymbol{\varepsilon})^2 + G(\boldsymbol{\varepsilon}^d - \boldsymbol{\varepsilon}^p) : (\boldsymbol{\varepsilon}^d - \boldsymbol{\varepsilon}^p) + \frac{1}{2}kc^2 + ac\,\mathrm{tr}\boldsymbol{\varepsilon} + c\mu_0 \tag{9}$$

where $\boldsymbol{\varepsilon}^d$ is the deviatoric strain and c is the concentration of lithium. In (9), K, G, a and μ_0 are material parameters. The constitutive relations (6) specialize as

$$\sigma_m = K\mathrm{tr}\boldsymbol{\varepsilon} + ac\ , \quad \mathbf{s} = 2G(\boldsymbol{\varepsilon}^d - \boldsymbol{\varepsilon}^p), \quad \mu = \mu_0 + kc + a\,\mathrm{tr}\boldsymbol{\varepsilon}, \tag{10}$$

where $\sigma_m = (\mathrm{tr}\boldsymbol{\sigma})/3$ is the hydrostatic stress and $\mathbf{s}$ is the deviatoric stress. The scalar material parameter a in (9) accounts for the chemo-mechanical coupling. In particular, the ratio $-a/K$ can be interpreted as the volumetric expansion coefficient associated with the insertion of lithium.

Fick's law is adopted for diffusion, i.e.

$$\mathbf{j} = -\frac{D}{k}\nabla\mu$$

where D is the diffusion coefficient. A Von Mises plasticity model is adopted. The corresponding elasticity domain if defined by

$$\frac{1}{2}\mathbf{s} : \mathbf{s} \leq \sigma_Y^2 \tag{11}$$

where σ_Y is the yield strength.

The numerical results presented in the following have been obtained using the parameters $E = 80$ GPa, $\nu = 0.3$, $\sigma_Y = 50$ MPa, $a = -2.72 \times 10^{-18}$ J, $k = 0.5 \times 10^{-13}$ J.m^3, $D = 10^{-16}$ m^2/s. The bulk modulus K and the shear modulus G are related to Young's modulus E and Poisson's ratio ν by the expressions $K = E/3(1 - -2\nu)$ and $G = E/2(1 + \nu)$. In Figs. 1 and 2 is shown the time evolution of the plastic strain field $\boldsymbol{\varepsilon}^p$ for two different sets of loading parameters. For both simulations the initial value $\boldsymbol{\varepsilon}^p(0)$ is non zero and taken as

$$\boldsymbol{\varepsilon}^p(0) = 0.003 \sin(\pi r/2R)(\mathbf{e}_1 \otimes \mathbf{e}_2 + \mathbf{e}_2 \otimes \mathbf{e}_1)$$

where $(\mathbf{e}_1, \mathbf{e}_2)$ is a reference orthonormal frame. Figure 1 corresponds to the loading parameters $H = 100$ mol/m^3, $\omega = 10/T_0$ where T_0 is a time scale defined by

$$T_0 = \frac{R^2}{D\left(1 - \dfrac{a\tilde{a}}{k}\right)} \text{with } \tilde{a} = \frac{3a}{3K + 4G}. \tag{12}$$

The map $\|\boldsymbol{\varepsilon}^p(t) - \boldsymbol{\varepsilon}^p(0)\|$ is shown at several time instants during the first two loading cycles. The plots in Fig. 1 suggest that the plastic strain stabilizes to a time-independent field, i.e. that *elastic shakedown* occurs. Figure 2 corresponds to the loading parameters $H = 100$ mol/m^3 and $\omega = 20/T_0$. The plots in Fig. 2 suggest that the plastic strain reaches a cyclic steady state, i.e. that *cyclic plasticity* occurs. Note that the same value of the parameter H has been used in Figs. 1 and 2, which means that the same number of lithium is injected in the particle. The only difference is the charging rate. The loading rate is thus found to have an influence on the plastic response of the system, even though rate-independent plasticity is considered in the constitutive equations. This is a result of the chemo-mechanical coupling: the

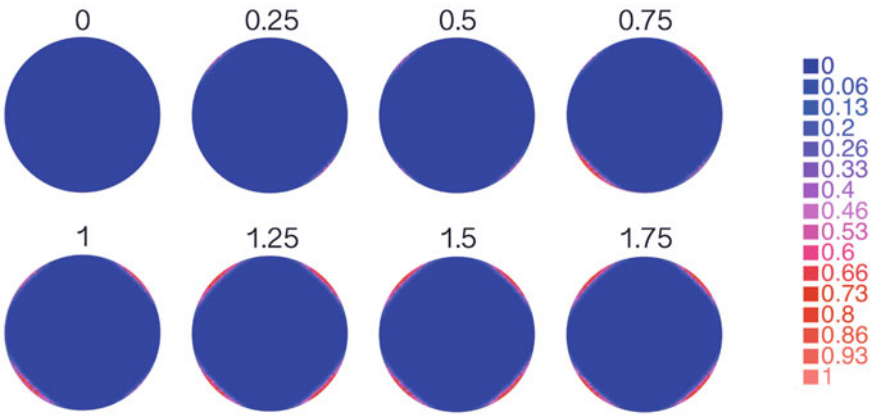

Fig. 1 Map of $\|\boldsymbol{\varepsilon}^p(t) - \boldsymbol{\varepsilon}^p(0)\|$ at several times instants t/T for a cylinder particle under cyclic lithiation. Case $H = 100$ mol/m^3, $\omega = 10/T_0$. Reported values of $\|\boldsymbol{\varepsilon}^p(t) - \boldsymbol{\varepsilon}^p(0)\|$ are normalized

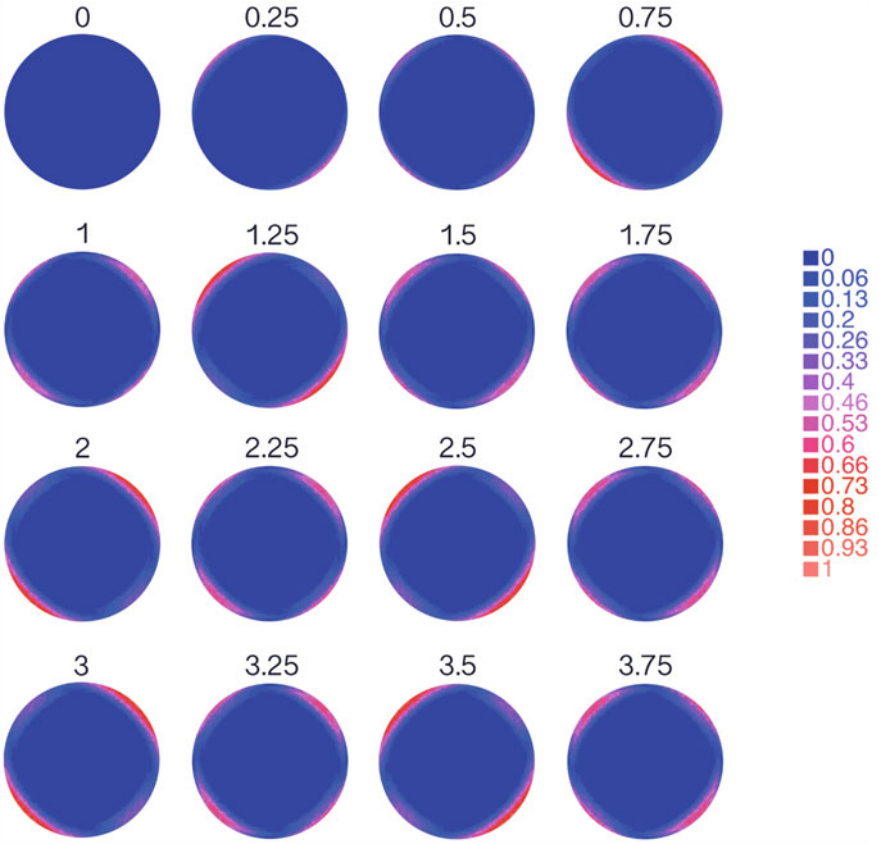

Fig. 2 Map of $\|\boldsymbol{\varepsilon}^p(t) - \boldsymbol{\varepsilon}^p(0)\|$ at several times instants t/T for a cylinder particle under cyclic lithiation. Case $H = 100$ mol/m^3, $\omega = 20/T_0$. Reported values of $\|\boldsymbol{\varepsilon}^p(t) - \boldsymbol{\varepsilon}^p(0)\|$ are normalized

combined facts that diffusion is a rate-dependent process and that the stress depends on the local concentration entail that the mechanical response of the system is rate-dependent.

In the electrochemical community, a quantity of interest is the charge–voltage response, relating the total charge C of lithium ions in the electrode particle to the voltage V on the surface of the particle. The charge C is obtained from the concentration field c by $C = \int_\Omega c d\Omega$. The voltage V is directly related to the chemical potential μ by $V = -(\mu - \mu_0)/e$ where e is the elementary charge. Let $C(t)$ and $V(t)$ be the charge and voltage at time t, as obtained in the finite element simulations. The trajectories of $(C(t), V(t))$ in the $C - V$ plane are shown in Fig. 3 for the two loadings considered previously. It can be observed that $(C(t), V(t))$ converges towards a cyclic steady state. Some hysteresis is displayed in the cyclic steady state, even in the case $\omega = 10/T_0$ for which elastic shakedown occurs. Indeed, even if plastic flow vanishes in the elastic shakedown regime, there remains the diffusion-related

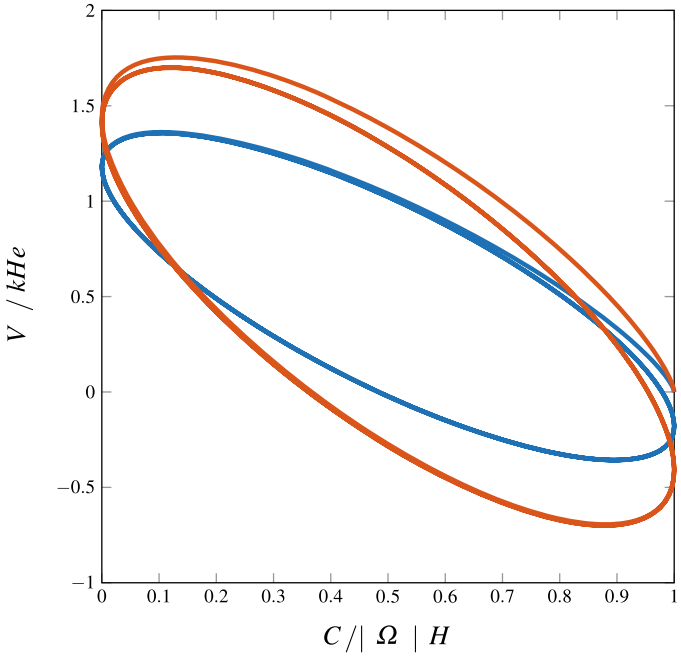

Fig. 3 Charge-Voltage response for $\omega = 10/T_0$ (blue curve) and $\omega = 20/T_0$ (red curve). The parameter H is set to $H = 100$ mol/m^3

dissipation corresponding to the cyclic insertion of lithium ions. By contrast, in the case $\omega = 20/T_0$, the diffusion-related dissipation and the plastic dissipation (due to cyclic plasticity) add up on the cyclic steady state. For designing lithium-ion batteries with improved electrochemical efficiency, it is beneficial to reduce the hysteresis in the $C - V$ response. In that regard, the shakedown regime is likely to be beneficial [1]. It can further be added that elastic shakedown is also beneficial for the mechanical fatigue behavior since elastic shakedown is typically associated with *high-cycle fatigue*—as opposed to cyclic plasticity which is associated with *low-cycle fatigue* [16].

The results in Figs. 1, 2 and 3 have been obtained for specific geometry, loading and material parameters. One can wonder to what extent those results are general. Considering a continuum of arbitrary shape submitted to a cyclic chemo-mechanical loading, the main questions to be addressed are

1. Is there always convergence to a steady state cycle?
2. How does the steady state cycle (if exists) depend on the initial state?
3. Is is possible to obtain a priori restrictions on the loading for ensuring that elastic shakedown occurs?

Regarding question 3 above, Melan theorem (also known as the *static* shakedown theorem) and Koiter theorem (also known as the *kinematic* shakedown theorem) come to mind [17–19]. In standard plasticity (without coupling with diffusion), those theorems provide bounds on the set of loadings for which elastic shakedown occurs. The classical reasoning used in the proof of those theorems consists in bounding the total dissipation on the time interval $[0, \infty)$. For the media considered here, there are two sources of dissipation, namely plasticity and diffusion. Bounding the total dissipation thus essentially means that there is no plastic flow and no diffusion in the large time limit. This is not really the situation of interest for applications such as lithium-ion batteries: one is instead interested in situations where there is no plastic flow in the large limit but diffusion still occurs as a result of cyclic lithiation, as in Fig. 1. In such situations, the total plastic dissipation on the time interval $[0, \infty)$ is bounded but the diffusion-related dissipation is not. There does not seem to be any obvious way to modify Melan's and Koiter's reasoning so as to bound only a part of the total dissipation (namely the plastic dissipation). As will shown in the following, shakedown theorems as desired can still be obtained at the price of first addressing the more general questions 1 and 2 listed above.

3 General Results on Steady State Cycles

In this section are presented some general results addressing questions 1–2 related to cyclic steady states in diffusion-induced plasticity. We first derive an evolution equation for the fields $(\boldsymbol{\sigma}, \mu)$ and proceed to discuss some properties of that equation. As a preliminary, observe that the free energy $w(\boldsymbol{\varepsilon}, \boldsymbol{\varepsilon}^p, c)$ in (4) can be put in the form

$$w(\boldsymbol{\varepsilon}, \boldsymbol{\varepsilon}^p, c) = \frac{1}{2}(\boldsymbol{\varepsilon} - \boldsymbol{\varepsilon}^p, c) \vdots \mathbb{M} \vdots (\boldsymbol{\varepsilon} - \boldsymbol{\varepsilon}^p, c) + c\mu_0 \tag{13}$$

where $\mathbb{M}$ is the symmetric operator defined by the relations

$$\mathbb{M} \vdots (\boldsymbol{\varepsilon} - \boldsymbol{\varepsilon}^p, c) = \left(\mathbb{L} : (\boldsymbol{\varepsilon} - \boldsymbol{\varepsilon}^p) + c\mathbf{A}, kc + \mathbf{A} : (\boldsymbol{\varepsilon} - \boldsymbol{\varepsilon}^p) \right).$$

for any $\boldsymbol{\varepsilon} - \boldsymbol{\varepsilon}^p$ and c. Under the assumptions (5), $\mathbb{M}$ can be verified to be positive definite. The operator $\mathbb{M}$ is thus invertible and its inverse $\mathbb{M}^{-1}$ is symmetric positive definite. For later reference, note that the constitutive relations (6) can be rewritten as

$$(\boldsymbol{\varepsilon} - \boldsymbol{\varepsilon}^p, c) = \mathbb{M}^{-1} \vdots (\boldsymbol{\sigma}, \mu - \mu_0). \tag{14}$$

Setting $\mathbf{B} = \mathbf{A} : \mathbb{L}^{-1}$ and $k' = k - \mathbf{A} : \mathbb{L}^{-1} : \mathbf{A}$, it can be calculated that

$$(\boldsymbol{\sigma}, \mu) \vdots \mathbb{M}^{-1} \vdots (\boldsymbol{\sigma}', \mu') \rangle = \boldsymbol{\sigma} : \mathbb{L}^{-1} : \boldsymbol{\sigma}' + \frac{1}{k'} \big((\mathbf{B} : \boldsymbol{\sigma})(\mathbf{B} : \boldsymbol{\sigma}') + \mu\mu' - \mu' \mathbf{B} : \boldsymbol{\sigma} - \mu \mathbf{B} : \boldsymbol{\sigma}' \big) \tag{15}$$

for any $(\boldsymbol{\sigma}, \mu)$ and $(\boldsymbol{\sigma}', \mu')$. To simplify the presentation, we will consider the case of viscoplasticity: the flow rule takes the form $\dot{\boldsymbol{\varepsilon}}^p = \phi'(\boldsymbol{\sigma})$ where ϕ is a positive, strictly convex, differentiable function of the deviatoric stress and such that $\phi(0) = 0$. The elasticity domain of the material is denoted by $\mathscr{C}$.

3.1 Evolution Equation for the Stress and the Chemical Potential

The fields $(\boldsymbol{\sigma}, \mu)$ are assumed to live in a closed subspace of $H(\mathrm{div}; \Omega) \times H^1(\Omega)$. Since $\mathbb{M}^{-1} \succ 0$, $\mathscr{H}$ is a Hilbert space for the scalar product $\langle \cdot, \cdot \rangle$ defined by

$$\langle (\boldsymbol{\sigma}, \mu), (\boldsymbol{\sigma}', \mu') \rangle = \int_\Omega (\boldsymbol{\sigma}, \mu) \vdots \mathbb{M}^{-1} \vdots (\boldsymbol{\sigma}', \mu')\, d\Omega$$

We denote $\mathscr{K}(\mathbf{f}, \mathbf{T}, M)$ the set of stress and chemical potential fields that are compatible with data $(\mathbf{f}, \mathbf{T}, M)$, i.e

$$\mathscr{K}(\mathbf{f}, \mathbf{T}, M) = \left\{ (\boldsymbol{\sigma}, \mu) \in \mathscr{H} : \mathrm{div}\boldsymbol{\sigma} + \mathbf{f} = 0 \text{ in } \Omega, \boldsymbol{\sigma} \cdot \mathbf{n} = \mathbf{T} \text{ on } \Gamma_T, \mu = M \text{ on } \Gamma_\mu \right\}.$$

Let $(\boldsymbol{\sigma}, \mu)$ be the stress and chemical potential in a given evolution satisfying the governing equations described in Sect. 2. We have $(\boldsymbol{\sigma}, \mu) \in \mathscr{K}(\mathbf{f}, \mathbf{T}, M)$ and it can be verified that

$$\langle (\dot{\boldsymbol{\sigma}}, \dot{\mu}), (\boldsymbol{\rho}, \nu) \rangle = -\int_\Omega (\phi'(\boldsymbol{\sigma}) : \boldsymbol{\rho} + \psi'(\nabla\mu) \cdot \nabla\nu)\, d\Omega - \int_{\Gamma_J} J\nu\, dS \quad \forall (\boldsymbol{\rho}, \nu) \in \mathscr{K}_0; \tag{16}$$

with $\mathscr{K}_0 = \left\{ (\boldsymbol{\sigma}, \mu) \in \mathscr{H} : \mathrm{div}\boldsymbol{\sigma} = 0 \text{ in } \Omega, \boldsymbol{\sigma} \cdot \mathbf{n} = 0 \text{ on } \Gamma_T, \mu = 0 \text{ on } \Gamma_\mu \right\}$. Equation (16) can be interpreted as an evolution equation for the stress and chemical potential fields $(\boldsymbol{\sigma}, \mu)$.

3.2 Contraction Properties

The norm in $\mathscr{H}$ is denoted by $\| \cdot \|$, i.e. $\|(\boldsymbol{\sigma}, \mu)\|^2 = \int_\Omega (\boldsymbol{\sigma}, \mu) \vdots \mathbb{M}^{-1} \vdots (\boldsymbol{\sigma}, \mu)\, d\Omega$. The two following lemmas can be proved [20]:

Lemma 1 *Let $\Sigma = (\boldsymbol{\sigma}, \mu)$ and $\Sigma' = (\boldsymbol{\sigma}', \mu')$ be two solutions of (16). Then*

$$\|\Sigma(t_2) - \Sigma'(t_2)\| \leq \|\Sigma(t_1) - \Sigma'(t_1)\| \text{ for all } t_1 < t_2.$$

Lemma 2 *Let $\Sigma = (\boldsymbol{\sigma}, \mu)$ and $\Sigma' = (\boldsymbol{\sigma}', \mu')$ be two solutions of (16) such that $\|\Sigma(t) - \Sigma'(t)\| = \|\Sigma(t_1) - \Sigma'(t_1)\|$ for all $t_1 \leq t$. Then*

$$\phi'(\boldsymbol{\sigma}(\mathbf{x},t)) = \phi'(\boldsymbol{\sigma}'(\mathbf{x},t)) \text{ for } t_1 \leq t.$$

Moreover, there exists a time-independent stress field $\boldsymbol{\rho}$ *and a constant* η *such that* $(\boldsymbol{\rho},\eta) \in \mathscr{K}_0$ *and*

$$\boldsymbol{\sigma}(\mathbf{x},t) - \boldsymbol{\sigma}'(\mathbf{x},t) = \boldsymbol{\rho}(\mathbf{x}),\ \ \mu(\mathbf{x},t) - \mu'(\mathbf{x},t) = \eta \text{ for } t_1 \leq t.$$

Lemma 1 means that the distance between two solutions decreases with time. It notably implies the uniqueness of the solution for a given initial state. Lemma 2 means that if the distance between two solutions is constant then the difference between those solutions is constant (which is not obvious at first sight).

3.3 Main Results

We are now in a position to prove the main results regarding $T-$periodic solutions to the evolution equation (16). Although such $T-$periodic solutions are not unique, they are quite similar to one another. More precisely, we have the following

Theorem 1 *Let* $\Sigma = (\boldsymbol{\sigma},\mu)$ *and* $\Sigma' = (\boldsymbol{\sigma}',\mu')$ *be two* $T-$*periodic solutions of (16). Then*

$$\phi'(\boldsymbol{\sigma}(\mathbf{x},t)) = \phi'(\boldsymbol{\sigma}'(\mathbf{x},t)) \text{ for } t_1 \leq t.$$

Moreover, there exists a time-independent stress field $\boldsymbol{\rho}$ *and a constant* η *such that* $(\boldsymbol{\rho},\eta) \in \mathscr{K}_0$ *and*

$$\boldsymbol{\sigma}(\mathbf{x},t) - \boldsymbol{\sigma}'(\mathbf{x},t) = \boldsymbol{\rho}(\mathbf{x}),\ \ \mu(\mathbf{x},t) - \mu'(\mathbf{x},t) = \eta.$$

Proof The result follows from Lemmas 1 and 2. Let $\Sigma = (\boldsymbol{\sigma},\mu)$ and $\Sigma' = (\boldsymbol{\sigma}',\mu')$ be two $T-$periodic solutions of (16). By Lemma 1 we have

$$\|\Sigma(T) - \Sigma'(T)\| \leq \|\Sigma(t) - \Sigma'(t)\| \leq \|\Sigma(0) - \Sigma(0)\| \tag{17}$$

for all $t \in [0,T]$. Since Σ and Σ' are $T-$periodic, we have $\|\Sigma(T) - \Sigma'(T) = \|\Sigma(0) - \Sigma(0)\|$. Hence (17) becomes $\|\Sigma(t) - \Sigma'(t)\| = \|\Sigma(0) - \Sigma(0)\|$ for all $t \in [0,T]$. Applying Lemma 2 proves the claim. □

We now arrive at the main result on the large time convergence of solutions to (16):

Theorem 2 *Assume that there exists a $T-$periodic solution to (16) and that the dimension of $\mathscr{H}$ is finite. For any solution $\Sigma(t)$ of (16) on $[0,\infty)$, there exists a $T-$periodic solution Σ' of (16) such that*

$$\Sigma(t) \to \Sigma'(t) \text{ as } t \to \infty.$$

Proof We will make use of Opial's lemma [21], which is a general result in Hilbert spaces that reads as follows:

Let F be a nonempty subset of $\mathscr{H}$ and $\{u_n\}$ a sequence in $\mathscr{H}$ such that:

(i) $\{\|u_n - f\|\}$ *converges for all* $f \in F$,
(ii) *the limit of every (weakly) convergent subsequence of $\{u_n\}$ is in F.*

Then the whole sequence $\{u_n\}$ (weakly) converges to a point of F.

Here we only consider the simplified situation where the dimension of $\mathscr{H}$ is finite, so that weak and strong convergences coincide. Considering an arbitrary solution $\Sigma(t)$ of (16), we wish to apply Opial's lemma to the sequence $\{u_n\} = \{\Sigma(nT)\}$ and to the set F formed by the initial values of $T-$periodic solutions to (16), i.e. $F = \left\{\tilde{\Sigma}(0) : t \mapsto \tilde{\Sigma}(t) \text{ is a } T-\text{periodic solution of (16)}\right\}$. To that purpose, the main effort consists in checking assumptions (i) and (ii) in Opial's lemma.

Let us begin with assumption (i). Consider $f \in F$ and let Σ' be a $T-$periodic solution of (16) such that $f = \Sigma'(0)$. Lemma 1 gives

$$\|\Sigma((n+1)T) - \Sigma'((n+1)T)\| \leq \|\Sigma(nT) - \Sigma'(nT)\|. \tag{18}$$

Since Σ' is $T-$ periodic, we have $\Sigma(nT) = \Sigma(0) = f$ for all n. Hence (18) becomes $\|u_{n+1} - f\| \leq \|u_n - f\|$. The positive sequence $\{\|u_n - f\|\}$ is decreasing. It follows that $\{\|u_n - f\|\}$ converges to a limit as $n \to \infty$, which shows that assumption (i) is verified.

We now proceed with assumption (ii). Let $\{u_{n_k}\}$ be a converging subsequence of $\{u_n\}$ and denote its limit by g. Denoting by $\Sigma^*(t)$ the solution of (16) for the initial condition $\Sigma^*(0) = g$, we wish to show that $\Sigma^*(t)$ is $T-$periodic. We consider a fixed t in the interval $[0, T]$ in what follows. Lemma 1 gives

$$\|\Sigma(n_k T + t) - \Sigma^*(t)\| \leq \|\Sigma(n_k T) - \Sigma^*(0)\| = \|u_{n_k} - g\| \underset{k\to\infty}{\longrightarrow} 0.$$

Thus

$$\Sigma(n_k T + t) \underset{k\to\infty}{\longrightarrow} \Sigma^*(t) \tag{19}$$

Let Σ' be a $T-$periodic solution to (16). Lemma 1 yields

$$\|\Sigma(n_{k+1}T) - \Sigma'(n_{k+1}T)\| \leq \|\Sigma(n_k T + t) - \Sigma'(n_k T + t)\| \leq \|\Sigma(n_k T) - \Sigma'(n_k T)\| \tag{20}$$

Setting $f = \Sigma'(0) \in F$ and noting that $\Sigma'(n_k T + t) = \Sigma'(t)$, (20) becomes

$$\|\Sigma(n_{k+1}T) - f\| \leq \|\Sigma(n_k T + t) - \Sigma'(t)\| \leq \|\Sigma(n_k T) - f\|. \tag{21}$$

By (i), both the left and the right terms in (21) converge to a limit A as $k \to \infty$. It follows that

$$\|\Sigma(n_k T + t) - \Sigma'(t)\| \underset{k\to\infty}{\longrightarrow} A. \tag{22}$$

Combining (19) and (22) shows that $\|\Sigma^*(t) - \Sigma'(t)\| = A$ for all t in $[0, T]$. Lemma 2 implies that $\Sigma^*(t) - \Sigma'(t)$ is time-independent. Hence $\Sigma^*(t)$ is $T-$periodic, i.e. $\Sigma^*(0) = g \in F$. Assumption (ii) is thus verified.

Applying Opial's lemma shows that there exists a $T-$periodic solution $\Sigma^*(t)$ such that $\Sigma(nT) \to \Sigma^*(0)$ as $n \to \infty$. By Lemma 1, it follows that $\Sigma(t) - \Sigma^*(t) \to 0$ as $t \to \infty$. □

Theorems 1 and 2 allow one to provide some answers to questions 1–2 listed in Sect. 2 regarding cyclic steady states in diffusion-induced plasticity. Theorem 2 indeed implies that the stress $\boldsymbol{\sigma}$, the plastic strain rate $\dot{\boldsymbol{\varepsilon}}^p$ and the chemical potential μ converge towards a cyclic steady state as $t \to \infty$. Using the constitutive relations (7) and (14), it follows that the flux $\mathbf{j}$ and the concentration c also converge towards a cyclic steady state. Since there is no uniqueness of $T-$periodic solutions to (16), the cyclic steady state depends on the initial state. However, Theorem 1 shows that some features of the cyclic steady state are unique, namely the stress rate, the plastic strain rate and the chemical potential (up to a constant). Using again (7) and (14), the flux and the concentration rate on the cyclic steady state are also unique, i.e. independent of the initial state.

Let us denote by $\dot{\boldsymbol{\varepsilon}}^p_\infty$ the plastic strain rate on the cyclic steady steady state. The facts that $\dot{\boldsymbol{\varepsilon}}^p_\infty$ is $T-$periodic and uniquely defined imply that there is either elastic shakedown, cyclic plasticity or ratchetting—with the exclusion of any other regime. Moreover, for a given structure, the type of asymptotic plastic behavior (i.e elastic shakedown, cyclic plasticity or ratchetting) is only determined by the loading, independently of the initial state. In a similar fashion, diffusion-related quantities reach a cyclic steady state which is largely independent of the initial state. In particular, for electrode particles in lithium-ion batteries, the charge-voltage response reaches a cyclic steady state which is uniquely defined (possibly up to a translation in the $C - V$ plane, depending on the type of chemical boundary conditions).

In such conditions, it makes sense to establish Bree-like diagrams mapping the space of load parameters to path-independent properties such as the type of asymptotic behavior, the plastic dissipation or the diffusion-related dissipation on the steady state cycle.

4 Shakedown Theorems in Diffusion-Induced Plasticity

Let us consider the fictitious *purely elasto-diffusive problem* obtained by discarding plastic flow in the original problem. As a special case of (16), the stress and chemical potential in the diffusive elasto-diffusive problem satisfy

$$\langle(\dot{\boldsymbol{\sigma}}, \dot{\mu}), (\boldsymbol{\rho}, \nu)\rangle = -\int_{\Omega} \psi'(\nabla\mu)\cdot\nabla\nu\, d\Omega - \int_{\Gamma_J} J\nu\, dS \quad \forall(\boldsymbol{\rho}, \nu) \in \mathscr{K}_0. \tag{23}$$

Periodic solutions to (23) play a central role in formulating shakedown conditions in diffusion-induced plasticity, as will be later demonstrated. Periodic solutions to (23) are not uniquely defined. As a particular case of Theorem 1, two periodic solutions of (23) differ by a time independent stress field $\boldsymbol{\rho}$ and a constant η such that $(\boldsymbol{\rho}, \eta) \in \mathscr{K}_0$. Conversely, if $(\boldsymbol{\rho}, \eta) \in \mathscr{K}_0$ and $(\boldsymbol{\sigma}^E, \mu^E)$ is a particular $T-$periodic solution to (23) then $(\boldsymbol{\sigma}^E, \mu^E) + (\boldsymbol{\rho}, \eta)$ can easily be verified to be a $T-$solution to (23). The whole set of $T-$periodic solutions to (23) is thus an affine space than can be written as

$$\{(\boldsymbol{\sigma}^E, \mu^E) + (\boldsymbol{\rho}, \eta) : (\boldsymbol{\rho}, \eta) \in \mathscr{K}_0\} \tag{24}$$

where $(\boldsymbol{\sigma}^E, \mu^E)$ denotes any given $T-$periodic solution to (23).

4.1 Static Shakedown Theorem

Assume that elastic shakedown occurs in the original problem involving diffusion-induced plasticity and denote by $(\boldsymbol{\sigma}_\infty, \mu_\infty)$ the stress and the chemical potential in the cyclic steady state. The fields $(\boldsymbol{\sigma}_\infty, \mu_\infty)$ form a $T-$periodic solution to (16). Elastic shakedown corresponds to the situation where $\dot{\boldsymbol{\varepsilon}}^p_\infty = \phi'(\boldsymbol{\sigma}_\infty) = 0$, hence we have

$$\langle(\dot{\boldsymbol{\sigma}}_\infty, \dot{\mu}_\infty), (\boldsymbol{\rho}, \nu)\rangle = -\int_{\Omega} \psi'(\nabla\mu_\infty)\cdot\nabla\nu\, d\Omega - \int_{\Gamma_J} J\nu\, dS \quad \forall(\boldsymbol{\rho}, \nu) \in \mathscr{K}_0; \tag{25}$$

Comparing (25) with (23) shows that $(\boldsymbol{\sigma}_\infty, \mu_\infty)$ is a $T-$periodic solution to the elasto-diffusive problem (23). Conversely, assume there exists a $T-$periodic solution $(\tilde{\boldsymbol{\sigma}}, \tilde{\mu})$ to the elasto-diffusive (23) such that $\phi'(\tilde{\boldsymbol{\sigma}}) = 0$. It can be directly checked that $(\tilde{\boldsymbol{\sigma}}, \tilde{\mu})$ is also a $T-$periodic to the Eq. (16). Noting that the associated plastic strain is zero and using Theorem 1, we obtain that the plastic strain rate vanishes for *any* $T-$periodic solution to (16), i.e. in any cyclic steady state. Consequently, elastic shakedown is characterized by the existence of a $T-$periodic solution $(\tilde{\boldsymbol{\sigma}}, \tilde{\mu})$ to (16) such that $\phi'(\tilde{\boldsymbol{\sigma}}) = 0$, i.e. such that $\tilde{\boldsymbol{\sigma}} \in \mathscr{C}$. Using (24), we can formulate the following result

Theorem 3 *If there exists a time-independent stress field* $\boldsymbol{\rho} \in \mathscr{A}_0$ *such that* $\boldsymbol{\sigma}^E(\mathbf{x}, t) + \boldsymbol{\rho}(\mathbf{x}) \in \mathscr{C}$ *for all* $\mathbf{x} \in \Omega$ *and* $t \in [0, T]$*, then elastic shakedown occurs (whatever the initial state is).*

In Theorem 3, $\mathscr{A}_0$ is the space of self-equilibrated stress fields, i.e.

$$\mathscr{A}_0 = \{\boldsymbol{\rho} : \mathrm{div}\boldsymbol{\rho} = 0 \text{ in } \Omega,\ \boldsymbol{\rho}.\mathbf{n} = 0 \text{ on } \Gamma_T\}.$$

Although the statement of Theorem 3 is similar to Melan theorem, we emphasize that its proof largely differs from the standard proof used in Melan theorem for pure plasticity. Theorem 3 motivates the introduction of a 'static security coefficient' m_S as

$$\begin{aligned} m_S = \sup\{m : &\text{ there exists } \boldsymbol{\rho} \in \mathscr{A}_0 \text{ such that} \\ &\boldsymbol{\rho}(\mathbf{x}) + m\boldsymbol{\sigma}^E(\mathbf{x}, t) \in \mathscr{C} \text{ for all } (\mathbf{x}, t) \in \Omega \times [0, T]\}. \end{aligned} \tag{26}$$

The value of m_S indeed determines the shakedown behavior according to the following rules

$$\begin{cases} m_S > 1 \Longrightarrow \text{shakedown occurs} \\ m_S < 1 \Longrightarrow \text{shakedown does not occur} \end{cases} \tag{27}$$

Lower bounds on m_S can be obtained by using Theorem 3 with particular stress fields in $\mathscr{A}_0$.

4.2 Kinematic Shakedown Theorem

Upper bounds on m_S can be obtained by convex duality, as used for instance by [22, 23]. Let $\mathscr{A}$ be the set of triplets $(m, \boldsymbol{\rho}^*, \tilde{\boldsymbol{\sigma}})$ such that $\boldsymbol{\rho}^*(\mathbf{x})$ is a time-independent stress field in $\mathscr{A}_0$ and $\tilde{\boldsymbol{\sigma}}(\mathbf{x}, t) \in \mathscr{C}$ for all $(\mathbf{x}, t)$. From (26) we have

$$m_S = \sup_{\substack{(m, \boldsymbol{\rho}^*, \tilde{\boldsymbol{\sigma}}) \in \mathscr{A}, \\ \boldsymbol{\rho}^* + m\boldsymbol{\sigma}^E = \tilde{\boldsymbol{\sigma}}}} m$$

This is a constrained maximization problem over the convex set $\mathscr{A}$. Denote by $\mathscr{L}$ the corresponding lagrangian, i.e.

$$\mathscr{L}(m, \boldsymbol{\rho}^*, \tilde{\boldsymbol{\sigma}}; \mathbf{d}) = m + \int_\Omega \int_0^T \mathbf{d}(\mathbf{x}, t) : (\tilde{\boldsymbol{\sigma}}(\mathbf{x}, t) - \boldsymbol{\rho}^*(\mathbf{x}) - m\boldsymbol{\sigma}^E(\mathbf{x}, t)) d\Omega dt. \tag{28}$$

We have

$$m_S = \sup_{(m,\boldsymbol{\rho}^*,\tilde{\boldsymbol{\sigma}})\in\mathscr{A}} \inf_{\mathbf{d}} \mathscr{L}(m,\boldsymbol{\rho}^*,\tilde{\boldsymbol{\sigma}};\mathbf{d}).$$

From the min-max inequality

$$\sup_{(m,\boldsymbol{\rho}^*,\tilde{\boldsymbol{\sigma}})\in\mathscr{A}} \inf_{\mathbf{d}} \mathscr{L} \leq \inf_{\mathbf{d}} \sup_{(m,\boldsymbol{\rho}^*,\tilde{\boldsymbol{\sigma}})\in\mathscr{A}} \mathscr{L} \tag{29}$$

we get

$$m_S \leq m_K \tag{30}$$

where

$$m_K = \inf_{\mathbf{d}} \sup_{(m,\boldsymbol{\rho}^*,\tilde{\boldsymbol{\sigma}})\in\mathscr{A}} \mathscr{L}(m,\boldsymbol{\rho}^*,\tilde{\boldsymbol{\sigma}};\mathbf{d}).$$

Rewriting the coefficient m_K in a more explicit form [24] leads to

$$m_K = \inf\{\int_\Omega \int_0^T \mathscr{D}(\mathbf{d}(\mathbf{x},t))d\Omega dt : \int_0^T \int_\Omega \mathbf{d}:\boldsymbol{\sigma}^E d\Omega dt = 1 \text{ and } \int_0^T \mathbf{d}dt \in \mathscr{B}_0\} \tag{31}$$

with $\mathscr{D}(\mathbf{d}) = \sup_{\boldsymbol{\sigma}\in\mathscr{C}} \boldsymbol{\sigma}:\mathbf{d}$ and

$$\mathscr{B}_0 = \{(\nabla\mathbf{u} + \nabla^t\mathbf{u})/2 : \mathbf{u} = 0 \text{ on } \Gamma_u\}.$$

If $m_K < 1$ then by (30) and (27) we can conclude that shakedown does not occur. A necessary condition for shakedown is thus that $m_K \geq 1$. We can thus formulate the following

Theorem 4 *If shakedown occurs, then* $1 \leq \int_\Omega \int_0^T \mathscr{D}(\mathbf{d}(\mathbf{x},t))d\Omega dt$ *for any history* $\mathbf{d}(\mathbf{x},t)$ *such that* $\int_0^T \int_\Omega \mathbf{d}:\boldsymbol{\sigma}^E d\Omega\, dt = 1$ *and* $\int_0^T \mathbf{d} \in \mathscr{B}_0$.

In practice, an upper bound m_K^+ on m_K (and therefore on m_S) can be obtained by constructing specific strain histories satisfying the requirements $\int_0^T \int_\Omega \mathbf{d}:\boldsymbol{\sigma}^E d\Omega\, dt = 1$ and $\int_0^T \mathbf{d} \in \mathscr{B}_0$.

4.3 Illustrative Example

As an illustration of the shakedown theorems, consider the example introduced in Sect. 2.3. A $T-$ periodic solution $(\boldsymbol{\sigma}^E, \mu^E, \mathbf{u}^E, c^E)$ to the corresponding purely elasto-diffusive problem has been calculated in closed-form in [20]. Denoting by $\Re$ (resp. $\Im$) the real (resp. imaginary) part of a complex valued quantity, we have in

particular

$$\boldsymbol{\sigma}^E(\mathbf{x},t) = \Re\left(e^{i\omega t}\frac{G\tilde{a}H}{2}(\hat{\sigma}_r\mathbf{e}_r\otimes\mathbf{e}_r + \hat{\sigma}_\theta\mathbf{e}_\theta\otimes\mathbf{e}_\theta + \hat{\sigma}_z\mathbf{e}_z\otimes\mathbf{e}_z)\right)$$

where

$$\hat{\sigma}_r = 1 - \frac{\hat{R}}{\hat{r}}\frac{J_1(\hat{r})}{J_1(\hat{R})},\quad \hat{\sigma}_\theta = 1 + \frac{\hat{R}}{\hat{r}}\frac{J_1(\hat{r})}{J_1(\hat{R})} - \frac{\hat{R}J_0(\hat{r})}{J_1(\hat{R})},\quad \hat{\sigma}_z = 2\nu - \frac{\hat{R}J_0(\hat{r})}{J_1(\hat{R})} \tag{32}$$

and

$$\hat{r} = \hat{\lambda}r,\quad \hat{R} = \hat{\lambda}R,\quad \hat{\lambda} = e^{i\frac{3\pi}{4}}\sqrt{\frac{\omega}{D(1-a\tilde{a}/k)}}. \tag{33}$$

In (32), J is the Bessel function of the first kind. The scalar $\tilde{a}$ in (33) is defined as in (12).

Let us denote by $\mathbf{s}^E$ the deviatoric part of $\boldsymbol{\sigma}^E$. Using Theorem 3 with $\boldsymbol{\rho} = 0$, we can see that if

$$\sup_{r,t}\|\mathbf{s}^E(r,t)\| \le \sqrt{2}\sigma_Y \tag{34}$$

then shakedown occurs. It can be verified that the supremum in (34) is reached at $r = R$. Condition (34) can thus be rewritten as

$$\|\mathbf{s}^E(R,t_0)\| \le \sqrt{2}\sigma_Y \tag{35}$$

where $t_0 \in [0,T]$ is such that $\|\mathbf{s}^E(R,t_0)\| = \sup_t \|\mathbf{s}^E(R,t\|$. By Theorem 3, condition (35) is a sufficient condition for shakedown. Theorem 4 shows that it is also necessary. Consider indeed the history defined by

$$\mathbf{d}(\mathbf{x},t) = \frac{1}{4\pi RL}\frac{\mathbf{s}^E(R,t_0)}{\|\mathbf{s}^E(R,t_0)\|^2}\delta(r-R)\left(\delta(t-t_0)-\delta(t-t_1)\right) \tag{36}$$

where L is the length of the particle in the $\mathbf{e}_z$ direction and δ is the Dirac distribution. The time instant t_1 in (36) is defined by $t_1 = (t_0 + T/2) \bmod T$. Observe in particular that $\mathbf{s}^E(R,t_1) = -\mathbf{s}^E(R,t_0)$. We have $\int_0^T \mathbf{d}(\mathbf{x},t)dt = 0$ hence $\int_0^T \mathbf{d}(\mathbf{x},t)dt \in \mathscr{B}_0$. Moreover we have $\int_\Omega\int_0^T \boldsymbol{\sigma}^E : \mathbf{d}d\Omega dt = 1$. Using Theorem 4 with the history $\mathbf{d}$ in (36) shows that a necessary condition for shakedown is

$$1 \le \int_\Omega\int_0^T \mathscr{D}(\mathbf{d}(\mathbf{x},t))d\Omega dt \tag{37}$$

For the Mises elasticity domain, the function $\mathscr{D}$ is given by $\mathscr{D}(\mathbf{d}) = \sqrt{2}\sigma_Y\|\mathbf{d}\|$ provided that $\mathbf{d}$ is deviatoric. It follows that

$$\int_\Omega \int_0^T \mathscr{D}(\mathbf{d}(\mathbf{x},t))d\Omega dt = \frac{\sqrt{2}\sigma_Y}{\|\mathbf{s}^E(R,t_0)\|}.$$

Condition (37) is thus the same as (35). This shows that Condition (35) is both a necessary and a sufficient for shakedown to occur.

Condition (35) can be rewritten as [20]

$$H \leq H_{SD}(\tilde{\omega}) \tag{38}$$

where

$$H_{SD}(\tilde{\omega}) = 2\frac{\sqrt{6}\sigma_Y}{G|\tilde{a}|}\left(A(\tilde{\omega}) + \sqrt{A^2(\tilde{\omega}) - B(\tilde{\omega})}\right)^{-\frac{1}{2}} \tag{39}$$

and

$$A(\tilde{\omega}) = 3(1-\nu)^2 + (\Re z - 1 - \nu)^2 + (\Im z)^2,\ B(\tilde{\omega}) = 12(1-\nu)^2(\Im z)^2; \tag{40}$$

with

$$\tilde{\omega} = \omega T_0, \quad z = \frac{\hat{R}J_0(\hat{R})}{J_1(\hat{R})}.$$

Using the values of the constitutive parameters reported in Sect. 2.3, we obtain that

$$H_{SD}(20) < 100\ \text{mol/m}^3 < H_{SD}(10) \tag{41}$$

For a loading parameter $H = 100$ mol/m^3, (41) means that elastic shakedown occurs for $\omega = 10/T_0$ but not for $\omega = 20/T_0$. Those predictions agree with the finite element simulations shown in Figs. 1 and 2. In the case $\omega = 10/T_0$ corresponding to elastic shakedown, a result from Theorems 1 to 2 is that the C–V response in the cyclic steady state coincide (up to a time-independent translation) with the cyclic C–V response of the purely elasto-diffusive problem. The latter can be calculated in closed form and is given by

$$C^E(t) = \frac{1}{2}(1+\sin\omega t), \quad \mu^E(t) = \frac{1}{4}\Re(e^{i\omega t} i z) \tag{42}$$

The C–V response provided by (42) is shown in Fig. 4 (red line). The curve obtained form the finite element simulations of the diffusion-induced plasticity problem is shown as a blue curve in Fig. 4. It appears that the steady state in the C–V plane is translated form the elasto-diffusive response as expected.

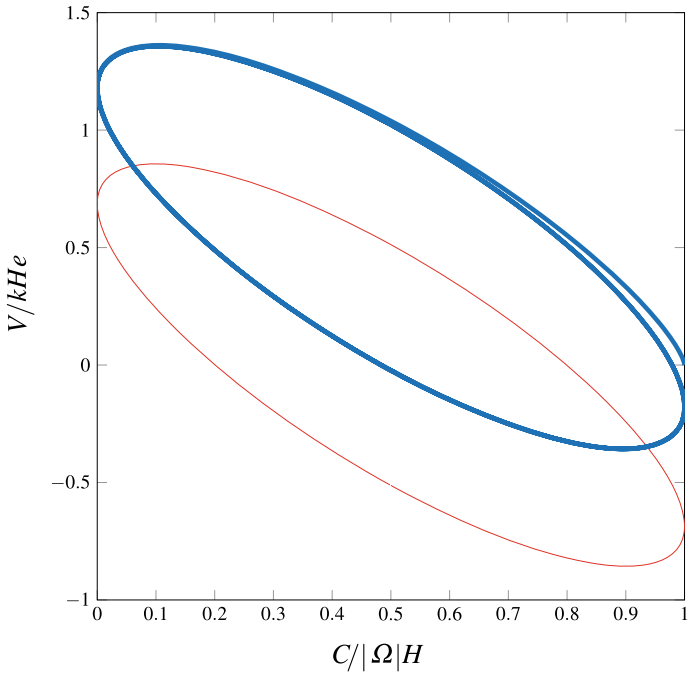

Fig. 4 Charge-Voltage response for $H = 100$ mol/m^3, $\omega = 10/T_0$. Diffusion-induced plasticity (blue curve), pure elasto-diffusion (red curve)

References

1. Brassart, L., Zhao, K., Suo, Z.: Cyclic plasticity and shakedown in high-capacity electrodes of lithium-ion batteries. Int. J. Solids. Struct. **49**, 1120–1129 (2013)
2. Frederick, C., Armstrong, P.: Convergent internal stresses and steady cyclic states of stress. J. Strain Anal. Eng. Des. **1**, 154–159 (1966)
3. Halphen, B.: Steady cycles and shakedown in elastic-viscoplastic and plastic structures. In: Structures et matériaux sous chargement cyclique. Association amicale des ingénieurs anciens éleves de l'E.N.P.C., pp. 203–229 (1978)
4. Johnson, C., Mercier, B., Nedelec, J.C.: Convergence to a periodic solution in perfect plasticity. In: Structures et matériaux sous chargement cyclique. Association amicale des ingénieurs anciens éleves de l'E.N.P.C., pp. 253–255 (1978)
5. Maitournam, H., Pommier, B., Thomas, J.J.: Détermination de la réponse asymptotique d'une structure anélastique sous chargement cyclique. C.R. Mecanique **330**, 703–708 (2002)
6. Peigney, M., Stolz, C.: Approche par contrôle optimal des structures élastoviscoplastiques sous chargement cyclique. C.R. Acad. Sci. Paris II **329**, 643–648 (2001)
7. Peigney, M., Stolz, C.: An optimal control approach to the analysis of inelastic structures under cyclic loading. J. Mech. Phys. Solids **51**, 575–605 (2003)
8. Spiliopoulos, K.V., Panagiotou, K.D.: A direct method to predict cyclic steady states of elasto-plastic structures. Comput. Methods Appl. Mech. Eng. **223**, 186–198 (2012)
9. Klarbring, A., Barber, J.R., Spagnoli, A., Terzano, M.: Shakedown of discrete systems involving plasticity and friction. Eur. J. Mech. A **64**, 160–164

10. Peigney, M.: Recoverable strains in composite shape memory alloys. J. Mech. Phys. Solids **56**, 360–375 (2008)
11. Peigney, M.: Shakedown theorems and asymptotic behaviour of solids in non-smooth mechanics. Eur. J. Mech. A **29**, 784–793 (2010)
12. Peigney, M.: On shakedown of shape memory alloys structures. Ann. Solid Struct. Mech. **6**, 17–28 (2014)
13. Peigney, M.: Shakedown of elastic-perfectly plastic materials with temperature-dependent elastic moduli. J. Mech. Phys. Solids **71**, 112–131 (2014)
14. Pham, D.C.: Consistent limited kinematic hardening plasticity theory and path-independent shakedown theorems. Int. J. Mech. Sci. **130**, 11–18 (2017)
15. Larché, F., Cahn, J.W.: A linear theory of thermochemical equilibrium of solids under stress. Acta Metall. **21**, 1051–1063 (1973)
16. Dang Van, K., Papadopoulos I.V.: Introduction to fatigue analysis in mechanical design by the multiscale approach. In: High-Cycle Metal Fatigue. Springer, Berlin (1999)
17. Koiter, W.T.: General theorems for elastic-plastic solids. In: Progress in Solid Mechanics (1960)
18. Melan, E.: Theorie statisch unbestimmter Systeme aus ideal-plastischen Baustoff. Sitz. Berl. Ak. Wiss. **145**, 195–218 (1936)
19. Symonds, P.S.: Shakedown in continuous media. J. Appl. Mech. **18**, 85–89 (1951)
20. Peigney, M.: Cyclic steady states in diffusion-induced plasticity with applications to lithium-ion batteries. J. Mech. Phys. Solids **111**, 530–556 (2018)
21. Opial, Z.: Weak convergence of the sequence of successive approximations for nonexpansive mappings. Bull. Am. Math. Soc. **73**, 591–597 (1967)
22. Débordes, O., Nayroles, B., et al.: Sur la théorie et le calcul à l'adaptation des structures élastoplastiques. J. Mecanique **15**, 1–53 (1976)
23. Nguyen, Q.S.: On shakedown analysis in hardening plasticity. J. Mech. Phys. Solids **51**, 101–125 (2003)
24. Peigney, M.: Static and kinematic shakedown theorems in diffusion-induced plasticity. J. Thero. App. Mech. **58**(2), 415–424 (2020)

Numerical Method for Quasi-static and Dynamic Elastoplastic Problems by Symplectic Brezis-Ekeland-Nayroles Non-incremental Principle

Xiaodan Cao, Abdelbacet Oueslati, An Danh Nguyen, Marcus Stoffel, Bernd Market, and Géry de Saxcé

Abstract Most computer-aided engineering software provide a classical incremental computation procedure for nonlinear problems. Although little used in the literature, the Brezis-Ekeland-Nayroles (BEN) principle, an alternative step-by-step algorithm, based on the time integration of the sum of the dissipation potential and its Fenchel polar can have a global view of whole evolution. In short, the BEN principle converts a mechanical problem to a constrained optimization problem. Recently, Buliga and de Saxcé have proposed a symplectic version of the BEN principle which generalizes the Hamiltonian inclusion formalism for the dissipative systems. In the present work, this formalism is specialized to the standard plasticity in small, finite strains, in statics and dynamics. We apply it numerically to solve the classical problem of a tube problem in plane strain subjected to an internal pressure in statics and dynamics. An excellent agreement is obtained between the numerical results obtained by the BEN approach and the reference numerical solution.

1 Introduction

A lot of mechanical problems have non-linear behaviors because of dissipative phenomena such as plasticity, damage, etc. Their analytical solutions cannot be determined easily. As it is unlikely to carry out all kinds of experiments for the similar problems, the computer-aided engineering (CAE) software has been developed in the last 30 years. For a non-linear problem, most of the software uses the step-by-step or incremental method [1–5] in computational solid mechanics.

In practice, by using the step-by-step method, some simulations cannot be completely performed because the convergence frequently fails before the end of the

X. Cao · A. Oueslati · A. D. Nguyen · M. Stoffel · B. Market · G. de Saxcé (✉)
FRE 2016 LaMcube Laboratoire de Mécanique Multiphysique Multiéchelle, CNRS, Centrale Lille, Université of Lille, Lille, France
e-mail: gery.de-saxce@univ-lille.fr

X. Cao
e-mail: xiaodan.cao@univ-lille.fr

A. A. Pisano et al. (eds.), *Direct Methods*, Lecture Notes in Applied and Computational Mechanics 95, https://doi.org/10.1007/978-3-030-48834-5_10

computation and it is difficult to restart. The only solution to overcome the difficulty often lies in reducing the step size but increases the computational time. Another difficulty arises because, in an iterative method, truncation error occur at each iteration. So the computation error of the usual step-by-step method based in radial return algorithm accumulates and grows as the number of step increases. This error cannot be avoided and it may strongly affect the whole accuracy of complex simulations.

Using step-by-step methods, we are going, as it were, with the head down. This is the breakthrough we want to get. To address this issue, there is few methods in literature. We propose to start with Brezis-Ekeland-Nayroles principle (in short, the BEN principle) [6, 7]. It is based on the dissipation potential and its Fenchel transform over the time integration. In [8–10], the BEN principle is extended in a pure mathematical manner a few to monotone operators and doubly nonlinear equations, or reworked in order to have a discretized form. Recently, Buliga and de Saxcé [11] generalized the BEN principle to the dynamics of dissipative systems by linking two worlds together, the one of smooth functions in symplectic geometry systems and the one of non-smooth functions for dissipative systems. They applied this symplectic BEN principle to standard plasticity [12] in dynamics and deduce from it the limit case of statics. The BEN principle is a tool perfectly designed to solve complex problem of evolution of dissipative systems. In place of computing in the step-by-step way and facing the convergence problem, the BEN principle allows to work simultaneously over all steps, that allows to have a consistent view of the whole evolution.

According to the authors' knowledge, no one has ever numerically applied the BEN principle to test its feasibility to work on all time steps simultaneously. The aim of this paper is to implement numerically the powerful BEN principle by solving a mechanical problem in statics and dynamics. When the analytical solution cannot be provided, the BEN principle solution is compared with the numerical solution of a standard finite element (FM) method solver.

The paper is divided in three parts. Firstly, we present directly the BEN principle for elastoplasticity in statics and dynamics. Then, we apply the general principle to the tube problem, using the mixed FE [13, 14] to avoid the drawbacks of the standard or displacement FE, like inaccuracy of the stress field, simulation results for elastic, elastoplastic regime in statics and dynamics. Simulation results are presented separately with different plastic criteria and behavior laws.

2 BEN Principle for Elastoplasticity

To illustrate the general formalism and to show how it allows to develop powerful variational principles for dissipative systems within the frame of continuum mechanics, we consider the standard plasticity and viscoplasticity in small deformations based on the additive decomposition of strains into elastic and plastic strains:

$$\varepsilon = \varepsilon^e + \varepsilon^p = S\,\sigma + \varepsilon^p$$

where S is the elastic compliance tensor. Let $\Omega \subset \mathbb{R}^n$ be a bounded, open set, with piecewise smooth boundary $\partial\Omega$. As usual, it is divided into disjoint parts, $\partial\Omega_0$ (called support) where the displacements are imposed and $\partial\Omega_1$ where the surface forces are imposed. U and E are suitable functional spaces of displacement and stress fields on Ω. The standard duality between stress and strain fields is:

$$\langle \sigma, \varepsilon \rangle = \int_\Omega \sigma : \varepsilon \, d\Omega$$

Applied to the quasi-static plasticity, the BEN principle claims that the evolution curves $\sigma : [0, T] \to E$ and $u : [0, T] \to U$ minimize:

$$\bar{\Pi}(\sigma, \dot{u}) = \int_0^T \left\{ \varphi(\sigma) + \varphi^*(\nabla \dot{u} - S\dot{\sigma}) - \langle \sigma, \nabla \dot{u} - S\dot{\sigma} \rangle \right\} \, \mathrm{dt} \tag{1}$$

among all curves satisfying:

- the equilibrium equations in statics:

$$\nabla \cdot \sigma + f = 0 \quad \text{in} \quad \Omega, \qquad \sigma \cdot n = \bar{f} \quad \text{on} \quad \partial\Omega_1 \tag{2}$$

- the equilibrium equations in dynamics:

$$\nabla \cdot \sigma + f = \rho \ddot{u} \quad \text{in} \quad \Omega, \qquad \sigma \cdot n = \bar{f} \quad \text{on} \quad \partial\Omega_1 \tag{3}$$

- the kinematical conditions on supports:

$$u = \bar{u} \quad \text{on} \quad \partial\Omega_0 \tag{4}$$

- and the initial conditions:

$$\sigma(0) = \sigma_0, \qquad u(0) = u_0 \tag{5}$$

The following is detailed in statics. To show the pertinence of the principle, we prove now that the stationarity condition of the variational principle restitues the expected equations governing the elastoplastic evolution problem. First, we introduce densities ϕ and ϕ^* such that:

$$\varphi(\sigma) = \int_\Omega \phi(\sigma) \, d\Omega, \qquad \varphi^*(\varepsilon^p) = \int_\Omega \phi^*(\varepsilon^p) \, d\Omega,$$

If ϕ and ϕ^* are differentiable, the yielding rule and the inverse law are:

$$\dot{\varepsilon}^p = \frac{\partial \phi}{\partial \sigma}, \qquad \sigma = \frac{\partial \phi^*}{\partial \dot{\varepsilon}^p} \tag{6}$$

Then Eq. (1) reads:

$$\bar{\Pi}(\sigma, \dot{u}) = \int_{\Omega} \{ \int_0^T \left[\phi(\sigma) + \phi^*(\nabla \dot{u} - S\dot{\sigma}) - \sigma : (\nabla \dot{u} - S\dot{\sigma}) \right] \mathrm{dt} \tag{7}$$

The stationarity conditions is:

$$\delta\bar{\Pi}(\sigma, \dot{u}) = \int_{\Omega} \{ \int_0^T \left(\frac{\partial \phi}{\partial \sigma} : \delta\sigma + \frac{\partial \phi^*}{\partial \dot{\varepsilon}^p} : \left(\nabla \delta\dot{u} - S \frac{d}{dt}(\delta\sigma) \right) - \delta\sigma : \nabla \dot{u} - \sigma : \nabla \delta\dot{u} + \delta\sigma : S\dot{\sigma} + \sigma : S \frac{d}{dt}(\delta\sigma) \right) \mathrm{dt} \tag{8}$$

Taking into account that the stress fields satisfy a priori the initial conditions (5):

$$\delta\sigma(0) = 0, \qquad \delta u(0) = 0$$

and time integrating by part leads to:

$$\delta\bar{\Pi}(\sigma, \dot{u}) = \int_{\Omega} \{ \int_0^T \left[\delta\sigma : \left(\frac{\partial \phi}{\partial \sigma} + S \frac{d}{dt} \left(\frac{\partial \phi^*}{\partial \dot{\varepsilon}^p} \right) - \nabla \dot{u} \right) + \left(\frac{\partial \phi^*}{\partial \dot{\varepsilon}^p} - \sigma \right) : \nabla \delta\dot{u} \right] \mathrm{dt} \tag{9}$$

Taking into account that the displacement fields satisfy a priori the kinematical conditions (4):

$$\delta u = 0 \quad \text{on} \quad \partial\Omega_0$$

and space integrating by part the second term of the former line gives:

$$\int_{\Omega} \int_0^T \left(\frac{\partial \phi^*}{\partial \dot{\varepsilon}^p} - \sigma \right) : \nabla \delta\dot{u} \ \mathrm{dt}\, d\Omega = \int_0^T [\int_{\partial\Omega_1} \delta\dot{u} \cdot \left(\left(\frac{\partial \phi^*}{\partial \dot{\varepsilon}^p} - \sigma \right) \cdot n \right) \mathrm{dS} - \int_{\Omega} \delta\dot{u} \cdot \left(\nabla \cdot \left(\frac{\partial \phi^*}{\partial \dot{\varepsilon}^p} - \sigma \right) \right) d\Omega] \, \mathrm{dt} \tag{10}$$

Taking into account that the stress fields satisfy a priori the equilibrium equations (2), the expression (10) becomes:

$$\int_{\Omega} \int_0^T \left(\frac{\partial \phi^*}{\partial \dot{\varepsilon}^p} - \sigma \right) : \nabla \delta\dot{u} \ \mathrm{dt}\, d\Omega = \int_0^T [\int_{\partial\Omega_1} \delta\dot{u} \cdot \left(\left(\frac{\partial \phi^*}{\partial \dot{\varepsilon}^p} \cdot n - \bar{f} \right) \right) \mathrm{dS} - \int_{\Omega} \delta\dot{u} \cdot \left(\nabla \cdot \frac{\partial \phi^*}{\partial \dot{\varepsilon}^p} + f \right) d\Omega] \, \mathrm{dt}$$

Introducing this expression into Eq. (9) and considering arbitrary field variations, we obtain for every time:

$$\nabla \dot{u} = \frac{\partial \phi}{\partial \sigma} + S \frac{d}{dt} \left(\frac{\partial \phi^*}{\partial \dot{\varepsilon}^p} \right) \quad \text{in} \quad \Omega \tag{11}$$

$$\nabla \cdot \frac{\partial \phi^*}{\partial \dot{\varepsilon}^p} + f = 0 \quad \text{in} \quad \Omega \tag{12}$$

$$\frac{\partial \phi^*}{\partial \dot{\varepsilon}^p} \cdot n = \bar{f} \quad \text{on} \quad \partial\Omega_1 \tag{13}$$

Condition (11) means that the stress and plastic strain given by Eq. (6) fulfill the classical strain decomposition into plastic and elastic parts:

$$\nabla \dot{u} = \dot{\varepsilon}^p + S\,\dot{\sigma} \quad \text{in} \quad \Omega$$

Condition (12) and (13) mean that the stress field given by the inverse law (6) verifies the equilibrium equations.

The previous framework is valid only under suitable assumptions of differentiability of dissipation potentials in viscoplasticity, for instance for Norton-Odqvist model. The case of classical plasticity is singular since the potential ϕ is non-differentiable as indicator function χ_K of the elastic domain K, equal to 0 on K and to $+\infty$ otherwise. This pitfall can be by-passed in practice by relaxing the plasticity criterion:

$$f_{vm/T}(\sigma) \leq 0 \tag{14}$$

thanks to a field of Lagrange multiplier λ, with f_{vm} von Mises criterion adn f_T Tresca one. Then BEN principle specialized to classical plasticity claims that the evolution curves $\sigma : [0, T] \to E$ and $u : [0, T] \to U$ minimize:

$$\bar{\Pi}(\sigma, \dot{u}, \lambda) = \int_0^T \left\{ \int_\Omega \lambda\, f(\sigma) + \varphi^*(\nabla \dot{u} - S\dot{\sigma}) d\Omega - \langle \sigma, \nabla \dot{u} - S\dot{\sigma} \rangle \right\} \text{dt} \tag{15}$$

among all curves satisfying the plasticity criterion (14), the equilibrium equations (2), the kinematical conditions on supports (4) and the initial conditions (5). Formally, the plasticity is a particular case of viscoplasticity, replacing the potential ϕ by $\lambda\, f$ and the yielding rule (6) provides the normality law:

$$\dot{\varepsilon}^p = \lambda \frac{\partial f_{vm/T}}{\partial \sigma}$$

3 The Tube Problem in Statics

The previous section provides some useful notions of the BEN principle. Thanks to the Eqs. (1, 2, 4, 5), the mechanical problem could be solved as an optimization problem. To start up, we choose a classical academic example, the thick tube subjected to an internal pressure.

To simplify, we take an axisymmetric problem. The internal and external radii of the tube are a and b respectively. The imposed internal pressure is p. For material

parameters, we have Young's modulus E, Poisson coefficient ν and yield stress σ_Y. Supposing that the thick tube is in plane strain and the initial fields are null, if the internal pressure increases in the monotone way from zero to limit charge, the internal wall of the tube will come to yield firstly, and successively the external wall.

One material behavior laws and two yield criteria are discussed, isotropic perfectly plastic behavior law, Tresca or von Mises criteria.

3.1 Application of the BEN Principle

Taking into account the is axisymmetry and the plane strain, the displacement u depends only the radius and is radial:

$$u = u_r(r)\, e_r \tag{16}$$

The stress and strain tensors are given in small deformations hypothesis by:

$$\sigma = \begin{pmatrix} \sigma_{rr} & 0 \\ 0 & \sigma_{\theta\theta} \end{pmatrix} \quad \varepsilon = \begin{pmatrix} \frac{du_r}{dr} & 0 \\ 0 & \frac{u_r}{r} \end{pmatrix} \tag{17}$$

The elastic domain is:

$$K = \{\sigma \quad \text{such that} \quad f \leqslant 0\}$$

The dissipation power by unit volume is:

$$D = \sigma : \dot{\varepsilon}^{\mathrm{p}}$$

where σ and $\dot{\epsilon}^{\,p}$ are associated by the normality law. The dissipation power is:

$$D = \sigma_Y \lambda \tag{18}$$

The dissipation potential for both criteria is:

$$\varphi(\sigma) = \int_{\Omega} \chi_K(\sigma)$$

with χ_K the indicator function of the elastic domain K. The Fenchel conjugate function is:

$$\varphi^*(\dot{\varepsilon}^{\,p}) = \int_{\Omega} \{D\}$$

Applying the BEN principle, we minimize the functional (15) that reads:

$$\bar{\Pi}(\sigma, u) = \int_{t_0}^{t_1} \left\{ \int_{\Omega} D - \langle \sigma, \nabla \dot{u} - S\dot{\sigma} \rangle \right\} \mathrm{d}t \tag{19}$$

among all the curves among all curves $(\sigma, u) : [t_0, t_1] \to U \times E$ such that $\sigma(0) = 0$, $u(0) = 0$, satisfying Tresca or von Mises yield condition, the normality rule and the equilibrium equations.

3.2 Mixed Finite Element Method for Thick Tube Problem

The mixed finite element method (FEM) is proposed to discretize the functional which allow to have different discretized fields at the same time like stress, displacement, plastic multiplier etc. The mixed FEM has a better convergence in a stress field which is statically admissible specially for beam, plate and shell element, also a good accuracy of stress in plasticity. For the thick tube problem, there are three unknown fields: radial and hoop stresses, radial displacement and plastic multiplier.

3.2.1 Stress Field

As the thick tube is modeled by an axisymmetric element ($a \leqslant r \leqslant b$), imposing an axisymmetric element inside the thick tube with $\alpha \leqslant r \leqslant \beta$, there are two stress connectors (radial and hoop stresses) per end of the element gathered in the vector:

$$g_e = \begin{bmatrix} g_{e,1} \\ g_{e,2} \\ g_{e,3} \\ g_{e,4} \end{bmatrix} = \begin{bmatrix} \sigma_{rr} \mid_{r=\alpha} \\ \sigma_{\theta\theta} \mid_{r=\alpha} \\ \sigma_{rr} \mid_{r=\beta} \\ \sigma_{\theta\theta} \mid_{r=\beta} \end{bmatrix} \tag{20}$$

In order to satisfy a priori the internal equilibrium equations in the constrained minimization problem, we choose a polynomial stress field σ_e which depends on the stress parameters h of the element. The expression of the hoop stress is derived from the equilibrium equation $\sigma_{\theta\theta} = \frac{d}{dr}(r\sigma_{rr})$, that gives in matrix form:

$$\sigma_e(r) = R_e(r)\, h \tag{21}$$

$$\begin{bmatrix} \sigma_{rr} \\ \sigma_{\theta\theta} \end{bmatrix} = \begin{bmatrix} 1 & r & r^2 & r^3 \\ 1 & 2r & 3r^2 & 4r^3 \end{bmatrix} \begin{bmatrix} h_1 \\ h_2 \\ h_3 \\ h_4 \end{bmatrix} \tag{22}$$

Owing to Eqs. (20) and (22), we have the stress connectors g_e in terms of the stress parameters h:

$$g_e = C_e h \tag{23}$$

$$\begin{bmatrix} g_{e,1} \\ g_{e,2} \\ g_{e,3} \\ g_{e,4} \end{bmatrix} = \begin{bmatrix} 1 & \alpha & \alpha^2 & \alpha^3 \\ 1 & 2\alpha & 3\alpha^2 & 4\alpha^3 \\ 1 & \beta & \beta^2 & \beta^3 \\ 1 & 2\beta & 3\beta^2 & 4\beta^3 \end{bmatrix} \begin{bmatrix} h_1 \\ h_2 \\ h_3 \\ h_4 \end{bmatrix}$$

By eliminating the stress parameters between Eqs. (21) and (23), the stress field σ_e is expressed in terms of stress connector g_e of the element:

$$\sigma_e(r) = R_e(r) C_e^{-1} g_e = T_e(r) g_e \tag{24}$$

3.2.2 Displacement Field

For the same element occupying $\alpha \leqslant r \leqslant \beta$, there is one displacement connector q_e at each end:

$$q_{e,1} = u_r \mid_{r=\alpha} \qquad q_{e,2} = u_r \mid_{r=\beta}$$

In order to provide a strain field which has the same number of parameters as the one of the stress field, we add two intermediate equidistant nodes inside the element:

$$\gamma = \frac{2\alpha + \beta}{3} \qquad \delta = \frac{\alpha + 2\beta}{3}$$

and two extra connectors $q_{e,3} = u_r \mid_{r=\gamma}$, $q_{e,4} = u_r \mid_{r=\delta}$. The four displacement connectors are gathered in the vector:

$$q_e = \begin{bmatrix} q_{e,1} \\ q_{e,2} \\ q_{e,3} \\ q_{e,4} \end{bmatrix} = \begin{bmatrix} u_r \mid_{r=\alpha} \\ u_r \mid_{r=\beta} \\ u_r \mid_{r=\gamma} \\ u_r \mid_{r=\delta} \end{bmatrix} \tag{25}$$

A polynomial displacement field u_r is proposed:

$$u_r = u_1 + u_2 r + u_3 r^2 + u_4 r^3$$

By defining a cubic Lagrange interpolation, we obtain the relation between the displacement field u_r and the displacement connectors q_e:

$$u_r(r) = N_e(r)\, q_e \tag{26}$$

with:

$$N_e^T(r) = \frac{1}{16} \begin{bmatrix} -(1-\eta)(1-9\eta^2) \\ -(1+\eta)(1-9\eta^2) \\ 9(1-\eta^2)(1-3\eta) \\ 9(1-\eta^2)(1+3\eta) \end{bmatrix} \qquad \eta = \frac{2r - (\beta + \alpha)}{\beta - \alpha}$$

The corresponding strain field ε_e can be expressed in terms of the displacement connectors of the element thanks to Eq. (17):

$$\varepsilon_e(r) = B_e(r)\, q_e \tag{27}$$

3.2.3 Plastic Multiplier Field

Introducing the plastic multipliers λ which are located at the four Gauss point for each element $\alpha \leqslant r \leqslant \beta$, the flow rule reads:

$$\dot{\varepsilon}_e^p = \lambda_e \frac{\partial f_T}{\partial \sigma} = \lambda_e\, N_Y \tag{28}$$

3.2.4 Discretization of the Functional

For the thick tube problem, we have three discretized fields for one element $\alpha \leqslant r \leqslant \beta$, stress σ_e, displacement u_r and plastic strain rate $\dot{\varepsilon}_e^p$ which depend on each connectors, stress connectors g_e, displacement connectors q_e and plastic multipliers λ_e:

$$\sigma_e(r) = T_e(r) g_e \qquad u_r(r) = N_e(r)\, q_e \qquad \dot{\varepsilon}_e^p = \lambda_e\, N_Y$$

We have now the BEN principle equation, the application of the mixed FEM. To numerically solve the thick tube problem, it remains to obtain the discretization form of Eq. (19).

1. Space integral discretization

For the space discretization, we would like to evaluated the stress and displacement fields in four Gauss point for each element where the plastic multipliers are located. So the space integral is approximated by the usual Gaussian quadrature numerical integration method on every axisymmetric element:

$$\int_\alpha^\beta A(r)\, 2\pi\, r\, dr \cong \sum_{g=1}^{4} 2\pi\, w_g\, A(r_g)\, r_g$$

Thanks to the localization matrices M_e, L_e, P_e for each unknown field, we could carry out the assembling:

$$g_e = M_e g, \quad q_e = L_e q, \quad \lambda_e = P_e \lambda$$

The discretized form of the functional Eq. (19) is:

$$\bar{\Pi}(g, q, \lambda) = \int_{t_0}^{t_1} \left(\Lambda^T \lambda(t) - \dot{q}^T(t) G\, g(t) + \dot{g}^T(t) F\, g(t) \right) \mathrm{dt} \tag{29}$$

with:

$$\Lambda = \sum_{e=1}^{n} P_e^T \Lambda_e,$$

$$G = \sum_{e=1}^{n} \int_{\alpha}^{\beta} L_e^T B_e^T(r)\, T_e(r)\, M_e\, 2\pi\, r\, dr, \qquad F = \sum_{e=1}^{n} \int_{\alpha}^{\beta} M_e^T T_e^T(r)\, S\, T_e(r)\, M_e\, 2\pi\, r\, dr$$

under the constraints of:

- equilibrium (on the boundary, the internal equilibrium being satisfied a priori):

$$g_1(t) = -p(t), \qquad g_{2(n+1)}(t) = 0 \tag{30}$$

- plasticity (at every Gauss point g of every element e):

$$N_{Y,e}^T(r_g)\, g - \sigma_Y \leq 0, \qquad \lambda_g \geq 0, \qquad N_Y \lambda_g = B_e(r_g)\, \dot{q}_e - S\, T_e(r_g)\, \dot{g}_e \tag{31}$$

- initial conditions:

$$g(t_0) = 0, \qquad q(t_0) = 0, \qquad \lambda(t_0) = 0 \tag{32}$$

with $N_{Y,e}(r_g) = M_e^T T_e^T(r_g) N_Y$.

2. Time integral discretization

For any physical quantity a, we impose $a_j = a(t_j)$, $\Delta a_j = a_j - a_{j-1}$. On each step, we approximate the time rate by $\dot{a} = \frac{\Delta a_j}{\Delta t_j}$. As the plasticity is independent of the time parameterization in statics, we use for convenience sake:

$$\Delta t_j = 1 \tag{33}$$

Considering m time step from t_0 to t_m and enforcing the yield condition only at the beginning and the end of the step, we have to minimize the objective function:

$$\bar{\Pi}(g_0, \ldots, g_m, q_0, \ldots, q_m, \lambda_0, \ldots, \lambda_m) = \sum_{j=0}^{j=m} (\Lambda^T \lambda_j - \Delta q_j^T G\, g_j + \Delta g_j^T F g_j) \tag{34}$$

under the constraints of:

- equilibrium (on the boundary, at each time step):

$$g_{0,j} = -p(t_j), \qquad g_{2(n+1)-1,j} = 0 \tag{35}$$

- plasticity (at every Gauss point g of every element e and at every time step):

$$N_{Y,e}^{T}(r_g)g_j - \sigma_Y \leq 0, \qquad \lambda_{g,j} \geq 0 \qquad N_Y(r_g)\lambda_{g,j} = B_e(r_g)\, L_e \Delta q_j - S\, T_e(r_g)\, M_e \Delta g_j \tag{36}$$

- initial conditions:

$$g_0 = 0, \qquad q_0 = 0, \qquad \lambda_0 = 0 \tag{37}$$

3.3 Implementation and Simulation Results

Matlab and its solver `fmincon` can find the minimum of constrained nonlinear multivariable function. The functional (34–37) is a quadrature non-linear function under linear (Tresca criterion) or quadrature (von Mises criterion) constraints.

In the program, one needs to impose a small tolerance for the equality constraint (Eq. 36) in the optimization problem because there always exists the computation error which deduces that the equality can not be satisfied exactly. For all fields in all temporal en points, their optimization depart points are 0.1.

For simulation work, the numerical values of the thick tube radius a, b, material parameters Young's modulus E, etc. need to be provided firstly. Then one needs to specify the number of elements and number of temporal end points. And the imposed pressure for each time step also the initial condition should be fixed. Finally, *Matlab* solver will minimize the BEN principle functional.

Here are three examples, the elastic and elastoplastic case with Tresca or von Mises criterion which are theoretically explained in the previous section. The numerical values for the thick tube and material parameters are: $a = 100$ mm, $b = 200$ mm, $E = 210$ GPa, $\nu = 0.3$ and $\sigma_Y = 360$ MPa. For the elastic case, the internal pressure is $p = 100$ MPa, and $p = 200$ MPa for the elastoplastic case.

3.3.1 Elastic Regime

In this regime, there are two fictive temporal end points, $t = 0$ and $t = 1$. When $t = 0$, all unknown fields are equal to zero (initial conditions). When $t = 1$, the internal pressure is imposed as $p = 100$ MPa. Simulation results are shown in Figs. 1 and 2. With one element ($ne = 1$), the convergence of radial stress is better than the one of the hoop stress (Fig. 1), because the radial stress is imposed as a constraint in the beginning of simulation. For radial displacement, convergence appears with 3 elements (Fig. 2). As the plastic multipliers are equal to zero in the elastic regime, its results are not represented here. By increasing the number of element to 3, the BEN principle result already converges to the analytical solution.

To conclude for the elastic regime, the BEN principle solution converges soon to the analytical solution while increasing the number of elements. Moreover, for one element, the convergence of stress field is faster than the one of radial displacement.

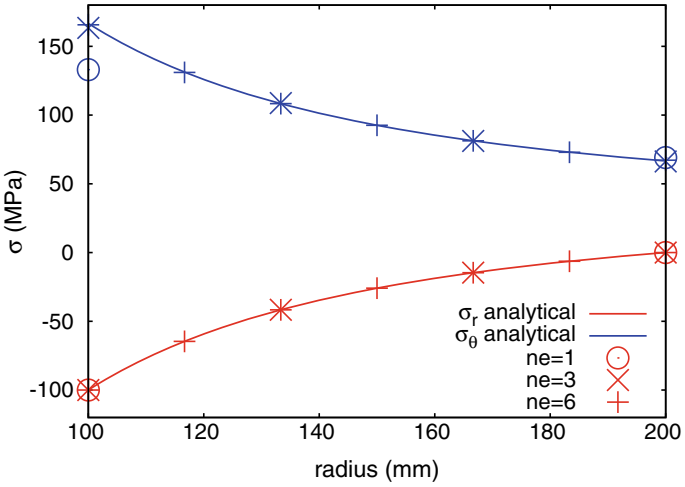

Fig. 1 Comparison between the BEN principle solution (symbols) and analytical solution (plain line) for radial and hoop stresses with 1 & 3 & 6 elements (ne) when $p = 100$ MPa, $t = 1$

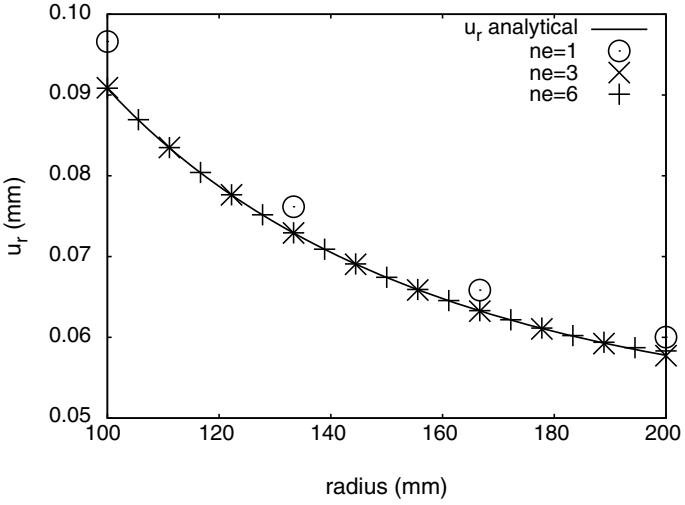

Fig. 2 Comparison between the BEN principle solution (symbols) and analytical solution (plain line) for radical displacement with 1 & 3 & 6 elements (ne) when $p = 100$ MPa, $t = 1$

3.3.2 Elasto-Plastic Regime (Tresca Criterion)

For the elastoplastic regime, there are also two fictive temporal end points, $t = 0$ for initial conditions and $t = 1$ directly for the imposed pressure $p = 200$ MPa which makes the internal wall come to yield. The mid temporal end point for the elastic regime is not necessary. As the BEN principle is based on dissipation potential, its characteristic allows to have a better performance in plastic regime which is an advantage comparing to usual computing code.

As the analytical solution in the plastic part is not easily to obtain, the numerical solution of software Cast3M is chosen as the reference solution. Cast3M is an open-source software developed in French Alternative Energies and Atomic Energy Commission (CEA).

Simulation results are shown in Figs. 3, 4 and 5. There is a better convergence for the stress field even with one element (Fig. 3) comparing to the elastic regime. That is a big advantage in mechanical simulation while the mechanism comes to yield. For radial displacement, there is the convergence when 3 elements are modeled. The extra Fig. 5 is the plastic multiplier. As these three unknown fields are linked by the constraint of decomposition of strains, so the plastic multiplier field converges to reference one also with 3 elements.

For the elastoplastic regime, the BEN principle solution converges to reference solution while increasing the number of elements. It has a better convergence than the elastic regime. The mid-step for elastic regime is not required.

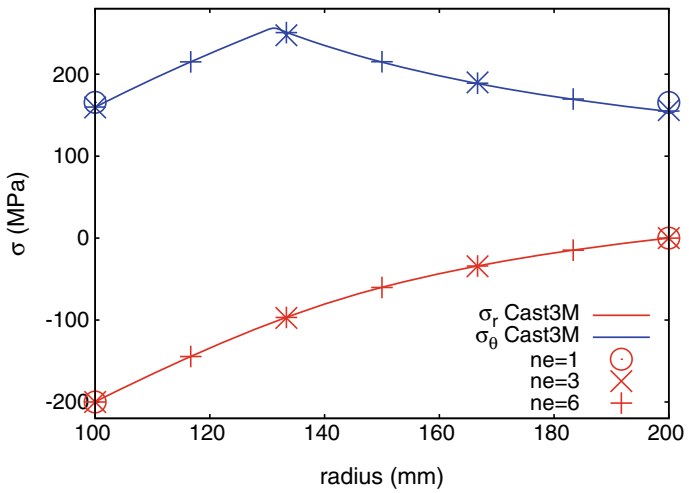

Fig. 3 Comparison between the BEN principle solution (symbols) and reference solution (plain line) for radial and hoop stresses with 1 & 3 & 6 elements (ne) and Tresca criterion when $p = 200$ MPa, $t = 1$

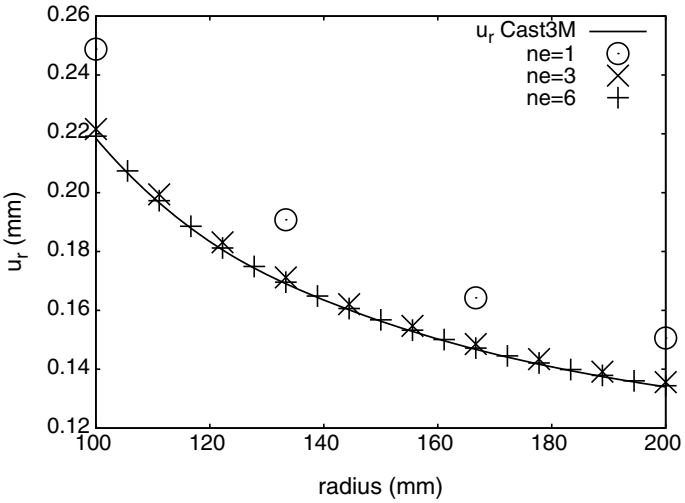

Fig. 4 Comparison between the BEN principle solution (symbols) and reference solution (plain line) for radial displacement with 1 & 3 & 6 elements (ne) and Tresca criterion when $p = 200$ MPa, $t = 1$

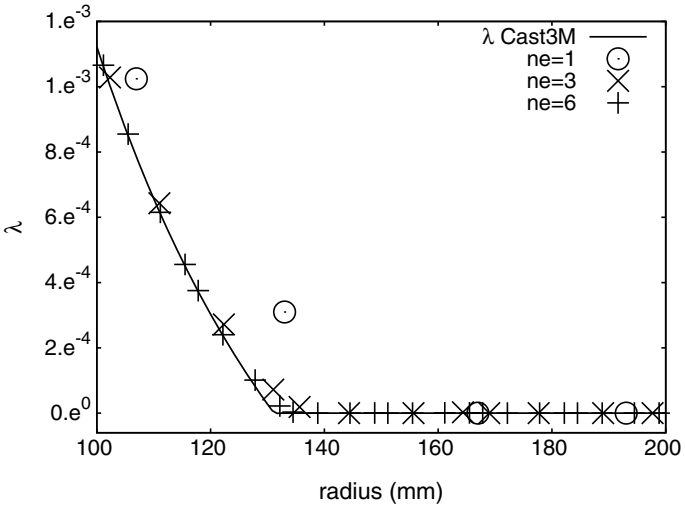

Fig. 5 Comparison between the BEN principle solution (symbols) and reference solution (plain line) for plastic multiplier with 1 & 3 & 6 elements (ne) and Tresca criterion when $p = 200$ MPa, $t = 1$

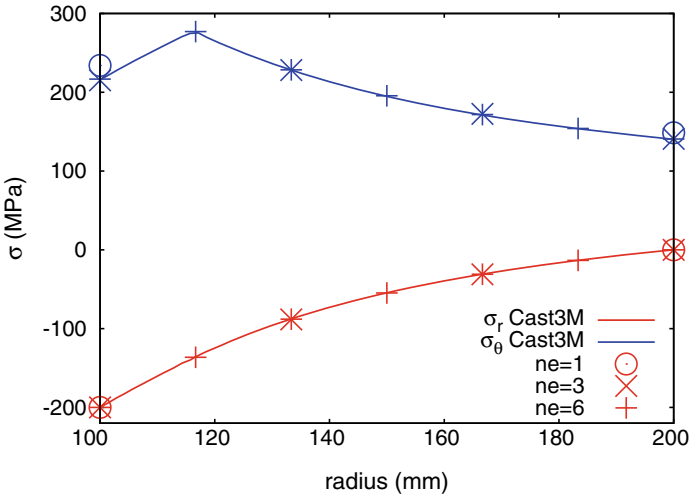

Fig. 6 Comparison between the BEN principle solution (symbols) and reference solution (plain line) for radial and hoop stresses with 1 & 3 & 6 elements (ne) and von Mises criterion when $p = 200$ MPa, $t = 1$

3.3.3 Elasto-Lastic Regime (von Mises Criterion)

The only difference between Tresca and von Mises criterion is the optimization constraint because of the computing of the equivalent stress. Only the results of stress field is represented here for the reason of page limit.

Simulation results are represented in Fig. 6. Comparing to the Tresca criterion, interface between elastic and plastic part of von Mises case is smaller. The convergence of displacement and plastic multiplier field with von Mises criterion is faster than the ones of Tresca. Convergence of the BEN principle while increasing the number of element is always satisfied as before.

4 The Tube Problem in Dynamics

In dynamics, we need to consider the inertia force, $\rho\ddot{u} \neq 0$. After some paper work, the functional to minimize is same as the one in statics. Expression of displacement field is always the same. The one of stress field is modified because of the change in equilibrium equation.

4.1 Stress Field

There are two different methods to discretize the stress field.

- Method A allows to satisfies the balance of momentum equation exactly.
- Method B considers the equation as an optimization constraint which is satisfied in Gauss points.

4.1.1 Method A: Balance of Momentum Satisfied Exactly

The principle is same as in the case of statics. Here we use the method due to Schaefer ([15, 16]) in order to find the solution of the equilibrium equation. The general solution of:

$$\nabla \cdot \sigma = \dot{p}$$

is the sum of the general solution σ_h of the homogeneous equation and a particular solution σ_d of the non homogeneous equation. Following a method due to Schaefer, this last one is of the form:

$$\sigma_d = 2\,\nabla w - (\nabla \cdot w)\, I\ , \tag{38}$$

where the vector potential w is solution of $\nabla^2 w = \dot{p}$. For the displacement field, we seek a radial vector potential. The previous equation reduces to:

$$\frac{d^2 w_r}{dr^2} + \frac{1}{r}\frac{dw_r}{dr} - \frac{w_r}{r^2} = \rho\,(\dot{v}_1 + \dot{v}_2 r + \dot{v}_3 r^2 + \dot{v}_4 r^3)$$

Clearly, a solution is given by a homogeneous polynomial in r of degree five. Introducing it in the previous equation, we obtain by identification:

$$w_r = \rho\left(\frac{\dot{v}_1}{3}r^2 + \frac{\dot{v}_2}{8}r^3 + \frac{\dot{v}_3}{15}r^4 + \frac{\dot{v}_4}{24}r^5\right)$$

condition (38) reads in polar coordinates:

$$\sigma_{rr} = 2\frac{dw_r}{dr} - \frac{1}{r}\frac{d}{dr}(r\,w_r), \quad \sigma_{\theta\theta} = 2\frac{w_r}{r} - \frac{1}{r}\frac{d}{dr}(r\,w_r)$$

leads to the expression of σ_d:

$$\sigma_{rr} = -\sigma_{\theta\theta} = \rho\left(\frac{\dot{v}_1}{3}r + \frac{\dot{v}_2}{4}r^2 + \frac{\dot{v}_3}{5}r^3 + \frac{\dot{v}_4}{6}r^4\right)$$

Besides, the homogeneous stress field being defined by four connectors is same as in statics. In matrix form, the total stress field in terms of stress and displacement parameters reads:

$$\begin{bmatrix} \sigma_{rr} \\ \sigma_{\theta\theta} \end{bmatrix} = \sigma_e(r) = R_e(r)\, h_e + S_e(r)\, \dot{v}_e$$

stress connectors are linearly depending on the stress and displacement parameters:

$$g_e = C_e h_e + D_e \dot{v}_e$$

Hence, one has: $h_e = C_e^{-1}(g_e - D_e \dot{v}_e)$. Eliminating the stress parameters provides the stress field in terms of stress and displacement connectors:

$$\sigma_e(r) = T_e(r) g_e + U_e(r) \ddot{q}_e$$

where:

$$T_e(r) = R_e(r) C_e^{-1}, \qquad U_e(r) = (S_e(r) - R_e(r) C_e^{-1} D_e)\, A_e$$

4.1.2 Method B: Balance of Momentum Satisfied in Gauss Points

We choose the same position for the radial and hoop stress field as the one of displacement.

$$\sigma_r = h_1 + h_2\, r + h_3\, r^2 + h_4\, r^3 \qquad \sigma_\theta = h_5 + h_6\, r + h_7\, r^2 + h_8\, r^3$$

There are four degrees of freedom for each stress:

$$g_1 = \sigma_r\,|_{r=\alpha}, \qquad g_2 = \sigma_r\,|_{r=\beta}, \qquad g_3 = \sigma_r\,|_{r=\gamma}, \qquad g_4 = \sigma_r\,|_{r=\delta} \tag{39}$$

$$s_1 = \sigma_\theta\,|_{r=\alpha}, \qquad s_2 = \sigma_\theta\,|_{r=\beta}, \qquad s_3 = \sigma_\theta\,|_{r=\gamma}, \qquad s_4 = \sigma_\theta\,|_{r=\delta} \tag{40}$$

Thus:

$$\sigma_e(r) = \begin{bmatrix} \sigma_{rr} \\ \sigma_{\theta\theta} \end{bmatrix} = \begin{bmatrix} N_e(r) & 0 \\ 0 & N_e(r) \end{bmatrix} \begin{bmatrix} g_e \\ s_e \end{bmatrix} = T_e(r)\, t_e$$

4.2 Spatial and Temporal Discretization

The discretized form of the functional adapts with the corresponding discretization of the stress field.

4.2.1 Method A

Performing the same assembling, the discretized form of the functional is:

$$\bar{\Pi}(g,q,\lambda) = \int_{t_0}^{t_1} \Big[\Lambda^T \lambda(t) - \dot{q}^T(t)\,(G\,g(t) + \tilde{G}\,\ddot{q}(t)) + g^T(t)\,F_1\,\dot{g}(t) + \ddot{q}^T(t)\,F_2\,\dot{g}(t) + g^T(t)\,F_3\,\dddot{q}(t) + \ddot{q}^T(t)\,F_4\,\dddot{q}(t) \Big] dt \tag{41}$$

with:

$$\Lambda = \sum_{e=1}^{n} P_e^T \Lambda_e,$$

$$G = \sum_{e=1}^{n} \int_{\alpha}^{\beta} L_e^T B_e^T(r)\,T_e(r)\,M_e\,2\pi\,r\,dr, \quad \tilde{G} = \sum_{e=1}^{n} \int_{\alpha}^{\beta} L_e^T B_e^T(r)\,U_e(r)\,L_e\,2\pi\,r\,dr,$$

$$F_1 = \sum_{e=1}^{n} \int_{\alpha}^{\beta} M_e^T T_e^T(r)\,S\,T_e(r)\,M_e\,2\pi\,r\,dr \quad F_2 = \sum_{e=1}^{n} \int_{\alpha}^{\beta} L_e^T U_e^T(r)\,S\,T_e(r)\,M_e\,2\pi\,r\,dr$$

$$F_3 = \sum_{e=1}^{n} \int_{\alpha}^{\beta} M_e^T T_e^T(r)\,S\,U_e(r)\,L_e\,2\pi\,r\,dr \quad F_4 = \sum_{e=1}^{n} \int_{\alpha}^{\beta} L_e^T U_e^T(r)\,S\,U_e(r)\,L_e\,2\pi\,r\,dr$$

The Brezis-Ekeland-Nayroles claims that we have to find the minimum of (41) with respect to the path $t \mapsto (g(t), q(t), \lambda(t))$ under the constrains of equilibrium, plasticity and initial conditions as in statics.

For the time discretization of any physical quantity a, we put:

$$a_j = a(t_j), \quad \dot{a}_j = \dot{a}(t_j), \quad \cdots$$

On each step, we approximate the time rates at $t = t_j$ by:

$$\dot{a}_j = \frac{a_j - a_{j-1}}{t_j - t_{j-1}}, \qquad \ddot{a}_j = \frac{\dot{a}_j - \dot{a}_{j-1}}{t_j - t_{j-1}}, \qquad \dddot{a}_j = \frac{\ddot{a}_j - \ddot{a}_{j-1}}{t_j - t_{j-1}}$$

Considering m time step from t_0 to t_m and enforcing the yield condition only at the beginning and the end of the step, we have to minimize the objective function:

$$\bar{\Pi}(g_0,\ldots,g_m,q_0,\ldots,q_m,\lambda_0,\ldots,\lambda_m) = \sum_{j=1}^{j=m} \Big[\Lambda^T \lambda_j - \dot{q}_j^T \left(G\,g_j + \tilde{G}\,\ddot{q}_j \right) + {g_j}^T(t)\,F_1\,\dot{g_j}(t) + {\ddot{q}_j}^T(t)\,F_2\,\dot{g_j}(t) + {g_j}^T(t)\,F_3\,\dddot{q_j}(t) + {\ddot{q}_j}^T(t)\,F_4\,\dddot{q_j}(t) \Big] (t_j - t_{j-1}) \tag{42}$$

under the constrains of:

- equilibrium (on the boundary, at each time step):

$$g_{r=a,j}(t_j) = -p(t), \quad g_{r=b,j}(t_j) = 0$$

- plasticity (at every integration point g of every element e and at every time step):

$$f_{g,j}(g, \ddot{q}) - \sigma_Y \leq 0, \quad \lambda_{g,j} \geq 0,$$

$$N_Y \lambda_{g,j} = B_e(r_g)\, L_e \dot{q}_j^T - S\left[T_e(r_g)\, M_e \dot{g}_j + U_e(r_g)\, L_e \ddot{q}_j\right]$$

- initial conditions:

$$g_0 = 0, \qquad q_0 = 0, \qquad \lambda_0 = 0, \qquad \dot{g}_0 = 0, \qquad \dot{q}_0 = 0, \qquad \ddot{q}_0 = 0, \qquad \dddot{q}_0 = 0$$

4.2.2 Method B

Performing the assembling thanks to the localization matrices L_e, M_e, P_e such that:

$$t_e = M_e t, \qquad q_e = L_e q, \qquad \lambda_e = P_e \lambda$$

the discretized form of the functional is:

$$\bar{\Pi}(t, q, \lambda) = \int_{t_0}^{t_1} (\Lambda^T \lambda(t) - \dot{q}^T(t) G\, t(t) + \dot{t}^T(t) F\, t(t))\, \mathrm{dt} \tag{43}$$

with:

$$\Lambda = \sum_{e=1}^{n} P_e^T \Lambda_e,$$

$$G = \sum_{e=1}^{n} \int_{\alpha}^{\beta} L_e^T B_e^T(r)\, T_e(r)\, M_e\, 2\pi\, r\, dr \quad F = \sum_{e=1}^{n} \int_{\alpha}^{\beta} M_e^T T_e^T(r)\, S\, T_e(r)\, M_e\, 2\pi\, r\, dr$$

The Brezis-Ekeland-Nayroles claims that we have to find the minimum of (43) with respect to the path $t \mapsto (t(t), q(t), \lambda(t))$ under the constrains of:

- equilibrium (on the boundary, the internal equilibrium being satisfies a priori):

$$g_{r=a}(t) = -p(t), \quad g_{r=b}(t) = 0, \quad \frac{d}{dr}\sigma_r(r_g) + \frac{1}{r_g}\left[\sigma_r(r_g) - \sigma_\theta(r_g)\right] = \rho \ddot{u}_r(r_g)$$

- plasticity and initial conditions are same as in the method A

By applying the same time discretization of method A, considering m time step from t_0 to t_m and enforcing the yield condition only at the beginning and the end of the

step, we have to minimize the objective function:

$$\bar{\Pi}(t_0, \ldots, t_m, q_0, \ldots, q_m, \lambda_0, \ldots, \lambda_m) = \sum_{j=1}^{j=m} (\Lambda^T \lambda_j - \dot{q}_j^T G\, t_j + \dot{t}_j^T F\, t_j) \quad (44)$$

under the constrains of:

- equilibrium (on the boundary, at each time step):

$$g_{r=a,j} = -p(t_j), \quad g_{r=b,j} = 0, \quad \frac{d}{dr}\sigma_r(r_{g,j}) + \frac{1}{r_{g,j}}\left[\sigma_r(r_{g,j}) - \sigma_\theta(r_{g,j})\right] = \rho \ddot{u}_r(r_{g,j})$$

- plasticity and initial conditions are same as in the method A

4.3 Simulation Results

The program is coded in *Matlab*, the solver *fmincon* is applied to find the local minimum of the constrained functional (42, 44). Material parameters are, $E = 210$ GPa, $\nu = 0.3$, $\sigma_Y = 360$ MPa, $a = 100$ mm, $b = 101$ mm, $\rho = 7.8\, e^{-9}$ Kg/mm^3. Internal pressure history is displayed in 7. The Simulation results are displayed in Figs. 8 and 9 for elastic and plastic cases.

There is a good consistence between the BEN principle solution and the analytical or numerical solution. The BEN principle requires sufficient time steps to have a better precision than the one of step-by-step (Fig. 8). The method A and B does not change

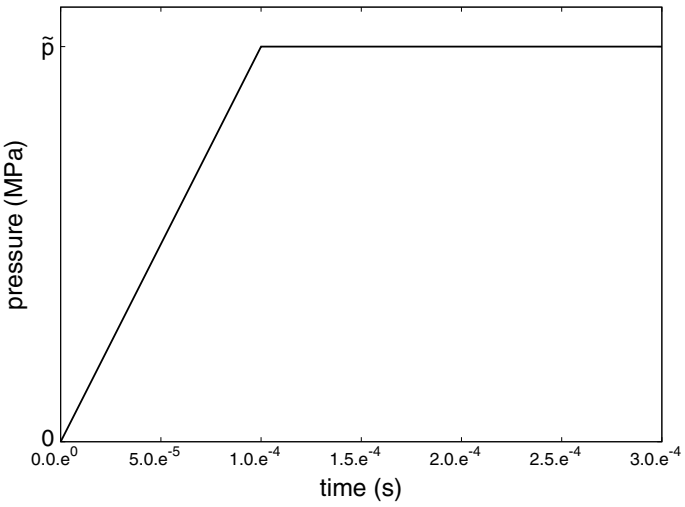

Fig. 7 Imposed pressure history

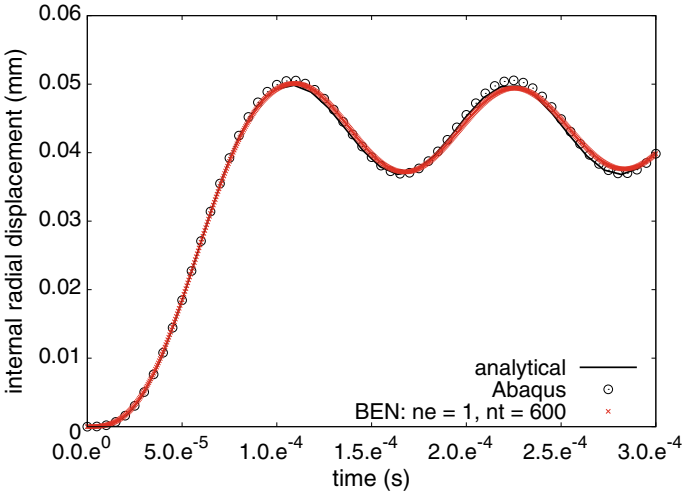

Fig. 8 Comparison of radial displacement history of different data when $\tilde{p} = 1$ MPa in elastic case (i) analytical solution (ii) reference numerical solution (Cast3M software) with 30 time steps (iii) BEN method A solution with 600 time steps

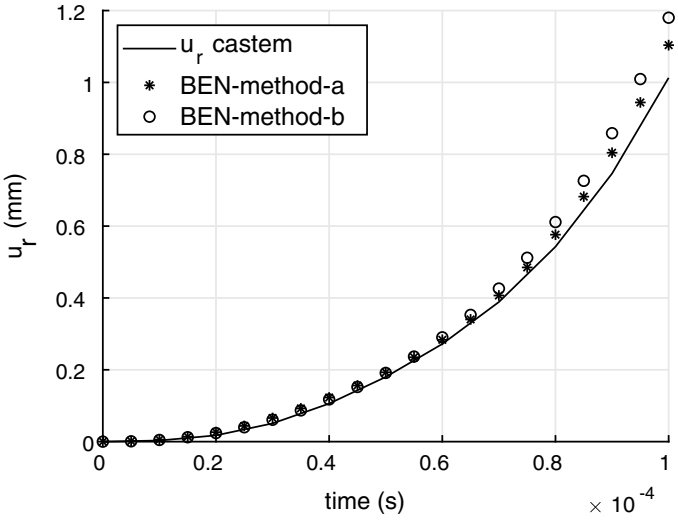

Fig. 9 Comparison of radial displacement history of different data when $\tilde{p} = 10$ MPa in plastic case (i) analytical solution (ii) reference numerical solution (Cast3M software) (iii) BEN method A solution with 400 time steps

the simulation results in elastic case (Fig. 8). As displayed in Fig. 9, the method A is more accurate than the method B in plastic case as the momentum equation is satisfied exactly.

5 Conclusions and Future Works

In this work, the BEN principle has numerically proven with success. It allows to transform a mechanical problem into an optimization problem under constraints, that is how the BEN principle has the ability to work simultaneously on all time steps in place of using the step-by-step method and facing the convergence problem. Comparing to an usual computing code, another advantage of the BEN principle is the convenience of implementation of special plastic criteria and material behavior laws, but it is not always a good choice to impose a refined mesh to have a better solution. By means of the simulations, the BEN principle solution has a fast convergence to the reference solution, especially for the stress field, that is a big advantage in a plastic regime.

In the future, a more effective minimization solver is necessary to solve a large optimization problem. Moreover, as this is a space-time coupling problem, the computing time is expensive. We would like to apply the Proper Generalized Decomposition (PGD) reduction method [17–19] to the problem in order to decrease the computation time. The main idea of the PGD method is to separate space and time and carry out the computation of each field separately. Moreover, this method allows to modify the initial problem to a parametric model which is very useful for the mechanical problem.

Acknowledgements The work is funded by the Dissipative Dynamical Systems by Geometrical and Variational Methods (DDGV) and Application to Viscoplastic Structures Subjected to Shock Waves international project by the French National Research Agency (ANR) in cooperation with the Institute of General Mechanics of RWTH Aachen University.

References

1. Larman, C., Basili, V.R.: Iterative and incremental developments a brief history. Computer **36**(6), 47–56
2. Boisse, P.H., Ladevèze, P., Rougée, P.: A large time increment method for elastoplastic problems. Eur. J. Mech. A. Solids **8**(4), 257–275 (1989)
3. Boisse, P.H., Bussy, P., Ladeveze, P.: A new approach in non? linear mechanics: the large time increment method. Int. J. Numer. Methods Eng. **29**(3), 647–663 (1990)
4. Ladevèze, P.: Sur une famille d'algorithmes en mécanique des structures. Comptes-rendus des séances de l'Académie des sciences. Série 2, Mécanique-physique, chimie, sciences de l'univers, sciences de la terre **300**(2), 41–44 (1985)
5. Ladevèze, P.: New advances in the large time increment method. In: New Advances in Computational Structural Mechanics, pp. 3–21. Elsevier, Amsterdam (1991)

6. Brézis, H., Ekeland, I.: Un principe variationnel associéa certaines equations paraboliques. Le cas independant du temps. CR Acad. Sci. Paris Sér. A **282**, 971–974 and 1197–1198 (1976)
7. Nayroles, B. (1976). Deux Theoremes De Minimum Pour Certains Systemes Dissipatifs
8. Appl, A.M.S.: Extension of the Brezis-Ekeland-Nayroles principle to monotone operators. Adv. Math. Sci. Appl **18**, 633–650 (2008)
9. Stefanelli, U.: The Brezis? Ekeland principle for doubly nonlinear equations. SIAM J. Control Optim. **47**(3), 1615–1642 (2008)
10. Stefanelli, U.: The discrete Brezis-Ekeland principle. J. Convex Anal. **16**(1), 71–87 (2009)
11. Buliga, M., de Saxcé, G.: A symplectic Brezis? Ekeland? Nayroles principle. Math. Mech. Solids **22**(6), 1288–1302 (2017)
12. Halphen, B., Nguyen, Q.S.: Sur les matériaux standard généralisés. J. de mécanique **14**, 39–63 (1975)
13. Roberts, J.E., Thomas, J.M., Ciarlet, P.G., Lions, J.L.: Mixed and hybrid methods. In: Handbook of Numerical Analysis (1991)
14. Brezzi, F., Fortin, M.: Mixed and Hybrid Finite Element Methods, vol. 15. Springer Science & Business Media (2012)
15. Schaefer, H.: Die Spannungsfuncktionen des dreidimensionalen Kontinuums und des elastischen Körpers. Z. Angew. Math. Mech. **33**, 356–362 (1953)
16. Gurtin, M., The linear theory of elasticity. In: Encyclopedia of Physics, S. Flügge, Mechanics of Solids II, vol. VIa/2. Springer, Berlin (1972)
17. Chinesta, F., Keunings, R., Leygue, A.: The Proper Generalized Decomposition for Advanced Numerical Simulations: A Primer. Springer Science & Business Media (2013)
18. Bognet, B., Bordeu, F., Chinesta, F., Leygue, A., Poitou, A.: Advanced simulation of models defined in plate geometries: 3D solutions with 2D computational complexity. Comput. Methods Appl. Mech. Eng. **201**, 1–12 (2012)
19. Giner, E., Bognet, B., Rdenas, J. J., Leygue, A., Fuenmayor, F.J., Chinesta, F.: The proper generalized decomposition (PGD) as a numerical procedure to solve 3D cracked plates in linear elastic fracture mechanics. Int. J. Solids Struct. **50**(10), 1710–1720 (2013)

Shakedown Limits of Slab Track Substructures and Their Implications for Design

Juan Wang, Hai-Sui Yu, and Shu Liu

Abstract This paper presents an approach to shakedown of slab track substructures subjected to train loads. The train load is converted into a distributed moving load on the substructure surface using a simplified track analysis. Based on the lower-bound dynamic shakedown theorem, shakedown solutions for the slab track substructures are obtained over a range of train speeds between zero and the critical speed of the track. It is found the shakedown limit is largely influenced by the ratio of layer elastic moduli and the ratio of train speed to critical speed rather than their absolute values. An attenuation factor, as a function of the critical speed and the friction angle of subsoil, is proposed to effectively obtain the shakedown limit of the slab track substructure at any train speed. In light of the shakedown solutions, improvements to the existing design and analysis approaches are also suggested.

Keywords Slab track · Shakedown · Design · Train loads · Trains speed

1 Introduction

Slab tracks have been widely used for high-speed railways. In China, around 70% of the high-speed railways are ballastless slab tracks. Slab tracks require very limited residual settlement/differential settlement as a result of long-term permanent deformation of supporting substructures which comprise compacted granular layers and subsoil.

J. Wang (✉) · S. Liu
Ningbo Nottingham New Materials Institute, University of Nottingham Ningbo China, 315100 Ningbo, China
e-mail: juan.wang@nottingham.edu.cn

H.-S. Yu
Faculty of Engineering, University of Leeds, LS2 9JT Leeds, UK

S. Liu
State Key Laboratory for GeoMechanics and Deep Underground Engineering, School of Mechanics and Civil Engineering, China University of Mining and Technology, 221116 Xuzhou, Jiangsu, China

A. A. Pisano et al. (eds.), *Direct Methods*, Lecture Notes in Applied and Computational Mechanics 95, https://doi.org/10.1007/978-3-030-48834-5_11

Nowadays, there is an increasing trend of using shakedown theory in the evaluation of the long-term stability of geotechnical structures under cyclic or variable loads. The shakedown theory has been proven to be very useful for solving design problems in foundations and pavements (e.g. [1]; [4, 8, 15, 16, 17, 19, 22, 23, 26, 27, 25]; [11, 24]). Recently, some shakedown analyses have been performed for the problem of railways subjected to train loads. For example, Zhuang and Wang [28] obtained the shakedown limits for ballast railways considering the effect of layer thickness and load distribution. Liu et al. [12] did shakedown analyses on ballastless slab tracks and assessed the effect of the increasing stiffness modulus with depth. However, the dynamic effect induced by the moving train was not taken into account in the above two articles. Wang et al. [21] and Liu and Wang [13] performed dynamic shakedown analyses for the substructure of typical slab tracks based on lower-bound dynamic shakedown theorem. Parametric studies were carried out and the results proved that the ratio of train velocity to the critical velocity of track is a key factor that affects the dynamic shakedown limits. Costa et al. [5] then included the effect of rest stress fields and found that neglecting the rest stress may underestimate the shakedown limit.

In this paper, both quasi-static and dynamic shakedown limits for a typical slab track substructure will be presented. The influencing factors of the shakedown limits and the relation between the dynamic shakedown solution and the quasi-static shakedown solution will be analysed. A fitting equation will then be proposed for predicting the dynamic shakedown limits by modifying the quasi-static shakedown limit with an attenuation factor. The implication of this approach for the slab track substructure design will be discussed finally.

2 Simplified Model of Slab Track Substructures

Figure 1 shows a typical slab track system which includes a superstructure and a supporting substructure. The superstructure is composed of two rails, a track slab, a concrete base, sleepers, pads and fastening systems. Table 1 summarises the properties of the key components of the superstructure. The dimensions of the track slab and the concrete base are taken from a typical Rheda 2000 single track system. The rail is UIC60. The substructure consists of an anti-frozen layer, a prepared subgrade layer and a subsoil layer of infinite depth. Four axle loads belonging to two adjacent bogies on two carriages move at a constant speed V along x-direction (Fig. 1). Each axle load is denoted by λP where P is a unit axle load and λ is a scale factor. No traction in the longitudinal or transverse direction is considered. Moreover, the magnitude of the loads is constant, without considering the effect of rail unevenness and vehicle suspension system.

This paper focuses on the shakedown analysis of the substructure. A simplified track analysis is proposed to convert the train loads and the superstructure into a distributed moving load on the substructure. It is considered that the superstructure components act together as a single infinite Euler-Bernoulli beam with a total $E_{\mathrm{b}}I$

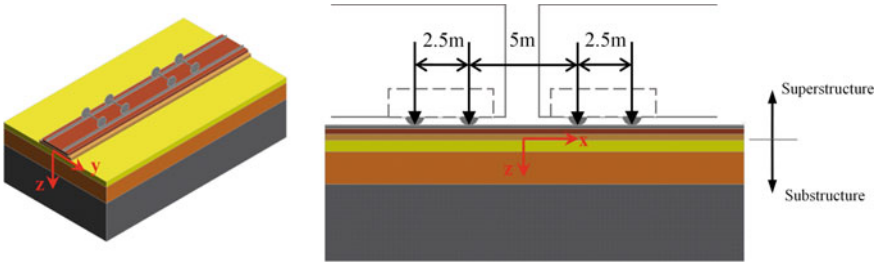

Fig. 1 A typical slab track structure and axle loads

Table 1 Material properties and dimensions of the key components of a slab track superstructure

Layer	Young's modulus E_b (GPa)	Width (cm)	Height (cm)	Second moment of area I (cm^4)	Mass per unit length (kg/m)
Rail	210	15	17.2	3055	60.03
Track slab	34	280	24	322560	1680
Concrete base	10	340	30	765000	2448

value (E_b is Young's modulus of the beam materials; I is second moment of inertia of the beam), while the supporting substructure is simplified as a Winkler's foundation. The pads and sleepers are ignored in this study as they do not contribute to the bending of the superstructure. In the assumption of Winkler's foundation, a reaction modulus k is used to describe the resilient response of the soil, which, however, is not a fundamental soil property. Relations between the reaction modulus and the material elastic modulus have been proposed theoretically or empirically by a number of authors for different situations (e.g. [2, 18, 20]. For the problem of an infinite slab track resting on a three-dimensional homogeneous isotropic elastic soil continuum, the relation between the reaction modulus k and the elastic modulus E of the soil has been proposed [12]:

$$k = \frac{0.583 E_\mathrm{b} I}{b^{1.267} d^{3.733}} \tag{1}$$

with

$$d = \left(\frac{(1 - \nu^2) E_b I}{E} \right)^{1/3} \tag{2}$$

where ν is Poisson's ratio of the soil; b is the half width of the slab track. For the problem of a layered soil, an equivalent reaction modulus k_eq or an equivalent stiffness modulus E_eq can be used by equating the maximum deflection of the beam with the maximum surface displacement of the elastic half-space [12]. In the current

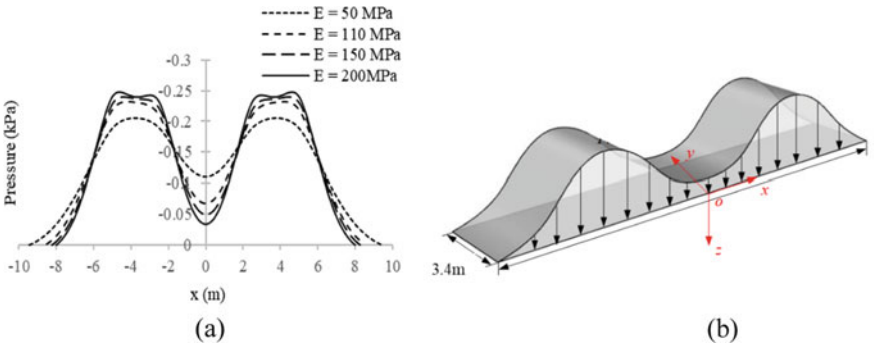

Fig. 2 Pressure distribution on the surface of track substructure

study, giving the material properties described in Table 1 and the soil Poisson's ratio of 0.3, Eq. 1 can be rewritten as:

$$k = 0.00314E^{1.2443} \tag{3}$$

Then, the four axle loads can be converted into a distributed load on the top of the substructure according to the following equation:

$$p = p_0 e^{-\mu|x|}(\cos\mu(x) + \sin\mu|x|) \tag{4}$$

where $p_0 = \lambda P\mu/4b$; $\mu = (2kb/E_bI)^{0.25}$.

Figure 2a exhibits the pressure distribution for different values of stiffness modulus. Reaction force due to upward displacement of the beam is taken as zero. As can be seen, the pressure is distributed more widely and uniformly when the reaction modulus is lower. In the transverse direction, the pressure is assumed to be distributed uniformly over the width of the concrete base (i.e. 3.4 m), as shown in Fig. 2b.

3 Dynamic Shakedown Analysis

Yu and Wang [25] proposed an approach to obtain the lower-bound shakedown limits of cohesive-frictional materials under three-dimensional surface loads assuming a quasi-static situation, based on Melan's lower-bound shakedown theorem. However, for the problem of high-speed railways, the dynamic shakedown analysis needs to be performed.

The lower-bound dynamic shakedown theorem of Ceradini (1980) [3] states that shakedown will occur in the real response if a fictitious response and a residual stress field may be found so that

$$f(\lambda\sigma_{ij}^{e}(t)+\sigma_{ij}^{r})\le 0 \tag{5}$$

where the residual stress field itself σ_{ij}^{r} must satisfy self-equilibrium and time-independence conditions; λ is a dimensionless factor; t is time; the fictitious response refers to the elastic response to the external actions (not real elastic-plastic response), such as the unit load-induced elastic stresses $\sigma_{ij}^{e}(t)$ and displacements $u_i^{e}(t)$, which should satisfy the following dynamic equilibrium conditions:

$$\sigma_{ij,j}^{e}(t)+X_i(t)=\rho\ddot{u}_i^{e}(t)-\chi\dot{u}_i^{e}(t) \tag{6}$$

$$\sigma_{ij}^{e}(t)-f_i(t)=0 \tag{7}$$

where is X_i body force field applied to the region V with an initial state; ρ is material density; χ is damping coefficient and f_i is surface force acting on the surface S. Tension positive notation is applied throughout this paper.

For the problem considered here, assuming the soil behaviour obeys the Mohr-Coulomb yield criterion, the lower-bound dynamic shakedown theorem requires that the total stress state of any point must not lie outside the Mohr-Coulomb yield surface at any time. On each x-z plane, since σ_{yy}^{r} can be chosen such that σ_{yy} is always an intermediate principle stress, the substitution of the total stresses into the Mohr-Coulomb yield criterion leads to the following expression:

$$f=(\sigma_{xx}^{r}+M)^2+N\le 0, \tag{8}$$

with

$$M=\lambda\sigma_{xx}^{e}-\lambda\sigma_{zz}^{e}+2\tan\varphi(c-\lambda\sigma_{zz}^{e}\tan\varphi), \tag{9}$$

$$\mathrm{N}=4(1+\tan^2\varphi)[(\lambda\sigma_{\mathrm{xz}}^{\mathrm{e}})^2-(c-\lambda\sigma_{\mathrm{zz}}^{\mathrm{e}}\tan\varphi)^2], \tag{10}$$

where φ and c are soil dynamic friction angle and cohesion, respectively; σ_{ij}^{e} is elastic stress field induced by the unit axle loads P, moving at a constant speed V. The elastic stress field can be obtained by using analytical solutions of Easton (1965) [6] for the case of a homogenous isotropic half-space or performing finite element simulations for a layered structure. A typical finite element model of the track substructure is shown in Fig. 3. The details of the model can be found in Wang et al. [21].

The residual stress σ_{xx}^{r} must be time-independent and self-equilibrated. For problems where the travelling speed of the surface load is constant and smaller than the wave propagation velocity, every points at the same depth experience an identical stress history. The elastic stress field over a period T at any given speed does not change with position. Using the Mohr-Coulomb yield criterion and the self-equilibrium condition of the residual stress field, it is found that the actual horizontal residual stress must be fully bracketed by the two critical residual stress fields, when the structure is at a shakedown status [21].

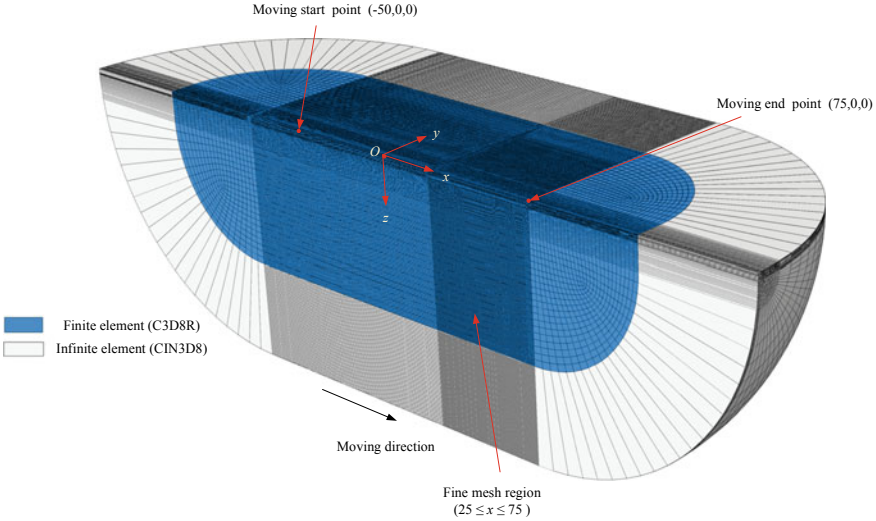

Fig. 3 Finite element model of track substructure

$$\sigma_{xx-l}^{r} = \max_{z=j}^{-\infty\le x\le\infty}\left(-M_i - \sqrt{-N_i}\right) \tag{11}$$

$$\sigma_{\mathrm{xx-u}}^{r} = \min_{z=j}^{-\infty\le x\le\infty}\left(-M_i + \sqrt{-N_i}\right) \tag{12}$$

in which i represents a general point at depth $z = j$. By substituting the load-induced elastic stress fields and either of the critical residual stress fields into the Mohr-Coulomb yield criterion $f(\sigma) \le 0$, the present shakedown problem can be rewritten as a mathematical optimisation problem:

$$\max\ \lambda \quad s.t.\ \begin{cases} f(\sigma_{xx}^{r}(\lambda\sigma^{e}), \lambda\sigma^{e}) \le 0 \text{ for all points} \\ \sigma_{xx}^{r}(\lambda\sigma^{e}) = \sigma_{xx-l}^{r} \text{ or } \sigma_{xx-u}^{r} \end{cases} \tag{13}$$

If λ is larger than the shakedown limit, f will be larger than 0 at some points; otherwise, f will always be equal or smaller than 0. The maximum admissible load factor is the shakedown limit multiplier of the substructure, denoted by λ_{sd}. The above shakedown condition can be reduced to a quasi-static shakedown solution when the train speed is very low. At any given speed, the above mathematical formulation then can be solved by using a procedure in Yu and Wang [25] and will not be repeated here.

For a layered structure, it is useful to know which layer is critical. The shakedown limit multiplier $\lambda_{sd}^{\mathrm{n}}$ of each layer can be calculated and compared. Finally, the shakedown limit of the whole structure is the lowest one among them:

$$\lambda_{\mathrm{sd}} = \min(\lambda_{sd}^{1}, \lambda_{sd}^{2}, \ldots, \lambda_{sd}^{n}) \tag{14}$$

where the superscript n (= 1, 2, 3…) means the nth layer.

4 Shakedown Limits

A typical slab track substructure, composed of an anti-frozen layer, a prepared subgrade, and a subsoil of a great depth, is considered in this study. According to Eqs. 8–10, the shakedown limit of a slab track is dependent on the plastic properties of the soils (i.e. ϕ and c) and the elastic stress distributions in the soils. The latter is controlled by the pressure distribution, the elastic parameters of the soils, and the moving speed of the train loads V with respect to the critical speed of the substructure V_{cr}. It should be noted that the stiffness modulus of a soil also depends on the frequency of loading. Therefore, in the stability analysis of high-speed railways, a dynamic stiffness modulus E_d, which is higher than the stiffness modules E, is normally employed instead. In light of this, the current research will investigate the quasi-static situation and the dynamic situation, respectively; and the effect of the stiffness modulus will be discussed. Table 2 shows the material properties and layer thicknesses of the three-layered substructure in this study.

4.1 Shakedown Limits in a Quasi-Static Situation

For the case of a stiff subsoil (i.e. $E_3 = 110$ MPa), the influence of the thickness of the prepared subgrade is first investigated. Figure 4 demonstrates that the increase of the subgrade thickness (2nd layer) decreases the shakedown limit of that layer but increases those of the other two layers. More significant changes occur in the subsoil (3rd layer). According to Eq. 14, the lowest shakedown limit among all layers is the overall shakedown limit of the substructure. Therefore, there exists an optimum subgrade thickness in this case, at around 1.7 m, above which further increase of the thickness barely changes the overall shakedown limit.

Table 2 Material properties and layer thicknesses of a three-layered substructure

Layer name	h_n (m)	E_n (MPa)	E_n^d (MPa)	ν_n	ϕ_n (°)	c_n (kPa)	ρ_n (kg/m^3)
Anti-frozen layer	0.4	200	290	0.3	50	1	2000
Prepared subgrade	1.3, 1.8, 2.3, 2.8	130	190	0.3	40	2	1850
Subsoil	∞	110 or 55	160	0.3	30	2	1800

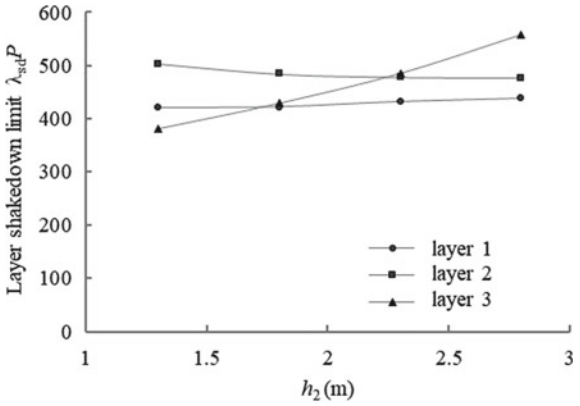

Fig. 4 Effect of subgrade thickness on the shakedown limit of each layer when $E_1 = 200$ MPa, $E_2 = 130$ MPa, $E_3 = 110$ MPa

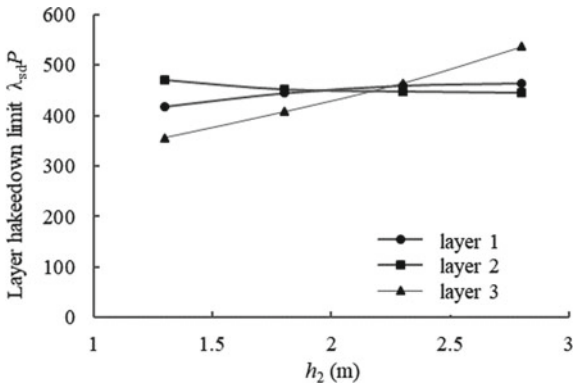

Fig. 5 Effect of subgrade thickness on the shakedown limit of each layer when $E_1^d = 290$ MPa, $E_2^d = 190$ MPa, $E_3^d = 160$ MPa

Figure 5 further examines the influence of the values of the stiffness moduli on the shakedown limit by using the values of the dynamic stiffness moduli E^{d} instead. The corresponding load distributions are applied. It should be noted that the ratio of the dynamic stiffness moduli $E_1^d/E_2^d/E_3^d$ is set to be identical to $E_1/E_2/E_3$. Compared to Fig. 4, this case shows similar trends of the shakedown limits of each layer; while the optimum layer thickness is moved to around 2.2 m. In Fig. 6, a direct comparison of the overall shakedown limits shows that increasing the stiffness moduli by 40% reduces the shakedown limit (by 7% at maximum) for the cases of a low h_2, but increases it (by 4% at maximum) for the cases of a high h_2. Further investigation reveals that the small differences are only attributed to the changed pressure distribution, not the values of the stiffness modulus, because the elastic stress fields under a specific distribution is only dependent on the ratio of layer stiffness moduli. For the cases of a high stiffness modulus, the pressure is less evenly distributed, leading to a lower shakedown limit of the first layer and higher shakedown limits of the other two layers. The above finding implies that, though the stiffness moduli of soils vary with the frequency of loading or the train speed, if the rates of

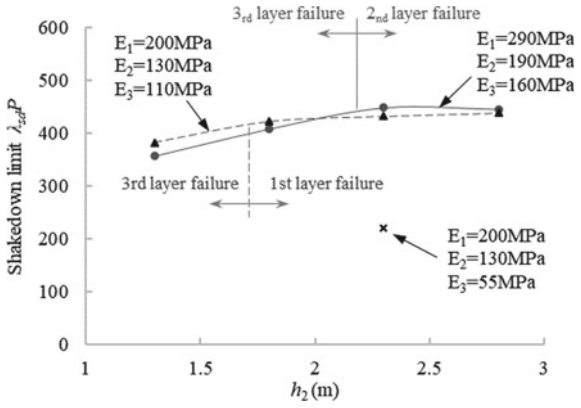

Fig. 6 Effects of stiffness modulus and subgrade thickness on the shakedown limit

the changes are similar for soils in different layers, it will barely have influence on the shakedown limit. Additionally, when the thickness of the prepared subgrade is relatively large, the subsoil layer becomes less critical, resulting in an increase of the shakedown limit of the subsoil; otherwise, the other two layers are more likely to fail.

Figure 4 also shows the shakedown limit of the substructure when the subsoil is soft (i.e. $E_3 = 55$ MPa). Compared to the case of a stiff subsoil, the shakedown limit is dropped significantly. If the design axle load is 250 kN, the substructure will definitely fail due to excessive permanent deformation. The shakedown limits of the three layers are 220 kN, 290 kN and 572 kN, respectively. This implies that for the case of a poor subsoil, more stresses are locked in the upper layers thus a higher possibility of failure in the subgrade.

4.2 Shakedown Limits in a Dynamic Situation

When the dynamic situation is considered, the elastic stress fields, and thus the shakedown limit, highly depend on V/V_{cr}, where V represents the moving speed of the train loads V and V_{cr} represents the critical speed of the track. Figure 7a demonstrates an accelerated decrease of the shakedown limit of each layer with rising train speed, when the dynamic stiffness moduli in Table 2 are utilised. The shakedown limit is the minimum when the train speed is close to the shear wave velocity of the bottom layer $V_{\text{s-layer3}}$, which can be recognised as the critical velocity of the slab track. If the stiffness moduli are reduced by the same rate (say 44%) while maintaining the pressure distribution, the shakedown limits of the three layers will be decreased, as shown in Fig. 7a. If the shakedown limits are replotted against a velocity factor α, defined as V/V_{cr}, the two cases will coincide with each other (Fig. 7b). As a result, the shakedown limit is controlled by the velocity factor rather than the values of the train speed.

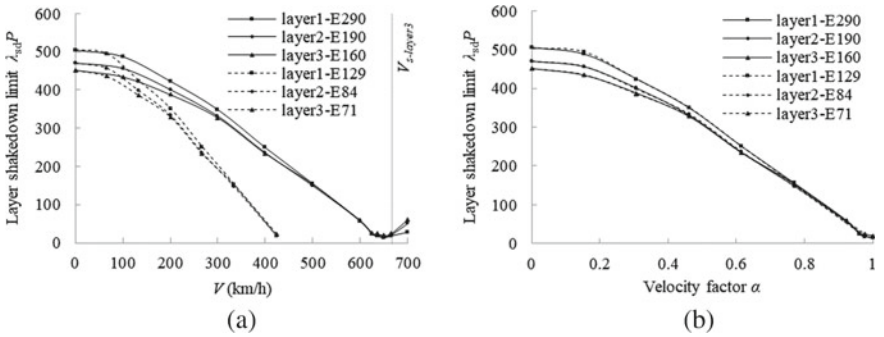

Fig. 7 Effect of train speed on dynamic shakedown limit when $h_2 = 2.3$ m

Indeed, a thicker prepared subgrade benefits to the long-term stability of the substructure. Despite of that, as the train speed is raised, this benefit becomes very limited, as shown in Fig. 8. For the case studied here, the slab track is able to sustain axle loads of 250 kN when the train speed is smaller than 280 km/h. If more loads or a higher train speed are to be applied, increasing the subgrade thickness alone will not help with the situation, because it cannot prevent the accumulating permanent deformation in the second layer. Instead, the material quality of this layer should be improved. More detailed comparisons for the shakedown limits of each layer considering different train speeds can be found in Wang et al. [21].

Figure 9 demonstrates that a decrease of the friction angle of the subsoil leads to a drop of the shakedown limit of the substructure. However, it does not affect the critical speed of the substructure. Therefore, the shakedown limit decreases more significantly with an increasing train speed for the case of a larger friction angle. This implies that though the high friction angle has a positive effect on the long-term stability of the track substructure, one should be very careful when trying to increase the train speed at those cases.

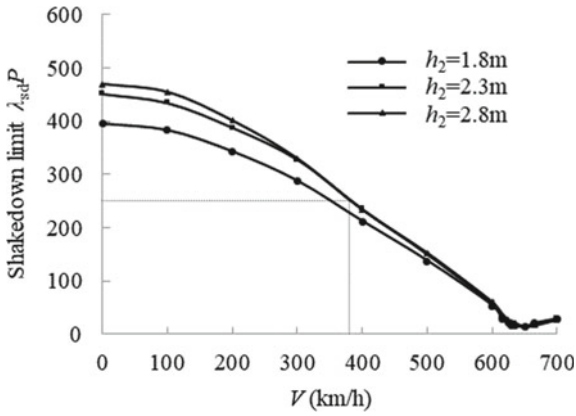

Fig. 8 Effect of subgrade thickness on dynamic shakedown limit

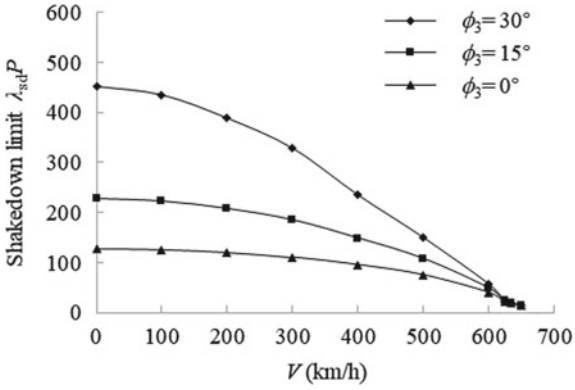

Fig. 9 Effect of friction angle on dynamic shakedown limit when $h_2 = 2.3$ m

4.3 Relationship Between Static and Dynamic Shakedown Limits

The effect of the train speed on the shakedown limit can be quantified by introducing an attenuation factor η, defined as the dynamic shakedown limit for the current speed $\lambda_{sd}^{d}P$ over that of the quasi-static case $\lambda_{sd}^{s}P$, so that the dynamic shakedown limit at any given speed can be estimated according to:

$$\lambda_{sd}^{d}P = \eta\lambda_{sd}^{s}P \tag{20}$$

Figure 10a shows the variation of the attenuation factor against the velocity factor for different values of subsoil friction angle. When the velocity factor is smaller than 0.1, the attenuation factor is close to 1; otherwise, it decreases with the rising velocity factor. Similar trends can be obtained in other cases (Fig. 11). And thus, a fitting equation is proposed as below:

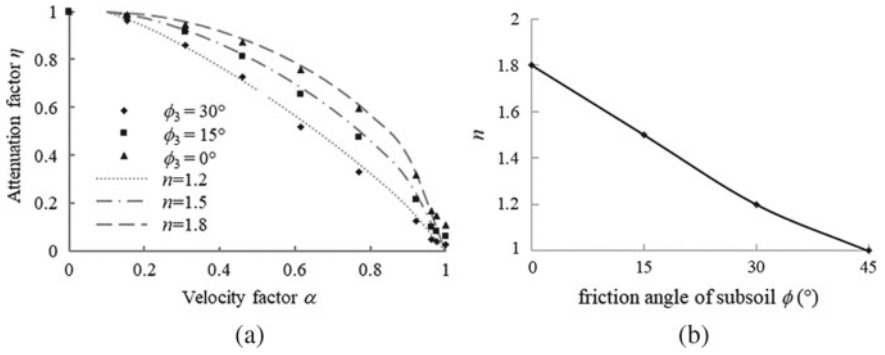

Fig. 10 Variation of attenuation factor when $h_2 = 2.3$ m

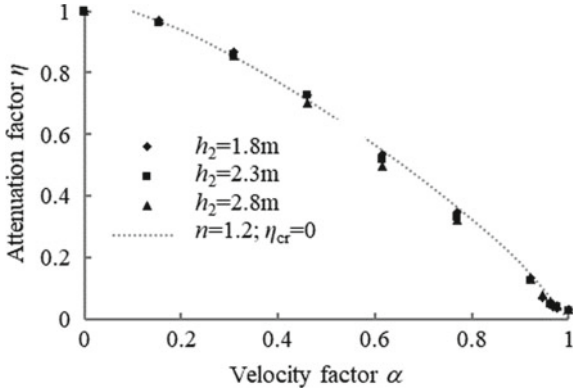

Fig. 11 Effect of subgrade thickness on attenuation factor

$$\eta = \begin{cases} 1 & \text{when } \alpha \le 0.1 \\ (1-\eta_{\mathrm{cr}})\sqrt[n]{1-\left(\frac{\alpha-0.1}{0.9}\right)^n} + \eta_{cr} & \text{when } 0.1 < \alpha < 1 \end{cases} \tag{21}$$

where n is a coefficient depending on the friction angle of the subsoil, the value of which can be obtained from Fig. 10b; η_{cr} is the attenuation factor when $V = V_{\mathrm{cr}}$, the value of which can be taken as 0 in common design situations (exception occurs when the stiffness of subsoil is extremely low compared to the stiffness of the upper layers). Figure 11 also reveals the attenuation factor was barely affected by the thickness of the prepared subgrade.

5 Implications for Design

5.1 Safe Train Speed

In practice, a quick evaluation of the maximum admissible train speed is useful for the design of high-speed railways. One rule-of-thumb approach is to use the 70% of the critical speed of the track [9]. However, in the shakedown analysis of a typical slab track substructure, Fig. 8 demonstrates that a safe train speed should be smaller than 60% of the critical speed, considering axle loads of 250 kN. Therefore, the use of 70% of the critical speed cannot guarantee the long-term stability of the slab track.

5.2 Amplification Factor

In the long-term stability analysis of slab track substructures, it is commonly required to determine the dynamic stresses on soils. For a slab track of good condition, the dynamic effect from rail unevenness or vehicle suspensions system is minor, and

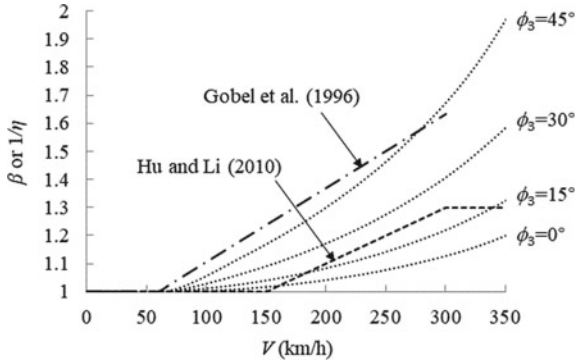

Fig. 12 Comparison with literatures

therefore the dynamic stresses on soils can be obtained by applying an amplified load P^d, which is the product of the static axle load P^s and an amplification factor β:

$$P^{\mathrm{d}} = \beta P^s \tag{22}$$

where β is a function of train speed. A range of values for the amplification factor can be found in literature, as shown in Fig. 12.

It should be noted that the reciprocal of the attenuation factor can be related with the amplification factor, since $P^d \leq \lambda_{sd}^d P$ and $P^s \leq \lambda_{sd}^s P$. If the applied load is the shakedown limit of the slab track substructure (i.e. $P^d = \lambda_{sd}^d P$ and $P^s = \lambda_{sd}^s P$), then

$$\beta = \frac{P^d}{P^s} = \frac{\lambda_{sd}^d P}{\lambda_{sd}^s P} = \frac{1}{\eta} \tag{23}$$

In light of this, $1/\eta$ from the shakedown analysis of the typical slab track substructure is compared with β in literature. A range of subsoil friction angle between 0° and 45° is considered. As can be seen, when the friction angle is 45°, the values of $1/\eta$ are close to the amplification factors of German design code (Gobel et al. 2007 [7]). The amplification factors of Hu and Li [10] are close to the values of $1/\eta$ for the cases of a relatively low friction angle. These results imply that the evaluation of the dynamic effect on the long-term stability of a slab track should have also considered the friction angle of subsoil.

6 Conclusions

Shakedown solutions of typical slab track substructures under moving train loads are presented in this paper. Key findings are summarised below:

1. A quasi-static shakedown condition can be assumed if the moving train velocity is no larger than 10% of the critical speed of the track.

2. Using the dynamic stiffness moduli of soils instead of the stiffness moduli will barely affect the shakedown limit of the substructure, as long as the ratio of layer stiffness maintains.
3. The dynamic shakedown limit at any given train speed can be obtained by multiplying the shakedown limit in the quasi-static situation by an attenuation factor. For typical slab track substructures, the attenuation factor is only dependent on the friction angle of subsoil and velocity factor.
4. A train speed of 70% of the critical speed cannot guarantee the long-term stability of slab tracks.
5. At a given train speed, the amplification factors of the axle load due to the dynamic effect of the train speed can be distinct from each other for the cases of different subsoil friction angle.

Acknowledgements Financial support from National Natural Science Foundation of China (Grant No. 51408326) and Ningbo Natural Science Foundation (Grant No. 2018A61035) is gratefully acknowledged.

References

1. Aboustit, B.L., Reddy, D.V.: Finite element linear programming approach to foundation shakedown. In: Proceedings of the International Symposium on Soils under Cyclic and Transient Loading, vol. 2, pp. 727–738. Swansea (1980)
2. Biot M (1937) Bending of an infinite beam on an elastic foundation. J Appl Mech Trans Am Soc Mech Eng 59: cA1–7
3. Ceradini, G.: Dynamic shakedown in elastic-plastic bodies. J. Eng. Mech. **106**(3), 481-499 (1980)
4. Collins, I.F., Cliffe, P.F.: Shakedown in frictional materials under moving surface loads. Int. J. Numer. Anal. Methods Geomech. **11**(4), 409–420 (1987)
5. Costa, P.A., Lopes, P., Cardoso, A.S.: Soil shakedown analysis of slab railway tracks: numerical approach and parametric study. Transp. Geotech. **16**, 85–96 (2018)
6. Eason, G.: The stresses produced in a semi-infinite solid by a moving surface force. Int. J. Eng. Sci. **2**(6), 581-609 (1965)
7. Gobel, C., Lieberenz, K., Richter, F.: Railway Foundation Engineering (Chinese). Translated by 2nd Railway Survey and Design Institute and PEC+S Group. Railway Publishing House, Beijing, China (2007)
8. Haldar, A.K., Reddy, D.V., Arockiasamy, M.: Foundation shakedown of offshore platforms. Comput. Geotech. **10**(3), 231–245 (1990)
9. Heelis, M.E., Collop, A.C., Dawson, A.R., et al.: Predicting and measuring vertical track displacements on soft subgrades. In: Railway Engineering. London (99 May 1999)
10. Hu, Y.F., Li, N.F.: Subgrade Design Principle of the High-speed Railway of Unballasted Track (Chinese). Railway Publishing House, Beijing, China (2010)
11. Liu, S., Wang, J., Yu, H.S., Wanatowski, D.: Shakedown solutions for pavements with materials following associated and non-associated plastic flow rules. Comput. Geotech. **78**, 218–266 (2016)
12. Liu, S., Wang, J., Yu, H.S., Wanatowski, D.: Shakedown for slab track substructures with stiffness variation. Geotech. Res. **5**(1), 31–38 (2018)

13. Liu, S., Wang, J.: Application of shakedown theory in track substructure design. Proc. Inst. Civi. Eng. Ground Improv. **172**(2), 116–123 (2019)
14. Melan, E.: Der spannungsgudstand eines Henky-Mises Schen Kontinuums Bei Verlandicher Belastung. Sitzungberichte der Ak Wissenschaften Wie **47**(73) (1938)
15. Nguyen, A.D., Hachemi, A., Weichert, D.: Application of the interior-point method to shakedown analysis of pavements. Int. J. Numer. Methods Eng. **75**, 414–439 (2008)
16. Ponter, A.R.S., Hearle, A.D., Johnson, K.L.: Application of the kinematical shakedown theorem to rolling and sliding point contacts. J. Mech. Phys. Solids **33**, 339–362 (1985)
17. Raad. L., Weichert, D., Najm, W.: Stability of multilayer systems under repeated loads. Transp. Res. Rec. **1207**, 181–186 (1988)
18. Sadrekarimi, J., Akbarzad, M.: Comparative study of methods of determination of coefficient of subgrade reaction. Electron. J. Geotech. Eng. **14**(s1–6), 211–216 (2009)
19. Sharp, R.W., Booker, J.R.: Shakedown of pavements under moving surface loads. J. Transp. Eng. **110**(1), 1-14 (1984)
20. Vesic, A.B.: Bending of beams resting on isotropic elastic solid. J. Eng. Mech. **87**(2), 35–54 (1961)
21. Wang, J., Liu, S., Yang, W.: Dynamics shakedown analysis of slab track substructures with reference to critical speed. Soil Dyn. Earthq. Eng. **106**, 1–13 (2018)
22. Wang, J., Yu, H.S.: Shakedown analysis for design of flexible pavements under movingloads. Road. Mater. Pavement Des. **14**, 703–722 (2013)
23. Wang, J., Yu, H.S.: Shakedown and residual stresses in cohesive-frictional half-space under moving surface loads. Geomech. Geoeng. Int. J. **8**, 1–14 (2013)
24. Wang, J., Yu, H.S.: Three-dimensional shakedown solutions for anisotropic cohesivefrictional materials under moving surface loads. Int. J. Numer. Anal. Methods Geomech. **38**, 331–348 (2014)
25. Yu, H.S., Wang, J.: Three-dimensional shakedown solutions for cohesive-frictional materials under moving surface loads. Int. J. Solids Struct. **49**, 3797–3807 (2012)
26. Yu, H.S.: Three-dimensional analytical solutions for shakedown of cohesive-frictional materials under moving surface loads. Proc. R Soc. A Math. Phys. Eng. Sci. **461**, 1951–1964 (2005)
27. Yu, H.S., Hossain M.Z.: Lower bound shakedown analysis of layered pavements using discontinuous stress fields. Comput Methods Appl. Mech. Eng. **167,** 209–222 (1998)
28. Zhuang, Y., Wang, K.Y.: Three-dimensional shakedown analysis of ballasted railway structures under moving surface loads with different load distributions. Soil. Dyn. Earthq. Eng. **100**, 296–300 (2017)

Investigations of Shakedown in the Presence of Ambient Creep Using Direct Methods for High Strength Steel Under Multiaxial Loadings

Daniele Barbera, Ali Charbal, I. Soner Cinoglu, and Natasha Vermaak

Abstract Life integrity assessment of industrial components often requires investigations of the cyclic inelastic response at a range of operating temperatures. Some high strength steels exhibit a well-known ambient temperature creep behaviour, which can also impact the cyclic behaviour, especially under long-term operation. In this study, a direct method known as the Linear Matching Method has been used to predict the cyclic shakedown and ratchet limits of high-strength steel (AISI 1144). The numerical predictions are compared with a recent testing campaign that was completed at room temperature to characterise the multiaxial behaviour of AISI 1144. Due to creep of the material, inelastic strain accumulation is also observed for loading conditions within the shakedown limit. The extended Direct Steady Cyclic Analysis (eDSCA) approach has been used to predict the cyclic behaviour in the presence of creep. In addition, for specific load cases of interest, a newly revised creep-ratcheting limit has been derived and compared with the experimental tests.

Keywords Shakedown · Ratcheting · Room temperature creep · Linear matching method

1 Introduction

The life integrity of engineering components is affected by several factors related to the environmental and operational conditions, including repeated multiaxial loadings where creep strains may be simultaneously occurring. The interaction between fatigue and creep, usually at high-temperature [1–7], has been widely investigated experimentally and numerically. Also, effects on crack initiation [8–11], propagation [12–14] and also for creep-ratcheting limit calculations [15] have been explored.

D. Barbera (✉)
School of Engineering, University of Glasgow, Glasgow G12 8QQ, UK
e-mail: daniele.barbera@glasgow.ac.uk

A. Charbal · I. Soner Cinoglu · N. Vermaak
Mechanical Engineering & Mechanics Department, Lehigh University, Bethlehem, PA 18015, USA

A. A. Pisano et al. (eds.), *Direct Methods*, Lecture Notes in Applied and Computational Mechanics 95, https://doi.org/10.1007/978-3-030-48834-5_12

However, the effect of creep at low temperature in conjunction with fatigue has only been marginally investigated. For example, different creep models based on simplified inelastic deformation responses [16, 17] or considering more refined models accounting for stress and strain rate effects [18], or microstructural states [19] have been applied in titanium alloys. For high-strength steels, the importance of creep at room temperature has been well-established [16, 20–23]. For example, Oehlert and Atrens [16], highlighted its impact on low temperature environmental assisted crack growth.

Whenever a component is subjected to cyclic loads within the plastic regime it can exhibit a series of responses. A simple way to graphically represents these responses has been proposed by Bree [24], who introduced the interaction diagram. In his work, the combination of a primary and secondary load can produce elastic response, elastic shakedown, alternating plasticity (plastic shakedown), ratcheting and plastic collapse. The shape of the bounding limits between these responses can change drastically depending on the structural and material behaviour [25]. In particular, creep at high temperature is known to introduce ratcheting due to the accumulation of inelastic strain, even when the loading conditions are expected to be in the elastic shakedown domain. This mechanism, which is also known as cyclic-enhanced-creep, has been widely addressed [15, 26, 27]. Despite the different mechanisms that drive room temperature creep, it is reasonable to expect a similar interaction between cyclic plasticity and creep. The additional inelastic strain accumulated may interact with the crack growth process making the creep-fatigue interaction more difficult to be assessed. In contrast to high-temperature creep, inelastic deformation at low temperature is generally neglected or not considered in assessment procedures. This is because the likelihood of having a major failure due to the sole contribution of this mechanism is very low. However, when considering the effect of cyclic loading and the potential interaction with more detrimental environmental mechanisms, neglecting inelastic deformation at room temperature may lead to inaccurate integrity assessments.

Typically structural assessment is done using coupled non-linear kinematic and isotropic hardening models. However, these models require non-trivial parameter calibration and are computationally expensive. This is particularly significant in design cases where only the stabilised response is required. To overcome these issues, a series of numerical procedures [28, 29] have been developed to efficiently determine cyclic plastic behaviours, including shakedown limit calculations. One of the most successful numerical methods that have been developed is the Linear Matching Method (LMM) [30, 31]. Besides, the LMM Framework (LMMF) [32] provides not only an accurate and robust numerical procedure for shakedown limit calculations but it has been extended to assess plastic limits, ratcheting, and also creep-rupture, creep-fatigue, and creep-shakedown interactions. For the case of shakedown within the creep regime, there is a dearth of creep-shakedown experiments available to demonstrate the importance of these interactions.

In the present work, the focus will be on the use of the LMMF to gain insight into the steady-state cycle and full creep-cyclic shakedown or plasticity interactions for recent ambient experiments on high strength steels (AISI 1144) [33]. AISI 1144

carbon steel cylindrical bars were subjected to ambient cyclic tension with nonzero mean stress and constant torque. In particular, the LMMF is used to identify the cyclic response, first without considering creep, to obtain shakedown and ratcheting limits. For the predicted shakedown domain, the extended Direct Cycle Analysis approach within LMMF is used to predict the creep behaviour. This analysis leads to the identification of cyclic behaviour with creep and allows for the modification of the shakedown limits. The numerical results are compared with experimentally observed cyclic behaviours. Finally, a new creep-ratcheting limit is obtained and compared with the AISI 1144 experiments.

2 High Strength Steel Material Response

Recently, ambient cyclic multiaxial tests were performed on high strength steel bars to demonstrate macroscopic shakedown behaviour [33]. However, in Charbal et al. [33], it was also found that cyclic creep was active in the loading regime explored. This complicated the interpretation and analysis of shakedown determination. In the following, numerical studies are presented to aid interpretation of the cyclic inelastic responses observed and in additional loading scenarios not experimentally attempted. Below, some of the experimental results from [33] are repeated and summarized for comparison with the numerical analysis in the following sections.

2.1 Monotonic and Cyclic Multiaxial Tests

Charbal's cyclic multiaxial experiments [33] were inspired by the shakedown experiments from Heitzer et al. [34] on hollow cylindrical ferritic steel tubes for the nuclear industry. In [33], in contrast to Heitzer et al. [34], solid cylindrical rods of a common high strength AISI 1144 medium carbon steel (ASTM A29, A311, A510) were tested. This was done to illicit non-homogeneous stress-states and add a structural aspect to the tests. In particular, the rods were subjected to cyclic tension with nonzero mean stress and constant torque at room temperature. The AISI 1144 rods were machined to the dimensions shown in Fig. 1 (ASTM E8, A370, E466) [35]. All tests were performed on a servo-hydraulic MTS multiaxial rig (MTS 319.25) and controlled

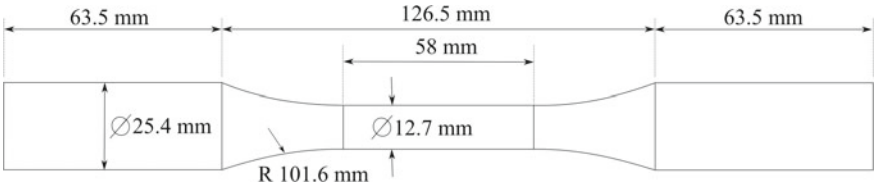

Fig. 1 Solid AISI 1144 rods used for multiaxial testing. Dimensions are in mm [33]

Table 1 Axial-torsional shakedown test program for AISI 1144 specimens

Load case	F_R (kN)	T_R (N-m)	□ΔF (kN)
Sample 1, Case #1	87	90	2
Sample 1, Case #2	90	90	2
Sample 1, Case #3	94	90	2
Sample 1, Case #4	98	90	2

via MTS FlexTest 40 and Multipurpose Software. Monotonic tests were conducted at an applied strain rate of 1×10^{-5} 1/s and the Young's Modulus was found to be E = 204 GPa and the elastic limit was 750 MPa. A stereo digital image correlation (DIC) system was used to acquire 3D surface displacement and strain fields in the gage section [33]. The acquisition frequency allowed for 10 images per loading cycle to be recorded. The DIC images were analysed using the CAD-based stereo DIC software and procedures described in references [36–38] across a region of interest at the tube axis (approximately 510 pixels across 12.7 mm).

Cyclic axial-torsional tests consisted of three stages: (1) an initial ramp in force (F_R) at a rate of 350 N/s (2.75 MPa/s). (2) A ramp in torque, T, at a rate of 210 N-mm/s (1.3 MPa/s) to achieve a target equivalent mean stress. After the ramp in torque, the final level was held constant for the remainder of the tests. A short dwell period at this stage with both force and torque held constant (for 1 min) was used to check for instrumentation stability before the cyclic stage of the testing program commenced. (3) The axial force was cycled around the target equivalent mean stress, with a frequency (f) that was the same rate as that applied in the initial ramp phase. A total of 150 load cycles were performed for each cyclic test. Note that during the cycling of force the torque remained constant. A list of the subset of experimental results [33] that are the focus of this article is given in Table 1. The mean force (F_R), maximum torque (T_R), and cyclic force amplitude (□ΔF) are provided. Note that the cyclic testing method from Lemaitre and Chaboche (Chap. 5) was applied such that each AISI 1144 sample was tested at several equivalent stress levels, increasing in severity (Fig. 2).

3 Numerical Schemes for Shakedown and Ratcheting Limit Analysis

To gain additional insight into the experimental responses due to cyclic loading (Table 1), a numerical upper bound approach is applied to determine which regime (shakedown, ratcheting, etc.) is expected under the loads applied.

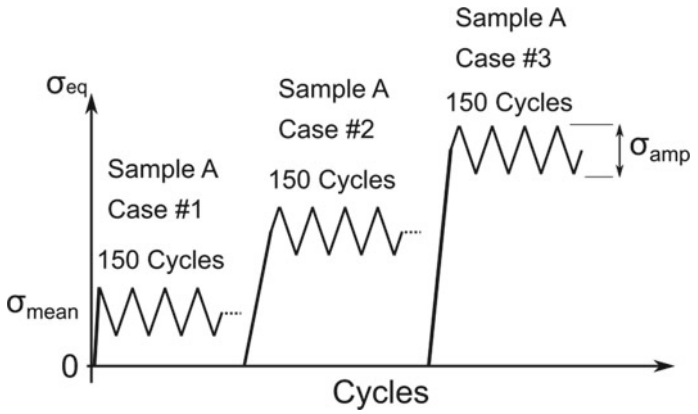

Fig. 2 Representation of the loading program for a single specimen with multiple load cases (Table 1) [33, 38]

3.1 Shakedown and Ratchet Limit

The theory behind the calculation of the upper bound shakedown limit is based on the well-known Koiter theorem [39]. Here the numerical implementation is briefly introduced and more details can be found in [30–32]. When calculating the shakedown limit the material is considered elastic-perfect plastic, and the material is contained in a generic domain. A crucial point resides in the definition of a loading history that affects the generic domain and that can be defined as an elastic stress field $\hat{\sigma}_{ij}$. This elastic stress field is associated with the combined effect of different elastic stress fields $\hat{\sigma}_{ij}^{\theta}$ and $\hat{\sigma}_{ij}^{P}$ (secondary and primary, respectively). To construct a wide range of loading histories, each field is multiplied by a load multiplier λ:

$$\lambda\hat{\sigma}_{ij} = \lambda\hat{\sigma}_{ij}^{\theta} + \lambda\hat{\sigma}_{ij}^{P} \tag{1}$$

The Linear Matching Method (LMM) uses the kinematic theorem developed by [39], which can be expressed by the incompressible and kinematically admissible strain rate history. The key feature resides in the integral definition of the compatible strain increment $\Delta\varepsilon_{ij}^{c}$, which is given by the integration of the strain rate $\dot{\varepsilon}_{ij}^{c}$. Based on this, the shakedown limit can be determined by calculating the load multiplier that makes the following equality valid:

$$\lambda_{shakedown} \int_V \int_0^{\Delta t} \left(\hat{\sigma}_{ij}\dot{\varepsilon}_{ij}^{c}\right) dt dV = \int_V \int_0^{\Delta t} \sigma_{ij}^{c}\dot{\varepsilon}_{ij}^{c} dt dV \tag{2}$$

This definition incorporates the applied loading history by considering the linear elastic stress field $\hat{\sigma}_{ij}$ for $\lambda = 1$, the stress at yield σ_{ij}^{c} associated with the strain rate

history $\dot{\varepsilon}_{ij}^{c}$. Combining the associated flow rule, the shakedown limit multiplier λ_{sh} can then be calculated by the following equation:

$$\lambda_{sh} = \frac{\int_V \int_0^{\Delta t} \sigma_y(t) \cdot \bar{\dot{\varepsilon}}\left(\dot{\varepsilon}_{ij}^{c}\right) dt dV}{\int_V \int_0^{\Delta t} \left(\hat{\sigma}_{ij} \cdot \dot{\varepsilon}_{ij}^{c}\right) dt dV} \tag{3}$$

where $\sigma_y(t)$ is the yield stress of the material depending on the temperature at each integration point. The two integral formulations shown in the Eq. (3) are volume integrals and can be easily estimated by using the plastic energy dissipation calculated by a finite element software tool like Abaqus.

This type of problem involves interacting loads and a monotonic minimisation of the shakedown multiplier. This is done by performing a series of subsequent linear analyses, where the first plastic strain rate (that can be seen as an initial guess) is used to generate a new strain history $\dot{\varepsilon}_{ij}^{c}$ as it is shown in Eqs. (4–5),

$$\dot{\varepsilon}_{ij}^{c\prime} = \frac{1}{\mu}\left(\lambda_{sh}^{i}\hat{\sigma}_{ij} + \bar{\rho}_{ij}^{c}\right)'$$

$$\dot{\varepsilon}_{kk}^{c} = 0 \tag{4}$$

$$\mu = \frac{\sigma_y}{\bar{\dot{\varepsilon}}^{i}} \tag{5}$$

where the notation ($'$) refers to the deviatoric component of stress and strain. The new strain rate will be calculated by accounting for the scaled elastic stress history and the associated constant residual stress field $\bar{\rho}_{ij}^{c}$. To match the behaviour between the linear and nonlinear materials, a matching condition must be adopted, and it is shown in the Eq. (5). The shear modulus μ is defined as the ratio between the yield stress σ_y and the equivalent strain rate $\bar{\dot{\varepsilon}}^{i}$. By integrating over the cycle time Eq. (4) the strain increment over the cycle is obtained:

$$\Delta\epsilon_{ij}^{c\prime} = \frac{1}{\bar{\mu}}\left(\bar{\rho}_{ij}^{c} + \sigma_{ij}^{in}\right)' \tag{6}$$

$$\sigma_{ij}^{in} = \bar{\mu}\left(\int_0^{\Delta t} \frac{1}{\mu(t)}\lambda_{sh}^{i}\hat{\sigma}_{ij}(t)dt\right)$$

$$\frac{1}{\bar{\mu}} = \int_0^{\Delta t} \frac{1}{\mu_n} dt \tag{7}$$

where $\Delta\varepsilon_{ij}^{c}$ is the plastic strain increment. Equation (7) includes the elastic stress components scaled σ_{ij}^{in} based on the previous shakedown multiplier and $\bar{\mu}$ is the overall shear modulus over the cycle time Δt. The load multiplier λ_{sh}^{f} can be obtained using the strain rate history $\dot{\varepsilon}_{ij}^{c}$ in the Eq. (3). As mentioned before, this is an iterative process, and at each increment, the new shakedown limit must satisfy the inequality: $\lambda_{sh}^{f} \leq \lambda_{sh}^{i}$.

When the ratcheting limit needs to be calculated, a similar procedure to that adopted for the shakedown limit can be used. However, the cyclic elastic stress solution needs to also consider the changing residual stress field and not only a constant one. The entire minimisation process aims to minimise the total changing residual stress field by scaling the load multiplier that can be calculated as follows:

$$\lambda_{rat} = \frac{\int_V \int_0^{\Delta t} \sigma_y(t) \cdot \bar{\dot{\varepsilon}}\left(\dot{\varepsilon}_{ij}^{c}\right) dt\, dV - \int_V \int_0^{\Delta t} \left(\hat{\sigma}_{ij}(t) + \rho_{ij}(t)\right) \cdot \dot{\varepsilon}_{ij}^{c}\, dt\, dV}{\int_V \int_0^{\Delta t} \left(\hat{\sigma}_{ij} \cdot \dot{\varepsilon}_{ij}^{c}\right) dt\, dV} \tag{8}$$

The second volume integrals added in Eq. (8) contain the response of the body subjected to the cyclic load history for the associated change of residual stress during the loading cycle. This process produces a reduction or an increase of the load multiplier if the component is going or not going to exhibit ratcheting. As for the shakedown limit multiplier, this process shows a monotonic reduction of the upper bound limit multiplier.

3.2 *Direct Cyclic Analysis with Creep*

The calculation of the steady-state cycle of a structure under combined creep and cyclic plasticity has been developed by [40, 41] and further tested by [42, 43]. The key idea is to calculate with an iterative minimisation process the changing residual stress and the constant one. This function is associated with a class of kinematically admissible strain rates $\dot{\varepsilon}_{ij}^{c}$, defined for L total number of loading instances and takes the form of $I\left(\dot{\varepsilon}_{ij}^{c}\right) = \sum_{l=1}^{L} I^{l}$. Its incremental form is expressed:

$$I^{l}\left(\Delta\varepsilon_{ij}^{l}\right) = \int_V \left\{\sigma_{ij}^{l}\Delta\varepsilon_{ij}^{l} - \left[\hat{\sigma}_{ij}^{l}(t_l) + \rho_{ij}^{l}(t_l)\right]\Delta\varepsilon_{ij}^{l}\right\} dV \tag{9}$$

where $\rho_{ij}^{l}(t_l)$ is the residual stress for each load point considered and it is obtained by the sum of the constant residual stress and the changing residual stress $\bar{\rho}_{ij}$ (which is calculated by the sum of all the previous changing residual stress field increments

$\Delta\rho_{ij}(t_l)$). This makes it possible to replace the strain rate history $\dot{\varepsilon}_{ij}^{c}$ with a series of increments of strain $\Delta\varepsilon_{ij}^{l}$, which occur during the cycle at each time t_o. The inelastic strain increment $\Delta\varepsilon_{ij}^{l}$ is then obtained by minimizing the function shown in the Eq. (9). A total of K cycles are required to reach convergence and within each k cycle, a total of L sub-cycles need to be performed. At each increment, the residual stress and inelastic strain are calculated based on the elastic stress and the previous accumulated residual stresses. When the load instance does not contain a creep dwell, the plastic strain increment $\Delta\varepsilon_{ij,k+1}(t_l)$ can be calculated by:

$$\Delta\varepsilon_{ij,k+1}(t_l)' = \frac{1}{2\bar{\mu}(t_l)}\left[\hat{\sigma}_{ij}(t_l) + \rho_{ij,k+1}(t_{l-1}) + \Delta\rho_{ij,k+1}(t_l)\right]' \tag{10}$$

where the notation ($'$) again refers to the deviatoric component of stress and strain, $\bar{\mu}$ is the iterative shear modulus [40], $\hat{\sigma}_{ij}$ is the associated elastic solution, $\rho_{ij,k+1}(t_{l-1})$ is the prior changing residual stress history and $\Delta\rho_{ij,k+1}(t_l)$ is the current changing residual stress associated with the inelastic strain increment. The plastic strain calculated is used to iteratively change the yield stress in the upcoming $k+1$ sub-cycle, considering a Ramberg-Osgood material response. In load cases where creep is present, the equivalent creep strain increment $\Delta\bar{\varepsilon}^{c}$ is calculated by the following equation for the associated dwell time Δt using the Norton-Bailey relation:

$$\Delta\bar{\varepsilon}^{c} = \frac{B(n-1)\Delta t^{m+1}(\bar{\sigma}_s - \bar{\sigma}_c)}{(\frac{1}{\bar{\sigma}_c^{n-1}} - \frac{1}{\bar{\sigma}_s^{n-1}})(m+1)} \tag{11}$$

where B, m and n are the creep constants of the material. $\bar{\sigma}_c$ represents the creep flow stress, which is the sum of the start-of-dwell stress $\bar{\sigma}_s$ and the residual stress $\Delta\rho_{ij,k+1}(t_l)$ caused by the dwell period. The creep flow stress is determined by accurately evaluating the creep strain rate $\dot{\bar{\varepsilon}}^{F}$ at the end of the dwell time:

$$\begin{aligned}
\bar{\sigma}_c &= \left(\frac{\dot{\bar{\varepsilon}}^{F}}{B\Delta t^{m}}\right)^{\frac{1}{n}} \\
\dot{\bar{\varepsilon}}^{F} &= \frac{\Delta\bar{\varepsilon}^{c}}{\Delta t}\frac{(m+1)}{(n-1)}\frac{\bar{\sigma}_c^{n}}{(\bar{\sigma}_s - \bar{\sigma}_c)}\left(\frac{1}{\bar{\sigma}_c^{n-1}} - \frac{1}{\bar{\sigma}_s^{n-1}}\right)
\end{aligned} \tag{12}$$

The residual stress at each increment is calculated via the solution of linear problems. The residual stress field and the iterative shear modulus obtained are updated for the subsequent cycle $k+1$ for each load instance t_l using the following relation:

$$\bar{\mu}_{k+1}(x, t_l) = \bar{\mu}_k(x, t_l)\frac{\sigma_y^{R}(x, t_l)_k}{\bar{\sigma}\left(\hat{\sigma}_{ij}(x, t_l) + \rho_{ij}^{r}(x, t_l)_k\right)} \tag{13}$$

where $\bar{\mu}_k(x, t_l)$ is the iterative shear modulus at the sub-cycle k for the lth load instance. $\sigma_y^R(x, t_l)_k$ is the iterative von-Mises yield stress associated with the flow rule considered at load instance t_l. When during a load instance creep occurs, the von-Mises yield stress must be replaced by the creep flow stress, which has been defined in Eq. (13). The last term $\rho_{ij}^r(x, t_l)_k$ is the summation of the constant residual stress field and the associated total changing residual stresses associated with the different load instances.

4 Experimental Results

For each of the load cases outlined in Table 1, below are plots of the axial stress versus axial strain used to determine the macroscopic safe shakedown or undesirable cyclic inelastic responses. Sample 1 Case #1 with $F_R = 87$ kN and $T_R = 90$ kN-m is presented in Fig. 3a, Sample 1 Case #2 with $F_R = 90$ kN and $T_R = 90$ kN-m is in Fig. 3b, and Sample 1 Case #3 with $F_R = 94$ kN and $T_R = 90$ kN-m is shown in Fig. 3c, It can be seen that in Fig. 3a,b and c the peak inelastic strains all continue to gradually increase with cycles and time, indicating accumulation of inelastic strain similar to ratcheting. However, for Sample 1 Case #4 ($F_R = 98$ kN and $T_R = 90$ N-m, Fig. 3d), an abrupt increase of inelastic strain is observed after the first

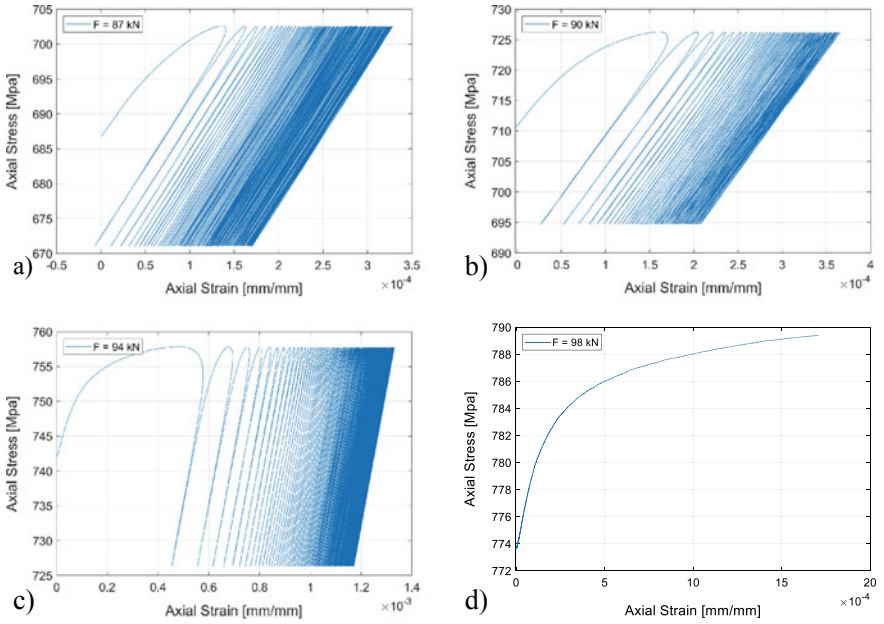

Fig. 3 Cyclic axial response of the four samples subjected to different axial cyclic force. **a** 87, **b** 90, **c** 94, **d** 98 kN and constant torque 90 kN mm (see Table 1)

cycle is nearly completed, and there is an apparent "failure" at a peak axial stress. This "failure" feature is an experimental artefact of the control software program that aborted the test if more than 6% strain was reached (to protect the extensometer). This cut-off limit in strain was set as a reasonable approximation to approaching ultimate collapse.

4.1 Cyclic Creep

By further examining the equivalent stress-strain response, it was found that significant rounding of the response curves during unloading was present for all of the loading cases in the test program (Table 1); this is a classic indicator for creep during cyclic loading [20, 44, 45]. An example from [33] is repeated here for reference (Fig. 3). The testing method proposed by Taleb and Cailletaud [20] (that is used to distinguish contributions to inelastic strain from time-dependent cyclic creep and from the time-independent accumulation of cyclic plastic strain) was used to further confirm that creep was the source of the cyclic accumulation of inelastic strain exhibited in the testing program (additional cyclic creep tests not shown) [33]. Indeed, cyclic loading induced creep at room temperatures and general ambient creep are well-established behaviours that have been reported elsewhere for different steels including some carbon steels [16, 20–23] (Fig. 4).

5 Numerical Results and Discussion

5.1 Numerical Model

To reproduce the results obtained within the experimental tests, a 3D bar is used as a finite element model, as shown in Fig. 5a. The mesh is composed of 16,848 quadratic quadrilateral elements C3D20R, with a reduced integration scheme. The mesh size has been biased to refine within the centre of the specimen. Two mechanical loads are applied, a cyclic force and a constant moment on the top gripping section of the specimen. Both the cyclic and constant mechanical loads are applied and their loading histories are shown in Fig. 5b (when creep is considered, the force is kept constant for a certain dwell time). A cyclic force $\Delta F = 2kN$ is applied and a constant axial force and torque are used to define the loading history. The bar is not exposed to any thermal gradient and the temperature is not changed. The elastic and inelastic material properties for this high strength steel are presented in Table 2.

The load history is simplified and constructed considering only the vertices of the load space diagram. This assumption is made considering that most of the plastic behaviour occurs at these extremes; this is ensured by the use of the von Mises yield condition for which plastic strain can accumulate only at these vertices. However,

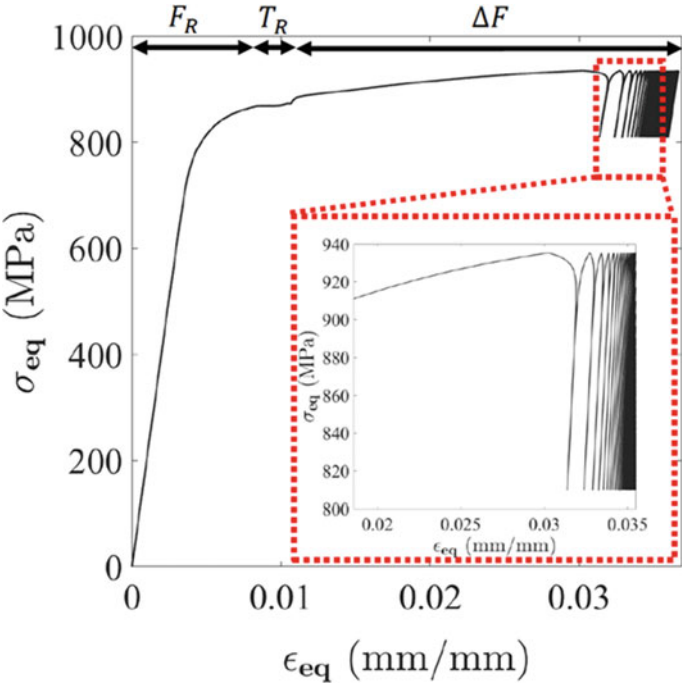

Fig. 4 A representative equivalent stress-strain response exhibited in all sample tests (Table 1; this case corresponds to $F_R = 110$ kN and $T_R = 20$ N-m with $\Delta F = 8$ kN [33]). The rounding of the curves during unloading is highlighted as a signature of cyclic creep [20, 44, 45]

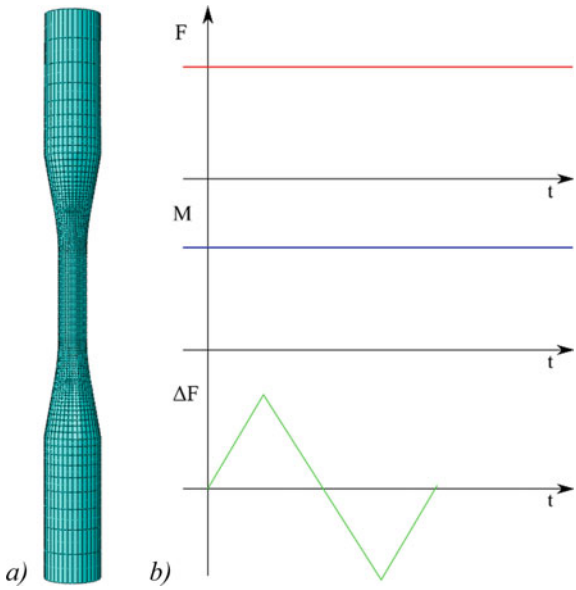

Fig. 5 **a** 3D numerical finite element model with associated mesh. **b** Loading history in force (F), torque (T or M), and cyclic force (ΔF) over time (t) adopted during the experiment [33] and numerical tests

Table 2 AISI 1144 material properties

Young's modulus (MPa)	Poisson's ratio	0.2% Proof stress (MPa)
204,000	0.3	750
Ramberg-Osgood Multiplier B [MPa]	1221.6	
Ramberg-Osgood Exponent α	0.0606	
Norton-Bailey multiplier A [MPa^{-1} s^{-1}]	$2.0e^{-21}$	
Norton-Bailey stress exponent n	5.26	
Norton-Bailey time exponent m	−0.743	

within this work creep also occurs during the cycle, without the presence of a constant load creep dwell. To simulate this, a numerical creep dwell is considered at the loading peak stress for a time equal to the cycle period.

5.2 Shakedown and Ratchet Limits

The first investigation done has been the calculation of the plastic limit load using an elastic-perfectly-plastic material model, which ensures an approximate but unique solution to the plastic collapse limit for both the axial and torque loads. Two separate analyses have been performed and each load has been applied for each load condition. The limit load due to the axial force is FL = 107 kN and the one due to the moment is ML = 261 kN mm. These two loads have been used to normalise the interaction diagram derived subsequently and shown in Fig. 6. In the interaction diagram depicted in Fig. 6, the upper bound and lower bound for the shakedown limit are shown. The solid circles are associated with the different experiments performed at an increasing level of axial force, as described in Table 1. It is interesting to see that all the experimental tests except for the one at 98 kN, are well within the shakedown limit. The 98 kN experiment is at the lower bound limit but still within the upper bound.

To add further insight into the cyclic plastic response of the specimens, a ratchet analysis has been performed. Due to the type of loading conditions and the load combinations, ratcheting and plastic collapse limits nearly overlap. Moreover, due to the type of loading conditions (two primary loads), the ratchet limit coincides exactly with the shakedown upper bound. In the case of two primary loads, this overlapping of ratcheting and upper bound shakedown limits has also been observed in other works [46]. Nevertheless, the calculated limits correspond with what has been experimentally observed: where the load case close to the upper bound (Sample 1

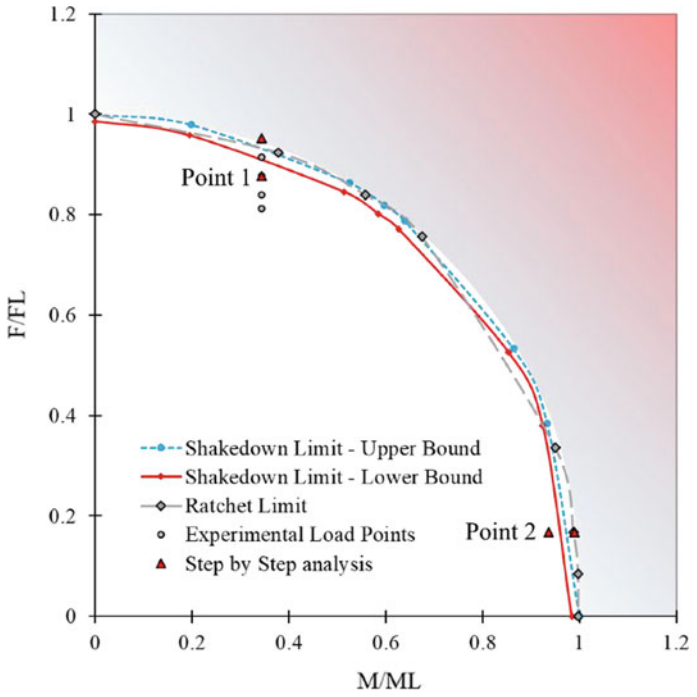

Fig. 6 Shakedown and Ratchet limits for the specimens subjected to combined constant moment and axial force and cyclic mean stress

Case #4, Table 1) suffers premature "failure" (reaching 6% cut-off strain approaching ultimate collapse).

To further verify these numerical predictions, four step-by-step analyses have been done using Abaqus. The results are shown in Fig. 7, where the plastic strain history is depicted for load point 1 and 2. In both cases a strict elastic shakedown behaviour is shown, confirming the shakedown limit determined via LMM. When the step-by-step analysis is performed outside the LMM shakedown limit, the response is a nearly instantaneous collapse. The analyses for the two load points outside the limit show a critical plastic strain accumulation that culminated with plastic collapse and more precisely with the impossibility to maintain equilibrium in the model. This once again is expected due to the nature of the loading conditions. However, as seen in the experimental section, for all the experimental load points within the shakedown limit, a ratcheting-like response has been observed (continued accumulation of inelastic strain with cycling).

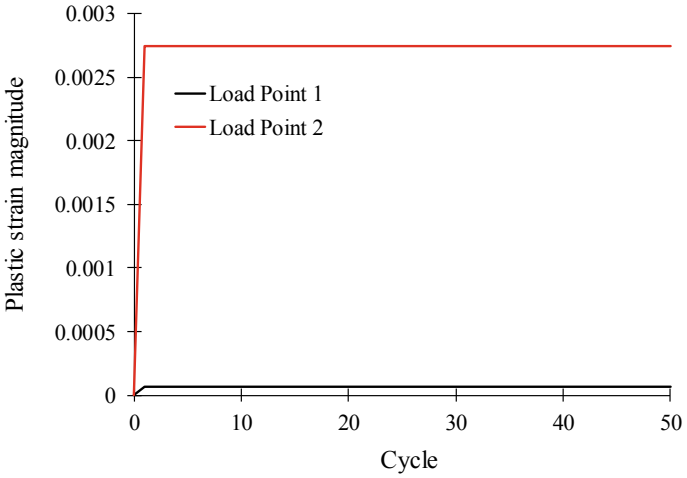

Fig. 7 Plastic strain magnitude for load point 1 and 2 within the shakedown limit with no creep considered

5.3 Limit Analysis Considering Creep

The analyses performed in the previous sections suggest that the inelastic strain accumulation observed during the experiments must be associated with the room temperature creep that occurs during the cyclic loading [33]. To predict this behaviour, the extended Direct Steady Cyclic Analysis method (eDSCA) within the Linear Matching Method Framework (LMMF) [32] has been used to calculate the cyclic response of the specimen due to the interaction between room temperature creep and fatigue. The creep dwell time has been set to the period of each cycle, which is around 23 s and it is calculated as a single dwell occurring at the peak stress. This assumption allows the use of the current formulation of the LMM and in the worst-case scenario yields a conservative result.

The four load cases (Table 1) have a constant and equal torque applied but an increasing axial force. The ratchet strain per cycle is calculated for the stabilised response and results are shown in Fig. 8a. The mechanism, as expected, is concentrated in the specimen's gauge and tends to localise as soon as the ratcheting strain becomes more severe. The increase of axial load tends to exacerbate the creep ratcheting mechanisms and any subsequent increase leads to a very large inelastic strain accumulation. This numerical trend matches the experimental observations, especially for Sample 1 Case #4.

To better compare the numerical solution with the experimental results, the maximum ratchet strain per cycle predicted is reported along with the experimental one in Fig. 9. In the eDSCA, creep strain is usually considered during a fixed time during which the load is kept constant. However, creep during the experiment occurs during the entire loading cycle, which has an overall length of 23 s. If the creep dwell

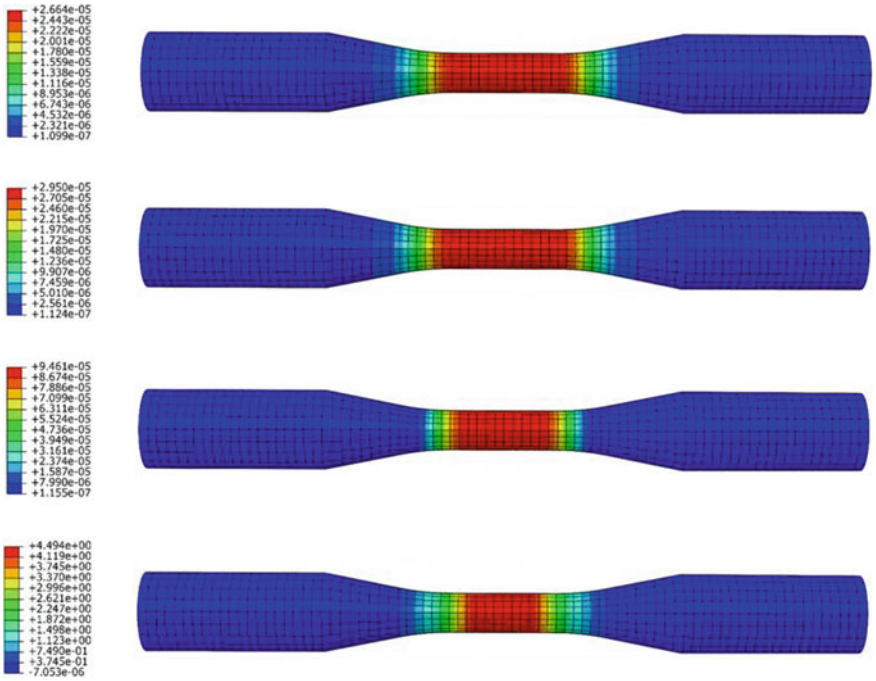

Fig. 8 Contours of ratchet strain per cycle with combined creep and cyclic plasticity

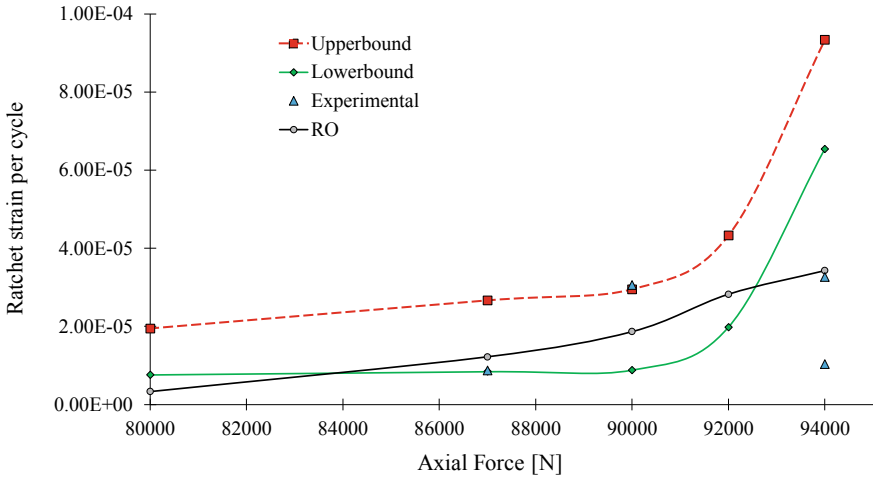

Fig. 9 Maximum ratchet strain per cycle predicted using creep dwell at tensile peak (upper bound) and intermediate tensile stress (lower bound) along with experimental tests performed [33] and limits obtained with Ramberg Osgood model

is considered starting at the maximum tensile stress, results could be too conservative. For this reason, two numerical cases have been considered, one with the creep dwell starting at the tensile peak and the second one with the creep dwell starting at the half of the maximum tensile peak. This approach, despite it being an approximation, gives confidence bounds in which experimental results should be located.

As it can be seen in Fig. 9, the two numerical cases do indeed bound the experimental behaviour at lower axial loads. However, for an applied force of 98 kN (Sample 1 Case #4) the predictions overestimate the ratcheting strain. This is due to the increasing impact of plasticity over creep with the associated increasing axial force. Also, these predictions are obtained using the elastic-perfectly-plastic material (EPP) model, that does not consider hardening. Also, the increase of the primary axial load causes the structure to approach its plastic limit (that for EPP models coincides with the ratchet limit); this causes the exponential growth of the ratcheting strain rate. When material hardening is considered via the use of the Ramberg Osgood model (RO) the results are less conservative and closer to the experiments. In particular, when the axial force increases the hardening limits, the plastic strain accumulated and the ratcheting is due to the increasing effect of creep strain.

5.4 Discussion: Extended Creep-Ratcheting Limit

At the moment in the literature, there is not an efficient method to derive the creep ratcheting limit of a structure subjected to a cyclic load and a creep dwell. It is important to emphasize why this remains challenging. Unlike classical plastic-ratcheting, creep-ratcheting is not only affected by the cyclic plastic behaviour, but also by the creep response and creep dwell time. Time in plastic-ratcheting does not make any difference since the response is time-independent. When creep is introduced, an additional amount of inelastic strain is accumulated within a cycle. This affects the response of cyclic load cases, even if these are chosen within the nominal shakedown domain. Despite these challenges, it is possible to use a combination of the extended Direct Steady Cycle Analysis (eDSCA) and python coding to estimate the creep ratcheting limit of a structure.

In Fig. 10a, both plastic and estimated creep-ratcheting (eDSCA) limits are reported. Calculating numerically the creep-ratcheting limit is very challenging. In general, ratcheting is caused by the presence of a non zero changing residual stress at the end of the cycle. An algorithm that allows the minimisation of the associated residual stress field is used to calculate the load multiplier. However, this approach is not feasible when creep is the cause of ratcheting. To estimate the creep ratcheting limit, the numerical ratchet strain per cycle is compared to the ratcheting strain per cycle observed experimentally at the lowest loading condition. The ratio between the numerical and experimental ratchet strain per cycle was then used to assess the cyclic behaviour and if required change the load multiplier for the elastic solution. This process was repeated automatically via a Python code.

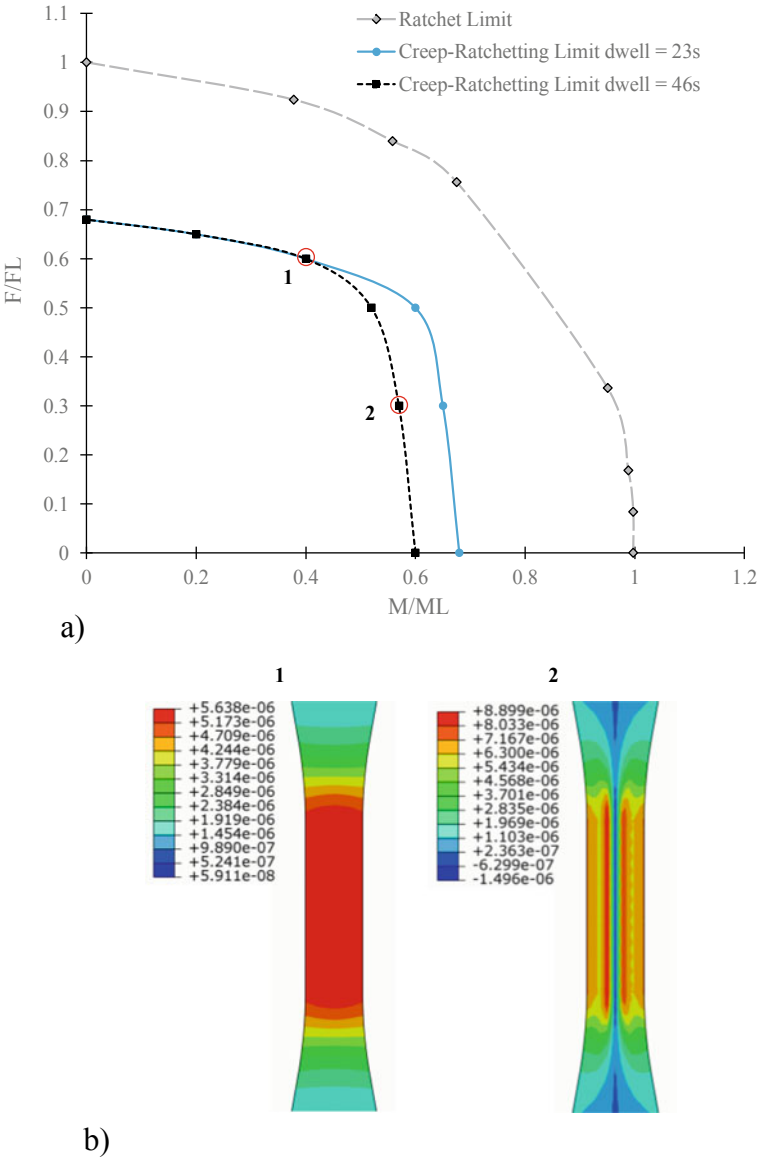

Fig. 10 **a** Plastic ratchet limit and creep ratcheting limits for two different numerical dwells, **b** ratchet strain per cycle at cyclic load point 1 and 2

By comparing the plastic and creep-ratcheting limits it is evident that creep tends to promote the accumulation of inelastic strain even at low load levels. It is important to clarify that when creep-ratcheting calculations have been used to identify the point of interception with the x and y-axes, these are not limit loads but only creep-ratchet limit points. This is due to the shift in the underlying inelastic mechanism from plastic to creep driven ratcheting. By comparing the limits calculated, a significant loss of around 30–40% in terms of non-ratcheting area is estimated for an equivalent creep dwell of 23 s. This trend was also observed in the experiments that show substantial ratcheting-like behaviour (accumulation of inelastic strain) for load cases within the nominal expected shakedown limit (not considering creep).

In an attempt to guide future experiments that could probe the creep-ratcheting domain, a second creep-ratcheting limit is calculated for an equivalent dwell time of 46 s. The results obtained show that for the low level of the applied moment the ratchet limit is not affected. For this case the response is elastic and the creep strain accumulated is very small due to the low level of stress present. This changes drastically when increasing the applied constant moment. A split is visible between the two curves after point 1 (Fig. 10a). Different mechanisms occur for point 1 and point 2 as it is shown in Fig. 10b. When the axial force is dominant (point 1) the entire cross-section tends to be uniformly affected, leading to a homogeneous strain accumulation along the cross-section. By point 1 the moment starts to dominate, leading to an inelastic strain peak in a circumferential area near the centre. The interaction between these two types of the mechanical load is the cause of asymmetry between the two axes in the Bree-like load interaction diagram shown in Fig. 10a. Figure 10a shows very well the impact of dwell time and more specifically of loading frequency on the inelastic strain accumulation. Due to the effect of time over the creep-ratcheting limit, it is evident that a unique creep-ratcheting limit is not possible as it is for plastic ratcheting. A three-dimension domain will be more representative for creep-ratcheting, due to the impact of dwell time, which plays a crucial role in the definition of the mechanism.

6 Conclusions

The Linear Matching Method Framework has been used to provide insight for recent experiments on the cyclic inelastic response of high strength steel rods under room temperature multiaxial loadings. A Bree-like load interaction diagram is constructed and numerical limits for plastic collapse, elastic shakedown, plastic-ratcheting, and creep-ratcheting are compared with the experimental loading cases and macroscopic inelastic strain accumulation with cycling. The models also confirm that the experimental load cases would exhibit shakedown if not for the presence of ambient creep. Regardless, it is found that for design and assessment purposes, the extended Direct Steady Cyclic Analysis method (eDSCA) within the Linear Matching Method Framework (LMMF) can provide bounds or conservative estimates for the ratchet (inelastic) strain per cycle observed experimentally. The effects of the loading conditions, which

include axial force and applied moment, have been evaluated demonstrating their impact over creep ratcheting. Applied moment and dwell times demonstrated to be more detrimental for the creep-ratcheting.

Acknowledgements Dr. Barbera gratefully acknowledges the support of the University of Glasgow and the Vermaak Lab's experimental work was supported, in part, by the Air Force Office of Scientific Research (AFOSR) under award number FA9550-16-1-0438.

References

1. Odqvist, F.K.G.: Mathematical theory of creep and creep rupture. Clarendon Press (1974)
2. Klueh, R., King, J.: Creep and creep rupture of ERNiCr-3 weld metal. J. Nucl. Mater. **98**(1–2), 173–189 (1981)
3. Ainsworth, R., Budden, P.: Design and assessment of components subjected to creep. J. Strain Anal. Eng. Des. **29**(3), 201–207 (1994)
4. Spindler, M.: The multiaxial creep ductility of austenitic stainless steels. Fatigue Fract. Eng. Mater. Struct. **27**(4), 273–281 (2004)
5. Saber, M., et al.: Determination of creep and damage properties for P92 at 675 C. J. Strain Anal. Eng. Des. **46**(8), 842–851 (2011)
6. Isobe, N., Yashirodai, K., Murata, K.I.: Creep damage assessment for notched bar specimens of a low alloy steel considering stress multiaxiality. Eng. Fract. Mech. **123**, 211–222 (2014)
7. Haque, M.S., Stewart, C.M.: A novel sin-hyperbolic creep damage model to overcome the mesh dependency of classic local approach Kachanov-Rabotnov model. In: ASME 2015 International Mechanical Engineering Congress and Exposition. American Society of Mechanical Engineers (2015)
8. Holdsworth, S.: Creep-fatigue failure diagnosis. Materials **8**(11), 5418 (2015)
9. Oh, C.-S., et al.: Creep failure simulations of 316H at 550 C: part I-A method and validation. Eng. Fract. Mech. **78**(17), 2966–2977 (2011)
10. Priest, R., et al.: Creep–fatigue assessment of a welded steel component. In: Creep: Characterization, Damage and Life Assessments, Lake Buena Vista (1992), pp 423–429
11. Sauzay, M., et al.: Creep-fatigue behaviour of an AISI stainless steel at 550 °C. Nucl. Eng. Des. **232**(3), 219–236 (2004)
12. Hyde, T.H., Saber, M., Sun, W.: Creep crack growth data and prediction for a P91 weld at 650 °C. Int. J. Press. Vessels Pip. **87**(12), 721–729 (2010)
13. Narasimhachary, S.B., Saxena, A.: Crack growth behavior of 9Cr − 1Mo (P91) steel under creep–fatigue conditions. Int. J. Fatigue **56**, 106–113 (2013)
14. Yatomi, M., Davies, C.M., Nikbin, K.M.: Creep crack growth simulations in 316H stainless steel. Eng. Fract. Mech. **75**(18), 5140–5150 (2008)
15. Porowski, J.S., O'Donnell W.J.: Creep ratcheting bounds from extended elastic core concept. In: Conference: International Conference on Structural Mechanics in Reactor Technology. Berlin, F.R. Germany, 13 Aug 1979. O'Donnell and Associates, Inc., Pittsburgh, PA (USA). Medium: ED; Size, pp. 18 (1979)
16. Oehlert, A., Atrens, A.: Room temperature creep of high strength steels. Acta Metall. Mater. **42**(5), 1493–1508 (1994)
17. Liu, C., et al.: Room temperature creep of a high strength steel. Mater. Des. **22**(4), 325–328 (2001)
18. Krempl, E.: An experimental study of room-temperature rate-sensitivity, creep and relaxation of AISI type 304 stainless steel. J. Mech. Phys. Solids **27**(5–6), 363–375 (1979)
19. Neeraj, T., et al.: Phenomenological and microstructural analysis of room temperature creep in titanium alloys. Acta Mater. **48**(6), 1225–1238 (2000)

20. Taleb, L., Cailletaud, G.: Cyclic accumulation of the inelastic strain in the 304L SS under stress control at room temperature: ratcheting or creep? Int. J. Plast **27**(12), 1936–1958 (2011)
21. Pilo, D., et al.: Cyclic induced creep of a plain carbon steel at room temperature. Fatigue Fract. Eng. Mater. Struct. **1**(3), 287–295 (1979)
22. Evans, J., Parkins, R.: Creep induced by load cycling in a C-Mn steel. Acta Metall. **24**(6), 511–515 (1976)
23. Deibler, L.A.: Room temperature creep in metals and alloys. Sandia National Lab (2014)
24. Bree, J.: Elastic-plastic behaviour of thin tubes subjected to internal pressure and intermittent high-heat fluxes with application to fast-nuclear-reactor fuel elements. J. Strain Anal. Eng. Des. **2**(3), 226–238 (1967)
25. Barbera, D., Chen, H., Liu, Y.: On creep fatigue interaction of components at elevated temperature. J. Press. Vessel Technol. **138**(4), 041403–041403 (2016)
26. Bradford, R.A.W., Ure, J., Chen, H.F.: The Bree problem with different yield stresses on-load and off-load and application to creep ratcheting. Int. J. Press. Vessels Pip. **113**, 32–39 (2014)
27. O'Donnel, W., Porowski, J.: Upper bounds for accumulated strains due to creep ratcheting. WRC Bull. **195**, 57–62 (1974)
28. Spiliopoulos, K.V., Panagiotou, K.D.: A residual stress decomposition based method for the shakedown analysis of structures. Comput. Methods Appl. Mech. Eng. **276**, 410–430 (2014)
29. Peng, H., Liu, Y., Chen, H.: Shakedown analysis of elastic-plastic structures considering the effect of temperature on yield strength: theory, method and applications. Eur. J. Mech. A. Solids **73**, 318–330 (2019)
30. Chen, H.F., Ponter, A.R.S., Ainsworth, R.A.: The linear matching method applied to the high temperature life integrity of structures. Part 1. Assessments involving constant residual stress fields. Int. J. Pressure Vessels Pip. **83**(2), 123–135 (2006)
31. Chen, H.F., Ponter, A.R.S., Ainsworth, R.A.: The linear matching method applied to the high temperature life integrity of structures. Part 2. Assessments beyond shakedown involving changing residual stress fields. Int. J. Pressure Vessels Pip. **83**(2), 136–147 (2006)
32. Barbera, D., et al.: Recent developments of the linear matching method framework for structural integrity assessment. J. Pressure Vessel Technol. **139**(5), 051101–051101-9 (2017)
33. Charbal, A., I.S.C., Vermaak, N.: Multiaxial shakedown analysis of structures using stereo digital image correlation. Submitted (2019)
34. Heitzer, M., et al.: Shakedown and ratchetting under tension–torsion loadings: analysis and experiments. Nucl. Eng. Des. **225**(1), 11–26 (2003)
35. ASTM International.: E8/E8M-09 Standard test methods for tension testing of metallic materials. West Conshohocken, PA; ASTM International (2009). https://doi.org/10.1520/E0008_E0008M-09
36. Beaubier, B., et al.: CAD-based calibration and shape measurement with stereo DIC. Exp. Mech. **54**(3), 329–341 (2014)
37. Dufour, J.-E., et al.: CAD-based displacement measurements with stereo-DIC. Exp. Mech. **55**(9), 1657–1668 (2015)
38. Charbal, A., C.I.S., Hild, F., Roux, S., Vermaak, N.: Stereo-DIC formalism considering brightness and contrast effects: application to torsional loadings. Under review (2019)
39. Koiter, W.T.: General theorems for elastic-plastic solids. North-Holland Amsterdam (1960)
40. Chen, H., Chen, W., Ure, J.: A direct method on the evaluation of cyclic steady state of structures with creep effect. J. Press. Vessel Technol. **136**(6), 061404–061404 (2014)
41. Chen, H., Ponter, A.R.: Linear matching method on the evaluation of plastic and creep behaviours for bodies subjected to cyclic thermal and mechanical loading. Int. J. Numer. Meth. Eng. **68**(1), 13–32 (2006)
42. Barbera, D., Chen, H., Liu, Y.: Creep-fatigue behaviour of aluminum alloy-based metal matrix composite. Int. J. Press. Vessels Pip. **139**, 159–172 (2016)
43. Gorash, Y., Chen, H.: Creep-fatigue life assessment of cruciform weldments using the linear matching method. Int. J. Press. Vessels Pip. **104**, 1–13 (2013)
44. Yoshida, F.: Uniaxial and biaxial creep-ratcheting behavior of SUS304 stainless steel at room temperature. Int. J. Press. Vessels Pip. **44**(2), 207–223 (1990)

45. Hassan, T., Taleb, L., Krishna, S.: Influence of non-proportional loading on ratcheting responses and simulations by two recent cyclic plasticity models. Int. J. Plast. **24**(10), 1863–1889 (2008)
46. Cho, N.-K., Chen, H.: Cyclic plasticity behavior of 90° back-to-back pipe bends under cyclic bending and steady pressure. In: 2018 26th International Conference on Nuclear Engineering. American Society of Mechanical Engineers Digital Collection (2018)